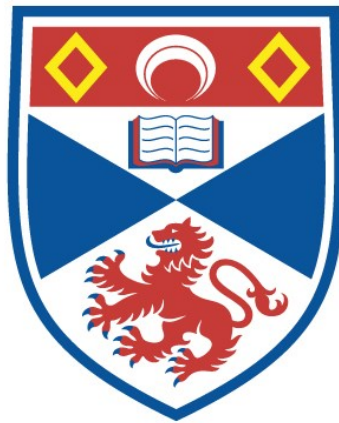


SECOND HARMONIC GENERATION IN SODIUM
VAPOUR INDUCED BY A MAGNETIC FIELD

Bruce David Sinclair

A Thesis Submitted for the Degree of PhD
at the
University of St Andrews



1987

Full metadata for this item is available in
St Andrews Research Repository
at:

<http://research-repository.st-andrews.ac.uk/>

Please use this identifier to cite or link to this item:

<http://hdl.handle.net/10023/13925>

This item is protected by original copyright

SECOND HARMONIC GENERATION
IN SODIUM VAPOUR
INDUCED BY A MAGNETIC FIELD

A thesis presented by
Bruce D. Sinclair, BSc.
to the
University of St Andrews
in application for the degree of
Doctor of Philosophy
April 1987



ProQuest Number: 10166961

All rights reserved

INFORMATION TO ALL USERS

The quality of this reproduction is dependent upon the quality of the copy submitted.

In the unlikely event that the author did not send a complete manuscript and there are missing pages, these will be noted. Also, if material had to be removed, a note will indicate the deletion.



ProQuest 10166961

Published by ProQuest LLC (2017). Copyright of the Dissertation is held by the Author.

All rights reserved.

This work is protected against unauthorized copying under Title 17, United States Code
Microform Edition © ProQuest LLC.

ProQuest LLC.
789 East Eisenhower Parkway
P.O. Box 1346
Ann Arbor, MI 48106 – 1346

TH A600

DECLARATIONS

I, Bruce David Sinclair, hereby certify that this thesis has been composed by myself, that it is a record of my own work, and that it has not been accepted in partial or complete fulfilment of any other degree or professional qualification. I was submitted to the Faculty of Science of the University of St Andrews under Ordinance General Number 12 in October 1983, and as a candidate for the degree of Ph.D. in April 1984.

In submitting this thesis to the University of St Andrews I understand that I am giving permission for it to be made available for public use in accordance with the regulations of the University Library for the time being in force, subject to any copyright vested in the work not being affected thereby. I also understand that the title and abstract will be published, and that a copy of the work may be made and supplied to any bona fide library or research worker.

B. D. Sinclair
April 1987

I hereby certify that Bruce David Sinclair has fulfilled the conditions of the Resolution and Regulations appropriate to the degree of Ph.D.

M. H. Dunn
Research Supervisor
April 1987

ABSTRACT

A high resolution study of magnetic-field-induced second harmonic generation in sodium vapour was performed using a single-frequency continuous-wave dye laser. Resonant enhancement was obtained by tuning the laser to the frequency of the 3S - 4D two-photon transition of the sodium atoms. Coherent parametric emission of the second harmonic radiation occurred in the presence of a symmetry-breaking magnetic field by means of a coherent electric-quadrupole emission at twice the laser frequency.

A theoretical model of the second harmonic generation (SHG) was developed, and includes the roles played by atomic selection rules, Zeeman splitting and eigenfunction mixing in a magnetic field, and the effects of homogeneous and inhomogeneous broadening.

The use of a single-frequency laser and an atomic nonlinear medium allowed an experimental investigation of a SHG process in unprecedented detail. This provided a stringent test of the theoretical model developed to predict the properties of the nonlinear interaction in terms of fundamental atomic parameters. The excellent agreement obtained between theoretical and experimental results vindicated the theoretical methods used in the modelling.

Line profiles of the SHG at different magnetic field strengths and laser polarisations were measured, and, for the first time, were not limited by the laser linewidth. Although the two-photon absorption line profile was due to $\Delta m_l = 0, \pm 1, \pm 2$ transitions, the quadrupole moments which

generated the second harmonic polarised perpendicular and parallel to the magnetic field were associated with only the $\Delta m_l = \pm 2$ and ± 1 transitions respectively. This was the first direct observation of the differences in selection rules between such processes. The modelled line profiles were in good agreement with experiment, and successfully predicted the squared dependence of the second harmonic (SH) power on magnetic field strength at fields less than 0.05 T, and the saturation of this dependence at higher fields. The latter effect was due to saturation of the state mixing and to Zeeman shifting moving transitions into and out of resonance. When both moments were driven the SH experienced magnetic-field-dependent rotation of polarisation and deviation from linear polarisation; this is the first study to report the considerable variation of the magnitudes of these effects across the line profile. These observations were in excellent agreement with the theoretical model, which explained the polarisation changes in terms of variations in the relative phases and magnitudes of the two moments.

The SH power was proportional to the square of the sodium density at atomic densities below 2×10^{20} atoms m^{-3} , and oscillatory thereafter, due to phase velocity mismatching. Increasing the argon buffer gas pressure caused a sharp drop in the SH power when the homogeneous linewidth exceeded the Doppler width. Finally, magnetic-field-induced SHG was used for the first time as a particle density probe, measuring the sodium density distribution in the oven.

TO MY PARENTS,

who have given me their love
for as long as experimental
nonlinear optics has existed.

CONTENTS

ABSTRACT

CONTENTS

ACKNOWLEDGMENTS

1	INTRODUCTION	
1.1	Introduction to nonlinear optics	1.1
1.2	Second harmonic generation in crystals and vapours	1.3
1.3	Introduction to magnetic-field-induced second harmonic generation in sodium vapour	1.8
2	REVIEW OF SECOND HARMONIC GENERATION AND RELATED PROCESSES IN VAPOURS	
2.1	Theoretical overview of second harmonic generation in quantised media	2.1
2.2	Electric-field-induced mixing processes	2.7
2.3	Three-wave-mixing processes with no external symmetry-breaking	2.22
2.4	Quadrupole radiation	2.30
2.5	Non-collinear quadrupole sum frequency mixing	2.33
2.6	Magnetic-field-induced three-wave mixing	2.37

3	THEORETICAL MODELLING OF MAGNETIC-FIELD-INDUCED SECOND HARMONIC GENERATION	
3.1	Description of the atomic eigenstates and eigenenergies	3.1
	The 3S states	3.2
	The 3P states	3.8
	The 4D states	3.8
3.2	Detailed theory of magnetic-field-induced second harmonic generation	3.12
4	EXPERIMENTAL APPARATUS AND TECHNIQUES	
4.1	Introduction	4.1
4.2	Dye laser system	4.1
	The dye laser	4.1
	Monitoring devices	4.3
	Data collection	4.5
4.3	Other apparatus	4.6
	Production of the metal vapour	4.6
	Production of the magnetic field	4.14
	Detection of the second harmonic	4.15
4.4	Spectroscopic techniques	4.17
	Saturated absorption spectroscopy	4.18
	Two-photon spectroscopy	4.20

5	MEASUREMENT OF THE PROPERTIES OF MAGNETIC-FIELD-INDUCED SECOND HARMONIC GENERATION IN SODIUM VAPOUR	
5.1	Initial considerations	5.1
	Basic properties of the second harmonic generation	5.1
	Measurement of the homogeneous and inhomogeneous linewidths of the $3S - 4D$ transition	5.4
5.2	Second harmonic power dependence on sodium atom density	5.10
5.3	Line profiles	5.17
5.4	Variation of the power and polarisation properties of the second harmonic with magnetic field	5.36
5.5	Second harmonic power dependence on the fundamental polarisation	5.43
5.6	Investigation of the asymmetry of the second harmonic line profiles in high magnetic fields	5.45
5.7	Effects of temperature change	5.53
5.8	Effects of changes in the buffer gas pressure	5.55
5.9	Use as a particle density probe	5.64
6	SUMMARY AND FINAL DISCUSSION	
6.1	Summary	6.1
6.2	Relevant future work	6.5

APPENDICES

A	Plasma dispersion function
B	Computer programs for modelling the second harmonic generation
C	Computerised system for data collection and analysis
D	Computer programs for data collection and analysis
E	Spectroscopic studies of the sodium dimer

REFERENCES

ACKNOWLEDGMENTS

I wish to thank my research supervisor, Dr Malcolm Dunn, for his guidance and encouragement throughout the course of this work, and I gratefully acknowledge his numerous useful suggestions made during our "chats". I am also grateful to Mr Alistair Poustie for his assistance with the construction of the computerised data collection system and for his help explaining tensor algebra. I thank all the technical staff of the department for their assistance, my fellow researchers for their advice on various matters, and the Science and Engineering Research Council for financial support. My thanks go also to Dr Malcolm Dunn and Dr William Sinclair for reading proofs of this thesis and offering many useful comments. The support of my family and friends over the past few years is also sincerely appreciated.

INTRODUCTION

CHAPTER ONE

INTRODUCTION

1.1 INTRODUCTION TO NONLINEAR OPTICS

Before the advent of the laser, optical electric fields had always been sufficiently weak that the polarisation induced in a medium by such fields was well described as being proportional to the electric field strength. Lasers, however, can produce very intense optical fields due to the high peak powers available, and the ability to focus the coherent laser radiation to a spot a few wavelengths across. In such arrangements, the optical electric field strengths may approach those of the intra-atomic electric fields, and so the polarisation of the atoms in a medium is likely to be markedly nonlinear in its dependence on optical electric field strength.

The first nonlinear effect at optical frequencies was reported by Franken et al in 1961 [1]; they generated the second harmonic frequency of light from a ruby laser, which operated at 694.2 nm, using quartz as the nonlinear medium. A phenomenological description of this, and many other nonlinear effects, may be given by expressing the polarisation \underline{P} induced in the medium as a power series in the incident optical electric field, \underline{E}_w

$$\underline{P} = \epsilon_0 \chi^{(1)} \underline{E}_w + \epsilon_0 \chi^{(2)} \underline{E}_w^2 + \epsilon_0 \chi^{(3)} \underline{E}_w^3 + \dots \quad (1.1.1)$$

The first term represents the well-known linear response of a material with first order susceptibility $\chi^{(1)}$, where ϵ_0 is the vacuum permittivity. The induced polarisation acts as a radiation source. The interaction between the fundamental wave and the wave reradiated at the fundamental frequency

gives rise to the refractive index of the material. If the incident electric field is of the form $E_w = E_{w0} \cos wt$, it is readily seen that the $\chi^{(2)}$ term gives rise to the polarisation $\epsilon_0 \chi^{(2)} E_{w0} (1 + \cos 2wt)/2$, which contains a component at the second harmonic frequency. This oscillating polarisation will then lead to a radiated wave at $2w$, the second harmonic radiation first reported by Franken et al.

Processes relying on the second order susceptibility are known as three-wave mixing processes: two waves interact to produce a third one. This class of effects includes, amongst others, second harmonic generation, sum and difference frequency mixing, optical rectification and parametric oscillation.

In the quarter century since the first generation of an optical harmonic, the field of nonlinear optics has grown rapidly. Nonlinear effects at optical or near-optical frequencies are now important as both useful and limiting processes. For example, stimulated Raman scattering in optical fibres may be used to generate coherent light at a number of wavelengths in the $1.06 \mu\text{m} - 1.6 \mu\text{m}$ region [2], but will also act as a loss mechanism limiting the peak powers that may be transmitted in a fibre optic communication system [3]. Many other experiments have investigated nonlinear effects, and some are reviewed in references 4, 5, and 6. Using these effects, radiation may be generated in regions of the spectrum where no coherent source is directly available. Although many types of nonlinear effects have been demonstrated, the rest of this discussion will be limited to second harmonic generation (SHG) and the closely related phenomena of sum frequency mixing (SFM) and difference frequency mixing (DFM).

Optical second harmonic generation has found particularly wide appeal as it allows the relatively convenient and efficient generation of light at

otherwise unattainable frequencies [7]. Of particular interest locally has been the use of nonlinear crystals to produce the second harmonic of dye laser radiation, thus providing a tunable source of ultraviolet laser light [8, 9].

1.2 SECOND HARMONIC GENERATION IN CRYSTALS AND VAPOURS

If only dipole radiation processes are considered, the generation of even harmonics is not possible in media which possess a centre of symmetry, which is why anisotropic crystalline materials have been the most important nonlinear media for second-harmonic generation.

Consider a medium possessing a centre of inversion. The potential energy, V , of an electron must reflect the symmetry of the medium, and thus in a one-dimensional model

$$V(x) = \frac{m}{2} \omega_0^2 x^2 + \frac{m}{4} A x^4 \quad (1.2.1)$$

where ω_0 and A are constants and m is the electronic mass. The constant A is usually very much less than ω_0 . The restoring force on the electrons may be calculated from the form of this potential and included in the equation of motion of the electrons. This may be solved to give the dependence of the polarisation on an applied field E as

$$\underline{p} \propto a \underline{E} + b \underline{E}^3 + \dots \quad (1.2.2)$$

where a and b are constants. Thus the symmetry of the medium restricts the polarisation to depend on only odd powers of the electric field, and so

the system re-radiates at only the fundamental and odd harmonic frequencies. (This treatment has assumed a dipole nature to the radiating process; if electric quadrupole radiation is considered, the gradient of the electric field is involved. However, if the medium is isotropic, the symmetry is such that the contributions of electric quadrupole processes to the SHG are also zero [10].) Selection rule arguments against collinear SHG in quantised isotropic media are given in section 2.1.

By contrast, in an anisotropic medium such as an asymmetric crystal, the condition $V(x) = V(-x)$ need no longer apply and so the potential of the electron may contain odd powers of x . This is equivalent to saying that a displacement of the electron in one direction may result in a larger restoring force than the same displacement in the opposite direction. In this case, the polarisation of the medium takes the form

$$\underline{p} \propto a \underline{E} + b \underline{E}^2 + c \underline{E}^3 \dots \quad (1.2.3)$$

and thus second harmonic generation and other second order processes are possible. This is discussed further by Franken and Ward [11] and Yariv [12].

Figure 1.2.1(a,b) shows possible relations between the applied electric field and the induced polarisation for a linear medium and for a medium lacking a centre of inversion. These dependences give rise to the polarisation waves shown in parts (c) and (d) of the same figure. The polarisation wave induced in the nonlinear medium may be Fourier analysed to give the components shown in figure 1.2.2. This shows clearly the origin of the polarisation at the second harmonic frequency. The polarisation wave in this medium will then radiate at the fundamental and second harmonic frequencies.

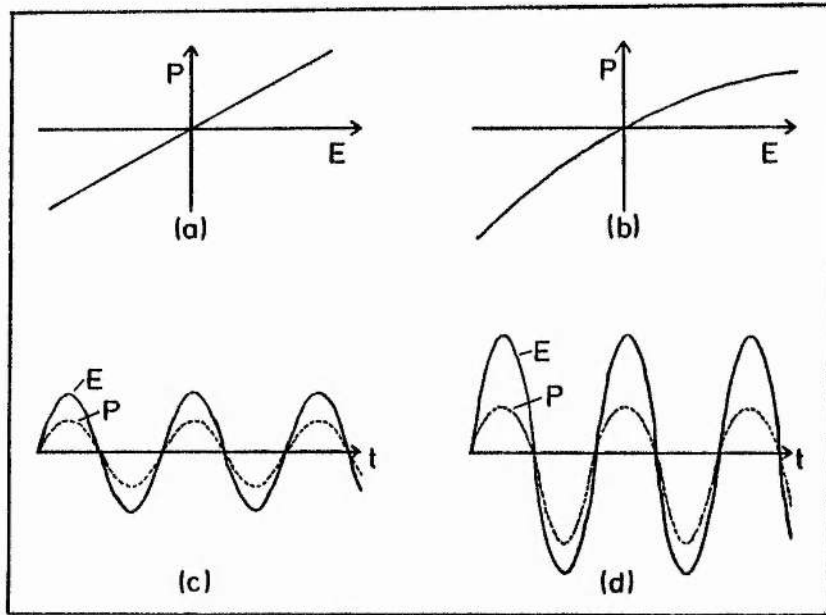


Figure 1.2.1. Schematic diagrams of (a) linear and (b) nonlinear dependences of the polarisation, \underline{P} , on the electric field strength, \underline{E} . If an oscillating electric field of frequency ω propagates through the media the induced polarisation waves will be as shown in (c) and (d) for linear and nonlinear media respectively.

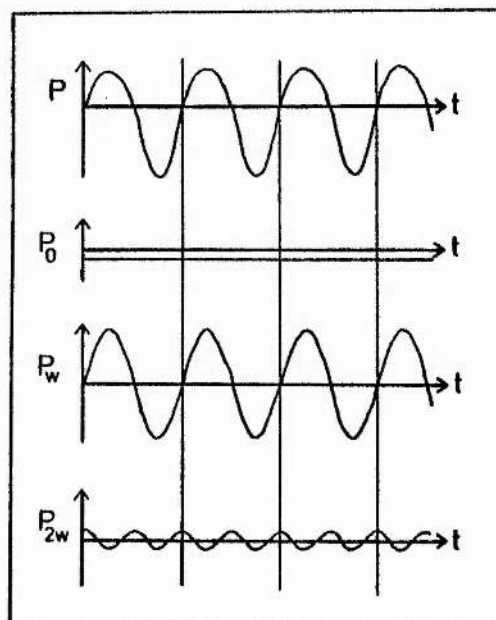


Figure 1.2.2. Fourier analysis of the polarisation wave in part (d) of the previous figure.

In crystals which do not have a centre of inversion, such as quartz or ammonium dihydrogen arsenate, second harmonic generation is therefore possible. In addition, the birefringence of nonlinear crystals may be used to match the phase velocities of the fundamental and second harmonic by compensating for the natural dispersion of the material. Thus most of the work in second harmonic generation has been performed using such crystalline materials. At high optical field intensities the SHG efficiency may be large. For example, one commercially available Nd:YAG laser produces 30 MW peak power of light at $1.06 \mu\text{m}$, and a deuterated potassium di-hydrogen phosphate crystal converts this to the second harmonic at 532 nm with 30% efficiency [13].

Considerable efforts have gone into developing crystals with a large second order susceptibility, good optical quality over several millimetres, good transparency to both fundamental and second harmonic, and sufficient birefringence to satisfy phase matching. The crystalline material must also be able to withstand the high radiation field intensities needed to produce significant quantities of the harmonic radiation [14].

These are stringent limitations, and while good crystalline materials have been developed, they still have certain limitations in transparency range and power handling capabilities. This has led to an increased interest in using gases or vapours as nonlinear media. These have the disadvantages of a low particle density, and an isotropy which leads to a zero second order susceptibility unless some form of symmetry-breaking arrangement is used. However, they do have the advantages that they are reasonably easy to prepare in large volumes with good optical quality, and do not suffer irreversible damage at high optical field intensities. Vapours can be used which have good transparency deep into the ultraviolet; most nonlinear crystals have an absorption edge around 200 nm. As the second order

susceptibility is zero, the most studied effects have been due to the $\chi^{(3)}$ term in equation 1.1.1, and much work has been published on third harmonic generation. To obtain conversion efficiencies comparable with those of doubling in crystals, very large optical field strengths have been used, and frequencies have been chosen to give large resonant enhancement to the third order susceptibility [14].

Recently, a number of experiments have been reported concerning the mixing of two optical fields in a vapour to produce a third field at the sum, difference or second harmonic frequency, despite the restrictions mentioned above. Some means of breaking the isotropy of the vapour was required in each case. This has been achieved by the application of a static electric or magnetic field, by quasistatic electric fields produced by the interaction of the laser pulse and the medium, or by imposing an asymmetry on the system by using a non-collinear beam geometry. The papers describing all such processes are discussed in chapter two in some depth, because no review of this field has been published.

The work on magnetic-field-induced second harmonic generation reported in this thesis is believed to be a significant contribution to the study of such processes, and to fundamental nonlinear optics. The use of a single-frequency laser and an atomic nonlinear medium has allowed for the first time the examination of the properties of a SHG process in such detail as to provide so stringent a test of a theoretical model developed to predict the basic properties of the nonlinear interaction in terms of fundamental atomic parameters.

1.3 INTRODUCTION TO MAGNETIC-FIELD-INDUCED SECOND HARMONIC GENERATION IN SODIUM VAPOUR

As an introduction to the reviews of chapter two, and as an overview of the detailed theoretical treatment given in chapter three, this section first gives a qualitative description of the process of magnetic-field-induced second harmonic generation in sodium vapour. The scheme described is the one used in the bulk of the work in this thesis.

The particular interest in sodium vapour for magnetic-field-induced second harmonic generation is due to the relatively simple nature of such a nonlinear medium, which consists of isolated atoms with well-defined selection rules. The interaction of the laser beam with the atoms of the vapour is amenable to accurate mathematical modelling in terms of fundamental atomic parameters.

Second harmonic generation in the vapour occurs by the simultaneous absorption of two photons from the fundamental beam and the emission of one photon of twice the energy. There need be no static population of the excited states of the atoms in such a conversion process, but near coincidences of the fundamental or second harmonic frequencies with the frequencies of atomic transitions may enhance the SHG by many orders of magnitude. Atomic selection rules, however, restrict which transitions may be used. The energy levels of the sodium atom are shown in figure 1.3.1. Resonant enhancement of the SHG is obtained by tuning the fundamental radiation to half the wavelength of the 3S - 4D two-photon transition in sodium, corresponding to a laser wavelength of 578.7 nm. Although there are no electric-dipole-allowed transitions between the 4D and 3S states, two-photon transitions are allowed, as are single-photon electric-quadrupole transitions.

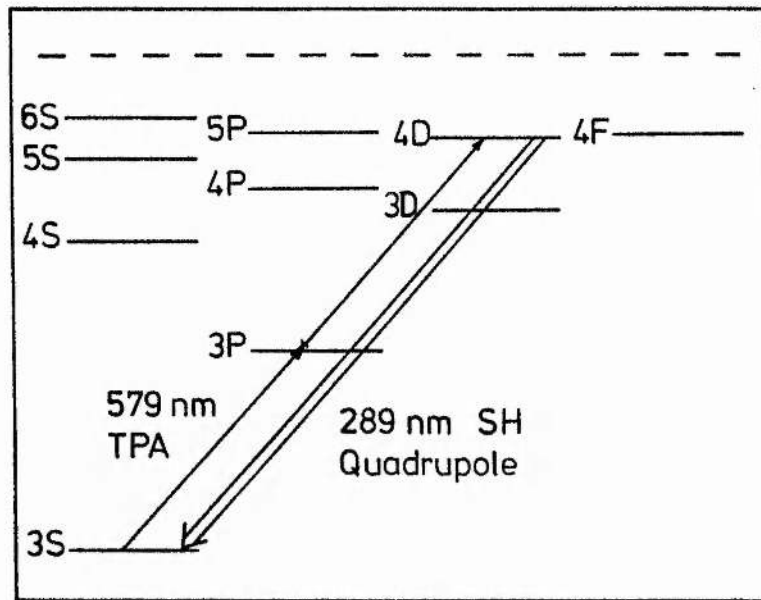


Figure 1.3.1 Energy levels scheme for second harmonic generation in atomic sodium vapour. The dotted line indicates the ionisation potential of the atom. The 3S ground state lies 5.14 eV below this level. There are many other states between the ionisation potential and the highest energy levels shown in the diagram.
 Key:- TPA = two-photon absorption
 SH = second harmonic

In studying radiative transitions in atoms, it is often a very good approximation to consider only single-photon electric-dipole-allowed transitions. However, when this type of transition is forbidden by selection rules, other types of (weaker) transition may become important. Two-photon transitions were first considered by Göppert-Mayer [15]. In such transitions, two photons are absorbed simultaneously; the transition rate is proportional to the square of the intensity of the radiation [16], and the selection rules associated with the transition are similar to those that would be obtained by applying single-photon electric-dipole-transition selection rules twice [17]. Electric-quadrupole transitions are due to oscillating quadrupole charge distributions in the atom, and are usually very much weaker than dipole-allowed transitions. Some of the physics of this type of transition is treated in section 2.4; in particular, it is explained there why the selection rules for quadrupole transitions are

different from those of the much better known electric-dipole-allowed transitions.

The two-photon absorption in the sodium atoms creates quadrupole moments which oscillate at the second harmonic frequency, but in the absence of an external magnetic field these do not radiate into the forward direction. An analysis of the magnetic sublevel populations indicates that the quadrupole emission lobes are perpendicular to the fundamental beam, so no coherent second harmonic may be generated. However, when a transverse magnetic field is applied to the vapour, the isotropy of the system is broken, and the quadrupole emission lobes rotate about the field due to state mixing and Zeeman shifting. This allows coherent generation of the second harmonic in the forward direction.

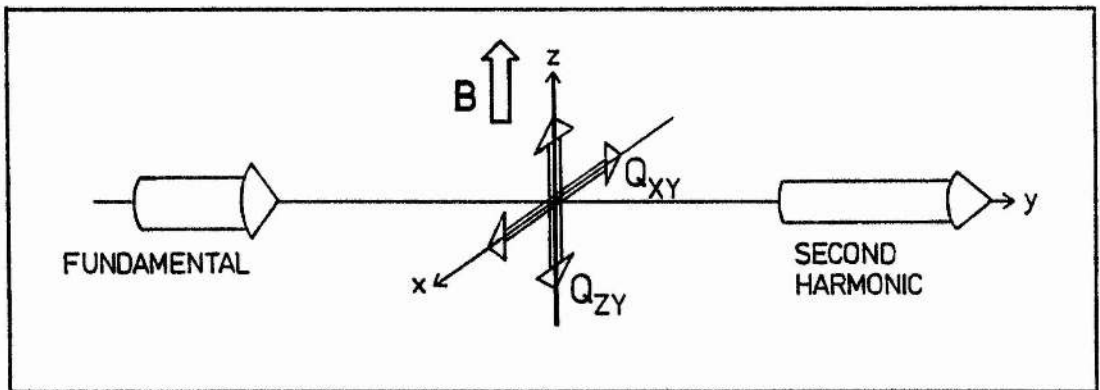


Figure 1.3.2. Geometry used to describe the second harmonic generation process. Q_{xy} and Q_{zy} are the quadrupole moments which act as "effective dipoles" for second harmonic generation.

The geometry used to describe the second harmonic generation process is shown in figure 1.3.2. The two quadrupole moments which may contribute to the second harmonic radiation are Q_{xy} and Q_{zy} . These may be considered to be "effective dipoles" parallel to the x and z axes respectively. The aim of the theoretical modelling of chapter three is to determine the amplitude

and phase of these effective dipoles as functions of the laser frequency and polarisation, the magnetic field strength, and the linewidths of the homogeneous and inhomogeneous broadening. Different magnetic sublevels are involved in the resonant enhancement of the two effective dipoles. Thus as the fundamental frequency is tuned across the enhancing two-photon line profile the relative magnitudes of the two effective dipoles will change as the appropriate magnetic sublevels are moved in and out of resonance. Once the properties of the effective dipoles are determined, the observables of the second harmonic radiation are readily calculated. For example, if the effective dipoles are of the same magnitude, and if the phase difference between them is zero or ninety degrees, the second harmonic radiation will be linearly or circularly polarised respectively.

The theoretical predictions were tested experimentally using the single-frequency dye laser system, which is described in chapter four. The effects on the SHG of the variation of the transverse magnetic field, sodium atom density, laser frequency and polarisation, buffer gas pressure and Doppler width were considered, and theory and experiment were found to be in remarkably good agreement, as shown in chapter five. The bulk effect of phase (mis)matching was also found to be important.

Second harmonic generation may occur only in the region where the laser beam and the magnetic field overlap. At low particle densities the second harmonic intensity is proportional to the square of the sodium atom density in the overlap region. Thus by moving the positions of the laser beam and the magnetic field a three-dimensional profile of the atomic density may be obtained. This was proposed by Dunn [18], and its first experimental use is reported in section 5.9.

A disadvantage of atomic vapours for harmonic generation is the limited

range of tunability of the process. Significant resonant enhancement is obtained over only a few gigahertz around the frequencies of each of a few suitable two-photon transitions. Molecular vapours offer the possibility of many more allowed two-photon transitions and preliminary experiments were performed to assess the suitability of the sodium dimer in vapour form as a nonlinear medium. These studies are outlined in appendix E.

The research reported in this thesis concentrates on the basic physics of the second harmonic generation process. The conversion efficiency, though small, was sufficiently high to enable such experiments to be undertaken. In order for the technique to find many applications, the efficiency and tunability would probably need to be increased; techniques for doing this are outlined in the final chapter.

REVIEW

OF SECOND HARMONIC GENERATION
AND RELATED PROCESSES
IN VAPOURS

CHAPTER TWO
 REVIEW OF SECOND HARMONIC GENERATION
 AND RELATED PROCESSES IN VAPOURS

This chapter begins with a simple theoretical treatment of second harmonic generation in a quantised medium. Second harmonic generation (SHG) does not occur in an isotropic medium unless the symmetry is somehow broken; four ways of doing this are then described, and the publications in these fields are reviewed. SI units will be used throughout this work.

2.1 THEORETICAL OVERVIEW OF SECOND HARMONIC GENERATION IN
 QUANTISED MEDIA

Consider the idealised three-level system shown in figure 2.1.1. Second harmonic generation occurs in such a system by the simultaneous absorption of two photons of the fundamental radiation and the emission of one photon of twice the energy.

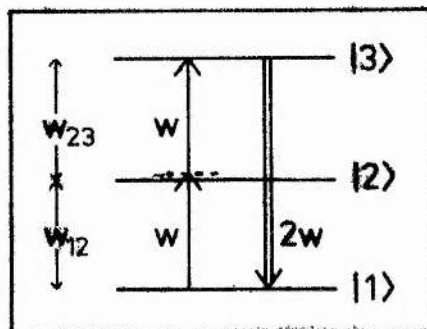


Figure 2.1.1 Energy level scheme for second harmonic generation in sodium vapour.

There need be no static population of the excited states in this parametric process, but near coincidences of the laser frequency, ω , with the allowed single-photon transition at ω_{21} , or of 2ω with the allowed two-photon transition at ω_{31} , will strongly enhance the generation process.

The wavefunction of the atom may be written as

$$\Psi = a_1(t) u_1 + a_2(t) u_2 e^{-i\omega_{21} t} + a_3 u_3 e^{-i\omega_{31} t} + \text{c.c.} \quad (2.1.1)$$

where a_n is the amplitude of u_n , which is the eigenfunction of level n . These amplitudes are considered to be slowly varying functions of time to allow for transitions in the medium. c.c. denotes the complex conjugate. The electric field of the fundamental beam may be described as

$$\underline{E}_\omega = \frac{1}{2} \underline{E}_{\omega 0} e^{-i\omega t} + \text{c.c.} \quad (2.1.2)$$

To calculate a_2 and a_3 , Ψ is inserted into the perturbed time-dependent Schroedinger equation

$$(H_0 + V)\Psi = -\hbar \frac{\partial \Psi}{i \partial t} \quad (2.1.3)$$

where the perturbation, V , in the dipole approximation, is given by

$$V = -e\mathbf{r} \cdot \underline{E}_\omega \quad (2.1.4)$$

and is caused by the electric field of the fundamental beam. If the resonances are as shown in figure 2.1.1, and if the excitation is weak, the time-dependence of a_2 and a_3 may readily be calculated to be

$$\dot{a}_2 = \frac{1}{2} i \langle 2 | e_{\underline{r}} | 1 \rangle \frac{E_{w_0}}{\hbar} e^{i(\omega_{21} - \omega)t} a_1 \quad (2.1.5)$$

$$\dot{a}_3 = \frac{1}{2} i \langle 3 | e_{\underline{r}} | 2 \rangle \frac{E_{w_0}}{\hbar} e^{i(\omega_{32} - \omega)t} a_2 \quad (2.1.6)$$

where $\langle i | e_{\underline{r}} | j \rangle$ is the dipole matrix element defined as $\int u_i^*(\underline{r}) u_j d\tau$, where the integration is over all space, and an electric dipole interaction is assumed. In the approximation of a relatively weak input wave, $a_1 = a_{10} =$ constant, and the above two equations may be integrated to give expressions for a_2 and a_3 . These are then inserted into equation 2.1.1 to give an expression for the wavefunction of the medium.

The expectation value of the polarisation of the atoms is given by

$$\langle \underline{p} \rangle = \int \Psi^* e_{\underline{r}} \Psi d\tau \quad (2.1.7)$$

where the polarisation is assumed to have a dipole nature. The calculated expression for Ψ is inserted into this equation, and the component oscillating at 2ω is extracted, giving the second harmonic polarisation as

$$\underline{p}_{2\omega} = \frac{|a_{10}|^2}{4 \hbar^2} \frac{\langle 1 | e_{\underline{r}} | 3 \rangle \langle 3 | e_{\underline{r}} | 2 \rangle \langle 2 | e_{\underline{r}} | 1 \rangle E_{w_0}^2 e^{-i2\omega t}}{(\omega_{21} - \omega)(\omega_{31} - 2\omega)} \quad (2.1.8)$$

The second order susceptibility $\chi^{(2)}$ is defined by

$$\underline{p}_{2\omega}^{(2)} = \epsilon_0 \chi^{(2)} E_w^2 \quad (2.1.9)$$

$$\text{so } \chi^{(2)}(-2\omega; \omega, \omega) = N \frac{\langle 1 | e_r | 3 \rangle \langle 3 | e_r | 2 \rangle \langle 2 | e_r | 1 \rangle}{\hbar^2 \epsilon_0 (\omega_{21} - \omega) (\omega_{31} - 2\omega)} \quad (2.1.10)$$

To include damping in equations 2.1.8 and 2.1.10 the factor $\pm i\gamma_{ij}$ must be inserted into each denominator with the resonant frequency ω_{ij} , with the signs chosen correctly [10, 19]. This is not important for the present discussion, though it is required in the more detailed analysis in chapter three.

Equations 2.1.8 to 2.1.10 describe the SHG process. For media with definite parity, such as atomic vapours in the absence of applied fields, $\chi^{(2)}$ will vanish in the dipole approximation. To see this, consider again the three level atom: if u_1 has even parity, then for $\langle 2 | e_r | 1 \rangle$ to be non-zero u_2 must have odd parity; similarly u_3 must have even parity, but now $\langle 1 | e_r | 3 \rangle$ is zero as both u_1 and u_3 are even. This is readily seen in the following example. Let states 1, 2 and 3 be the 3S, 3P and 4D states of the sodium atom. The $\Delta l = \pm 1$ selection rule for dipole radiation is well known, and so while 3S - 3P and 3P - 4D transitions are allowed, 4D - 3S is not.

If electric quadrupole or other higher order radiation processes are considered, $\chi^{(2)}$ may no longer be parity-forbidden. The electric quadrupole matrix element is of the form $\langle i | e_{rr} | j \rangle$, so a chain of two dipole transitions and one quadrupole transition would seem to be allowed. In the example given above, transitions from 4D to 3S are allowed by quadrupole radiation processes. However, a more detailed study shows that collinear three-wave mixing in an isotropic vapour is still forbidden. In order to see this, consider three waves of frequency and wave vector $(\omega_1, \underline{k}_1)$, $(\omega_2, \underline{k}_2)$ and $(\omega_3, \underline{k}_3)$ where $\omega_3 > \omega_2 \geq \omega_1$, and assume that these three waves are propagating collinearly through the vapour. As the

state of an atom is unchanged in a parametric process, the waves must satisfy certain conservation laws. Photon energy and momentum conservation demand that $\omega_3 = \omega_2 + \omega_1$ and $\underline{k}_3 = \underline{k}_2 + \underline{k}_1$ respectively. Angular momentum must also be conserved among the three waves. It is permissible to choose the axis of quantisation along the direction of collinear propagation, z , (or any other axis, as the medium is isotropic). Thus $m_3 = m_2 + m_1$, where m_n is the z component of angular momentum of the n th photon. As the electromagnetic wave is transverse, each photon must carry ± 1 units of angular momentum along z , regardless of the type of radiation from which it arose. There is no way in which three photons can obey such a conservation law, and so collinear three-wave mixing in an isotropic medium is not possible. This is a general result, independent of the type of matrix elements involved.

Despite these restrictions, methods have still been found to mix three optical fields in a vapour:-

- i) A static electric field may be applied to perturb the eigenfunctions of the medium, mixing together states of opposite parity. This is often described in terms of a third order nonlinearity, where two photons of the fundamental field are mixed with one of the zero frequency electric field to produce the second harmonic photon.
- ii) The transverse intensity gradient of high-intensity laser pulses at the fundamental frequency may produce quasistatic electric fields which then act to break the vapour's symmetry in a manner analagous to (i).
- iii) Two intersecting, orthogonally-polarised, focussed beams can produce a quadrupole radiation field at the sum or difference frequency, using the second order nonlinearity.

iv) A static transverse magnetic field may be applied to the focal region of a single beam, causing the quadrupole radiation at the second harmonic frequency to radiate coherently in the forward direction.

The study of this last type of symmetry-breaking process forms the bulk of this thesis; all four types are described in more detail in the following sections.

2.2 ELECTRIC-FIELD-INDUCED MIXING PROCESSES

The second harmonic polarisation produced in a quantised medium of atomic density N by an optical electric field $\underline{E}_w = (1/2) \underline{E}_{w0} e^{-i\omega t} + \text{c.c.}$ is

$$\underline{P}(2\omega) = \frac{N \langle 1|e_{\underline{r}}|3\rangle \langle 3|e_{\underline{r}}|2\rangle \langle 2|e_{\underline{r}}|1\rangle \underline{E}_{w0}^2 e^{-i2\omega t}}{4 \hbar^2 (\omega_{31} - 2\omega) (\omega_{21} - \omega)} \quad (2.2.1)$$

For media with definite parity, such as atomic vapours, at least one of the $\langle i|e_{\underline{r}}|j\rangle$ dipole matrix elements in equation 2.2.1 must be zero. However, the application of an external static electric field can mix levels of opposite parity, thus allowing all three dipole matrix elements to be non-zero. The static field imposes a preferred direction on the vapour, and it is no longer permissible to quantise the angular momentum of the atom along the propagation direction; the momentum must be quantised along the direction of the static electric field. Conservation of angular momentum among the three waves is possible in this direction, so second harmonic generation becomes allowed by both parity and angular momentum arguments.

For atoms and symmetrical molecules there is usually no linear shift in energy levels with an electric field \underline{E}_0 (linear Stark effect), as they do not possess permanent dipole moments which would interact with the field. However, an electric field can induce such a dipole moment in the atom, proportional to \underline{E}_0 , and thus give rise to energy level shifts proportional to \underline{E}_0^2 . This is called the quadratic Stark effect. If the states of opposite parity are well separated in energy, second order perturbation theory may be used to determine the effect of a weak electric field on the atom [20]:

$$W(\alpha JM) = W_0(\alpha J) + |E_0|^2 \sum_{\alpha', J'} \frac{|\langle \alpha' J' M | e_r | \alpha JM \rangle|^2}{W(\alpha J) - W(\alpha' J')} \quad (2.2.2)$$

$$\Psi(\alpha JM) = \psi(\alpha JM) - |E_0| \sum_{\alpha', J'} \psi(\alpha' J' M) \frac{\langle \alpha' J' M | e_r | \alpha JM \rangle}{W(\alpha J) - W(\alpha' J')} \quad (2.2.3)$$

where W is the energy level of the state, E_0 is the static electric field, and Ψ and ψ are the perturbed and unperturbed eigenfunctions respectively.

These relationships break down at fields which are sufficiently strong that the Stark splittings are comparable to the energy differences between states of opposite parity. The same is true when the basis states are almost degenerate, as in the hydrogen atom, or in high level Rydberg states, which have hydrogenic eigenfunctions. In these cases the Stark effect can be shown to produce energy level shifts proportional to the electric field strength [20,21].

As a specific example of an electric-field-induced mixing process in which only the quadratic Stark effect is involved, consider the scheme reported by Bethune et al [22] where sodium vapour was used as the nonlinear medium. The angular frequencies ω_1 and ω_2 of the optical electric fields were chosen to be close to the 3S - 3P and 3P - 4D resonances. With no static electric field applied, the dipole matrix elements involved were $\langle 3s | e_r | 4d \rangle \langle 4d | e_r | 3p \rangle \langle 3p | e_r | 3s \rangle$, the first of which is zero. When a static electric field was applied to the vapour, eigenfunctions of opposite parity were mixed as described by eq. 2.2.3. Equation 2.2.1, modified for mixing rather than second harmonic generation, then becomes

$$\begin{aligned}
 \underline{P}(2\omega) = & \frac{N}{\hbar^2} \sum_n \left(\frac{-\langle 3s | e_{\underline{r}} | np \rangle \langle np | e_{\underline{r}} | 4d \rangle + \langle np | e_{\underline{r}} | 4d \rangle \langle 3s | e_{\underline{r}} | np \rangle}{\hbar(\omega_1 + \omega_2 - \omega_{np})} \right) \cdot E_0 \\
 & \times \frac{\langle 4d | e_{\underline{r}} | 3p \rangle \langle 3p | e_{\underline{r}} | 3s \rangle E_1 E_2 e^{-i(\omega_1 + \omega_2)t}}{(\omega_{4d} - \omega_1 - \omega_2 - iT)(\omega_{3p} - \omega_1)} \quad (2.2.4)
 \end{aligned}$$

Thus the sum frequency polarisation is proportional to the static electric field E_0 , and to the two optical electric fields. This dependence on three electric fields has led most authors to describe such processes using $\chi^{(3)}$ nonlinearities, even though the expression was derived from a $\chi^{(2)}$ type of description. Although the formalism described above is restricted to certain cases, similar arguments apply to non-resonant processes, and to other atoms and molecules in which the quadratic Stark effect is the dominant perturbation.

Two ways of visualising the symmetry-breaking properties of the static electric field have been proposed. The first follows the eigenfunction mixing argument as above; the second considers the mixing process in ways similar to conventional $\chi^{(3)}$ processes such as third harmonic generation. The latter model treats the static electric field in the same manner as the optical fields, and the sum frequency output is considered as the mixing of two fields of frequency ω and one of frequency zero. Four-wave mixing is allowed by dipole selection rules; the zero-frequency transition in this model is essentially the same as the effects of state mixing considered in the first description.

Situations where the quadratic Stark effect is not applicable have been reported; they are described separately in the following literature review. The number of papers discussing electric-field-induced SHG is much greater than that of any other type of symmetry-breaking process.

Terhune and co-workers [23] were the first to report electric-field-induced second-harmonic generation (ESHG) in a medium with a centre of symmetry. They focussed a one joule pulse from a ruby laser through a calcite crystal, which was in an electric field, and used the birefringence of the crystal to phase-match the process. The intensity of the ESHG was measured to be proportional to the square of the dc electric field strength.

A small amount of second harmonic was generated when no field was applied; this was explained as a second order process involving a quadrupole transition. The quadrupolar route was possible as calcite is not isotropic, as explained in more detail by Pershan [24]. (Bulk quadrupolar SHG is currently of interest in centrosymmetric semiconductors; see, for example, reference 25.)

The first reports of ESHG in vapours, which are isotropic, were by Mayer and co-workers [26, 27], and by Finn and Ward [28]. Purely theoretical treatments were given by Kielich [29, 30]. These pioneering studies are summarised in table 2.2.1. Finn and Ward verified that the second harmonic power $P_{2\omega}$ was given by

$$P_{2\omega} \propto (P_{\omega})^2 E_0^2 |\chi^{(3)}/\Delta k_0|^2 \quad (2.2.5)$$

where P_{ω} is the fundamental power, E_0 is the dc electric field strength, $\Delta k_0 = (2k_{\omega} - k_{\omega})$ is the mismatch between the fundamental and second harmonic wave vectors, and $\chi^{(3)}$ is the appropriate element of the effective third order polarisability tensor (as discussed below). The constants of proportionality appropriate to the experimental arrangement were derived, and good agreement was obtained between theory and experiment. The number of photons generated per pulse from their 1 MW ruby laser ranged from 600 for xenon to 4000 for helium.

Paper	Type	Medium	Laser	Findings
23] 1962 Terhune Maker Savage	ESHG	calcite	ruby 694 nm 1 J	Finite SH power ($P_{2\omega}^0$) at zero field, but $(P_{2\omega} - P_{2\omega}^0) \propto E_0^2$. Conversion efficiency 5×10^{-4} that of KDP.
26] 1968 Mayer (In French)	ESHG	various gaseous molecules	ruby 694 nm 7 MW 25 ns	Second harmonic power proportional to square of fundamental power, except near breakdown fields in C_2H_5I and C_2H_5Br . Phase matching, and the difference between polar and nonpolar molecular nonlinear media noted. 10^{-13} conversion efficiency.
29] 1968 Kielich	ESHG THEORY			Theory. Nonpolar molecules contribute only to the purely electronic third order hyperpolarisation. Dipolar molecules also contribute a temperature-dependent second order term due to orientation of the dipoles in the electric field.
30] 1969 Kielich	ESHG THEORY			Extension of [29], to include "electric saturation" effects.
28] 1971 Finn Ward	ESHG	inert gases	ruby 694 nm 0.8 MW	In Helium, $P_{2\omega} \propto P_{\omega}^n (E_0)^m$, $n = 2.00 \pm 0.06$, $m = 2.06 \pm 0.06$ for conditions used. Also phase (mis)matching, dependence on electrode position and confocal parameter, measurement of hyperpolarisabilities of inert gases. 10^{-13} conversion efficiency.
27] 1971 Hauchecorne Kerherve Mayer (In French)	ESHG	various gaseous molecules	ruby 694 nm	As [26]. Also studied Raman effects, and found hyperpolarisabilities. $P_{2\omega}$ 9 times stronger with $E_{\omega} \parallel E_0$ than with $E_{\omega} \perp E_0$. Propose mechanism for increased ESHG near breakdown fields in ethyl bromide and ethyl iodide.

Table 2.2.1. Pioneering experiments in electric-field-induced second harmonic generation. None of these processes used resonant enhancement. $P_{2\omega}$ and E_0 are the second harmonic power and the symmetry-breaking static electric field respectively.

Many papers have since been published on electric-field-induced mixing processes, and these are summarised in the tables in this section. The reports have been arranged in groups according to the aim of the papers.

The largest group contains those papers concerned with measuring the hyperpolarisabilities of atoms and molecules, which are defined in an analogous way to linear polarisabilities. The dipole moment \underline{p} induced in a system by an electric field \underline{E} is

$$p_i = \epsilon_0 \left(\alpha_{ij} E_j + \frac{1}{2} \beta_{ijk} E_j E_k + \frac{1}{6} \gamma_{ijkl} E_j E_k E_l \right) \quad (2.2.6)$$

where α is the polarisability and β and γ are the first and second hyperpolarisabilities respectively [31]. β and γ are sometimes also referred to as the second and third order (in electric field) polarisabilities. A review of the properties of molecular hyperpolarisabilities is given by Buckingham and Orr [31], though it was written before most of the papers listed here were published. The major cause of interest in hyperpolarisabilities at that time was the importance of β and γ in the Pockels and Kerr effects respectively. In the Pockel's effect the birefringence of a material varies linearly with the electric field strength, and cannot occur in a centrosymmetric medium. The Kerr effect may occur in such a medium, and depends on the square of the electric field strength. Most of the papers summarised in table 2.2.2 use a slightly different notation for the hyperpolarisabilities, where $1/6 \gamma_{ijkl}$ is written as $3/2 \chi_{FGHM}^e$.

Consider a gaseous sample of molecules in a dc electric field and with light of frequency ω passing through it. These molecules develop induced dipole moments at the second harmonic frequency [32]; the average moment,

Paper	Type	Medium	Laser	Findings
27J 1971 Hauchecorne Kerherve Mayer (In French)	ESHG	various molecules	ruby 694 nm	Measurement of $\chi^{(3)}$ and $\chi^{(2)}$ using ESHG and Raman effects. $R = \chi_{\parallel}^{(3)}/\chi_{\perp}^{(3)} = 3$ using ethyl bromide.
28J 1971 Finn Ward	ESHG	inert gases	ruby 1 MW 694 nm	$\chi^{(3)}$ of inert gases.
34J 1974 Bigio Ward	ESHG	inert gases	ruby 1 MW 694 nm	$R = \chi_{\parallel}^{(3)}/\chi_{\perp}^{(3)}$ of inert gases all equal to three to within experimental error.
35J 1974 Finn Ward	ESHG	halogenated methanes	ruby 1 MW 694 nm	$\chi_{\parallel}^{(3)}$ of CH_4 and CF_4 directly from SH intensity, $\chi_{\parallel}^{(2)}$ of CH_2F_2 , CHF_3 , CF_4 , CClF_3 , CBrF_3 from SH intensity minus theoretical estimate of $\chi_{\parallel}^{(3)}$.
32J 1975 Ward Bigio	ESHG	halogenated methanes	ruby 1 MW 694 nm	Temperature dependence of SH intensity measured to give $\chi_{\parallel}^{(3)}$, $\chi_{\perp}^{(3)}$, $\chi_{\parallel}^{(2)}$ and $\chi_{\perp}^{(2)}$ for CH_4 , CH_3F , CH_2F_2 , CHF_3 , CF_4 , CClF_3 and CBrF_3 . BAA good for $\chi^{(3)}$ but poor for $\chi^{(2)}$.
36J 1977 Miller Ward	ESHG	halogenated methanes	ruby 1 MW 694 nm	As [32], extended to all $\text{CX}_n\text{Y}_{4-n}$ with $X, Y = \text{F}, \text{Cl}, \text{H}$.
37J 1978 Ward Elliot	ESHG	ethylene 1,3,butadiene 1,3,5,hexatriene benzene	ruby 1 MW 694 nm	Temperature dependence of SH intensity measured to give $\chi_{\parallel}^{(3)}$ and $\chi_{\perp}^{(3)}$ for these molecules.
38J 1979 Ward Miller	ESHG	"small molecules"	ruby 1 MW 694 nm	As [32], for H_2 , N_2 , O_2 , CO , CO_2 , H_2O , H_2S , NH_3 , SF_6 , $(\text{CH}_3)_2\text{O}$, CH_3OH .

Table 2.2.2, continued overleaf.

Paper	Type	Medium	Laser	Findings
39J 1982 Shelton Buckingham	PPM ESHG	various molecules	Ar ⁺ cw 1 W 458 - 514 nm	Frequency dependence of $\chi_{ }^{(3)}$ for He and CH ₄ , vibrational resonance seen in CH ₄ . Temperature dependence of SHG gives $\chi_{ }^{(2)}$ and $\chi_{ }^{(3)}$ for He, N ₂ , H ₂ , N ₂ , CO ₂ , CH ₄ , CH ₃ F, CHF ₃ , CF ₄ , SF ₆ at 514.5 nm.
40J 1984 Hameka Svendsen	ESHG THEORY			Expressions for third-order frequency-dependent hyperpolarisabilities of molecules. Also review of previous theoretical work.
41J 1984 Elliot Ward	ESHG	various molecules		Deviations from Kleinman symmetry.
42J 1985 Dudley Ward	ESHG	HF, HCl	ruby 1 MW 690 nm	Temperature dependence of SHG measured to give $\chi_{ }^{(3)}$ and $\chi_{ }^{(2)}$ for HF and HCl. Values for HF do not agree well with theory.
33J 1985 Mizrahi Shelton	PPM ESHG	various	Ar ⁺ , dye cw 1 W 488, 515 590 nm	Frequency dependence of $R = \chi_{ }^{(3)}/\chi_{\perp}^{(3)}$, R significantly different from 3, for He, Ar, Kr, Xe, CH ₄ , CF ₄ , SF ₆ , H ₂ , D ₂ , N ₂ , O ₂ , CO ₂ , C ₂ H ₆ , CHF ₃ , C ₂ H ₄ .
43J 1985 Mizrahi Shelton	PPM ESHG	Ar, N ₂ , O ₂	Ar ⁺ , dye cw 1 W 458 - 700 nm	Frequency dependence of $\chi_{ }^{(3)}$ (gas)/ $\chi_{ }^{(3)}$ (He) measured, nonlinear dispersion > linear dispersion.
44J 1985 Mizrahi Shelton	PPM ESHG	H ₂ , D ₂	Ar ⁺ , dye cw 1 W 458 - 700 nm	Frequency dependence of $\chi_{ }^{(3)}$ (H ₂)/ $\chi_{ }^{(3)}$ (He) and $\chi_{ }^{(3)}$ (H ₂)/ $\chi_{ }^{(3)}$ (D ₂) measured. Extrapolated to zero frequency to test ab initio calculations which are too high. Vibrational resonances significant.

Table 2.2.2 (continued). Papers reporting measurements of hyperpolarisabilities using electric-field-induced second harmonic generation (ESHG). None of these reports used resonant enhancement of the process. $\chi_{||}^{(3)}$ and $\chi_{\perp}^{(3)}$ are χ_{YYYY} and χ_{YYXX} respectively, the two independent non-zero components of the hyperpolarisability tensor [32]. BAA is the bond additivity approximation; the calculated contributions for each bond are added together to give an estimate for the total effect [31]. PPM is periodic phase matching [39]. All of the quoted power conversion efficiencies were around 10^{-14} ; the low power of the continuous wave laser was compensated for by using periodic phase matching to increase the generation length.

\underline{p} , per molecule is

$$p_F = (3/2) \chi_{FGHM}^e(-2w;0,w,w) E_G^0 E_H^\omega E_M^\omega \quad (2.2.7)$$

where $\chi_{FGHM}^e(-2w;0,w,w)$ is an effective molecular hyperpolarisability, the "E"s are electric field amplitudes at frequencies indicated by the superscripts, and F, G, H, M stand for X, Y, or Z in the laboratory coordinate frame. The factor 3/2 is included in accordance with the convention that $\chi(-w_0;w_1,w_2,w_3)$ should tend to $\chi(0;0,0,0)$ as all the frequency terms tend to zero [28].

In non-polar molecules the only contribution to χ_{FGHM}^e comes from the third order polarisability. However, molecules with a permanent dipole moment μ will undergo a temperature-dependent partial alignment in a dc field, and the second order polarisability is then non-zero due to the induced anisotropy [32]. The two contributions may be written explicitly as

$$\begin{aligned} \chi_{FGHM}^e(-2w;0,w,w) = & \chi_{FGHM}^{(3)}(-2w;0,w,w) \\ & + (\mu/9k_B T) \chi_{FGHM}^{(2)}(-2w;w,w) \end{aligned} \quad (2.2.8)$$

These laboratory-frame-averaged hyperpolarisabilities are related to the molecular hyperpolarisabilities by relations given in reference 32. The laboratory frame coefficients are subject to symmetry restrictions due to the macroscopic isotropy of the gas. This implies that there are only two independent non-zero spatial components for each hyperpolarisability. These are conventionally chosen as the YYY component, which is measured with the optical and dc electric fields parallel (\parallel), and the YYXX component, which is measured with the optical and dc electric fields perpendicular to each other (\perp).

One approximate-symmetry property of the hyperpolarisabilities is that they are invariant under any permutation of their spatial indices; this is called Kleinman symmetry [31, 33]. This symmetry is exact at zero frequency and results in $R = \chi_{\parallel}^{(3)}(\omega=0)/\chi_{\perp}^{(3)}(\omega=0) = 3$. This relationship is expected to hold at frequencies far below the first electronic resonance. Tests of this relationship are listed in table 2.2.2.

The temperature dependence of the second order polarisability allows independent determination of $\chi^{(3)}$ and $\chi^{(2)}$ by measuring the variation of SH power with vapour temperature, as noted in the same table.

Most of the ESHG experiments used high peak power pulsed lasers in order to obtain a measurable number of second harmonic photons. There was no resonant enhancement of the ESHG and the efficiency was also limited by phase mismatching. A significant advance was made by Shelton and Buckingham [39] who used periodic phase matching. An array of electrodes was used which was designed to reverse the polarity of the electric field every coherence length $l_c = \pi/(2k_w - k_{2w})$, where k_w is the wavevector at frequency w in the gas. The resulting periodic phase shift in the generated second harmonic served to cancel the accumulated phase shift due to dispersion in the medium, thus allowing continued growth of the SH signal over the whole length of the sample. This allowed Shelton and co-workers to perform various measurements using relatively low power continuous-wave lasers.

Table 2.2.3 summarises the results of some ESHG experiments in liquids. The theory of the process is similar to that of non-resonant ESHG in gases. The data obtained were interpreted to determine various parameters of the molecules involved, such as the properties of hydrogen bonding. Levine and Bethea [47] reviewed some of these possibilities.

Paper	Type	Medium	Laser	Findings
45] 1974 Levine Bethea	ESHG LIQ	nitrobenzene nitromethane iodomethane	Nd:YAG 1.06 μm	Measurement of hyperpolarisabilities; conjugated bonds make strongest contribution.
46] 1974 Levine Bethea	ESHG LIQ	nitrobenzene		Determination of sign of hyperpolarisability by interference of ESHG and other types of SHG. See also [60].
47] 1976 Levine Bethea	ESHG LIQ	nitrobenzene- benzene mixtures, water-methanol mixtures		ESHG gave information on dipolar forces, hydrogen bonding, charge transfer interactions and other solute-solute and solute-solvent effects. Also review.
48] 1976 Levine Bethea	ESHG LIQ	pyridine-I ₂	Nd:YAG 1.32 μm 100 kW 70 ns	$\chi^{(2)}$ of this charge transfer complex dissolved in benzene measured to be 30 times that of pyridine, theoretical agreement.
49] 1984 Song Cho Lee Chang (In Korean)	ESHG LIQ	monosubstituted benzenes		ESHG measured and compared with theory

Table 2.2.3. Papers reporting electric-field-induced second harmonic generation in liquids (ESHG LIQ). All these processes were non-resonant.

Of more direct relevance to the subject of this thesis are the reports of resonant ESHG listed in table 2.2.4. The use of resonant enhancement permits extremely high values of the nonlinear susceptibility to be obtained; Boyd and co-workers [54 - 57] have studied electric-field-induced sum frequency mixing using Rydberg levels of the sodium atom for resonant enhancement and have measured the susceptibility for second harmonic generation to be ten times that of the well known harmonic generation crystal, potassium dihydrogen phosphate (KDP). The process was not phase matched, however, so the power conversion efficiency was low. The Rydberg levels are hydrogenic and are thus affected predominantly by the linear Stark effect. The wave-function mixing in this case is not proportional to the static electric field strength, but is almost independent of it in the range where the linear Stark effect is greater than both the fine structure splitting and the quadratic Stark splitting. Boyd and Xiang therefore class this as a $\chi^{(2)}$ process.

Earlier, Abrams et al [51, 52] had used resonances of the NH_2D molecule to enhance difference-frequency mixing of a carbon dioxide laser beam and a microwave signal, generating a single sideband of the CO_2 laser radiation in a microwave Stark cell. The quadratic Stark effect does not describe the energy splitting well, as the Stark splittings are greater than the separation of states of opposite parity. The chain of dipole matrix elements was calculated to be zero at high and zero field strengths, but finite at intermediate field strengths. The electric field strength was chosen to shift the energy levels of the molecule into the position of maximum resonant enhancement. The complicated dependence on electric field strength led the researchers to classify this as a $\chi^{(2)}$ process, induced by an electric field.

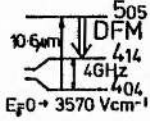
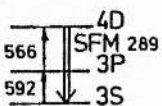
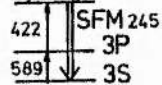

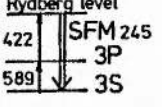
Paper	Type	Medium	Laser	Findings
50] 1974 Krochik Khronopulo	ESHG			Theoretical treatment of resonant ESHG; non-polar and polar molecules considered.
51, 52] 1977 Abrams Yariv Yeh Asawa Plant Popa	EDFM	NH ₂ D 	cw single mode CO ₂ 10.6 μm; microwave TWT 4 W 4 GHz	Single sideband IR generation. Difference frequency power proportional to microwave power. Maximum generation efficiency when levels Stark-shifted into exact resonance. DFM linewidth 130 MHz. 2 x 10 ⁻³ conversion of microwave power to difference frequency wave.
22, 53] 1977 Bethune Smith Shen	ESFM and NCSFM	Sodium 	dye 592 nm & 566 nm 10 W and 100 W	Measurement of $\chi_Q^{(2)}/\chi^{(3)}$ by interference between ESFG and non-collinear SFG, which was driven by a quadrupole moment; gives value for 3S - 4D quadrupole matrix element.
54] 1982 Boyd Xiang	ESFM THEORY	Near resonant Rydberg level 		Theoretical treatment for SFM using Rydberg states for resonant enhancement; laser should be tuned between Stark-shifted levels. Predicts SHG susceptibility > 100 times that of KDP.
55] 1983 Gauthier Krasinski Boyd	ESFM	Sodium Rydberg level 	dye 422 nm & 589 nm "few ns"	Experimental verification of [54]. ESHG susceptibility ten times that of KDP. Not phase matched, so power conversion efficiency only 10 ⁻⁵ . Suggestions for improving susceptibility and efficiency.
56, 57] 1984 Boyd Gauthier Krasinski Malcuit	ESFM	Sodium Rydberg level 	dye 422 nm & 589 nm 125 kW 4ns Δν=5 GHz	Same susceptibility as [55]. Blue laser scanned and resonant enhancement seen for each Stark-shifted level. Effects of tuning yellow laser shown. Max efficiency 3 x 10 ⁻⁴ . Also some SHG at zero electric field.

Table 2.2.4. Papers reporting resonantly-enhanced electric-field-induced mixing processes. Wavelengths in the diagrams are given in nm unless otherwise stated. The energy level shifts with field in the schemes used in [22] and [53] are described well by the quadratic Stark effect. Papers [54 - 57] deal with hydrogenic atoms, and thus the linear Stark effect is dominant. In [51] and [52] the electric field is a very large perturbation, and there is no simple dependence of DFM efficiency on electric field strength.

Electric-field-induced sum frequency mixing was demonstrated using the sodium atom for resonant enhancement by Bethune et al [22, 53]. They used a crossed-beam geometry so that a quadrupole-driven SFM process could also occur. The interference between the two types of mixing process allowed a determination of the magnitude and sign of the $\langle 3s | r^2 | 4d \rangle$ quadrupole matrix element.

The remainder of the electric-field-induced mixing experiments are listed in table 2.2.5. The first two describe the use of ESHG as a sensitive probe of the focal region of a laser beam. This probe is more sensitive than conventional methods for determining mode distortions, and with a 10^{-14} conversion efficiency it is very loosely coupled. The report by Bethea [60] of ESHG in glass is important due to the use of glass cell walls in containing gases and liquids under investigation.

Paper	Type	Medium	Laser	Findings
58] 1975 Bigio Finn Ward	ESHG	air	ruby 694 nm 1 MW 20 ns	ESHG as a probe of the focal region of the laser beam; theory and experiment. ESHG sensitive to small deviations from TEM ₀₀ mode. 10 ⁻¹⁴ conversion efficiency.
59] 1976 Guha	ESHG	air	ruby 694 nm 50 MW 20 ns	ESHG as beam probe. Extension of theory in [58] to higher order beam modes. Good agreement between theory and experiment.
60] 1975 Bethea	ESHG	glass	Nd:YAG 1.06 μm 250 kW 20 ns	ESHG coefficients determined. Generation efficiency 10 ⁻⁶ that of quartz.
61] 1981 Dudley Ward	ESHG	chloromethane	ruby 694 nm 0.25 MW 40 ns	ESHG in crossed beam geometry, but no quadrupole driven SHG. ESHG collinear with each beam and along the bisector. Dependences on particle density and electrode geometry determined.
62] 1982 Lam Thirunamach- andran	ESHG THEORY			Theoretical treatment of ESHG in chiral molecules, including electric quadrupole and magnetic dipole transitions.
63] 1986 Shelton Mizrahi	PPM ESHG	He, Ar, H ₂ , D ₂ , N ₂ , O ₂	Ar+, dye 458 - 700 nm 1 W	Measurements of the refractive indices of these gases as functions of frequency. 10 ⁻¹⁵ conversion efficiency.

Table 2.2.5. Other reports of electric-field-induced mixing processes. None of these was resonantly enhanced.

2.3 THREE-WAVE-MIXING PROCESSES WITH NO EXTERNAL SYMMETRY-BREAKING

The arguments against the possibility of collinear second-harmonic generation in the absence of an applied field are strictly valid only for the hypothetical infinite plane wave. In a conventional mixing experiment a focussed Gaussian beam of limited diameter is used, typically 300 μm . In this type of arrangement, some asymmetry can be imposed upon the medium by the beam itself; the transverse intensity gradient of the beam imposes an anisotropy along the radial direction. Although no SHG has been observed using low power lasers [64], there have been numerous reports of SHG in otherwise isotropic vapours when high power pulsed lasers were used to provide the fundamental radiation; these papers are summarised in table 2.3.1. Several different mechanisms have been proposed [65 - 67, 69, 71, 76], and it seems likely that different mechanisms may predominate in different situations. However, most reports suggest that a quasistatic electric field is set up in the direction of the intensity gradient of the beam, and thus electric-field-induced second harmonic generation of the type reviewed in the previous section may occur; the origin of these quasistatic electric fields is the subject of some controversy. In a minority of reports, totally different mechanisms have been proposed, including optical pumping of Zeeman sublevels, collisional state mixing, and quadrupolar processes depending on the optical electric field gradient.

The first observation of SHG induced by a high power beam (PSHG) in the absence of external symmetry breaking was by Mossberg et al [65]. A nitrogen-laser-pumped dye laser with 5 kW peak power was tuned to the $6^2P_{1/2} - 7^2P_{1/2}$ two-photon transition in thallium vapour, and a small amount of SHG was observed in the absence of any external fields. Second harmonic radiation was detected only under conditions suitable for

Paper	Type	Medium	Laser	Findings
65J 1978 Mossberg Flusberg Hartmann	PSHG	Thallium $6^2P_{1/2} - 7^2P_{1/2}$ $6^2P_{1/2} - 8^2P_{1/2}$	dye 568 nm 5 kW 7 ns	$P_{2\omega} \propto N^2 P_{\omega}^2$, 10^{-22} efficiency, SH unpolarised, SHG dependent on two photon absorption, independent of magnetic field. <u>Proposed mechanism:</u> Multiphoton ionisation followed by radial charge separation, to produce ESHG.
66J 1979 Miyazaki Sato Kashiwagi	PSHG	Non resonant Sodium	Nd:YAG 1.06 μ m 1.8 GW 28 ps	$P_{2\omega} \propto N^2 P_{\omega}^n$, $n > 4$, saturation at high P_{ω} , SH radially polarised, zero SH at centre, <u>Proposed mechanism:</u> Spontaneous field due to radiation pressure, to produce ESHG.
67J 1980 Heinrich Behmenburg	PSHG	Barium $6s^2 1S_0 - 6s8s 1S_0$ $6s^2 1S_0 - 5d7s 1D_2$	dye 582 nm 20 kW 4 ns $\Delta\nu = 10$ GHz	$P_{2\omega} \propto P_{\omega}^2$, <u>Proposed mechanisms:</u> Possibly optical pumping of Zeeman sublevels, quadrupolar transitions.
68J 1981 Miyazaki Sato Kashiwagi	PSHG	Non resonant Sodium	Nd:YAG 1.06 μ m 1.8 GW 28 ps	$P_{2\omega} \propto N^2 P_{\omega}^n$, $n > 4$, saturation at high P_{ω} , SH radially polarised, zero at centre, <u>Proposed mechanism:</u> Spontaneous field due to radiation pressure, to produce ESHG.
69J 1981 Okada Fukuda Matsuoka	PSHG	Lithium $2^2S_{1/2} - 3^2S_{1/2}$	dye 735 nm 1 MW 30 ps $\Delta\nu = 60$ GHz	$P_{2\omega} \propto N^n P_{\omega}^2$, $n = 2$ till phase mismatching, 10^{-8} efficiency, SH polarised along intensity gradient of fundamental. Degree of ionisation measured, quasistatic electric field strengths measured by SHG and by ratio of SHG/third harmonic generation. <u>Proposed mechanism:</u> Multiphoton ionisation followed by free expansion of photoelectrons, to produce ESHG. (Ambipolar diffusion and radiation pressure effects considered to be negligible).

Table 2.3.1, continued overleaf.

Paper	Type	Medium	Laser	Findings
70J 1981 Bokor Freeman Panock White	PSHG	Mercury $6s^2 1S_0 - 6s6d 1D_2$	doubled dye 280 nm 4 MW 4 ns $\Delta\nu=9$ GHz	Observation of resonant enhancement. 10^{-5} efficiency No SHG on $6s^2 1S_0 - 6s6d 1D_2$
71, 72J 1981 Bethune	PSHG THEORY	Sodium Resonant and non resonant	Theory	Theoretical Review. <u>Proposed mechanisms</u> all depend on transverse nonuniformity of pump intensity. Claims [68] incorrect. Gives magnitudes under different conditions for ESHG using field due to: free electrons driven by radiation force; free expansion of photoelectrons; nonuniform polarisation of neutral atoms via $\chi^{(2)}$; and also: direct SHG from nonuniform free electron distribution; Direct SHG due to $\chi^{(2)}$ of neutral atoms.
73, 74J 1981 Arkhipkin Makarov Popov Timofeev Epstein	PSHG	Calcium $4s^2 1S_0 - 5s^1 1S_0$	dye 600 nm 10 kW 10 ns $\Delta\nu=60$ GHz	10^{-4} efficiency, SH radially polarised.
75, 76J 1981 Freeman Bjorkholm Panock Cooke	PSHG	Sodium i) 3S - 4D ii) 3S - 5P	dye 579 nm 571 nm 10^9 Wcm ⁻² $\Delta\nu=9$ GHz	$P_2 \propto P_w^n$, $n>2$, 2, 1 with increasing P_w , 10^{-5} efficiency, SH modes and polarisation: i) bimodal and same linear polarisation as w ii) donut and same linear polarisation as w In both cases mode width of SH > fundamental Resonant enhancement distorted, implying bulk effects important. <u>Proposed mechanism</u> : None of above mechanisms fit (see text). Working on quadrupolar model.

Table 2.3.1, continued overleaf.

Paper	Type	Medium	Laser	Findings
77J 1982 Jamroz Larocque Stoicheff	PSHG	Zinc i) $4s^1s_0^{-4}d_2^1$ ii) $4s^1s_0^{-4}d_2^1$	dye 320 nm 358 nm 10 kW 12 ns $\Delta\nu=15$ GHz	i) 10^{-5} efficiency; ii) 10^{-6} efficiency, Intensity SHG/third harmonic generation measured to find quasistatic field strengths i) 5.2 kVcm^{-1} , ii) 4 kVcm^{-1} , 2% atoms ionised. Generation bandwidths: i) 90 GHz, ii) 30 GHz. <u>Proposed mechanism:</u> multiphoton ionisation followed by free expansion of photoelectrons to produce ESHG.
78J 1983 Dinev de Garcia Meystre Salomaa Walther	PSHG	Potassium $3S - nS, P, D$	dye 572 nm - 615 nm 600 kW 5 ns	SHG when tuned to any nS, nP or nD (7D - 34P) Peak efficiency at $n = 11$. $P_{2\omega} \propto N^2$ for S and D, N^4 for P. SH unpolarised for S, as pump for D, \mathcal{L} pump for P. Doubts on radial fields or quadrupole transitions. <u>Proposed</u> <u>mechanism:</u> mixing of l values by collisions.
57J 1984 Boyd Krasinski Malcuit	PSFM	Sodium Rydberg states	dye 420 nm & 590 nm 100 kW 4 ns	Peaks when sum frequency equal to frequency of S or D Rydberg states. Consistent with multiphoton ionisation followed by free expansion of photoelectrons to produce ESHG.
79,80J 1985 Kiyashko Popov Timofeev Makarov Epstein	PSHG 4thHG	Magnesium $3s^2^1s_0^{-4}s^1s_0$	dye 460 nm 20kW 7ns; 920 nm 1.2MW 30ns	10^{-4} efficiency for SHG, 10^{-10} efficiency for 4th harmonic generation. Phase mismatch behaviour seen.
64J 1986 Mizrahi Shelton	PSHG PPM	Not two photon resonant Sodium	cw dye 589.3 nm 500 mW	Low power fundamental, sensitive detection, No SHG observed.

Table 2.3.1, continued. Reports of second-harmonic-generation types of mixing processes in vapours with no external symmetry breaking used. All used resonant enhancement unless otherwise noted. PPM is periodic phase matching (see section 2.2).

two-photon absorption, and the SH power increased when another laser was tuned to a non-resonant frequency to increase the multi-photon-ionisation that was occurring. The SH intensity was independent of an external magnetic field, and was unpolarised. Mossberg et al proposed a mechanism which was later confirmed by the experiments of Okada et al using lithium vapour as a nonlinear medium. The latter authors investigated the polarisation of the second harmonic more thoroughly and found that it was always in the direction of the transverse intensity gradient of the fundamental beam, and that the SH power was zero at the centre of the beam. The dominant contribution to the SHG was calculated to be electric-field-induced second harmonic generation, where the electric field was produced by the free expansion of photoelectrons produced by multiphoton ionisation.

In the Okada arrangement [69], four-photon ionisation of the lithium vapour produced 1.35 eV photoelectrons which would have had an initial velocity of about $7 \times 10^5 \text{ ms}^{-1}$. These electrons were fast enough to travel a significant fraction of the beam diameter during the laser pulse and so a radial electric field, due to the macroscopic charge separation, was superimposed on the local random electric field due to the ionisation. Such an electric field would be zero at the centre of the Gaussian beam, and would lie along the radial direction of the beam. This effect was modelled theoretically by Okada et al; their results are reproduced as figure 2.3.1. These authors also estimated the quasistatic electric field strength experimentally from measurements of the second harmonic power and from the ratio of the intensities of the second and third harmonic radiation that were produced concurrently. The two methods gave results of 7 kVcm^{-1} and 60 kVcm^{-1} respectively, in fair agreement with each other and the theoretical calculations.

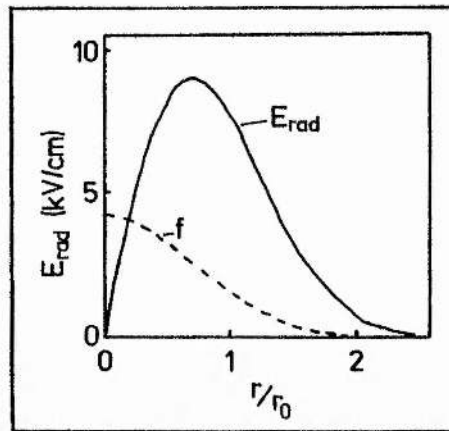


Figure 2.3.1. Distribution of the radial electric field E_{rad} against the radial distance r for a photoelectron density $n = 10^{21} \text{ m}^{-3}$. The initial distribution of the photoelectrons $f(r,0)$ is also shown. From [69].

Other mechanisms for the generation of the quasistatic electric fields have been proposed; Bethune [71,72] predicts the relative magnitudes of these processes in his comprehensive review of the subject. He shows that the photoelectrons may also be driven radially by radiation pressure, but not in the manner that was proposed by Miyazaki et al [66, 68]; Bethune [71] and Okada et al [69] agree that the spontaneous generation of a field due to radiation pressure, proposed by Miyazaki and coworkers, did not give a correct description of the physics of the process.

The results in most subsequently published papers have been consistent with the free expansion of photoelectrons producing suitable electric fields for ESHG. Several of the two-photon transitions that were used for resonant enhancement by various authors had upper and lower states as S states. In these cases the electric field mixed these states with the P states of opposite parity to explain the generation process as in section 2.2. In the absence of an electric field there is no possibility of even a quadrupolar or other higher order radiation process being used for the return route as this is not allowed by selection rules.

However, quadrupolar-driven processes may become important in other arrangements, though Bethune [71] calculates them to be weak. Heinrich and Behmenburg [67] proposed that in their SHG experiment the symmetry of the barium vapour may have been broken by optical pumping of the Zeeman sublevels or by quadrupolar processes relying on the electric field gradient.

More recently, Freeman et al [75, 76] have generated the second harmonic of a pulsed dye laser in sodium vapour, using the $3S - 3P$ and $3S - 4D$ transitions for resonant enhancement. The results obtained were not consistent with any of the proposed models. The second harmonic power did not increase with increased photoionisation caused by another laser, so the process did not seem to rely upon multiphoton ionisation in the same way as others described above. The polarisation of the second harmonic was not along the intensity gradient of the fundamental, ruling out the ESHG theories. Bethune [81, and section 2.4 of this thesis] has proposed quadrupolar routes for SHG which may be important in the case of focussed beams with mixed transverse modes; scrambling the transverse modes in Freeman's experiment had no effect. In addition, the maxima of the second harmonic modes were well outside those of the fundamental. The authors calculated the magnitude of the quadrupole moment produced by the focussed beam due to the field gradient, but found this to be 10^{-6} of the moment calculated from the observed SH power. They reported that they were "working on a mechanism ... that relies upon ionisation and quadrupole coupling". Rather than the ionisation being important due to the static electric fields produced, it was being considered to be important in the spatial variation of the atomic ground state density. Freeman et al claim that when this is coupled with the spatial variation of the intensity of the fundamental, qualitative agreement is obtained with observations.

Dinev et al [78] propose yet another possible mechanism. They observed well-collimated DFM when their laser was tuned into two-photon resonance with any nS, nP or mD ($n = 9 - 34$, $m = 7 - 34$) level of potassium. Their results were not consistent with quasistatic-electric-field induced SHG, or quadrupole SHG. Instead, they suggested that, at the relatively high densities of potassium atoms used, the high collisional cross sections of the Rydberg states led to collisional effects being of importance. The S and D states may be collisionally mixed with the P states, and the authors proposed that the radiation from the collisionally induced dipole moments may add coherently, giving rise to SHG.

It would seem that in contrast to the well understood area of conventional ESHG, a considerable amount of work has yet to be done to obtain a full explanation of second harmonic generation caused by high intensity Gaussian beams in otherwise isotropic media.

2.4 QUADRUPOLE RADIATION

As discussed in section 2.1, three-wave mixing in atomic vapours is not forbidden by parity arguments if electric quadrupole transitions are taken into consideration. Electric quadrupole radiation has been treated by several authors, for example [21, 82 - 84]; a brief introduction to the differences between electric dipole and electric quadrupole processes is given here. Examples of classical static electric dipoles and quadrupoles are shown in figure 2.4.1.

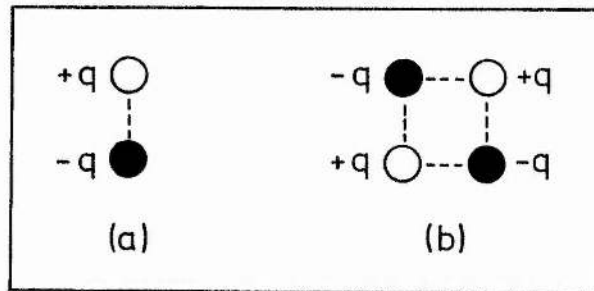


Figure 2.4.1. a) Classical electric dipole
b) One type of classical electric quadrupole.

It is well known that an oscillating electric dipole radiates an electromagnetic wave. The electric quadrupole in figure 2.4.1 has no net dipole moment, but if the dipoles within this quadrupole were to oscillate, each dipole would radiate. However, if their phase relationship remains fixed as shown in the diagram, and if the dimensions of the quadrupole are very much less than the wavelength of the radiation, the radiation fields from the two dipoles will interfere destructively, and no radiation will be observed. The assumption that the size of an oscillating charge distribution is very much less than the wavelength of the radiation it produces gives rise to the "dipole approximation", in which it is assumed that oscillating dipoles are the only significant source of radiation. However, the destructive interference in the above example will not be complete if the source is of a finite size. The small amount of residual

radiation is what is known as quadrupole radiation.

The dipole approximation is often very good; for example, the size of an atom is of the order of 10^{-12} m, and visible light has a wavelength of the order of 5×10^{-7} m. It would be unwise to consider the radiation processes of the atom purely in this classical manner, but it is found that classical [82] and quantum mechanical [83] treatments provide similar results, and dipole transitions are the dominant radiative processes in atomic physics.

In the semiclassical [21] atom-field theory the full matrix elements for a transition between energy states of an atom take the form $\langle j | \hat{\epsilon} \cdot \mathbf{p} e^{i\mathbf{k}\cdot\mathbf{r}} | i \rangle$, where $\hat{\epsilon}$ is a unit vector in the direction of polarisation of the radiation, \mathbf{k} is the wavevector of the radiation, i and j denote the quantum numbers of the two atomic states, and $\mathbf{p} = q\mathbf{r}$ is the dipole moment of the electronic charge distribution, q is the electronic charge, and \mathbf{r} is its position vector. The exponential term is included to allow for phase retardation of the wave produced by the electron at different positions \mathbf{r} . For small $\mathbf{k}\cdot\mathbf{r}$ the exponential may be expanded to give

$$e^{i\mathbf{k}\cdot\mathbf{r}} = 1 + i\mathbf{k}\cdot\mathbf{r} + \dots \quad (2.4.1)$$

In the dipole approximation, in which phase retardation is neglected, the exponential is approximated to unity. The term involving $\mathbf{k}\cdot\mathbf{r}$ gives rise to higher order multipole radiation, specifically magnetic dipole radiation and electric quadrupole radiation. In many situations in atomic physics the dipole approximation is quite adequate, as $\mathbf{k}\cdot\mathbf{r}$ is often very small. Simple arguments show that the ratio of electric dipole to electric quadrupole transition rates (if allowed) is of the order of $(Z/130)^2$ where Z is the atomic number of the atom [21, 85].

The matrix elements of electric dipole and quadrupole transitions are significantly different. Dipole matrix elements take the form $\langle j | \hat{e} \cdot \mathbf{q} | i \rangle$, while the quadrupole element is $\langle j | \hat{e} \cdot \mathbf{q} \mathbf{r} \mathbf{r} | i \rangle$. This results in the selection rules for the (weaker) electric quadrupole transitions being significantly different from those of the better known dipole transitions. In particular, the electric quadrupole operator has even parity. Thus, if an electric dipole transition is forbidden by selection rules, a higher order multipole transition may be observable, if rather weak. The selection rules for the three types of radiation mentioned above are summarised in table 2.4.1.

Electric dipole	Magnetic dipole	Electric quadrupole
(1) $\Delta J = 0, \pm 1$ (0 ↔ 0)	$\Delta J = 0, \pm 1$ (0 ↔ 0)	$\Delta J = 0, \pm 1, \pm 2$ (0 ↔ 0, ½ ↔ ½, 0 ↔ 1)
(2) $\Delta M = 0, \pm 1$	$\Delta M = 0, \pm 1$	$\Delta M = 0, \pm 1, \pm 2$
(3) Parity change	No parity change	No parity change
(4) One electron jump $\Delta l = \pm 1$	No electron jump $\Delta l = 0$ $\Delta n = 0$	One or no electron jump $\Delta l = 0, \pm 2$
(5) $\Delta S = 0$	$\Delta S = 0$	$\Delta S = 0$
(6) $\Delta L = 0, \pm 1$ (0 ↔ 0)	$\Delta L = 0$	$\Delta L = 0, \pm 1, \pm 2$ (0 ↔ 0, 0 ↔ 1)

Table 2.4.1. Selection rules for different types of transition. From Garstang [86]

2.5 NON-COLLINEAR QUADRUPOLE SUM FREQUENCY MIXING

Even when quadrupole matrix elements are taken into account, collinear three-wave mixing in an isotropic vapour is still forbidden due to the angular momentum conservation laws discussed in section 2.1. However, if two non-collinear beams with wavevectors \underline{k}_1 and \underline{k}_2 are used, and the quantisation direction is taken as $\underline{k}_1 + \underline{k}_2$, there is a non-zero probability amplitude for one of the photons to have $\Delta m = 0$, thus allowing SFM. Also, the natural dispersion of the medium may be used to satisfy the energy and momentum conservation laws at a particular angular separation of the beams. Papers reporting non-collinear sum frequency mixing (NCSFM) are listed in table 2.5.1. Bethune et al [87] were the first to report such quadrupole wave mixing, and used the 3S - 3P and 3S - 4D transitions of the sodium atom for single and two photon resonant enhancement respectively. The 4D - 3S quadrupole transition was used to complete the chain of matrix elements. These authors produced a theory, on which they later expanded [10], which was in good agreement with experiment. The spherical symmetry of the atoms restricts the elements of the quadrupole tensor which may contribute to SFM. It can be shown [53] that the effective dipole $\underline{P}_{\text{eff}}$ of the quadrupole radiation with wavevector $\underline{k}_3 = n_3 \omega_3 / c \hat{e}_3$ is

$$\begin{aligned} \underline{P}_{\text{eff}} &= -i \underline{k}_3 \cdot \vec{Q} \\ &= -i \chi_Q^{(2)} [(\underline{k}_3 \cdot \underline{E}_1) \underline{E}_2 + (\underline{k}_3 \cdot \underline{E}_2) \underline{E}_1 - (2/3)(\underline{E}_1 \cdot \underline{E}_2) \underline{k}_3]. \end{aligned} \quad (2.5.1)$$

The scalar products show that a non-collinear geometry is required, and that the SFM is a maximum for orthogonally polarised beams. The output power is a maximum when the wave-vector mismatch $\Delta \underline{k} = (\underline{k}_3 - \underline{k}_1 - \underline{k}_2)$ is zero, in which case the generated wave stays in phase with the fundamental beams throughout the interaction length. The phase matching condition was satisfied by tuning one laser close to the 3S - 3P transition

Paper	Type	Medium	Laser	Findings
87] (1976) Bethune Smith Shen	NCSFM	Sodium 3S - 4D	dye 590 nm & 568 nm 100 W pulsed $\Delta\nu=9$ GHz	Theory given. Resonant enhancement at 3S-4D, linewidth limited by lasers. Phase matching angle ($\sim 2.3^\circ$) agrees with theory. $P_{\text{SFM}} \propto P_1 P_2 N^2$ 10^{-8} conversion efficiency.
22] (1977) Bethune Smith Shen	NCSFM	Sodium 3S - 4D	as above	Interference of quadrupole SFM and ESFM to find $\chi^{(2)}/\chi^{(3)}$ and hence 3S-4D quadrupole matrix element.
88] (1977) Flusberg Mossberg Hartmann	NCSFM	Sodium 3S - 4D	dye 590 nm & 568 nm 170 kW 6 ns $\Delta\nu=21$ GHz	Interference of quadrupole SHG and magnetic field induced SHG for various magnetic field and laser polarisation directions. 10^{-9} conversion efficiency.
10] (1978) Bethune Smith Shen	NCSFM	Sodium 3S - 4D	dye 590 nm & 568 nm ~ 100 W 600 ns $\Delta\nu=4$ GHz	Theoretical treatment of quadrupole SFM, including spin-orbit and Zeeman effects, Doppler effect and Laser Linewidth. Otherwise expansion of [87], including limiting processes (see text).
53] (1978) Bethune Smith Shen	NCSFM	Sodium 3S - 4D	as above	Less formal version of [10] and [87].
89] (1978) Flusberg Mossberg Hartman	NCSFM	Sodium 3S - 4D		Review of non-collinear and magnetic-field-induced sum frequency mixing.
81] (1981) Bethune	NCSHG	Theory	Theory	Theoretical treatment of quadrupole SHG for focussed beams of arbitrary transverse mode structure and polarisation. Beam with mix of TEM_{00} and TEM_{01} modes gives 10^{10} increase in SHG over two TEM_{00} modes.

Table 2.5.1. Papers reporting non-collinear quadrupolar three wave mixing. All used resonant enhancement.

and choosing an intersection angle to create $\Delta k = 0$. Bethune et al verified the above properties experimentally, and showed that this second-order dipole-forbidden process was as strong as a third-order, dipole-allowed process such as third harmonic generation.

They also considered processes which would limit the generation efficiency [10]. The squared dependence on atomic density, N , observed for $N < 10^{22} \text{ m}^{-3}$, saturated at higher densities due to linear absorption of the pump beam, thus limiting the vapour density which may be used. The sum frequency power P_3 is expected to vary linearly with both P_1 and P_2 , but this saturated at high input intensities due to saturation of the two-photon absorption. The most serious limiting process was found to be induced refractive index changes through saturation of the dispersion [90], two-photon resonance [91] and population redistribution. This led to self-defocussing which resulted in smaller intensities at the focus. Rather more important was the breaking of phase matching produced by these changes of refractive index. Three-photon ionisation may also limit the maximum powers used, by causing changes in the refractive index, but the amount of ionisation measured was less than expected.

Bethune et al [10] also considered theoretically the effect of a magnetic field on this process, and determined that magnetic-field-induced SFM should be comparable with the noncollinear process at a field strength of only 1 mT (10 gauss). Flusberg et al [88] had looked at this experimentally, using the same atomic transitions. They found the two processes to be of comparable efficiency at 2.5 mT (25 G). Depending on the relative directions of the polarisations of the two fundamental beams and the magnetic field, the SFM was enhanced or degraded by the application of the external field. Their results were in good agreement with their clearly presented theory.

The interference between non-collinear SFM and electric-field-induced SFM was used by Bethune et al [22] to determine the 3S - 4D quadrupole matrix element of sodium. The power of the generated wave is given by

$$P_3 \propto |[-ik_3 \cdot \chi_Q^{(2)} + \chi^{(3)} \cdot E_0] : E_1 E_2|^2 \quad (2.5.2)$$

where E_0 is the applied dc field, and $\chi^{(3)}$ is the third-order nonlinear susceptibility. The two processes were of the same efficiency when a field of 20 kVm^{-1} was applied. The interference between the two generation processes as E_0 was varied allowed a value for $\chi_Q^{(2)} / \chi^{(3)}$ to be measured. Knowing this quantity, and the dipole matrix elements involved, the quadrupole matrix element was calculated. This was found to be 50% larger than that calculated theoretically by Tull et al [92].

Finally, Bethune [81] considered theoretically the effects of mixed transverse modes in a single laser beam. He found that quadrupole SFM may be relatively strong if two different spatial modes with orthogonal polarisations are present in the beam.

2.6 MAGNETIC-FIELD-INDUCED THREE-WAVE MIXING

The use of a magnetic field to break the symmetry of a vapour was first proposed by Hänsch and Toschek [93]. However, in their scheme, the field did not break the symmetry in the direct manner of the processes described in the previous sections. They suggested that a net polarisation may be introduced in the medium by optical pumping of atoms between Zeeman levels of the ground state. This effect has not yet been unambiguously observed.

Magnetic-field-induced three-wave mixing is now well known, and comes about from the mixing of the wavefunctions of the Zeeman sublevels by the magnetic field, in much the same way that an applied electric field mixes states of different angular momentum quantum number. Consider the conservation laws listed earlier. At low atomic densities the dispersion of the medium is often negligible at the wavelengths of interest, so $k_1 + k_2 = k_3$. Energy is conserved, as $w_1 + w_2 = w_3$. The two-photon absorption creates a coherence between the wavefunctions of the upper and lower levels, with $\Delta l = 0, \pm 2$, and $\Delta m = 0, \pm 2$, where the quantisation axis is taken along the common direction of propagation of the beams. The use of a quadrupole or magnetic dipole transition from the upper to lower levels allows the $\Delta l = \pm 2$ transition, and, incidentally, the $\Delta l = 0$ transition if the angular momentum quantum number of the lower state is not zero. However, only a $\Delta m = \pm 1$ transition may radiate along the quantisation axis, regardless of the type of transition involved [84], and so three-wave mixing is forbidden. This is equivalent to saying that the $m_1 + m_2 = m_3$ conservation rule is impossible to satisfy. When a transverse magnetic field is applied, the wavefunctions of the magnetic sublevels are perturbed, and receive a rotation transformation. This brings about new components of the quadrupole moment with $\Delta m = \pm 1$, which may radiate along the forward direction, thus generating the second harmonic. A qualitative

description of magnetic-field-induced second harmonic generation (BSHG) was given in section 1.3, and a detailed theoretical analysis is given in chapter 3.

Flusberg et al [94] were the first to report magnetic-field-induced three-wave mixing in a vapour; this was difference frequency mixing in atomic thallium vapour. Resonant enhancement was used to produce the difference frequency of two nitrogen laser pumped dye lasers operating at 378 and 535 nm; the difference frequency wave was driven by a magnetic dipole transition between the $6^2P_{3/2}$ and $6^2P_{1/2}$ levels. The energy level scheme is shown in table 2.6.1, along with other reports of magnetic-field-induced three wave mixing. Flusberg et al considered the symmetry-breaking mechanism proposed by Hänsch and Toschek, but calculated that the effect of wavefunction mixing was about 10^4 times stronger than the effects of the induced transverse polarisation of the ground state Zeeman levels. They used symmetry considerations to find a formula for the induced magnetic dipole moment, and confirmed experimentally that the difference frequency wave power varied as $N^2 P_1 P_2 B^2$, where B is the magnetic field strength perpendicular to the propagation direction, N is the particle density, and P_1 and P_2 are the laser powers. No DFM was observed in a longitudinal magnetic field up to 0.03 T, nor with an electric field up to 50 kVm^{-1} . At sufficiently high vapour densities the 378 nm laser beam produced stimulated Raman scattering at around 235 nm, which was then used for the same scheme of DFM.

These researchers considered the mixing of the hyperfine levels to be the dominant means of symmetry breaking; Matsuoka et al [95] disputed this, determining that the mixing of the hyperfine levels was of secondary importance to the mixing of the initially degenerate magnetic sublevels. This group was also the first to report magnetic-field-induced second

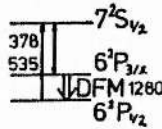
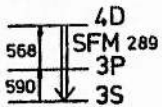
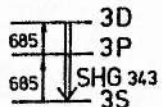
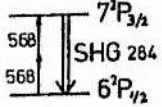
Paper	Type	Medium	Laser	Findings
94] 1977 Flusberg Mossberg Hartmann	BDFM	Thallium 	dye 378 nm & 535 nm 2 kW, 5 ns 1-10 GHz	Theory given. Magnetic dipole moment stronger than electric quadrupole moment. Transverse magnetisation small and unimportant. Claim mixing of hyperfine levels is important. $P_{SFM} \propto N^2 B^2 P_1 P_2$, though stimulated Raman scattering seen at large P_1 . 10^{-6} conversion efficiency.
88] 1977 Flusberg Mossberg Hartmann	BSFM	Sodium 	dye 3 kW 590 nm & 568 nm 170 W, 6 ns 12 & 21 GHz	Quadrupole driven. Interference between magnetic-field-induced SFM and non-collinear SFM. 10^{-8} efficiency.
95] 1977 Matsuoka Nakatsuka Uchiki Mitsunaga	BSHG	Sodium 	dye 685 nm 3 kW 500 ns 32 GHz	Theory given, but hyperfine splitting neglected. $P_{2\omega} \propto N^2 B^2 P_w^2 \sin^2 \theta$. Field transforms initially degenerate magnetic sub-levels. Also used Calcium vapour with similar results. 7×10^{-7} efficiency.
89] 1977 Mossberg Flusberg Hartmann	BSFM			Review of magnetic-field-induced SFM and non-collinear SFM.
10] 1978 Bethune Smith Shen	BSFM	Sodium	theory	Mostly non-collinear SFM, but some theory on magnetic-field-induced SFM.
65] 1978 Mossberg Flusberg Hartmann	BSHG	Thallium 	dye 568 nm 5 kW, 7 ns 1-10 GHz	$P_{2\omega} \propto N^2 B^2 P_w^2$, and deviation from phase matched behaviour. Also includes section on spontaneous-field-induced SHG.

Table 2.6.1, continued overleaf.

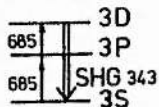
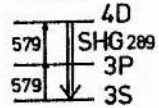
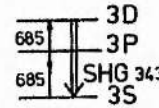
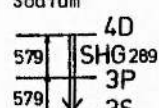
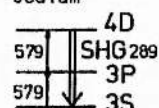
Paper	Type	Medium	Laser	Findings
96J 1979 Uchiki Nakatsuka Matsuoka	BSHG	Sodium 	dye 685 nm 2 kW 2.5 ns 64 GHz	Detailed theory, but hyperfine splitting ignored. SH intensity saturates at 100 mT, and polarisation of SH is rotated. 5×10^{-7} efficiency.
18J 1983 Dunn	BSHG	Sodium 	cw dye 579 nm ~ 1 W cw < 5 MHz	$P_{2\omega} \propto N^2 B^2 P_w^2$, and deviation from phase matched behaviour. SH generation linewidth 2.8 GHz at 15 mT measured with single frequency laser. 8×10^{-11} efficiency.
97J 1983 Uchiki Nakatsuka Matsuoka	BSHG	Sodium 	dye 685 nm 3 kW, 500 ns 1 kW, 2.5 ns 32 & 64 GHz	Detailed theory including fine, hyperfine and Zeeman splitting. At 8 mT $P_{2\omega} \propto N^2 B^2 \sin^2 \theta$. and collisional decay rate of 3D - 3S transition measured. Start of saturation of $P_{2\omega}$ with field at 50 mT, and rotation of polarisation of SH. 10^{-6} efficiency.
98J 1985 Yiqun (In Chinese)	BSHG	Sodium 	dye 579 nm 1 MW, 30 ns 8 GHz.	B^2 dependence below 30 mT, saturation at 90 mT. Pulse length of SH was 26 ns.
99, 100J 1986 Sinclair Dunn	BSHG	Sodium 	cw dye 579 nm 0.5 W cw 0.5 MHz	As reported in this thesis. Theory of [97J] extended. Deviation from phase matched behaviour. Line profiles of SHG at different fields and polarisations, and comparison with line profiles of 3S - 4D absorption. Power and polarisation properties as functions of field and frequency. 6×10^{-8} efficiency.

Table 2.6.1, continued. Papers reporting magnetic-field-induced three wave mixing in vapours. All except [94] rely solely on a quadrupole moment to drive the generated wave. All use resonant enhancement. The laser characteristics given are the wavelength of the laser light in nanometres, the peak pulsed power in watts, the pulse length in seconds, and the laser linewidth in hertz.

harmonic generation in a vapour. The second harmonic of their 685 nm pulsed dye laser was generated in sodium vapour, using the $3S - 3D$ transition for two-photon resonant enhancement. They determined experimentally that the transverse magnetisation produced through optical pumping in the magnetic field was unimportant: if the magnetisation were responsible for the BSHG, the SH power would not vary simply as the square of the fundamental power, and the SH power should follow the slowly precessing magnetisation (about 50 ns/radian); a squared dependence on fundamental power was observed, and there was no delay in the growth of the SH output.

Matsuoka and coworkers have produced two more papers on SHG in sodium [96, 97], refining their theoretical treatment with each publication. Their latest paper on the subject [97] modelled the sodium atomic system taking into account fine, hyperfine and Zeeman splitting terms. The expectation values of the quadrupole moments induced by the two photon absorption were calculated, taking into account the rotation of these moments about the magnetic field. This derivation is followed in chapter three, but there the homogeneous and inhomogeneous broadening processes are treated separately. Using a multimode, pulsed dye laser Matsuoka and coworkers calculated the intensity and polarisation of the second harmonic radiation. They found theoretically and experimentally that at magnetic fields less than 0.05 T (0.5 kG) the second harmonic power varied as $N^2 P_w^2 B^2 \sin^2 \theta$, where theta is the angle between the magnetic field and the polarisation of the fundamental radiation. When the Zeeman splitting was of the order of the Doppler width the squared dependence of the SH power on magnetic field saturated, and the polarisation of the second harmonic was significantly rotated ($\sim 10^\circ$). The addition of a buffer gas to the vapour decreased the SH power by increasing the damping constant used to describe the coherence between the $3D$ and $3S$ levels. This effect was used to determine the

collisional decay rate of the dipole-forbidden $3D - 3S$ transition to be 14 MHz/mbar, but no independent measurement of this quantity had been made to confirm this result.

Their SHG experiment using the $4s^2\ ^1S_0 - 4s3d\ ^1D_2$ two-photon transition in calcium [95] was important in showing that it is the mixing of the initially degenerate magnetic sublevels by the magnetic field that is important to the generation process, rather than the mixing of hyperfine levels [94]. The ground level of calcium has no net spin, and the excited level has no hyperfine splitting, so the transformation of the quadrupole moment was possible only through the transformations in the magnetic sublevels of the 1D_2 state.

Deviation from a squared dependence of SH power on particle density was first noted by Mossberg et al [65]. At sufficiently high particle densities, the difference in refractive index of the vapour between fundamental and second harmonic radiation is sufficient to cause the wavevector of the second harmonic to be significantly different from twice that of the fundamental. In this case, the SH generated in one region of the vapour will be out of phase with that generated at another region, and the waves will interfere destructively. The need to match the phase velocities of fundamental and second harmonic is well known in SHG in crystals, and is treated by Yariv [12], amongst others. The phase velocity mismatch leads to an oscillatory dependence of SH power on particle density at high particle densities. This subject is treated in more detail in section 5.2. Mossberg and coworkers also reported interference between magnetic-field-induced and non-collinear sum frequency mixing [88, 89].

Dunn [18] is the only author to have used a continuous wave laser as the fundamental light source. All other investigators have used pulsed lasers,

with pulse durations less than 500 ns and linewidths in excess of 1 GHz. Dunn used the $3S - 4D$ transition in sodium for resonant enhancement of BSHG; intracavity and extracavity arrangements were used. In the latter case the laser linewidth was less than 5 MHz. This allowed him to determine the SHG line profile to be 2.8 ± 0.1 GHz (FWHM) when a 0.015 T (150 G) transverse magnetic field was applied to the vapour, which was at a temperature of 400 °C. This linewidth was in good agreement with the estimated width taking into account fine, hyperfine and Zeeman splitting of the atomic states broadened by the Doppler effect. Dunn also observed an oscillatory dependence of SH power on atomic density at high densities, and proposed that the process may be phase matched using a suitable buffer gas to offset the dispersion of the sodium vapour. He also suggested the use of the sodium dimer as a nonlinear medium to give increased tunability, and the use of BSHG to determine spatial distributions of vapour temperatures. These topics will be discussed further in appendix E and section 5.9 respectively.

There have been a few other reports of continuous-wave three-wave mixing in vapours, but all using an electric field for symmetry breaking. Only Abrams et al used a single frequency source. In all other cases any linewidth measurements have been associated with the linewidth of the fundamental radiation, rather than the nonlinear medium.

The laser used in the work reported in this thesis had a linewidth of less than 0.5 MHz. This allowed a detailed study of properties of the SHG process that changed across the line profile of the resonantly enhancing two-photon transition [99, 100]. This is reported in full in the following chapters.

THEORETICAL MODELLING

OF MAGNETIC-FIELD-INDUCED
SECOND HARMONIC GENERATION
IN SODIUM VAPOUR

CHAPTER THREE
 THEORETICAL MODELLING OF MAGNETIC-FIELD-INDUCED
 SECOND HARMONIC GENERATION

3.1 DESCRIPTION OF THE ATOMIC EIGENSTATES AND EIGENENERGIES

The levels of the sodium atom that are directly concerned in the second harmonic generation are the $3^2S_{1/2}$ ground states, the $3^2P_{3/2,1/2}$ states and the $4^2D_{5/2,3/2}$ states. The 3S - 4D two-photon transition is used for resonant enhancement of the SHG; the single-photon allowed 3S - 3P transition also contributes some resonant enhancement, being some 300 wavenumbers from resonance with the laser light frequency. In order to predict properties of the SHG which change across the line profile of the 3S - 4D two-photon transition, the description of the atomic eigenstates must include fine, hyperfine and Zeeman splitting terms. Some relevant energy levels of the sodium atom are depicted in figure 3.1.1.

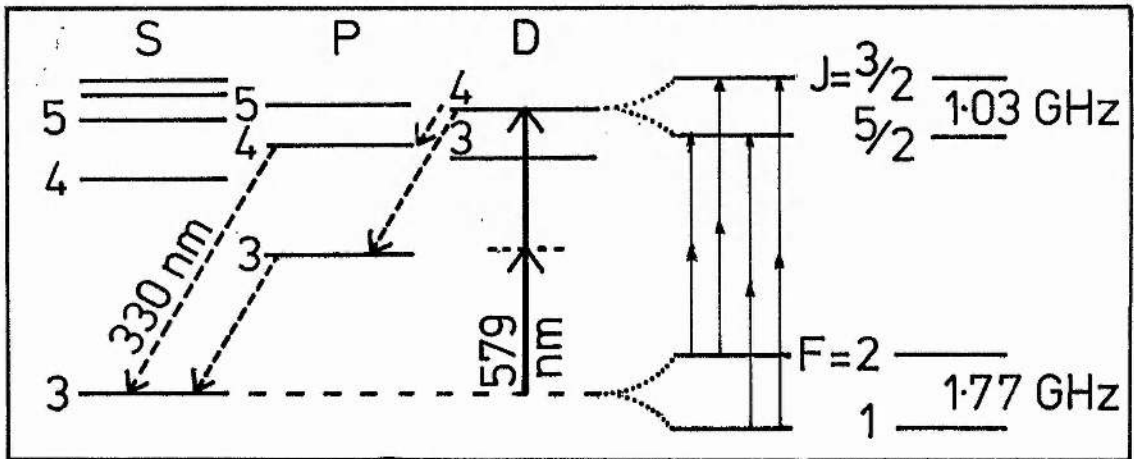


Figure 3.1.1. Energy levels of the sodium atom.

3.1.1 The 3S states

With no external magnetic field applied, the ground states of the sodium atom are split into two sets of states by the hyperfine interaction. This effect is reviewed by Arimondo et al [101]. The nucleus of the atom possesses a magnetic moment, $\mu_I = -g_I \mu_B I$, where g_I is the nuclear g factor, μ_B is the Bohr magneton and I is the nuclear spin quantum number. The nuclear magnetic moment interacts with the magnetic field at the nucleus produced by the orbiting electrons. This interaction gives rise to energy shifts $\Delta E(F)$ given by

$$\Delta E(F) = \frac{a}{2} [F(F+1) - I(I+1) - J(J+1)]. \quad (3.1.1)$$

Here F is the total atomic angular momentum, $F = I + J$, and J is the electronic angular momentum. In sodium $I = 3/2$, and in the 3S state the only contribution to the electronic angular momentum is from the electronic spin, and thus $J = S = 1/2$. The separation of the states with different F values may be measured very precisely using atomic beam magnetic resonance techniques. In the sodium atom this separation is 1771.6261288(10) MHz [102, 103]; the hyperfine constant, a/h , is half this value.

The application of an external magnetic field lifts the degeneracy of the energy states. At low fields, when the Zeeman energy shifts are small, the levels are given by

$$\begin{aligned} \Delta E(F, m_F) = & \frac{a}{2} [F(F+1) - I(I+1) - J(J+1)] \\ & - \{\mu_I [I(I+1) + F(F+1) - J(J+1)]/I \\ & + \mu_J [J(J+1) + F(F+1) - I(I+1)]/J\} \frac{m_F B}{2F(F+1)} \end{aligned} \quad (3.1.2)$$

where μ_J is the atomic magnetic moment, and B is the magnetic field

strength. In this regime, the energy shifts due to the magnetic field are small and so the energy levels are calculated by treating the Zeeman interaction as a small perturbation to the eigenstates. F and m_F are good quantum numbers and the energy level shifts are proportional to m_F .

In very high magnetic fields, the $\underline{I} - \underline{J}$ coupling is broken down and the hyperfine interaction can be considered as a small perturbation to the Zeeman effect. In this case, the energy levels are given by

$$\Delta E(I, J, m_I, m_J) = a m_I m_J - \frac{\mu_J B m_J}{J} - \frac{\mu_I B m_I}{I} \quad (3.1.3)$$

where m_I and m_J are the quantum numbers for the projection of \underline{I} and \underline{J} on \underline{B} . As $|\mu_I| \ll |\mu_J|$, the dominant magnetic-field-dependent term in the above equation is the one involving μ_J . In this range of magnetic field strengths the energy level shift is proportional to m_J . In the case of S states $m_J = m_S$. Figure 3.1.2 shows that this gives rise in high fields to two groups of levels corresponding to $m_S = \pm 1/2$.

To determine the eigenfunctions at intermediate field strengths, a secular equation must be solved, as neither the Zeeman splitting nor the hyperfine interaction may be regarded as a small perturbation on the other. An (m_I, m_J) representation may be chosen, giving matrix elements of the form $\langle m_I, m_J | H | m_I, m_J \rangle$. As $J = S = 1/2$ in the case under consideration, the problem is not unduly complicated. The solution for the eigenenergies was first presented by Breit and Rabi [104], and the derivation is given by Ramsey [105]. The method will be outlined here due to its importance in the modelling of the SHG, and the difficulty in finding a treatment which gives all the quantities required in the SHG model.

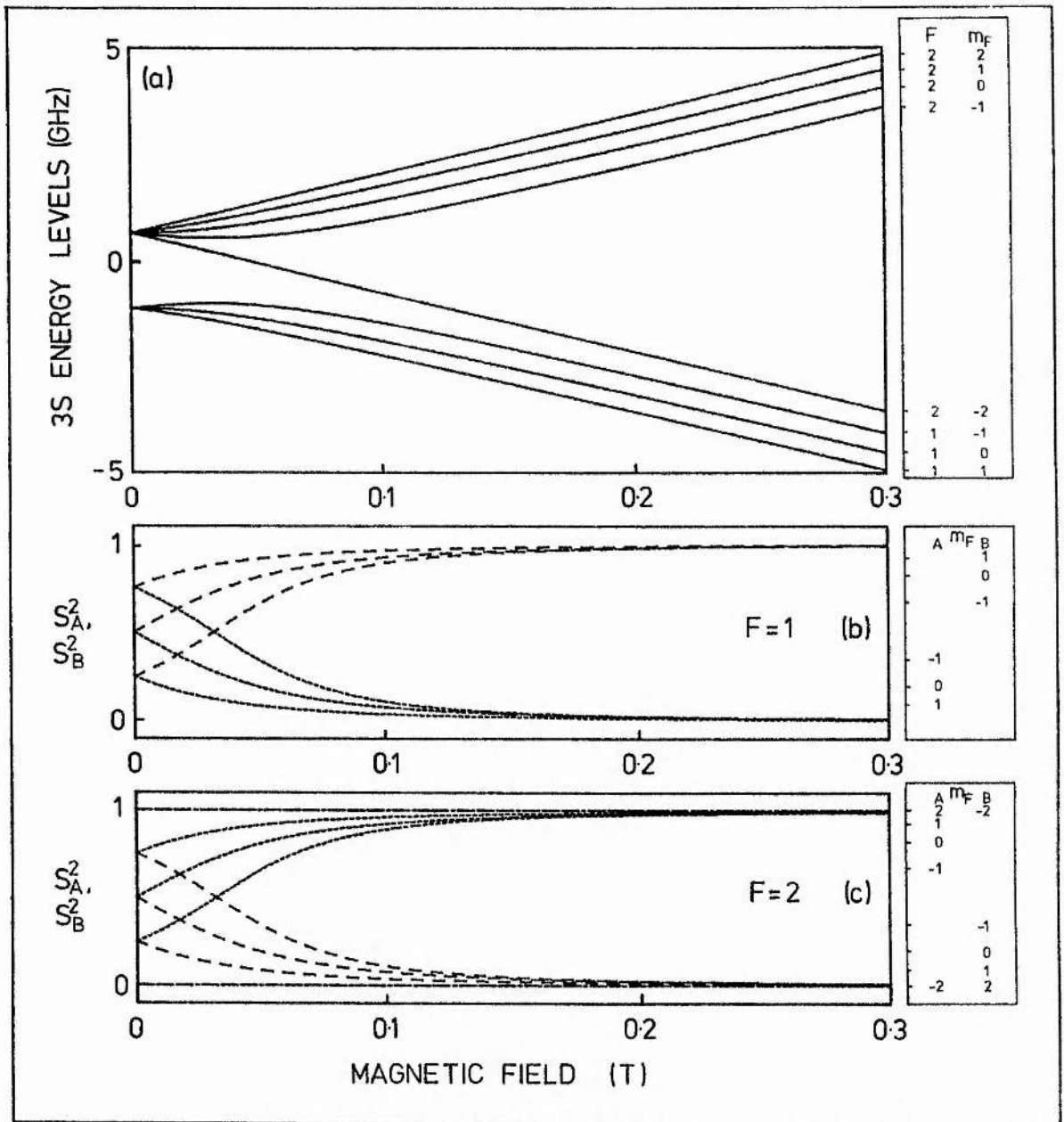


Figure 3.1.2 (a) Energy levels and (b and c) eigenfunction components of the 3S states plotted as functions of magnetic field strength. The box by (a) shows the F, m_F quantum numbers of each level, the other two boxes identify each $S_{A,B}^2$ curve with its quantum numbers. The curves with the short dashes are drawn for S_A^2 , the longer dashes for S_B^2 .

The wavefunctions of the 3S states may be described in the $|l s I m_l m_s m_I\rangle$ scheme by

$$|S_F^{m_F}\rangle = S_A(F, m_F, H) \left| 0 \frac{1}{2} \frac{3}{2} 0 \frac{1}{2} m_F - \frac{1}{2} \right\rangle + S_B(F, m_F, H) \left| 0 \frac{1}{2} \frac{3}{2} 0 -\frac{1}{2} m_F + \frac{1}{2} \right\rangle \quad (3.1.4)$$

abbreviated to $\phi = S_A \Psi_A + S_B \Psi_B$. The two wavefunctions which are chosen as Ψ_A and Ψ_B are the wavefunctions of the 3S levels in a high magnetic field, in which the hyperfine coupling is broken. Ψ_A and Ψ_B form a very good approximation to a complete orthonormal set under the fields in question, as the energy differences between these states and other states of the atom are large compared with the Zeeman splitting. The orthonormality implies that $S_A^2 + S_B^2 = 1$.

When $m_F = I + 1/2$, only the state ($m_I = I, m_J = 1/2$) can give the necessary m_F , so S_A and S_B are 1 and 0 respectively, at all magnetic field strengths. A similar argument holds for $m_F = I - 1/2$. Thus in figure 3.1.2 the $F=2, m_F = \pm 2$ levels are the ones which have a linear dependence of energy on magnetic field strength at all fields, and have S_A^2 and S_B^2 constant.

The eigenenergies and eigenfunctions of the other states are found by using the Rayleigh Ritz method. The derivatives of the state energy with respect to S_A and S_B are set to zero to find the minimum energy of the state. The energy of the state $|S_F^{m_F}\rangle$ is given by

$$E = \frac{\int \phi^* \mathcal{H} \phi \, d\tau}{\int \phi^* \phi \, d\tau} \quad (3.1.5)$$

and the state energy is minimised when

$$S_A (H_{AA} - E) + S_B H_{AB} = 0, \quad (3.1.6)$$

and
$$S_A H_{BA} + S_B (H_{BB} - E) = 0, \quad (3.1.7)$$

where
$$H_{ij} = \int \psi_i^* H \psi_j \, d\tau. \quad (3.1.8)$$

This may be written as the secular equation

$$\begin{vmatrix} H_{AA} - E & H_{AB} \\ H_{BA} & H_{BB} - E \end{vmatrix} = 0. \quad (3.1.9)$$

As the integrals in the secular equation are known, expressions for E may be found, and S_A and S_B determined from equations 3.1.6 and 3.1.7.

The energy shifts due to the hyperfine interaction and the external magnetic field are given by

$$H = a \underline{I} \cdot \underline{J} - \frac{\mu_I B I_z}{I} - \frac{\mu_J B J_z}{J} \quad (3.1.10)$$

and, knowing the commutation and expectation value relations for the angular momenta involved, expressions for H_{ij} may be found [105].

This gives the Breit Rabi formula:

$$\Delta E(F, m_F) = - \frac{\Delta W}{2(2I + 1)} - \frac{\mu_I B m_F}{I} \pm \frac{\Delta W}{2} \sqrt{\frac{(1 + 4m_F x + x^2)}{2I+1}} \quad (3.1.11)$$

where
$$x = (-\mu_J/J + \mu_I/I)B/\Delta W \quad (3.1.12)$$

and ΔW is the separation of the $F = I + 1/2$ and $F = I - 1/2$ levels at zero magnetic field. The upper sign is taken for states belonging to

$F = I + 1/2$ at zero field, and the lower sign for the other states. Uchiki et al [97] use the notation

$$E(S_F^{M_F}) = b + \sigma(a^2 + c^2)^{1/2} \quad (3.1.13)$$

where $a = [m_F A + (g_J - g_I)\mu_B B]/2 \quad (3.1.14)$

$$b = -A/4 + m_F g_I \mu_B B \quad (3.1.15)$$

$$c = A[(2 - m_F)(2 + m_F)]^{1/2}/2 \quad (3.1.16)$$

$$\sigma = \begin{cases} 1 & \text{for } F = I + 1/2 \\ -1 & \text{for } F = I - 1/2 \end{cases} \quad (3.1.17)$$

The gyromagnetic ratios g_J and g_I are 2.002 and -0.0008 respectively [101], and $A/h = \Delta W/2h = 885.813064$ MHz, where h is Planck's constant.

Insertion of the energy values to equation 3.1.6 gives expressions for the two wavefunction components as

$$S_A = [a + \sigma\sqrt{(a^2 + c^2)}]/t \quad (3.1.18)$$

$$S_B = c/t \quad (3.1.19)$$

where $t = [(a + \sigma\sqrt{(a^2 + c^2)})^2 + c^2]^{1/2}. \quad (3.1.20)$

The values of S_A^2 and S_B^2 are plotted as functions of magnetic field strength in figure 3.1.2. For $m_F = 2$, it is seen that $S_A^2 = 1$ and $S_B^2 = 0$; the reverse is true for $m_F = -2$. In these cases only one combination of (m_I, m_J) can contribute to the eigenfunction. For all other values of m_F , both S_A^2 and S_B^2 are field dependent. At zero field the $m_F = 0$ wavefunctions are composed of equal amounts of the two basis functions, whereas the $m_F = 1$ (-1) state contains more (less) of the $m_S = 1/2$ basis state. As the field is increased the admixtures change. At the highest fields shown, there is little variation of the values of S_A^2 and S_B^2

from 0 or 1. This is because the (m_L, m_S) representation is now the one which best describes the atomic wavefunctions; the coupling between the nuclear and electronic angular momenta has been broken down, and F is therefore no longer a good quantum number.

3.1.2 The 3P states

The $3^2S_{1/2} - 3^2P_{3/2,1/2}$ transitions at 589.0 and 589.6 nm give rise to the well known sodium D lines. These single-photon transitions contribute some resonant enhancement to the SHG, but as the 3P states are some 300 cm^{-1} off resonance with the fundamental radiation the 3P states are not populated. The change in energy levels of the 3P states with magnetic fields or pressure is negligible compared to the detuning of the fundamental from single-photon resonance, so these perturbations may be neglected. The eigenstates may be expressed using 3-j notation [20] as

$$|P_J^{m_J}\rangle = \sum_{m_L, m_S} (-1)^{m_J + 1/2} \sqrt{2J + 1} \begin{pmatrix} 1 & 1/2 & J \\ m_L & m_S & -m_J \end{pmatrix} \times |L S m_L m_S\rangle |I m_I\rangle. \quad (3.1.21)$$

3.1.3 The 4D states

The interaction between the orbital and spin angular momenta of the electron in the 4D state gives rise to fine (spin-orbit) splitting. The angular momentum quantum number J can take values $3/2$ and $5/2$; simple atomic theory suggests that the $J = 3/2$ state should have the lower energy. However, the nD ($n = 3$ to 16) levels of the sodium atom are found to be

inverted, that is, the states with the higher J value have the lower energy [106, 107]. This was first noted by Meissner and Luft [108], who also measured the 4D fine splitting to be 1038 ± 50 MHz. Beck and Odabasi [109] have gone some way to explaining the inversion in terms of corrections due to relativistic and correlation effects.

The fine splitting of the 4D states was measured with high precision in the mid-1970s, when the dye laser had been developed to the point where it was a useful spectroscopic tool, and various groups used it to perform two-photon spectroscopy of the 3S - 4D transition. Using an atomic beam to minimise Doppler broadening, Pritchard et al [110] determined the splitting to be 1025 ± 6 MHz, while Hänsch et al [111] performed the first reported Doppler-free two-photon spectroscopy experiment obtaining a value of 1035 ± 10 MHz. The most precise measurement to date was reported by Fredrickson [112] who used level-crossing spectroscopy to obtain a value of 1028.3 ± 0.6 MHz.

As the wavefunctions of the 4D states do not penetrate the nucleus significantly, the hyperfine splitting of these states is expected to be much less than that of the 3S states. Indeed, the hyperfine splitting of the 4D states has been shown to be smaller than the natural linewidth of these levels; Schenck and Pilloff [113] used a quantum-beat method to obtain a value for the hyperfine splitting constant for the $4^2D_{3/2}$ levels of 0.507 ± 0.068 MHz. This is very much smaller than the 35 MHz pressure-broadened linewidths determined in the course of this work, and so the effect of the hyperfine interaction on the 4D levels may be safely neglected.

The effect of an applied magnetic field on the 4D energy levels is similar to that described for the 3S levels. At low fields the splitting is

proportional to m_J , but in the high field limit the splitting is proportional to $m_L + g_S m_S$, where m_L and m_S are the orbital and spin magnetic quantum numbers, and g_S is the g value for the electron, which is approximately equal to two. The case of intermediate fields is treated by Condon and Shortley [84] in an analogous way to that described for the 3S states. The eigenfunctions are described in the $|l s m_L m_S\rangle$ scheme as

$$|D_J^{m_J}\rangle = D_A(J, m_J, B) |2 \ 1/2 \ m_J - 1/2 \ 1/2\rangle + D_B(J, m_J, B) |2 \ 1/2 \ m_J + 1/2 \ -1/2\rangle \quad (3.1.22)$$

The eigenenergies are [97]

$$E(D_{5/2}^{\pm 5/2}) = (1 \pm 3y)\gamma \quad (3.1.23)$$

$$E(D_{5/2}^{m_J}) = (-1/4 + m_J y + \sqrt{4y^2 + 8m_J y + 25}/4) \quad (m_J \neq \pm 5/2) \quad (3.1.24)$$

$$E(D_{3/2}^{m_J}) = (-1/4 + m_J y - \sqrt{4y^2 + 8m_J y + 25}/4) \quad (3.1.25)$$

where $y = \mu_B B/\gamma$, and $\gamma/h = -411.3 \pm 0.2$ MHz is the spin perturbation, equal to 2/5 of the separation of the levels at zero magnetic field. The wavefunction components are

$$\left. \begin{aligned} D_A(5/2, 5/2, B) &= 1, & D_B(5/2, 5/2, B) &= 0, \\ D_A(5/2, -5/2, B) &= 0, & D_B(5/2, -5/2, B) &= 1, \end{aligned} \right\} \quad (3.1.26)$$

and for $m_J \neq \pm 5/2$,

$$D_A(J, m_J, B) = (m_J + y + \eta \sqrt{y^2 + 2m_J y + 25/4})/d, \quad (3.1.27)$$

$$D_B(J, m_J, B) = \sqrt{(5/2 + m_J)(5/2 - m_J)}/d, \quad (3.1.28)$$

where $d = [(5/2 + m_J)(5/2 - m_J) + (m_J + y + \eta \sqrt{y^2 + 2m_J y + 25/4})^2]^{1/2}, \quad (3.1.29)$

and $\left. \begin{aligned} \eta &= 1 \text{ for } J = 5/2 \\ \eta &= -1 \text{ for } J = 3/2 \end{aligned} \right\} \quad (3.1.30)$

The energy levels and wavefunctions are plotted as functions of magnetic field in figure 3.1.3. Similar results hold as in the 3S state, but in the 4D states the spin orbit coupling is being progressively broken down by the magnetic field, rather than the hyperfine interaction in the case of the ground states.

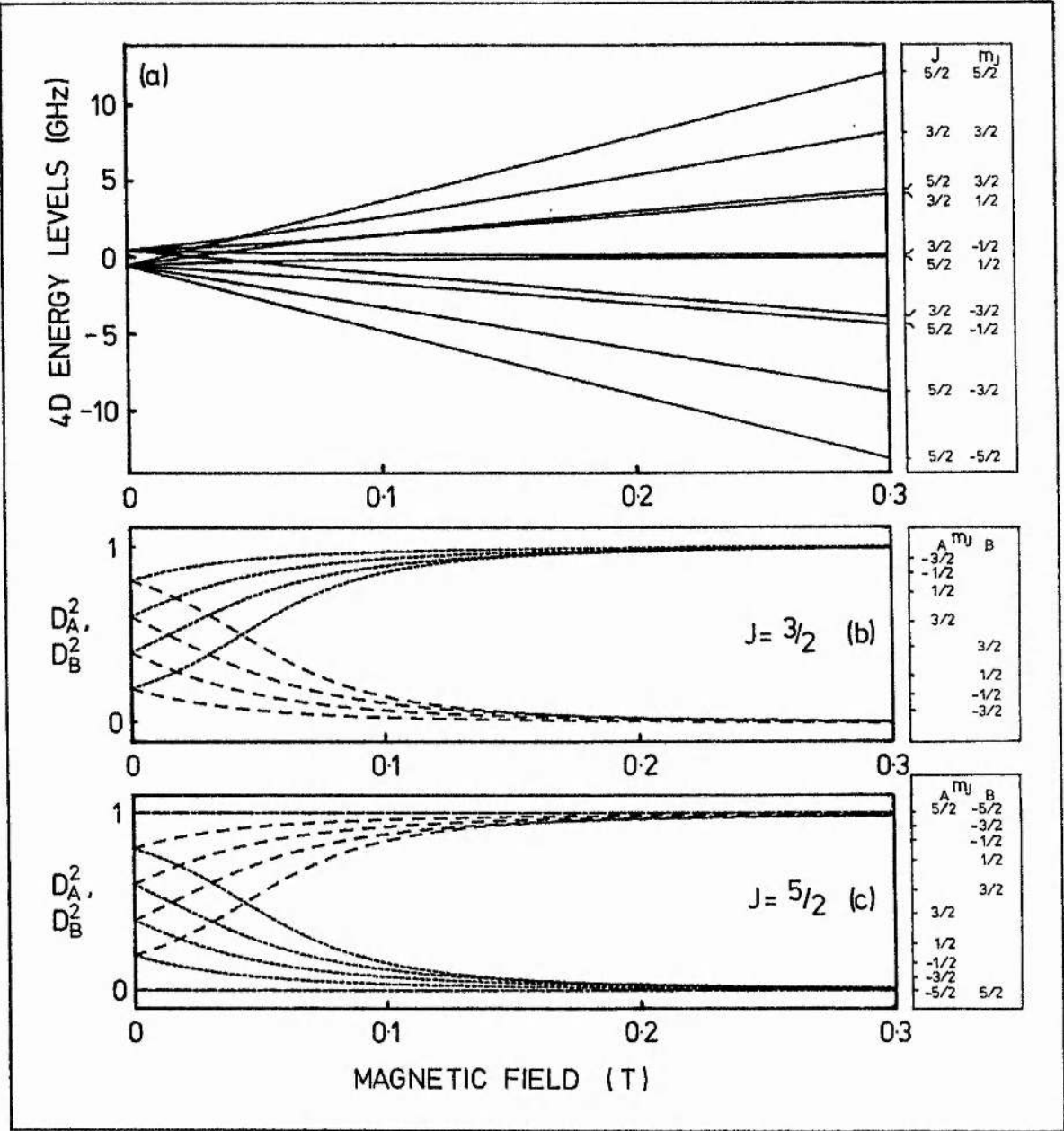


Figure 3.1.3 (a) Energy levels and (b,c) eigenfunction components for the 4D states plotted as functions of magnetic field strength. The box by part (a) shows the J, m_J quantum numbers of each level; the other two boxes identify each curve with its magnetic quantum numbers. The curves with short (long) dashes are drawn for D_A^2 (D_B^2).

3.2 DETAILED THEORY OF MAGNETIC-FIELD-INDUCED SECOND HARMONIC GENERATION

The analysis of second harmonic generation in sodium vapour presented here follows that of Uchiki et al [97], but their theoretical treatment is extended by distinguishing between homogeneous and inhomogeneous broadening processes, and by consideration of the special case of single frequency fundamental radiation. The use of a single frequency fundamental beam permits examination of many interesting effects which would have been "smudged out" by a large linewidth laser.

The absorption of two-photons from the fundamental beam by an atom can induce a coherence between its 4D and 3S states. Under certain conditions this can cause second harmonic generation in the forward direction, by means of an electric quadrupole transition. The aim of the theoretical modelling described here is to calculate the value of the 3S - 4D quadrupole moments under the conditions of interest. Expressions are thus obtained for the power and polarisation of the second harmonic beam as functions of the laser frequency, the magnetic field strength and the power and polarisation angle of the fundamental light.

The atomic system is considered to consist of the three groups of states listed in the previous section, that is, the 3S ground states, the 3P intermediate states and the resonantly enhancing 4D states of the sodium atom. These are labelled s, p and d respectively. The Hamiltonian, H_0 , of the atomic system includes fine, hyperfine and Zeeman splitting terms as described above. The homogeneous linewidth enters the analysis as a damping constant in the two-photon-induced coherence between the upper and

lower states. The inhomogeneous (Doppler) linewidth is taken into account by integrating the equations for the induced quadrupole moments across the Maxwellian velocity distribution of the sodium atoms, with appropriately shifted atomic resonant frequencies.

The expectation values of the quadrupole moment oscillating at the second harmonic frequency can be derived by consideration of the time evolution of the density matrix operator ρ [12]. The quantum mechanical system is considered to be in a state

$$\phi(r,t) = \sum_n c_n(t) \Psi_n(r), \quad (3.2.1)$$

where $c_n(t) = \int \Psi_n^*(r) \phi(r,t) d\tau$, and $\Psi_n(r)$ form a complete orthonormal set of eigenfunctions. The average value of an expectation value of an operator A is

$$\langle A \rangle = \sum_{nm} \overline{c_m^* c_n} A_{mn}, \quad (3.2.2)$$

where $A_{mn} = \int \Psi_m^*(r) A \Psi_n(r) d\tau. \quad (3.2.3)$

Density matrix elements are defined as the ensemble average

$$\rho_{nm} = \overline{c_m^* c_n}, \quad (3.2.4)$$

and the matrix form of these elements is known as the density matrix [12]. The time evolution of this matrix may be determined from the time-dependent Schroedinger equation

$$\mathcal{H} \phi(r,t) = i\hbar \frac{\partial \phi(r,t)}{\partial t}, \quad (3.2.5)$$

as each system in the ensemble must satisfy this equation. This leads to the Liouville equation for the time evolution of the density matrix

$$\frac{\partial \rho}{\partial t} = \frac{i}{\hbar} [\rho, \mathcal{H}], \quad (3.2.6)$$

The effect of collisions may be introduced by modifying this equation to

$$\frac{\partial \rho_{ij}}{\partial t} = \frac{-i}{\hbar} [\mathcal{H}, \rho]_{ij} - \chi_{ij} (\rho - \bar{\rho})_{ij} \quad (3.2.7)$$

where $\mathcal{H} = \mathcal{H}_0 + \mathcal{H}_1$ (3.2.8)

$$\mathcal{H}_1 = -\underline{p} \cdot \underline{E} = V \exp[-i\omega t] + \text{c.c.}, \quad (3.2.9)$$

and $\bar{\rho} = \frac{\exp[-\mathcal{H}_0/k_B T]}{\text{tr}(\exp[-\mathcal{H}_0/k_B T])}$ (3.2.10)

is the thermal equilibrium value of the density matrix [12]. Here χ_{ij} is defined to be the relaxation rate for the population in level i , which depends on spontaneous emission as well as collision processes, and χ_{ij} ($i \neq j$) is the rate at which ρ_{ij} relaxes to zero. This quantity describes the phase coherence between levels i and j , which will decay due to collisional dephasing. \mathcal{H}_1 is the perturbation caused by the electric dipole interaction energy between the fundamental laser field $\underline{E}_w = \underline{E} \exp[-i\omega t] + \text{c.c.}$ and the atomic system, where \underline{E} and ω are the amplitude and angular frequency of the fundamental field respectively. A representation is chosen in which $(\mathcal{H}_0)_{ij} = E_i \delta_{ij}$, and w_{ij} is defined as $w_{ij} = (E_i - E_j)/\hbar$. The thermal equilibrium values of the density matrix elements then take the form

$$\bar{\rho}_{ij} = 0 \quad \text{for } i \neq j \quad (3.2.11)$$

$$\bar{\rho}_{ii} = \exp[-E_i/k_B T] / \left(\sum_{\text{all states}} \exp[-E_j/k_B T] \right) \quad (3.2.12)$$

The subscripts i and j correspond to the s , p and d states of the sodium atom. The equations of motion of the density matrix are then

$$\frac{\partial \rho_{ij}}{\partial t} = -i\omega_{ij}\rho_{ij} - \frac{i}{\hbar}[V, \rho]_{ij} - \gamma_{ij}(\rho - \bar{\rho})_{ij} \quad (3.2.13)$$

where $[V, \rho]_{ij} = \sum_V (\rho_{iV}\mu_{Vj} - \mu_{iV}\rho_{Vj})E(t)$, (3.2.14)

and μ_{ij} is the ij element of the dipole moment operator. An integral perturbative solution may be found for ρ [12] as

$$\rho_{ij}^{(n)}(t) = (-i/\hbar) \int_{-\infty}^t \exp[i(\omega_{ij} - i\gamma_{ij})(t'-t)] \times [V(t'), \rho^{(n-1)}(t')]_{ij} dt' \quad (3.2.15)$$

where $\rho_{ij} = \rho_{ij}^{(0)} + \rho_{ij}^{(1)} + \rho_{ij}^{(2)} + \dots$ (3.2.16)

and $\rho_{ij}^{(0)} = \bar{\rho}_{ij} \delta_{ij}$. (3.2.17)

Equation 3.2.17 describes the populations of the states when no electromagnetic field is present. In the magnetic fields used in this study the maximum splitting of the $3S$ states is less than 0.1% of $k_B T$, so the equilibrium populations of these states are essentially equal. The energy of the $3S - 3P$ transition is about thirty times greater than $k_B T$, so the populations of the $3P$ and $4D$ states are essentially zero in thermal equilibrium. The zero value for off-diagonal matrix elements ρ_{ij} ($i \neq j$) is due to the lack of coherence between states when no electromagnetic field is present; any coherence that had been generated by an electromagnetic field previously is assumed to have been lost due to damping processes.

Equation 3.2.15 may now be evaluated to give the higher order terms in equation 3.2.16. The optical electric field amplitudes of the fundamental

radiation are taken as constant for the cw excitation under consideration. The "rotating wave approximation" is used, in which only near resonant terms are kept; in this case

$$\rho_{ps}^{(1)} = - \frac{\rho_{ss}^{(0)} V_{ps} \exp[-i\omega t]}{\hbar(\omega_{ps} - \omega - i\gamma_{ps})} \quad (3.2.18)$$

The excitation is assumed to be weak, so all other $\rho_{ij}^{(1)}$, including $\rho_{ss}^{(1)}$, are zero to first order in the perturbation. The matrix element which drives the second harmonic is ρ_{ds} . It may be calculated from the above equations as

$$\begin{aligned} \rho_{ds} &= \rho_{ds}^{(2)} \\ &= \sum_P \frac{\rho_{ss} \exp[-2i\omega t]}{\hbar^2(\omega - \omega_{ps} + i\gamma_{ps})} \\ &\quad \times \int_{-\infty}^t \exp[i(2\omega - \omega_{ds} + i\gamma_{ds})(t-t')] V_{dp} V_{ps} dt'; \end{aligned} \quad (3.2.19)$$

$$\text{and } \therefore \rho_{ds} = \sum_P \frac{\rho_{ss} V_{dp} V_{ps} \exp[-2i\omega t]}{\hbar^2(\omega - \omega_{ps} + i\gamma_{ps})(2\omega - \omega_{ds} + i\gamma_{ds})} \quad (3.2.20)$$

if V_{nm} are not time dependent. As $\omega - \omega_{ps}$ is of the order of 300 wavenumbers, the small differences in $(\omega - \omega_{ps} + i\gamma_{ps})$ between different 3S - 3P state combinations, and between small laser detunings, will not affect the resonant denominator significantly, and so this quantity may be replaced by its mean value and moved outside the summation over P states.

Following Shore and Menzel [20] and Uchiki et al [97], the quadrupole moment operator is defined as

$$Q_{uv} = -e (r_u r_v - r^2 \delta_{uv} / 3) \quad (u, v = x, y, z); \quad (3.2.21)$$

this is different by a factor of three from the expression given by some other authors [25, 114]. The expectation value of this operator is thus

$$\langle Q_{uv} \rangle = \text{Tr}(\rho Q_{uv}) = \sum_{ds} \rho_{ds} (Q_{uv})_{ds} + \text{c.c.} \quad (3.2.22)$$

where the summation is taken over all the 3S and 4D states. The slowly varying amplitude of $\langle Q_{uv} \rangle$ is then given by

$$\begin{aligned} \langle \tilde{Q}_{uv} \rangle = & \sum_{ds} \frac{\rho_{ss}}{i\hbar^2 \langle w - w_{ps} + i\gamma_{ps} \rangle} \\ & \times \int_{-\infty}^t \exp[i(2w - w_{ds} + i\gamma_{ds})(t-t')] \sum_p V_{dp} V_{ps} (Q_{uv})_{ds} dt'. \end{aligned} \quad (3.2.23)$$

Calculation of $\sum_p V_{dp} V_{ps} (Q_{uv})_{ds}$ is most readily achieved using spherical tensor formalism [20]. In this case, the quadrupole matrix elements may be expressed by the spherical tensor elements Q_q defined as

$$Q_0 = -\sqrt{3/2} Q_{zz} \quad (3.2.24)$$

$$Q_{\pm 1} = \pm (Q_{xz} \pm iQ_{yz}) \quad (3.2.25)$$

$$Q_{\pm 2} = - (Q_{xx} - Q_{yy} \pm 2iQ_{xy})/2 \quad (3.2.26)$$

$$\begin{aligned} \text{and thus } \langle \tilde{Q}_q \rangle = & \sum_{ds} \frac{\rho_{ss}}{i\hbar^2 \langle w - w_{ps} + i\gamma_{ps} \rangle} \\ & \times \int_{-\infty}^t \exp[i(2w - w_{ds} + i\gamma_{ds})(t - t')] T_q dt' \end{aligned} \quad (3.2.27)$$

$$\text{where } T_q = \sum_p V_{dp} V_{ps} (\tilde{Q}_q)_{ds} \quad (3.2.28)$$

$$= \sum_p e^2 \langle D_{J_d}^{m_d} | \underline{\epsilon} \cdot \underline{r} | P_{J_p}^{m_p} \rangle \langle P_{J_p}^{m_p} | \underline{\epsilon} \cdot \underline{r} | S_F^{m_f} \rangle \langle S_F^{m_f} | \tilde{Q}_q^{(2)} | D_{J_d}^{m_d} \rangle \quad (3.2.29)$$

The selection rules of the SHG are embodied in the two dipole matrix elements and the quadrupole matrix element. Evaluation of T_q is made easier by the $\Delta m_s = 0$ selection rule for both dipole and quadrupole transitions. This allows each wavefunction to be described in terms of its $m_s = \pm 1/2$ components, which may then be treated separately. The geometry of the system lies in the m_l values of the states. This geometrical dependence may then be determined with the aid of the Wigner Eckart theorem [20], which may be used to split the matrix elements into two parts:

$$\langle \alpha J m | T_q^{(k)} | \alpha' J' m' \rangle = \frac{(J' m'; k q | J m)}{\sqrt{2J+1}} \langle \alpha J || T^{(k)} || \alpha' J' \rangle. \quad (3.2.30)$$

$(J' m'; k q | J m)$ is a Clebsch Gordon coefficient which contains the geometry of the system, while $\langle \alpha J || T^{(k)} || \alpha' J' \rangle$ is a reduced matrix element, which is independent of the geometry. The properties of the Clebsch Gordon coefficients are described by Shore and Menzel [20], whose notation is used in this work. The reduced matrix element corresponds to the square of the transition probability summed over all magnetic quantum numbers m . α symbolises all the other quantum numbers of each of the two states.

As the hyperfine splitting of the 4D states is so small, the selection rules associated with the hyperfine interaction may be neglected. By expansion of the wavefunctions in the way described in the previous section, the quadrupole matrix element may be written as

$$\langle S_F^{m_F} | Q_q^{(2)} | D_{J_d}^{m_d} \rangle = \langle S_A \psi_{s,1/2} + S_B \psi_{s,-1/2} | Q_q^{(2)} | D_A \psi_{d,1/2} + D_B \psi_{d,-1/2} \rangle. \quad (3.2.31)$$

Then, by use of the Wigner Eckart theorem and the $\Delta m_s = 0$ selection rule

$$\begin{aligned}
 \langle S_F^{m_F} | Q_q^{(2)} | D_{J_d}^{m_d} \rangle = & \\
 & \frac{S_A^D}{\sqrt{5}} (-1)^{2-q} \delta \left(\begin{matrix} m_d - 1 + q \\ - \\ 2 \end{matrix} \right) \langle \Psi_{s,1/2} | Q_q^{(2)} | \Psi_{d,1/2} \rangle \\
 & + \frac{S_B^D}{\sqrt{5}} (-1)^{2-q} \delta \left(\begin{matrix} m_d + 1 + q \\ - \\ 2 \end{matrix} \right) \langle \Psi_{s,-1/2} | Q_q^{(2)} | \Psi_{d,-1/2} \rangle
 \end{aligned} \tag{3.2.32}$$

The scalar product $\underline{\epsilon} \cdot \underline{r}$ in spherical coordinates [20] is

$$\underline{\epsilon} \cdot \underline{r} = \sum_t (-1)^t \epsilon_t r_{-t} \tag{3.2.33}$$

so T_q may be written as

$$\begin{aligned}
 T_q = & \sum_{J_p, m_p} \sum_{q_1, q_2} e^2 (-1)^{q_1 + q_2} \epsilon_{q_1}^{(1)} \epsilon_{q_2}^{(1)} \\
 & \times \langle D_{J_d}^{m_d} | r_{-q_1}^{(1)} | P_{J_p}^{m_p} \rangle \langle P_{J_p}^{m_p} | r_{-q_2}^{(1)} | S_F^{m_F} \rangle \langle S_F^{m_F} | Q_q^{(2)} | D_{J_d}^{m_d} \rangle.
 \end{aligned} \tag{3.2.34}$$

The quadrupole matrix element may be replaced using equation 3.2.32, and then the wavefunctions for the S, P and D states given in equations 3.1.4, 3.1.21 and 3.1.22 may be inserted into the dipole matrix elements in a similar manner to that used in equation 3.2.31. Use of the $\Delta m_s = 0$ selection rule and the Wigner Eckart theorem on the resultant dipole matrix elements give

$$\begin{aligned}
T_q = & \sum_{J_p, m_p} \sum_{q_1, q_2} e^{2(-1)^{q_1+q_2}} \varepsilon_{q_1} \varepsilon_{q_2} (-1)^{q+1} (2J_p+1) (1/5\sqrt{3}) \\
& \times \left\{ S_{AA}^2 D_{AA}^2 \begin{pmatrix} 1 & 1/2 & J_p \\ m_p-1/2 & 1/2 & -m_p \end{pmatrix}^2 (1, m_p-1/2; 1, -q_1 | 2, m_d-1/2) \right. \\
& \times (0, 0; 1, -q_2 | 1, m_p-1/2) \delta(m_d - 1/2 + q) \\
& \times \langle \psi_{d, 1/2} || r || \psi_{p, 1/2} \rangle \langle \psi_{p, 1/2} || r || \psi_{s, 1/2} \rangle \langle \psi_{s, 1/2} || Q^{(2)} || \psi_{d, 1/2} \rangle \\
& + S_{BB}^2 D_{BB}^2 \begin{pmatrix} 1 & 1/2 & J_p \\ m_p+1/2 & -1/2 & -m_p \end{pmatrix}^2 (1, m_p+1/2; 1, -q_1 | 2, m_d+1/2) \\
& \times (0, 0; 1, -q_2 | 1, m_p+1/2) \delta(m_d + 1/2 + q) \\
& \left. \times \langle \psi_{d, -1/2} || r || \psi_{p, -1/2} \rangle \langle \psi_{p, -1/2} || r || \psi_{s, -1/2} \rangle \langle \psi_{s, -1/2} || Q^{(2)} || \psi_{d, -1/2} \rangle \right\} \quad (3.2.35)
\end{aligned}$$

where the m_p are the magnetic quantum numbers of the total angular momentum for the 3P states. The second Clebsch Gordon coefficient in each pair is equal to $\delta(m_{p\mp 1/2} + q_2)$, so $m_{p\mp 1/2}$ may be replaced by $-q_2$, and similarly the $\delta(m_d \pm 1/2 + q)$ terms, which arose from the quadrupole matrix element, allow $m_d \pm 1/2$ to be replaced by $-q$. Then, since $q_1 + q_2$ must equal q to give a non-zero value for the remaining Clebsch Gordon coefficients, and calculating the values of the 3-j symbols using the relationships in [20] and [84], in particular

$$\begin{pmatrix} J+1/2 & J & 1/2 \\ M & -M-1/2 & 1/2 \end{pmatrix} = (-1)^{J-M-1/2} \left[\frac{J-M+1/2}{(2J+2)(2J+1)} \right]^{1/2}, \quad (3.2.36)$$

T_q may be evaluated to be

$$T_q = -B_q (F, m_F, J_d, m_d, B) (\varepsilon\varepsilon)_{2,q} e^2 r_{dp} r_{ps} r_{sd}^2 / 5\sqrt{3}, \quad (3.2.37)$$

where

$$\begin{aligned}
B_q = & D_A^2 (J_d, m_d, B) S_A^2 (F, m_F, B) \delta(m_d - 1/2 + q) \\
& + D_B^2 (J_d, m_d, B) S_B^2 (F, m_F, B) \delta(m_d + 1/2 + q), \quad (3.2.38)
\end{aligned}$$

and B is the magnetic field strength. $(\epsilon\epsilon)_{2,q}$ is a second rank spherical tensor defined by

$$(\epsilon\epsilon)_{2,q} = \sum_{q_1, q_2} (1, q_1; 1, q_2 | 2, q) \epsilon_{q_1} \epsilon_{q_2}, \quad (3.2.39)$$

where ϵ_{q_1} and ϵ_{q_2} are the first rank spherical tensor elements of equation 3.2.33. The quantity $r_{dp} r_{ps} Q_{sd}$ is the product of the reduced matrix elements of the three original matrix elements.

The spherical tensor matrix elements of the quadrupole moment may therefore be written as

$$\begin{aligned} \langle \tilde{Q}_q \rangle = & - \sum_{d\phi} \int_{-\infty}^t P_{ss} \frac{\exp[i(2\omega - \omega_{ds} + i\gamma_{ds})(t-t')]]}{i 5\sqrt{3} \hbar^2 \langle \omega - \omega_{ps} + i\gamma_{ps} \rangle} \\ & \times B_q (\epsilon\epsilon)_{2,q} e^2 r_{dp} r_{ps} Q_{sd} dt' \end{aligned} \quad (3.2.40)$$

As the quantum numbers of the P states do not appear in this equation, the 4D state quantum numbers will now be written as J, m_j for the total angular momentum and the magnetic quantum number of the angular momentum respectively.

The geometry of the system is defined in figure 1.3.2; the fundamental laser beam propagates along the y axis, and thus the second harmonic wave is driven by the effective dipole

$$(P_x, P_z) = -i |k_2| (Q_{xy}, Q_{zy}) / 2 \quad (3.2.41)$$

where k_2 is the wavevector of the second harmonic radiation, and Q_{xy} and Q_{zy} are two of the quadrupole matrix elements defined in

equation 3.2.21. To find the values of these elements it is necessary to convert from the spherical tensor formalism, which was appropriate for the calculation of $T_{q'}$ to Cartesian tensor formalism, using the relations

$$2 Q_{xy} = i (Q_2 - Q_{-2}) \quad (3.2.42)$$

and $2 Q_{zy} = -i (Q_1 + Q_{-1})$. (3.2.43)

Then
$$2 Q_{xy} = - \sum_{d,s} \int_{-\infty}^t \frac{\rho_{ss} \exp[i(2w - w_{ds} + i\gamma_{ds})(t-t')]}{5\sqrt{3} \hbar^2 \langle w - w_{ps} + i\gamma_{ps} \rangle} e^2 r_{dp} r_{ps} Q_{sd} \times [B_2 (\epsilon\epsilon)_{2,2} - B_{-2} (\epsilon\epsilon)_{2,-2}] dt' \quad (3.2.44)$$

and
$$2 Q_{zy} = \sum_{d,s} \int_{-\infty}^t \frac{\rho_{ss} \exp[i(2w - w_{ds} + i\gamma_{ds})(t-t')]}{5\sqrt{3} \hbar^2 \langle w - w_{ps} + i\gamma_{ps} \rangle} e^2 r_{dp} r_{ps} Q_{sd} \times [B_1 (\epsilon\epsilon)_{2,1} + B_{-1} (\epsilon\epsilon)_{2,-1}] dt' \quad (3.2.45)$$

The $(\epsilon\epsilon)_{2,q}$ terms are evaluated using equation 3.2.39 to give

$$Q_{xy} = - \sum_{d,s} \int_{-\infty}^t \frac{\exp[i(2w - w_{ds} + i\gamma_{ds})(t - t')]}{20 \sqrt{3} \hbar^2 \langle w - w_{ps} + i\gamma_{ps} \rangle} (B_2 - B_{-2}) \times \epsilon_x^2 e^2 r_{dp} r_{ps} Q_{sd} \rho_{ss} dt' \quad (3.2.46)$$

and
$$Q_{zy} = - \sum_{d,s} \int_{-\infty}^t \frac{\exp[i(2w - w_{ds} + i\gamma_{ds})(t - t')]}{20 \sqrt{3} \hbar^2 \langle w - w_{ps} + i\gamma_{ps} \rangle} 2(B_1 - B_{-1}) \times \epsilon_x \epsilon_z e^2 r_{dp} r_{ps} Q_{sd} \rho_{ss} dt'. \quad (3.2.47)$$

The geometry of the system is now included only in the B_q terms and the laser polarisation. The laser used in the work covered in this thesis was a single mode, linearly polarised continuous wave laser, the field of which

may be described as

$$(\mathbf{E}_x, \mathbf{E}_z) = \mathbf{E} \exp[-i\omega t] (\sin\theta, \cos\theta) + \text{c.c.} \quad (3.2.48)$$

where θ is the angle between the plane of polarisation of the laser and the z axis. In this case the integrals in equations 3.2.46 and 3.2.47 are readily calculated to give

$$\tilde{Q}_{xy} = \frac{-iK\epsilon_x^2}{\langle \omega_{ps} - \omega - i\gamma_{ps} \rangle} \sum_{\substack{F, m_F, \\ J, m_J}} \frac{B_2 - B_{-2}}{(\omega_{ds} - 2\omega - i\gamma_{ds})} \quad (3.2.49)$$

$$\tilde{Q}_{zy} = \frac{-iK\epsilon_x \epsilon_z}{\langle \omega_{ps} - \omega - i\gamma_{ps} \rangle} \sum_{\substack{F, m_F, \\ J, m_J}} \frac{2(B_1 - B_{-1})}{(\omega_{ds} - 2\omega - i\gamma_{ds})} \quad (3.2.50)$$

where
$$K = \frac{e^2 r_{dp} r_{ps}^2 \alpha_{sd} \rho_{ss}}{20 \sqrt{3} \hbar^2} \quad (3.2.51)$$

The thermal motion of the atoms is taken into account by including the effect of the Doppler shift in these equations [10, 12]. The angular transition frequency of an atom moving with velocity v_y along the direction connecting the observer and the atom is

$$\omega_{ds} = \omega_{ds0} + k_{2\omega} v_y \quad (3.2.52)$$

where ω_{ds0} is the resonant angular frequency of an atom at rest relative to the observer and $k_{2\omega}$ is the wavevector of the second harmonic. The Maxwellian velocity distribution function for a gas with atomic mass M at an absolute temperature T is

$$f(v_y) = \sqrt{M/2\pi k_B T} \exp[-Mv_y^2/2k_B T] \quad (3.2.53)$$

where k_B is Boltzmann's constant. Equations 3.2.49 and 3.2.50 are therefore modified to the form

$$\tilde{Q}_{xy} = \frac{-iK\epsilon_x^2 \sqrt{M/2\pi k_B T}}{\langle w_{ps}^{-w-i\gamma_{ps}} \rangle} \times \sum_{\substack{F, m_F \\ J, m_J}} \int_{-\infty}^{\infty} \frac{(B_2 - B_{-2}) \exp[-Mv_y^2/2k_B T] dv_y}{(w_{ds} + kv_y - 2w - i\gamma_{ds})} \quad (3.2.54)$$

$$\therefore \tilde{Q}_{xy} = \frac{-iK\epsilon_x^2}{\langle w_{ps}^{-w-i\gamma_{ps}} \rangle \Omega} \sum_{\substack{F, m_F \\ J, m_J}} (B_2 - B_{-2}) Z[(2w - w_{ds} + i\gamma_{ds})/\Omega] \quad (3.2.55)$$

$$\text{and } \tilde{Q}_{zy} = \frac{-iK\epsilon_x \epsilon_z}{\langle w_{ps}^{-w-i\gamma_{ps}} \rangle \Omega} \sum_{\substack{F, m_F \\ J, m_J}} 2(B_1 - B_{-1}) Z[(2w - w_{ds} + i\gamma_{ds})/\Omega] \quad (3.2.56)$$

$$\text{where } \Omega = 2w\sqrt{2k_B T/Mc^2} \quad (3.2.57)$$

is the Doppler width (half width $1/e$ maximum) of the second harmonic radiation, and $Z(a + ib)$ is the plasma dispersion function

$$Z(a + ib) = \frac{1}{\sqrt{\pi}} \int_{-\infty}^{\infty} \frac{\exp[-t^2] dt}{t - (a + ib)} \quad (3.2.58)$$

The properties of this function are described by Fried and Conte [115]. Its value must be found for each of the 80 pairs of energy levels $(F, m_F) \rightarrow (J, m_J)$, for every laser frequency, and for any homogeneous and inhomogeneous linewidth of interest. The plasma dispersion function and the numerical routines used for calculating its value are described in appendices A and B respectively.

The above theoretical treatment allows calculation of the quadrupole moments of each atom. In some situations bulk effects in the medium modify the overall result, but this treatment was found to be an excellent basis on which to work.

The two quadrupole moments Q_{xy} and Q_{zy} may be regarded as effective dipoles generating second harmonic radiation parallel to the x and z axes respectively. As expected from the quadrupole selection rules [83], the Q_{zy} moment is driven by $\Delta m_l = \pm 1$ transitions, and the Q_{xy} moment is driven by $\Delta m_l = \pm 2$ transitions. These selection rules enter the theoretical treatment as the B_Q terms of equation 3.2.37 and 3.2.38. The intensity and polarisation properties of the second harmonic may be derived from the magnitudes and relative phases of the two quadrupole moments.

The intensity of the second harmonic radiation is given by

$$I_{SH} \propto (\hat{e}_x \tilde{Q}_{xy}^* + \hat{e}_z \tilde{Q}_{zy}^*)(\hat{e}_x \tilde{Q}_{xy} + \hat{e}_z \tilde{Q}_{zy}) \quad (3.2.58)$$

$$= \tilde{Q}_{xy}^* \tilde{Q}_{xy} + \tilde{Q}_{zy}^* \tilde{Q}_{zy}. \quad (3.2.60)$$

The second harmonic light is, in general, elliptically polarised. Its polarisation state is specified by the orientation of the ellipse axes, and their lengths a and b. The latter information may be given in terms of the second harmonic power, and the eccentricity [116] of the ellipse,

$$\eta = (a - b)/a. \quad (3.2.61)$$

If the radiation is examined through an analyser which has its transmission axis at θ_A to the z axis, the intensity of the detected signal is given by

$$I_{SH}(\theta_A) \propto |\tilde{Q}_{xy} \sin\theta_A + \tilde{Q}_{zy} \cos\theta_A|^2 \quad (3.2.62)$$

The value of θ_A which gives the maximum value of $I_{SH}(\theta_A)$ is

$$\theta_{Amax} = 0.5 \tan^{-1} [(\tilde{Q}_{xy} \tilde{Q}_{zy}^* + \tilde{Q}_{xy}^* \tilde{Q}_{zy}) / (|\tilde{Q}_{zy}|^2 - |\tilde{Q}_{xy}|^2)] \quad (3.2.63)$$

This corresponds to the angle between the z axis and the major axis of the ellipse describing the light. The eccentricity of the polarisation ellipse of the light can then be obtained from

$$\eta = 1 - (I_{SH}(\theta_{Amax} + 90^\circ) / I_{SH}(\theta_{Amax}))^{1/2}. \quad (3.2.64)$$

The results of this treatment will be presented alongside the experimental results in chapter five, but some general comments are given here. If no magnetic field is present, $B_2(J, m_J, F, m_F, 0) = B_{-2}(J, -m_J, F, -m_F, 0)$ and $w_{ds}(J, m_J, F, m_F, 0) = w_{ds}(J, -m_J, F, -m_F, 0)$; this leads to a zero result for the sum in equation 3.2.55 which gives \tilde{Q}_{xy} , and so no effective dipole for SHG exists in the x direction. A similar argument holds for the effective dipole in the z direction. When a transverse magnetic field is applied to the vapour, Zeeman splitting breaks these equalities and so SHG is then possible.

The $B_{\pm q}$ terms are dependent on the magnetic field strength but not the laser frequency. They describe the mixing of the magnetic quantum level eigenfunctions by the magnetic field as the field is increased from zero, through the low-field Zeeman effect, and into the Paschen-Back and Back-Goudshmidt regions. All the $B_{\pm q}$ terms are non-negative, and if B_q is finite for a particular transition B_{-q} will be zero (and vice-versa), as the q indicates the change in the value of m_l between the initial and final states. The B_{-q} term enters equation 3.2.55 as $-B_{-q}$; B_q and $-B_{-q}$ are plotted as functions of magnetic field in figure 3.2.1. As noted in the previous paragraph, at zero field $B_{+q}(J, m_J, F, m_F, 0) = B_{-q}(J, -m_J, F, -m_F, 0)$ for all such pairs of transitions, this is indeed seen in the diagrams. As the magnetic field is increased from zero the $B_{\pm q}$ values change. Examination

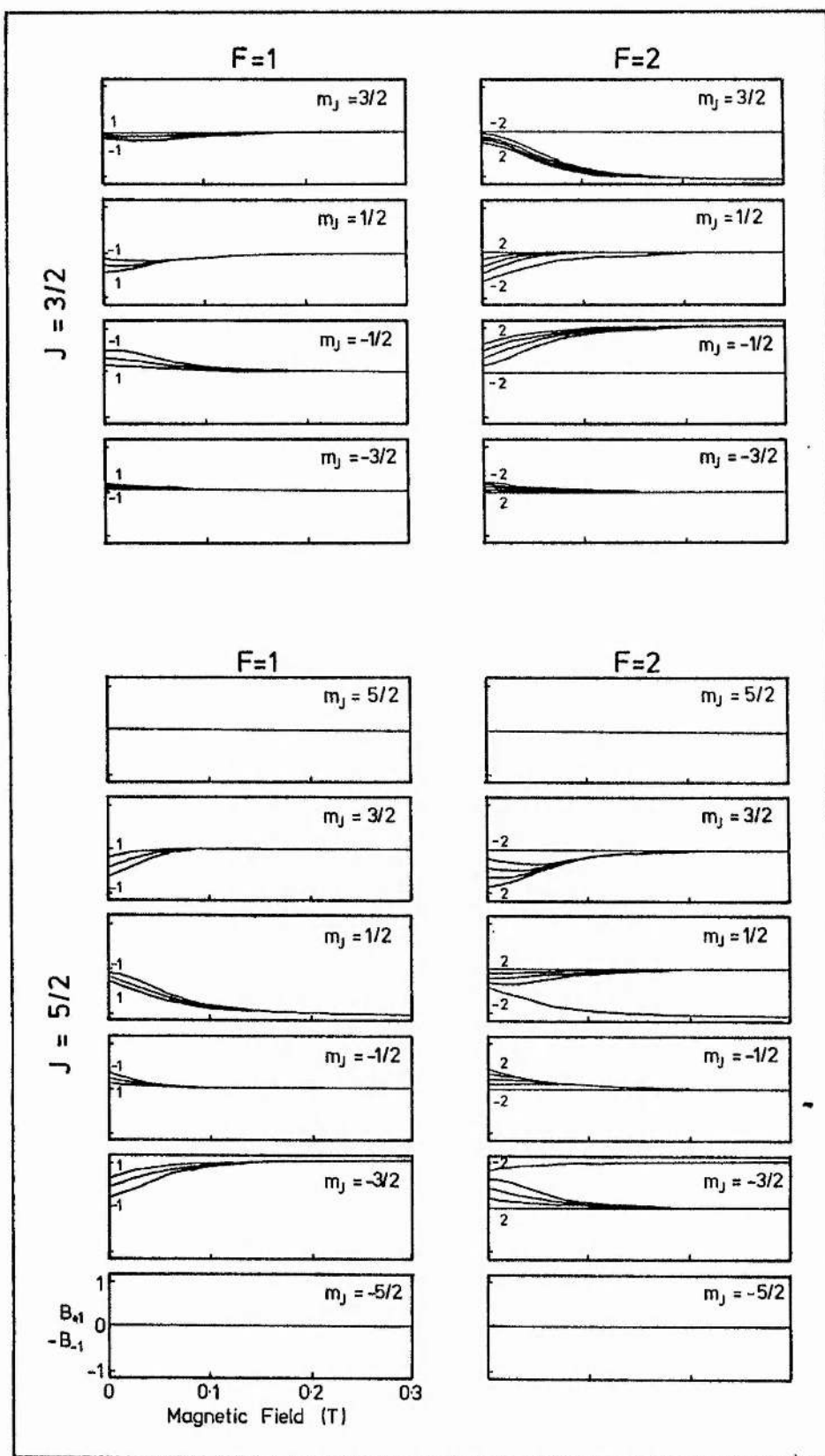


Figure 3.2.1(a). $B_{+1} - B_{-1}$ plotted as functions of magnetic field strength for all the $3S - 4D$ transitions. Positive (negative) values of $B_{+1} - B_{-1}$ are due to the B_{+1} (B_{-1}) term.

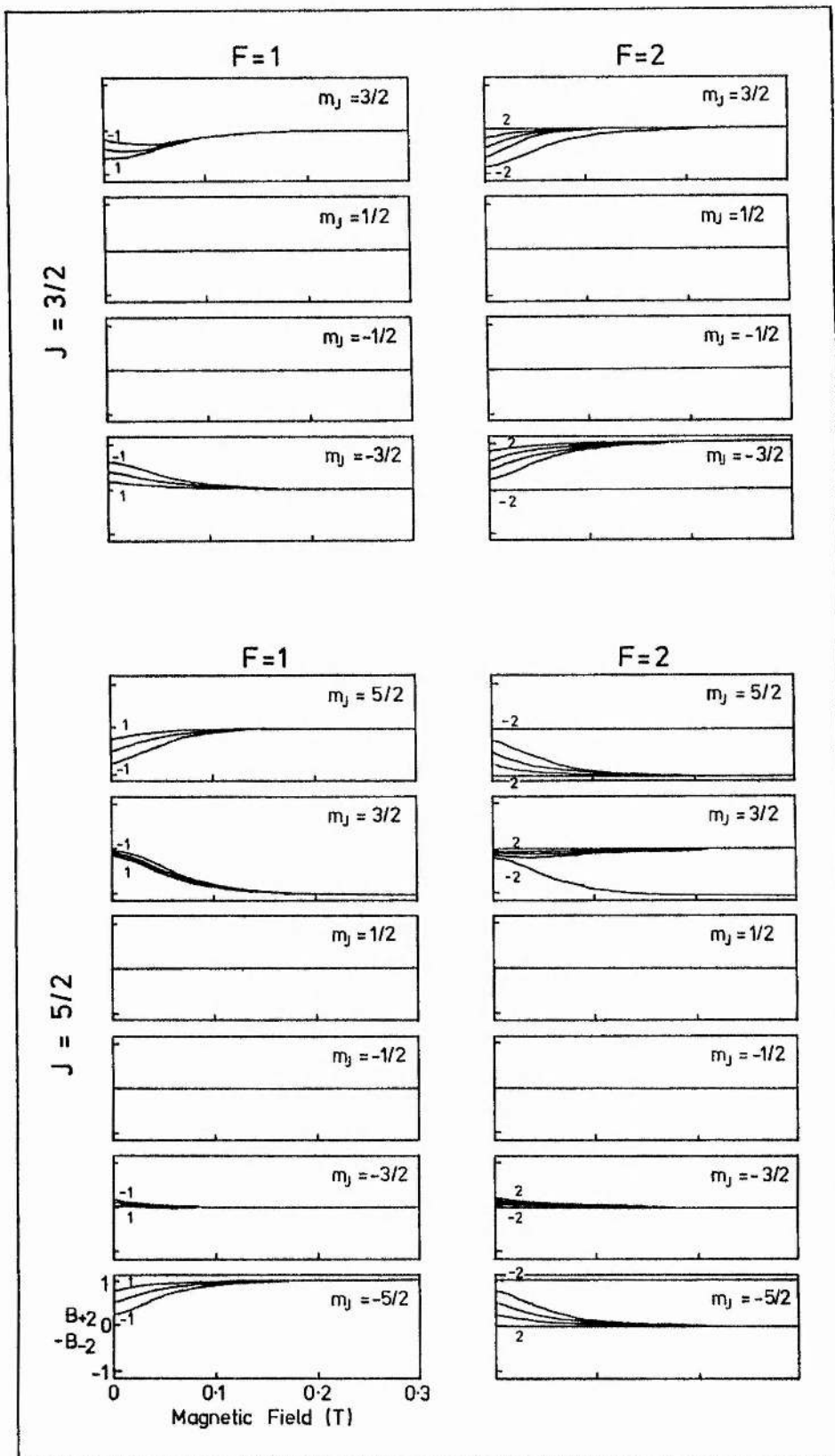


Figure 3.2.1(b). As part (a), but for $B_2 - B_{-2}$.

of these graphs shows at any field which transitions are involved in the SHG. There is little change in the values of $B_{\pm q}$ above 0.15 T, as the hyperfine and spin-orbit interactions have largely been broken down by the Zeeman effect, causing m_s and m_l to be good quantum numbers.

The resonant denominators, however, are dependent on both the magnetic field strength and the laser frequency. The contribution to the resonant enhancement of the SHG made by any transition depends on its detuning from the SH frequency, and hence on the magnetic field through Zeeman splitting.

Consider this in more detail for the case of the laser polarisation at 90° degrees to the magnetic field. In this arrangement only the Q_{xy} moment may be non-zero, due to ϵ_z being zero in equation 3.2.56. It is seen in equations 3.2.38 and 3.2.55 that only $\Delta m_l = \pm 2$ transitions may contribute to the Q_{xy} moment. The contribution of each transition to the amplitude of this quadrupole moment is

$$\begin{aligned} \tilde{Q}_{xy}(J, m_d, F, m_F, B) &= -iK' Z[(2w-w_{ds})/\Omega + i\gamma_{ds}/\Omega] (B_2 - B_{-2}) \\ &= -iK' Z[(2w-w_{ds})/\Omega + i\gamma_{ds}/\Omega] \times \\ &\quad \{D_A^2 S_A^2 \delta(m_J + 3/2) + D_B^2 S_B^2 \delta(m_J + 5/2) \\ &\quad - D_A^2 S_A^2 \delta(m_J - 5/2) - D_B^2 S_B^2 \delta(m_J - 3/2)\} \end{aligned} \quad (3.2.65)$$

where K' is a constant whose real part is very much greater than its imaginary part. At most one of the terms with the Kronecker delta functions may be finite for any one transition.

It is perhaps more illuminating to look at the contributions of pairs of transitions with magnetic quantum numbers $(+m_J, +m_F)$ and $(-m_J, -m_F)$, where the signs of m_J and m_F are chosen such that the first pair result in

a zero value for B_{-2} and the second pair a zero value for B_{+2} . In this case

$$\begin{aligned} \tilde{Q}_{xy}(J, +m_J, F, +m_F, B) + \tilde{Q}_{xy}(J, -m_J, F, -m_F, B) = \\ iK' B_{+2}(J, +m_J, F, +m_F, B) Z[(2w - w_{ds}(J, +m_J, F, +m_F, B))/\Omega + i\gamma_{ds}/\Omega] \\ - iK' B_{-2}(J, -m_J, F, -m_F, B) Z[(2w - w_{ds}(J, -m_J, F, -m_F, B))/\Omega + i\gamma_{ds}/\Omega] \end{aligned} \quad (3.2.66)$$

At zero field the B_{+2} and B_{-2} terms are equal, as are the two Z terms, and so no net contribution is made to the SHG by this pair of transitions (or any other such pair). As a magnetic field is applied the B_{+2} terms change as described above, and the real arguments of Z change due to Zeeman shifting. $B_{+2}(J, +m_J, F, +m_F, B) - B_{-2}(J, -m_J, F, -m_F, B)$ is proportional the magnetic field strength at low fields, so as long as the changes in Z are small, the net result is that the magnitude of $\tilde{Q}_{xy}(J, +m_J, F, +m_F, B) + \tilde{Q}_{xy}(J, -m_J, F, -m_F, B)$ is approximately proportional to the magnetic field strength. The size of the change in Z depends on the original detuning of the transition from exact resonance with the laser, but when this argument is extended to cover all such pairs of transitions it is found that the proviso for the quadrupole moment being proportional to the magnetic field strength is that the Zeeman splitting should be somewhat less than the Doppler width. Thus at low magnetic field strengths the second harmonic power, which is proportional to the square of \tilde{Q}_{xy} , is proportional to the square of the magnetic field strength. At higher fields, the B_{+2} components may be in resonance while the B_{-2} are far from it (or vice versa), and $|Z|$ is much larger in the former case than the latter. Clearly the low field relations break down, and the second harmonic power dependence on the magnetic field strength saturates.

The interference in the SHG amongst the various routes is calculated in the computer model using the above equations. The contributions to the SHG of

the various transitions are shown in figure 3.2.2 at a selection of magnetic field strengths. A vapour temperature of 300°C and a homogeneous linewidth of 35 MHz (HWHM) were used in the calculations, and the laser frequency was chosen to lie approximately 3 GHz from the centre of the two-photon absorption. The upper graph at each field strength shows the amplitudes of the contributions which are in phase with E_w^2 , and the lower graph shows those which are in quadrature. These correspond to the real and imaginary parts of equation 3.2.55 respectively. The thick line alongside each graph shows the sum of these contributions. At zero field these sums are zero, but as the field is increased the B_2 and B_{-2} terms change due to state mixing, and Zeeman splitting changes the resonant frequencies. The different transitions then no longer interfere totally destructively, and a net quadrupole moment results, as outlined above. The amplitude and phase of these moments are represented by the length and direction of the line in the centre of the circles at the top of the diagrams. At the frequency which is illustrated there are considerable changes in the phase of the SH as the field is varied.

The homogeneous and inhomogeneous linewidths enter this description in the dependence of Z on the detuning of the laser from the resonant frequency of each transition. Although the transitions are plotted in figure 3.2.2 at their centre frequencies, the frequencies of the transitions measured in the laboratory frame will vary due to the Doppler effect. However, the greater the detuning between the laser and the centre frequency of a transition, the fewer atoms will be Doppler shifted into resonance with the laser; the width of this resonance depends on the natural linewidth. The combination of these effects results in the shapes of the curves describing the plasma dispersion function. The evaluation of Z is discussed in appendix A, where figure A.1 shows the dependence on detuning of the real and imaginary parts of Z . The different shapes of these curves result in the

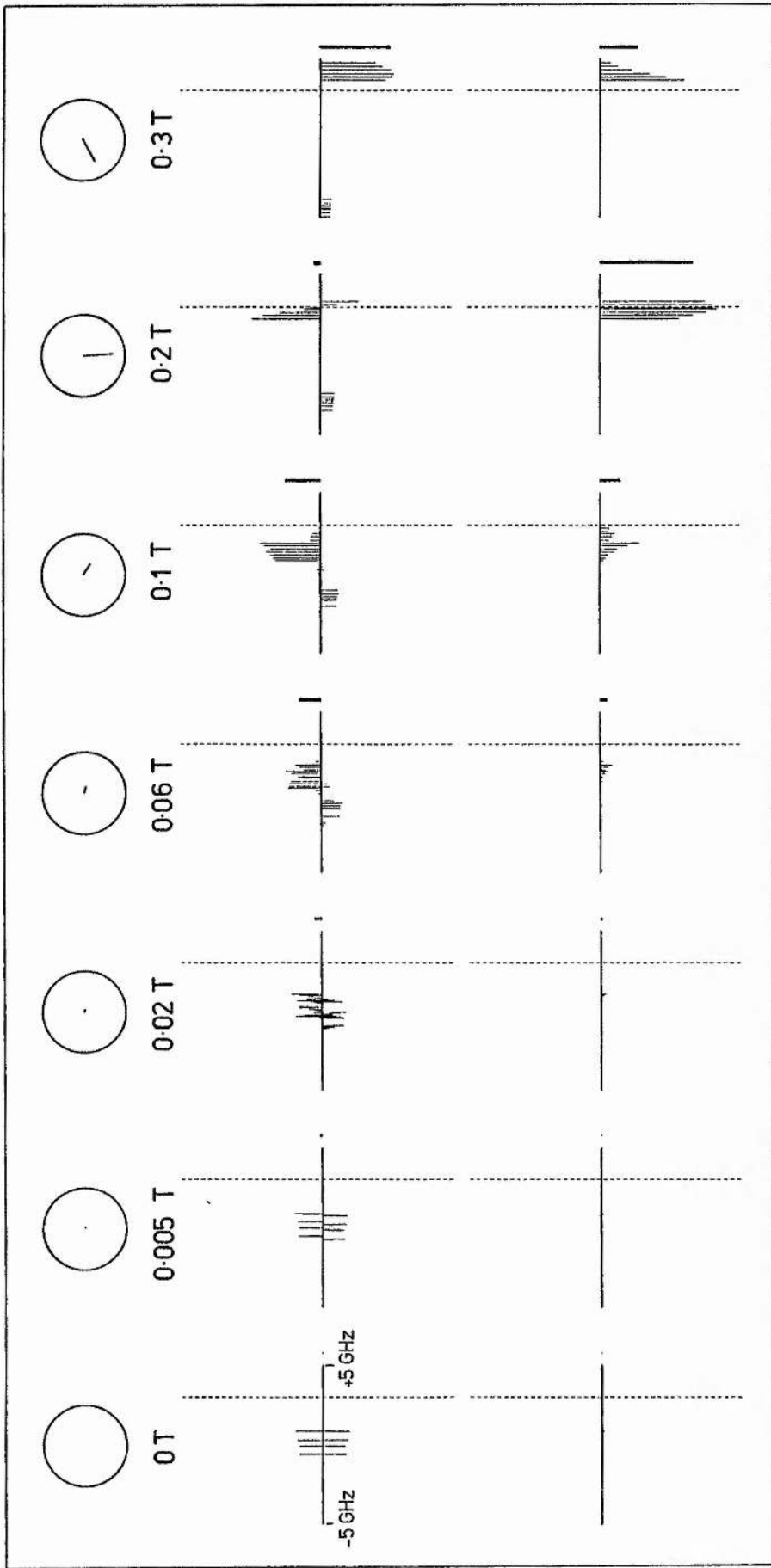


Figure 3.2.2. Contributions to the BSHG made by the $3S - 4D$ transitions when the laser was tuned to $f_0 + 3$ GHz, and at the magnetic field strengths shown; the magnetic field was perpendicular to the laser polarisation. The vectors in the circles represent the phase and magnitude of the effective dipoles for SHG; the vector for E^2 would be drawn in the positive x direction. The top (bottom) row of graphs shows the contributions to the in phase (in quadrature) components of the effective dipole made by each transition, plotted at its centre frequency. The sum of all such contributions is proportional to the length of the thick line at the side of each diagram. The laser frequency is indicated by the dashed line. All the graphs are drawn with the same axes; the frequency detuning is listed at the laser frequency.

imaginary part of the effective dipole being very much more sharply peaked about the resonant frequencies than the real part. The result of this is seen in figure 3.2.2 as the SH being in phase with the fundamental except when the laser is tuned to be very close to the resonant frequencies.

As $\text{Re}(Z(a + ib)) = -\text{Re}(Z(-a + ib))$ the sign of the contribution to the real part of the effective dipole of any transition changes as that transition is Zeeman shifted through exact resonance (frequency detuning = $a = 0$). This is seen in figure 3.2.2 around 0.2 T for the high frequency group of transitions. The figure also shows the effects of Zeeman splitting moving the enhancing transitions in and out of the Doppler broadened resonance, these transitions then contribute more and less to the SHG.

At low fields, in which the Zeeman splitting is very much less than the Doppler width, \tilde{Q}_{xy} and \tilde{Q}_{zy} are both proportional to the magnetic field strength; this causes the second harmonic intensity to be proportional to the square of the magnetic field strength, and the second harmonic to have the same linear polarisation as the fundamental. At higher fields differences in Zeeman splitting between the sets of sublevels enhancing the two quadrupole moments become comparable to the Doppler width. In this case the amount of resonant enhancement of the two effective dipoles is different, and the two quadrupole moments of interest grow at different rates, causing a rotation of the polarisation of the second harmonic. The real and imaginary parts of each moment also have different dependencies on the magnetic field strength, which results in a phase difference between the two effective dipoles, and hence a deviation from linear polarisation of the second harmonic light.

All of these points will be discussed further in connection with the experimental results reported in chapter five.

EXPERIMENTAL

APPARATUS AND TECHNIQUES

CHAPTER FOUR
EXPERIMENTAL APPARATUS AND TECHNIQUES

4.1 INTRODUCTION

A schematic diagram of the system used to investigate the second harmonic generation is shown in figure 4.1.1. The components of this system are described in more detail in the following sections.

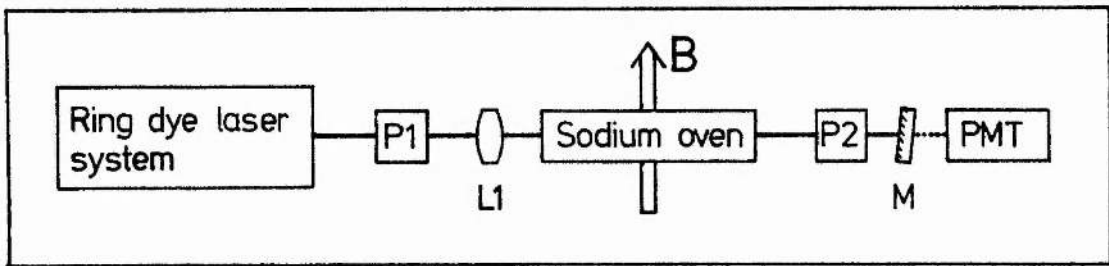


Figure 4.1.1. Experimental apparatus used to study BSHG in sodium vapour. Key:- P1 and P2 - polarising optics, L1 - 20 cm focal length lens, B - variable DC magnetic field, M - dichroic mirror, transmitting at 289 nm, reflecting at 579 nm, PMT - filtered solar blind photomultiplier tube.

4.2 DYE LASER SYSTEM

4.2.1 The dye laser

A Spectra Physics 380D actively stabilised ring dye laser was used as the source of the fundamental radiation. The narrow linewidth radiation produced by this device (about 150 kHz [9]) allowed investigation of the properties of BSHG in such detail as described in this thesis. The principles of dye laser operation have been reviewed by Schafer [117], and this particular model of laser is described by the manufacturer's literature [118], and by Kane [9].

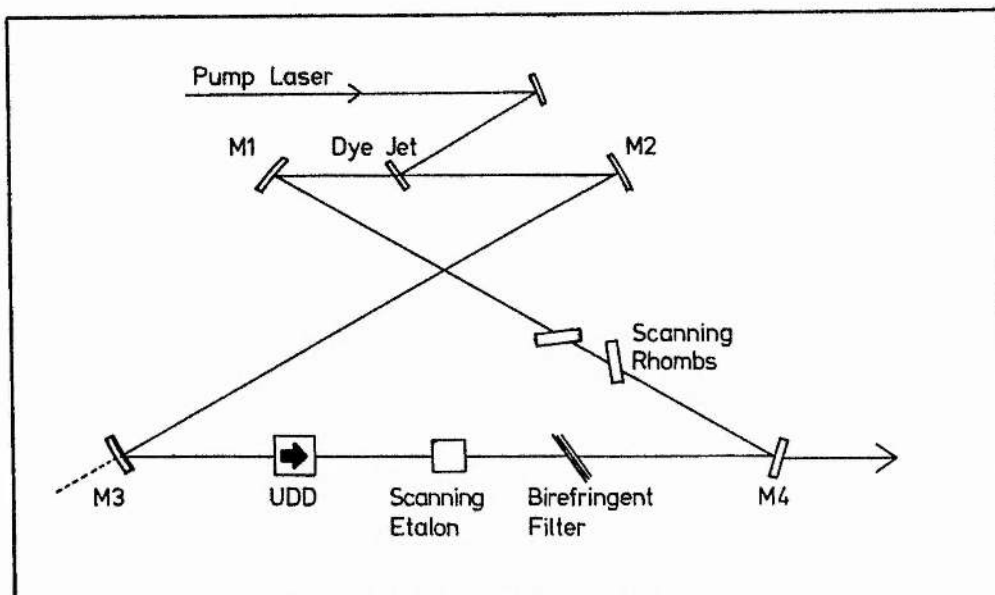


Figure 4.2.1. Schematic diagram of the ring dye laser.
 Key:- M1 to M4 - laser mirrors, UDD - uni-directional device.

The active medium of the dye laser was a free-flowing jet of a 2×10^{-3} molar solution of Rhodamine 6G dye dissolved in ethylene glycol. A Spectra Physics 171/07 argon ion laser, which produced 4 W of light at 514.5 nm, was used to pump the dye laser. The dye laser cavity was in the form of a ring, as shown in figure 4.2.1. The birefringent filter and the air-spaced Fabry Perot etalon acted as coarse and fine tuning elements respectively. The unidirectional device constrained the laser radiation field to travel in one direction. The use of a travelling wave rather than a standing wave made it much easier to obtain single mode operation of the laser, as there was then no spatial nonuniformity of the gain depletion that would occur due to "hole burning" by a standing wave. The laser wavelength was scanned by tilting the two Brewster-angled quartz rhombs; this altered the optical path length of the cavity, and thus the lasing wavelength. In this configuration, the laser would operate reliably on a single longitudinal cavity mode at output powers of up to 700 mW, though 400 mW was typical. The laser was tunable in the 570 - 620 nm range.

Although the laser operated on a single cavity mode, the frequency of this mode was not stable, as the cavity length was susceptible to disturbances due to temperature changes, dye jet fluctuations, and acoustic disturbances. To counteract these problems, the laser was actively stabilised. To do this, a small amount of light was split off from the dye laser output and passed through two external confocal Fabry Perot interferometers (Spectra Physics model 488 Stabilok system), the longer of which was temperature stabilised. As the laser frequency drifted, the transmission of the interferometers would change; photodiodes detected such changes, and suitable correction signals were generated by the electronics of the system. These signals moved the Brewster-angled rhombs and the piezoelectric mount of mirror M2 to keep the optical path length of the cavity constant. The manufacturer claims that the effective linewidth of the laser, which is due to residual frequency jitter, is less than 1 MHz RMS; Kane measured the linewidth of this particular laser to be 150 kHz [9].

4.2.2 Monitoring devices

A block diagram of the laser system assembled for the work described in this thesis is shown in figure 4.2.2. Beam splitters take small amounts of the laser beam to various monitoring instruments.

The wavelength of the dye laser was measured conveniently to a precision of 1 part in 10^6 by a Kowalski-style travelling wavemeter [119, 120]. This was essentially a double Michelson interferometer in which the length of one arm was scanned. The wavelengths of a polarisation-stabilised helium-neon laser and the dye laser were compared by fringe-counting techniques; the wavelength of the second harmonic of the dye laser radiation was displayed directly by the counting electronics. This useful piece of apparatus has been described in full by Kane [9].

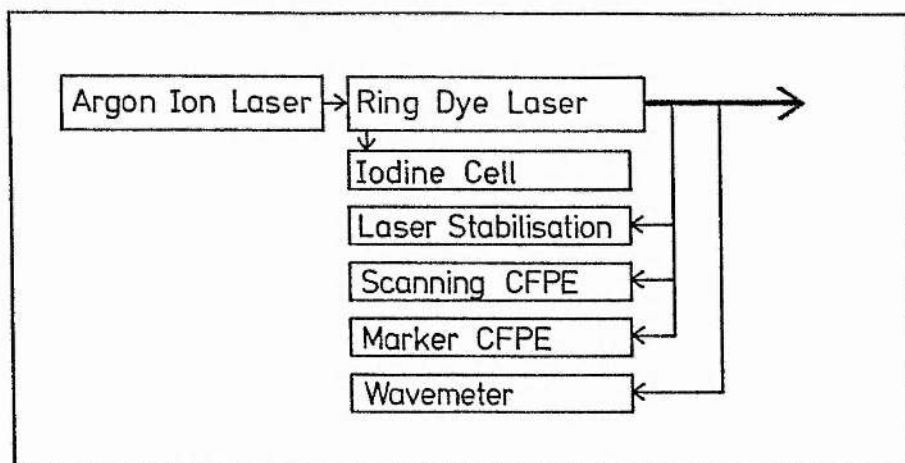


Figure 4.2.2. Schematic diagram of the laser system. Key:- CFPE - confocal Fabry-Perot interferometer.

The mode structure of the laser was analysed by a scanning confocal Fabry Perot interferometer, which confirmed that the laser was operating on a single mode. Laser stabilisation is the reference station, consisting of two interferometers, which was described in section 4.2.1.

The marker interferometer was a confocal Fabry Perot interferometer with a 30 cm mirror separation; this instrument therefore had a free spectral range of 250 MHz. The interferometer was thermally stabilised to better than ± 0.1 C. As the laser was scanned, the laser light transmitted by the interferometer was monitored by a photodiode. The 250 MHz fringes so measured acted as a frequency calibration for the experiment.

The reflectivity of dye laser mirror M3 was not 100%; the few milliwatts of laser light that passed through this mirror was sent through a glass cell containing iodine vapour. The fluorescence of the excited iodine molecules was detected at right angles to the laser beam by a photomultiplier (RCA 931B). The absorption spectrum of iodine has been carefully studied using

Fourier Transform Spectroscopy; Gerstenkorn and Luk [121] have published an atlas showing the absorption spectrum of I_2 from 14800 to 20000 wavenumbers. Comparison of portions of the atlas with the iodine spectrum obtained when the laser was scanned allowed a determination of the laser frequency to an accuracy of one part in 10^8 . The wavemeter was still required, however, to determine in which part of the atlas to look for matching.

4.1.3 Data collection

Second harmonic generation line profiles may be recorded by scanning the laser across the 3S - 4D transition while recording simultaneously on a chart recorder the signal from the SH detector and the transmission of the marker interferometer. This procedure was followed in the earlier stages of this project, and by Kane [9]. However, the dye laser scan was not strictly linear with time. To compensate for changes in the laser scan speed when the results are on chart recorder paper is rather difficult. Instead, a computerised data collection system was designed and constructed. This is described in more detail in appendix C. Signals from the following devices were recorded by a BBC model B microcomputer: the SH detector (or any other detector); the photodiode monitoring the transmission of the marker interferometer; and the photomultiplier measuring the iodine fluorescence. These signals were all displayed on the VDU screen in real time, which proved to be very convenient. The results were later transferred to the University's VAX 11/785 mainframe computer. This machine used a simple algorithm to linearise the data by ensuring that the interferometer fringes were equally spaced; one such Fortran program is listed in Appendix D. Apart from the linearisation, this system was also very useful in aiding the comparison of data from different runs: graphs could be drawn to specified scalings, and the absolute frequency of the laser, measured using the iodine cell, was also available.

The fundamental laser beam was usually chopped at about 360 Hz, and the signal from the SH detector was passed through a phase-sensitive detector (PSD) tuned to the appropriate phase and frequency. This system proved efficient at improving the signal to noise ratio. The time constant on the PSD was set between 0.1 and 3 seconds depending on the conditions in the experiment.

4.3 OTHER APPARATUS

4.3.1. Production of the metal vapour

Sodium was chosen as the nonlinear medium for a number of reasons: it is relatively easy to produce sodium vapour; the atomic energy levels of the sodium atom are well known; the sodium atom has a strong two-photon resonance at a wavelength readily accessible by Rhodamine 6G dye lasers; and SHG in sodium has been reported by other workers [18, 66, 68, 71, 72, 75, 76, 95-97]

Sodium melts at 97.8 °C [122] and can be made to evaporate or boil to produce a moderately dense vapour at reasonable temperatures. This vapour consists mainly of sodium atoms, Na, but a small percentage of these combine to form sodium dimers, Na₂. The particle density of a saturated sodium vapour is shown in figure 4.3.1. The circles represent experimental determinations of the sodium vapour pressure as compiled by Nesmayanov [123]. The solid line is from a formula quoted by Miles and Harris [124], who relate the atomic density, N, to the absolute temperature, T, by the approximate formula

$$N = \frac{9.66084 \times 10^{24}}{T} \exp\left[\frac{-12423.3}{T} + 17.3914\right] \text{ atoms m}^{-3} \quad (4.3.1)$$

The Line showing the dimer concentration is deduced from data given by Lapp and Harris [125] on the percentage of dimers present in the vapour at any temperature. The vapour pressure is given by $P(\text{mbar}) = NT \times 1.38 \times 10^{-25}$, at 300 °C it is 0.02 mbar.

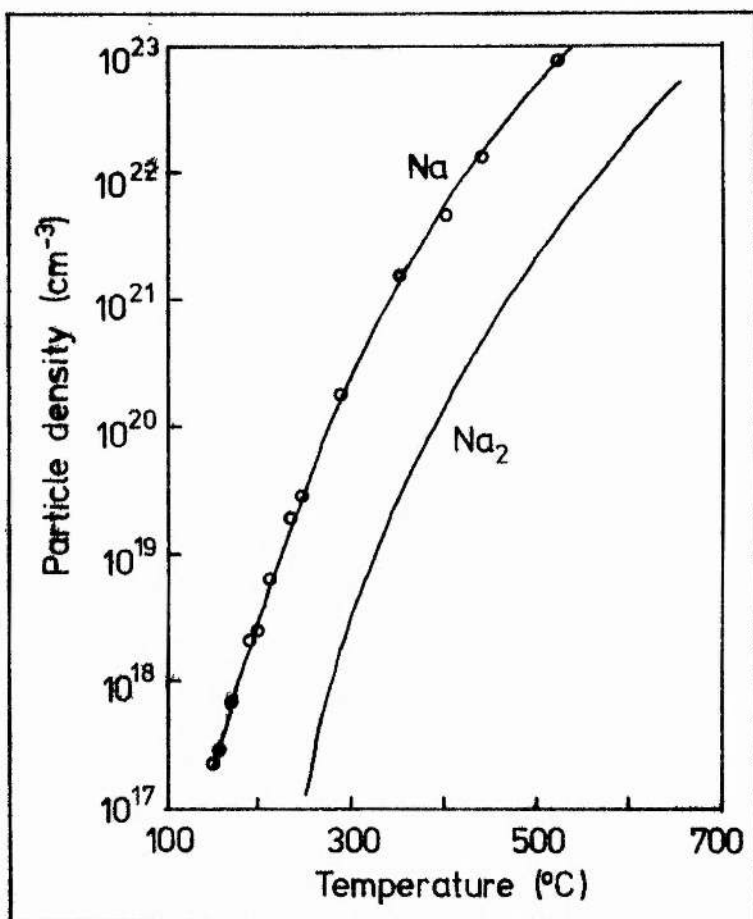


Figure 4.3.1. Particle density of saturated sodium vapour plotted as a function of temperature. See text for details.

Two methods of producing volumes of sodium vapour with uniform density have been widely reported: heat pipe ovens and gehlenite glass cells. To produce a density of 10^{21} atoms m^{-3} the sodium must be heated to 344 °C. Sodium is very reactive at these temperatures, so care must be taken in the choice of containment materials; it is also essential to prevent the sodium from condensing on the optical windows used in any device.

The gehlenite glass cell has the advantage of relative simplicity, but the windows must be kept at a higher temperature than the rest of the cell to minimise fogging problems due to condensation of the sodium vapour.

Woerdman [126] describes a suitable cell, which he used to produce sodium vapour with temperatures greater than 500 °C. The gehlenite glass cell was placed in a quartz tube covered with a transparent semiconducting material which served as an oven. The transmission of the system was poor: 70% at 600 nm and 30% at 330 nm.

The heatpipe oven was first proposed by Vidal and Cooper [127]. It is shown schematically in figure 4.3.2. The main body of the oven consists of a material with which the vapour does not readily react, stainless steel for example. Inside the tube is a wick of a few turns of fine stainless steel mesh. The centre of the pipe is heated and the ends are water cooled. As the ends do not get hot, the windows may be fixed to the ends with conventional O-ring seals.

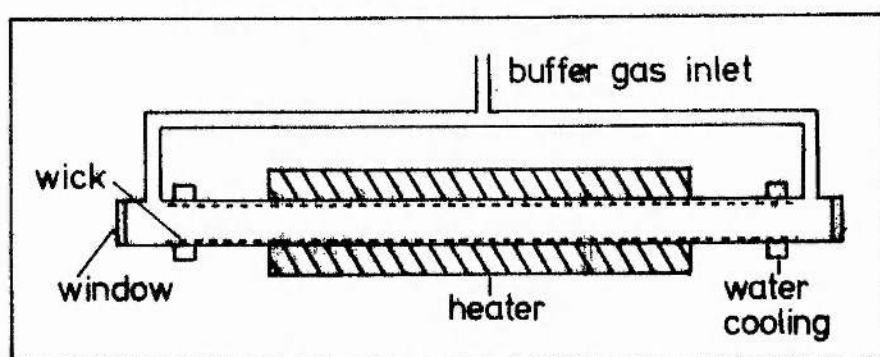


Figure 4.3.2. Schematic diagram of a heat pipe oven.

The initial charge of metal is placed in the centre of the oven and an inert buffer gas is introduced into the pipe. As the metal is heated it melts and wets the wick; the metal boils when its vapour pressure reaches the pressure of the buffer gas. The vapour moves out towards the ends of

the tube where it hits the cooled buffer gas and there it condenses on to the wick to be returned to the centre of the oven by capillary action. In an ideal heat pipe the temperature at which the metal boils is determined by the pressure of the buffer gas, and a zone of high uniformity of metal vapour density is formed. Extra heating should not affect the temperature of the vapour significantly, but should extend the vapour zone to nearer the cooling coils.

Heat pipe ovens were chosen for this study, as the technology for constructing these devices was readily available. In most cases the ovens were not operated in the true "heat pipe" mode. This was because the pipes were typically operated at sodium vapour pressures of 0.02 mbar; if the argon were at the same pressure the mean free path of the atoms would be of the order of 20 cm, which would result in condensation of the sodium on the end windows; thus the buffer gas pressure was usually at least 1 mbar. However, these devices did produce a sufficiently uniform vapour zone for the purposes of this work.

Several different ovens were used; they are shown in figure 4.3.3. A detailed cross section of one of them is shown in figure 4.3.4. All the ovens were fabricated from stainless steel. The main body of each was lined with several turns of stainless steel mesh (32 wires/cm, 39 SWG wire). The end windows were optically polished quartz discs (Jencons Scientific Ltd.), which were either mounted directly on to the end flanges using viton O-rings, or cemented on to the ends of "Pyrex" glass tubes which had been sealed to stainless steel flanges (Vacuum Generators). The ends of the ovens were water cooled, and the central sections were heated using resistance heating cords (Electrothermal - HC503, 400 W, 800°C maximum temperature, or HC104, 480 W, 450°C maximum temperature). These heating cords were wound non-inductively to minimise any stray magnetic

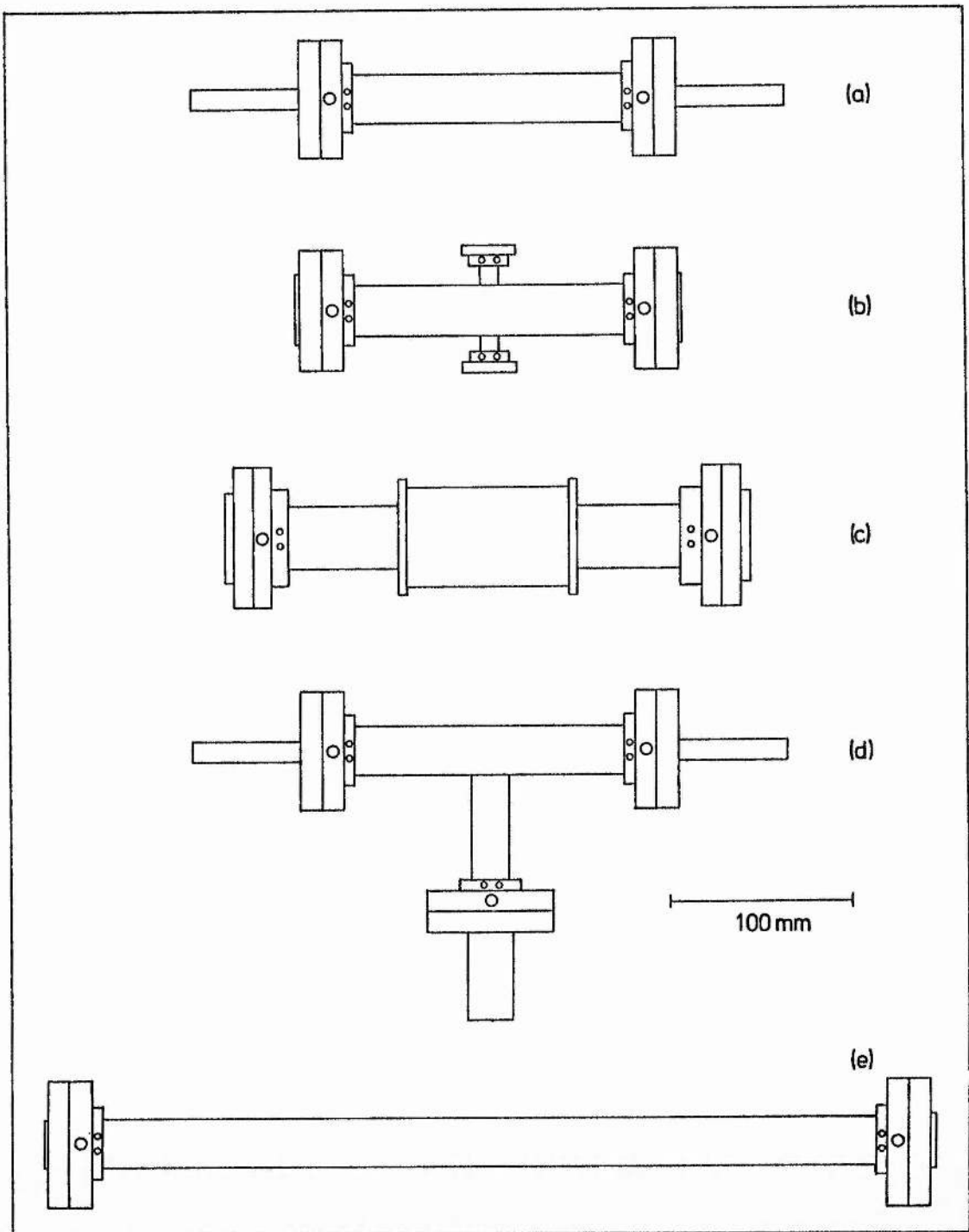


Figure 4.3.3. Heatpipes used in this work. The main body of each pipe is shown, the central region of each was covered with the heating element and insulation. The pipes in parts (a) and (d) were terminated with quartz windows cemented on to pyrex tubes, the others had the quartz windows fixed to the end flanges by "O" ring seals. The single circles in the end flanges represent the connection to the gas handling system; the pairs of circles indicate the pipes for water cooling.

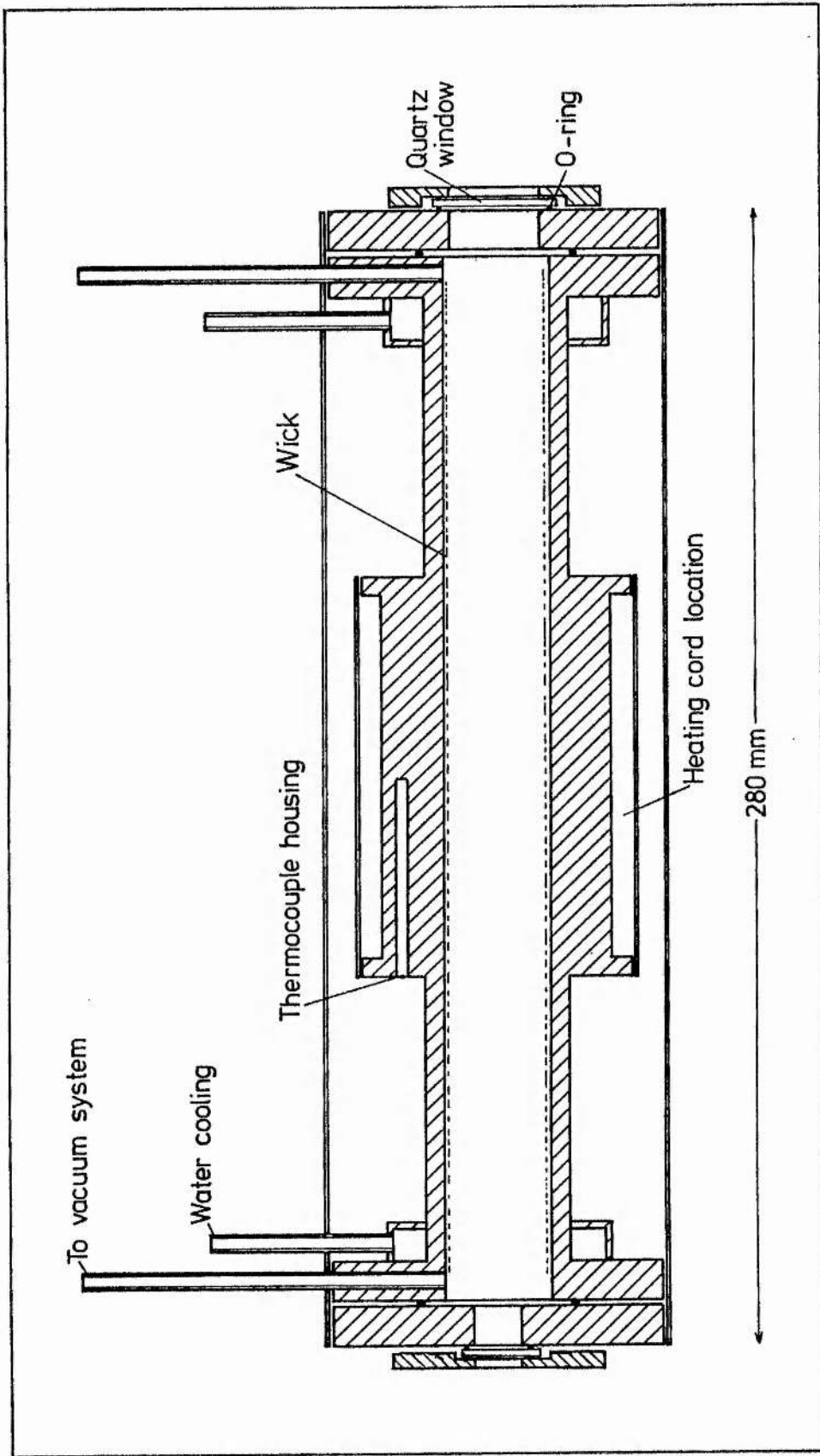


Figure 4.3.4. Cross section of the heatpipe shown in figure 4.3.3 (c). The space between the main pipe and the outer shield was filled with mineral wool insulation.

fields due to the heater current, which was up to two amps. The heaters were lagged with mineral wool insulation. The temperature of the central body of the oven was measured using a thermocouple (Comark Electronics mineral-insulated stainless-steel-sheathed NiCr/NiAl type K thermocouple KM30/L2PS, or a similar probe marketed by Electroplan, TC4 probe).

For many of the experiments the oven temperature was varied simply by altering the power input by using a "Variac" variable transformer. After some three-quarters of an hour the oven would stabilise at a temperature determined by the heat input and the rate of cooling of the oven. As the ovens were not operating in the true heat-pipe mode, variations in the heat-input/heat-loss balance did affect the sodium temperature, and numerous small adjustment to the "Variac" were needed to keep the temperature within 2°C of the desired level. In the later stages of the project a three-term temperature controller was used (FGH Controls Ltd, Type S900-K-2-0-240 Vigilant temperature controller). This drove a triac power controller (FGH Controls Ltd type TRZ-10-240 with zero crossover control); the combination had a two second cycle time, which was considerably less than the thermal time constant of the oven. This system proved to be very convenient, as the warm-up time was much reduced, and the temperature measured by the thermocouple was stable to better than 1°C. When stabilised, the fluctuations in second harmonic output power were less than $\pm 3\%$, which corresponds to a temperature stability of ± 0.2 C. The use of SHG as a particle density or temperature probe is considered further in section 5.9.

The temperature measured by the thermocouple at the outside wall of the oven was not the same as the temperature of the sodium vapour, as there were temperature gradients within the cell walls. To allow for this effect, a thermocouple and flange were inserted into the oven in place of

one of the end windows; this thermocouple was embedded in the molten sodium while the oven was operated under its usual conditions. The temperature measured on both thermocouples was noted as the oven temperature was increased; these results were then used to estimate the sodium temperature from the temperature measured by the external thermocouple. A cooling curve was also taken using the internal thermocouple; a plateau was observed in the temperature/time relationship at within 1.5°C of the accepted value of the melting point of sodium.

The preliminary experiments were performed using the heat pipe shown in figure 4.3.3(a). The pipe that was used for most of the experiments reported in sections 5.2 to 5.5 had walls of uniform thickness, and is shown in figure 4.3.3(b); the small side windows were not used in these experiments. Most of the other experiments in chapter five were performed using the heatpipe shown in figure 4.3.3(c) and figure 4.3.4. This pipe had a thickened central region to increase the thermal time constant of the oven and to allow the thermocouple to be mounted between the heater and the sodium. For the study of the sodium dimer, which is reported in appendix E, a "T" heat pipe was constructed, as shown in figure 4.3.3(d). This had a side arm of 12 mm internal diameter, fixed to the centre of the oven. The arm had a wick and heater similar to those in the main body, and was terminated by a quartz window, which allowed observation of the spontaneous fluorescence from the excited states of the sodium atom and dimer at right angles to the exciting beams. Figure 4.3.3(e) shows the longer heat pipe which was constructed for the experiments of section 5.9.

The ovens were cleaned using the reagent aqua regia, and then rinsed in running water. After assembly and testing of a pipe, about 4 cm^3 of sodium metal was loaded into its centre. The sodium was supplied as metal blocks under paraffin (Hopkin and Williams, laboratory reagent: sodium,

metal lump). These blocks were rinsed in petroleum spirit to remove the paraffin, then immersed in ethanol to remove the surface layers of oxidised sodium in the reaction between the ethanol and the sodium and its oxide. The sodium was again rinsed in petroleum spirit before being transferred to the heat pipe, which was being purged with dry nitrogen. The oven was then evacuated to a pressure of less than 10^{-3} mbar. During use the oven was filled with argon buffer gas (BOC Research Grade) at pressures from 0.7 mbar to several hundred mbar, but typically 1 mbar.

Before being used in the experiments the oven was cycled through its full temperature range several times, being evacuated between cycles. This allowed the sodium to distribute itself through the wick, and some of the impurities were removed by the evacuations. It was noted, in particular, that when the sodium was melted for the first time there was a small rise in pressure on the mechanical pressure gauge, but a very much larger increase in the reading of the Pirani gauge. It is well known that the Pirani gauge head is more sensitive to some gases than others. The argon pressures were therefore normally measured using the mechanical absolute pressure gauge, which was calibrated against oil and mercury manometers. In the experiments using argon pressures greater than 50 mbar, a mercury manometer was attached to the gas handling system through a liquid nitrogen cold trap.

4.3.2 Production of the magnetic field

Various arrangements were used to produce the transverse magnetic field which was needed to break the symmetry of the vapour. The simplest arrangement used polymer-based cobalt-samarium permanent magnets (Magnetic Polymers, Hera magnets) mounted on mild steel pole pieces which ran down each side of the pipe. The magnetic fields were measured using a Hall

probe (Scientifica and Cook). The magnets produced a field of 0.02 T (200 G), which was uniform to a few percent for 50 mm along the beam.

A small electromagnet (Newport Instruments type C) was used to provide a variable magnetic field. This was used with coned polepieces to provide a field of up to 0.14 T (1.4 kG), which dropped to half that value 32 mm from the centre of the polepieces. This magnet was used mostly for the spectroscopy carried out using the "T" oven. In this case the uniformity of the field was not important, as only a small region, about 10 mm, of the beam could be observed.

For most of the second harmonic generation study, a large electromagnet (Newport Instruments type A) was used. The 100 mm diameter plane pole-pieces were separated by 80 mm. This arrangement produced fields of up to 0.3 T (3 kG). The field dropped to half this value 74 mm from the centre of the pole-pieces.

4.3.3 Detection of the second harmonic

The second harmonic radiation produced in these experiments had a wavelength of 289.3 nm. Hence, normal glass, which is opaque at this wavelength (the transmission of borosilicate glass drops sharply from 95% at 360 nm to 8% at 310 nm [122]), was unsuitable as a window material. The windows of the heat pipe were made of fused silica ("quartz"), which transmits radiation of wavelengths down to 200 nm. In most cases a dichroic mirror was inserted in the SH beam to discriminate against the fundamental radiation. This mirror was highly reflecting in the visible, but highly transmitting in the ultraviolet. The substrate of this mirror was made of quartz, as were the lens and neutral density filters which were sometimes placed in the SH beam.

The SH radiation was normally detected by a filtered solar-blind photomultiplier tube (Hamamatsu R166UH tube with two Corning 9863 filters). The photomultiplier tube was largely surrounded by a permalloy cylinder of high permeability, which shielded the tube from the effects of magnetic fields. The tube was operated at 1 kV; the spectral responsivity of the system is shown in figure 4.3.5.

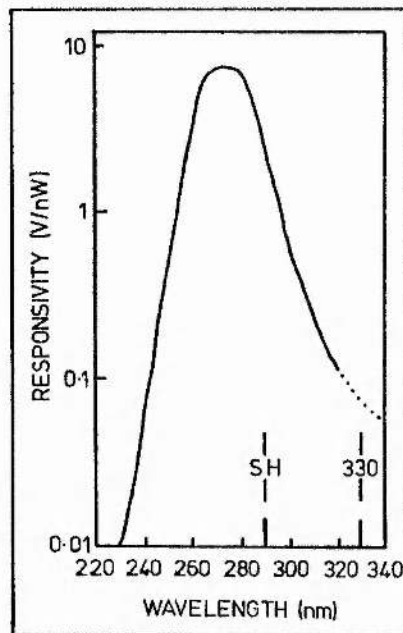


Figure 4.3.5. Spectral responsivity of the filtered solar-blind photomultiplier tube [122, 128].

The arrangement was chosen to provide high sensitivity at the SH wavelength, but to be insensitive at the wavelengths of the other dominant radiations: the fundamental beam at 578.7 nm, and the spontaneous fluorescence at 330 nm, 568 nm and 589 nm from the cascade decay of the 4D states. The 330 nm radiation was the most difficult to discriminate against, but, as shown in figure 4.3.5 the responsivity of the system is a factor of 40 down at this wavelength compared with that of the second harmonic. Moving the photomultiplier some distance from the cell, or

putting an iris diaphragm of physically small aperture around the fundamental beam helped the discrimination; the SH followed the path of the fundamental, whereas the 330 nm was emitted into 4π steradians.

The photomultiplier tube was a side window type with a circular cage electron multiplier; such tubes have poor spatial uniformity of gain [128]. This caused problems in one experimental scheme where the SH beam position on the photomultiplier tube changed. In that case, a null measuring method was devised, as described in section 5.4.

The 330 nm radiation was measured using another filtered photomultiplier tube, a Hamamatsu R212 with two Corning 9863 filters. This combination had a responsivity of 18 V/nW at 330 nm and 13 V/nW at 289 nm. The responsivity at the fundamental wavelength was more than five orders of magnitude less.

4.4 SPECTROSCOPIC TECHNIQUES

At various stages in this work it was necessary to use nonlinear laser spectroscopy to measure features that would otherwise have been obscured by Doppler broadening. An example is the measurement of the pressure-broadened linewidth of the sodium 3S - 4D transition; this is around 70 MHz full width at half maximum (FWHM) at the atomic frequency, while the Doppler width of the transition is 3.7 GHz at 400°C. These techniques are reviewed in references [107, 117, 129], amongst others. Two basic types of Doppler-free spectroscopy were used, these are described in this section. Saturated absorption spectroscopy probes transitions of the same energy as the laser photons, while two-photon spectroscopy probes transitions of twice this energy. For some of the experiments on the sodium dimer, a combination of both techniques was used.

4.4.1 Saturated absorption spectroscopy

Consider the two-level atoms as indicated in figure 4.4.1(a). These atoms will be moving, and thus their resonant frequencies measured in the laboratory frame will be shifted due to the Doppler effect. A single frequency laser beam passing through the atomic vapour will interact with only one velocity packet, producing the population changes shown in part (b) of the figure. As the laser is tuned across the transition the "hole" will move across this curve. A saturated absorption spectroscopy experiment is set up as in part (c). A strong "pump" beam acts in the manner described above, depleting the population of the lower state at one particular frequency. A low power "probe" beam of the same frequency as the pump beam is passed through the vapour in the opposite direction. The population of the lower level will then be as shown in part (d). As the two laser beams are propagating in different directions, they will interact with different velocity packets of atoms. However, when the laser beams are tuned to the centre of the transition, both beams will interact with the zero velocity packet of atoms. In this case the probe beam is absorbed much less than it would be in the absence of the pump beam. The probe field absorption is plotted in part (e). The dip in the centre of the curve has the linewidth associated with homogeneous broadening in the sample, and is thus "Doppler-free". The pump beam is usually chopped at a known frequency, and the signal from the probe beam detector is passed through a phase-sensitive detector tuned to this frequency. The resultant signal, which is sketched in part (f), shows the Doppler-free line profile of the transition. This technique essentially selects out those atoms with zero velocity along the laser beam direction to contribute to the signal.

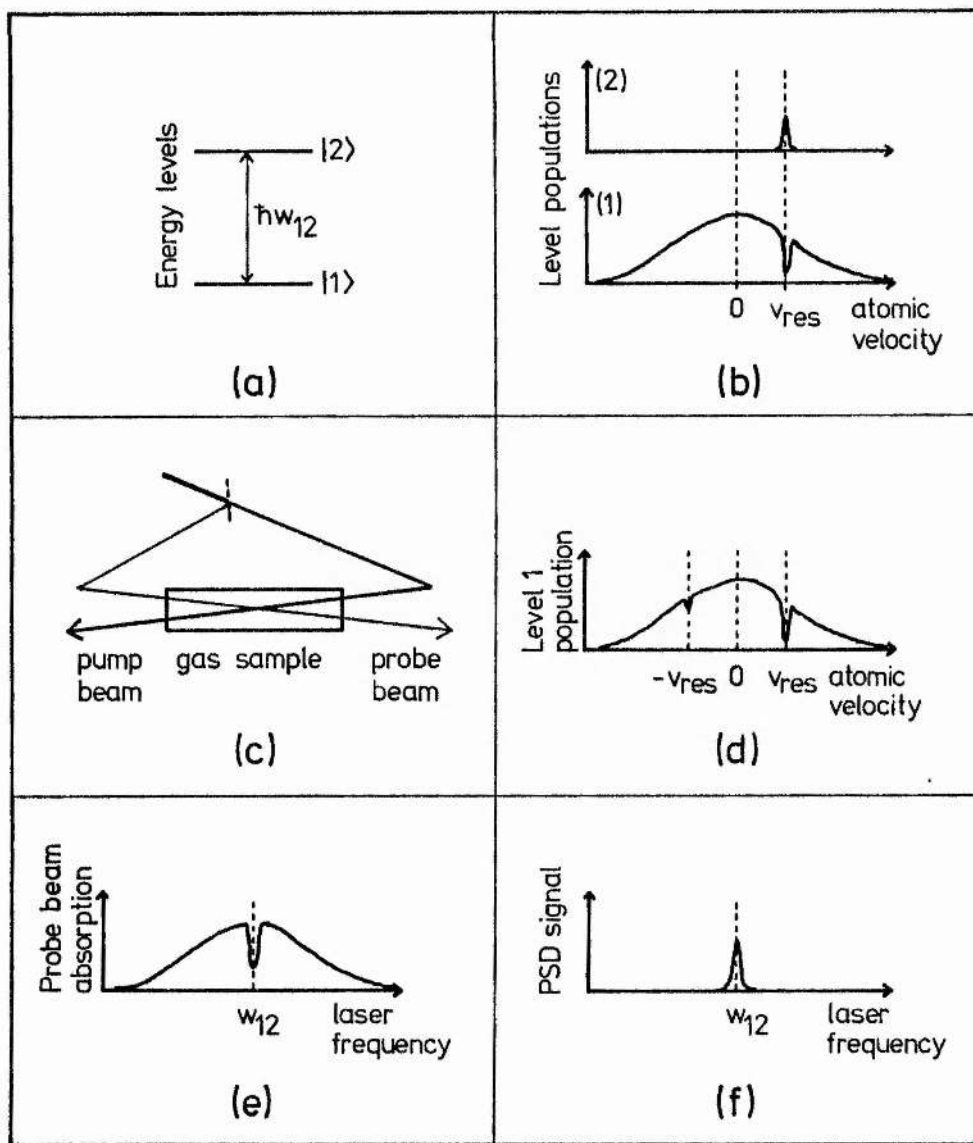


Figure 4.4.1. Diagrams for the explanation of saturated absorption spectroscopy, see the text for full details.

4.4.2 Two-photon spectroscopy

This form of spectroscopy makes use of two-photon transitions, and is thus fundamentally different from the type of spectroscopy described in the previous section. Again, consider a two-level atom with resonant frequency ω_{12} . Atoms of velocity v in the direction of the laser beam will be excited by two photons from a unidirectional laser beam when the laser frequency ω satisfies the relationship $\omega_{12} = 2(\omega - kv)$ where k is the wavevector of the laser radiation. This is obviously a Doppler-limited condition. However, the atoms may absorb one photon from each of two counter-propagating laser beams when $\omega_{12} = (\omega + kv) + (\omega - kv) = 2\omega$. Thus when the laser is tuned to the atomic resonant frequency, all the atoms may absorb one photon from each beam to be excited, regardless of their velocity; this gives rise to a large increase in absorption at this frequency, and the Doppler-free signal. These effects are shown schematically in figure 4.4.2.

The experimental arrangement used in this work for two-photon spectroscopy of the sodium dimer is shown in figure 4.4.3. The laser light was focussed into the sodium heat pipe by a 20 cm focal length lens, and was reflected back along the same path by a concave mirror. The absorption of the laser beam was very small; instead the two-photon spectroscopy relied on monitoring the population of the 4D states by measuring the ultraviolet radiation produced in their cascade decay back to the ground states.

The isolator was necessary to prevent feedback of light into the laser cavity, which made the laser unstable. A Soleil-Babinet compensator was used as a circular polariser. The retroreflected beam had its direction of circular polarisation reversed on reflection, and so the beam passing back through the quarter-wave plate had its linear polarisation at 90 degrees to

the initial laser beam. This return beam was then readily blocked by using a linear polariser.

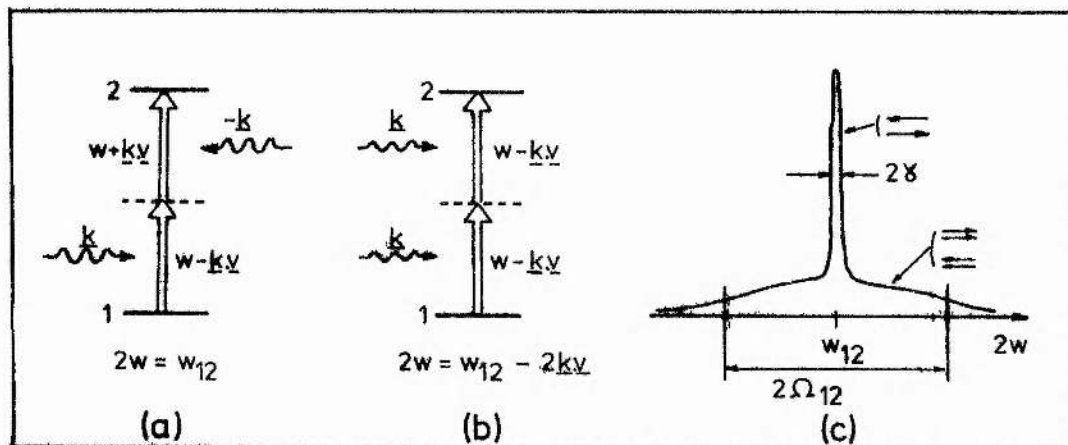


Figure 4.4.2. Two-photon resonance in a standing wave. a) Cancellation of the Doppler shift by absorbing one photon from each of the two counterpropagating beams. b) No cancellation of the Doppler shift by absorbing both photons from the same beam. c) The shape of the absorption (or fluorescence) signal produced in a Doppler-free two-photon spectroscopy experiment.

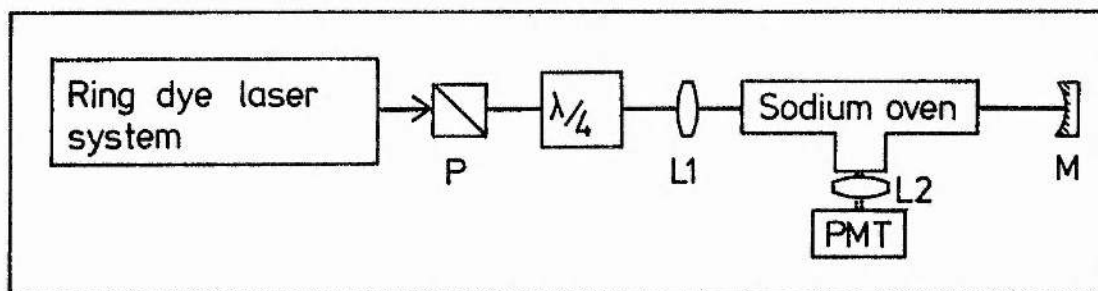


Figure 4.4.3. Experimental arrangement for two-photon spectroscopy of the sodium dimer. Symbols are as in figure 4.1.1, but here L2 is a 12.7 cm focal length quartz lens.

Four peaks were recorded in the two photon spectroscopy of the Na 3S - 4D transition, as presented in figures 5.1.4 and C.2, and by other authors [17]. The second peak, corresponding to the 3S (F=2) - 4D (J = 5/2) transition was often used as a frequency reference in the SHG experiments. This frequency is defined here as f_0 .

MEASUREMENT
OF PROPERTIES OF
MAGNETIC-FIELD-INDUCED
SECOND HARMONIC GENERATION

CHAPTER FIVE
MEASUREMENT OF THE PROPERTIES OF MAGNETIC FIELD
INDUCED SECOND HARMONIC GENERATION IN SODIUM VAPOUR

5.1 INITIAL CONSIDERATIONS

5.1.1 Basic properties of the second harmonic generation

The laser system was set up as described in section 4.1. A 20 cm focal length lens focussed the dye laser beam through the sodium heat pipe shown in figure 4.3.3(c). The divergence of the beam beyond the heatpipe was measured, from which the radius of the beam waist was calculated to be $90 \mu\text{m} \pm 20\%$. The power of the laser beam at the oven was typically 200 mW, from which the power density at the focus was inferred to be of the order of 10^7 Wm^{-2} .

The oven was filled with argon buffer gas at a pressure of 0.9 mbar and heated to 285 °C. A magnetic field of 0.018 T was applied perpendicular to the laser beam and to the laser polarisation. When the laser was tuned to a wavelength of 578.7 nm, the second harmonic was generated. With the aid of the iodine cell the laser frequency at which the second harmonic generation was a maximum was measured to be $17274.368 \text{ cm}^{-1} \pm 0.002 \text{ cm}^{-1}$; this figure is very close to the tabulated value for the separation of the sodium 3S and 4D levels, $2 \times 17274.5 \text{ cm}^{-1}$ [130]. Additionally, it is shown in the following section that the SHG line profiles are intimately connected with the line profile of the 3S - 4D two-photon absorption.

The wavelength of the second harmonic radiation was measured using a 1 m

monochromator (Monospek 1000) to be $289.48 \text{ nm} \pm 0.12 \text{ nm}$. This was, as expected, half the wavelength of the fundamental radiation.

The laser frequency, atomic density and magnetic field strength were adjusted to be at the optimum for SHG, 17274.37 cm^{-1} , $3.4 \times 10^{20} \text{ atoms m}^{-3}$ and 0.1 T respectively. When a fundamental power of 120 mW was measured immediately before the heat pipe, the second harmonic power was measured to be 7 nW . This corresponds to an efficiency of 6×10^{-8} . The computer model of the SHG described in chapter three and appendix B evaluates that

$$\left| \sum_{\substack{F, m_F, \\ J, m_J}} (B_{+2} - B_{-2}) Z \right| / \Omega = 1.0 \times 10^{-9} \quad (5.1.1)$$

under these conditions. Using the matrix elements tabulated by Miles and Harris [124] and Tull et al [92] the expected SH power was calculated to be 2.1 nW .

In this chapter the following abbreviations will be used in the figure captions:- f_L = laser frequency; T = sodium vapour temperature; B = magnetic field strength; P = approximate argon pressure; heatpipes a to e = the heatpipes sketched in figures 4.3.3 (a) to (e).

Equations 3.2.55 and 3.2.60 predict a squared dependence of the second harmonic power on the fundamental laser power. To test this, various neutral density filters were inserted in the fundamental beam while monitoring the SH power. A beamsplitter and photodiode were used to measure the fundamental power immediately before the heatpipe. This produced the results shown in figure 5.1.1. The two sets of results were taken at the centre of the SHG line profile, at magnetic field strengths of 0.018 T and 0.297 T . The gradients of these graphs are 1.97 ± 0.02 and 2.08 ± 0.02 respectively. When other sources of error are taken into

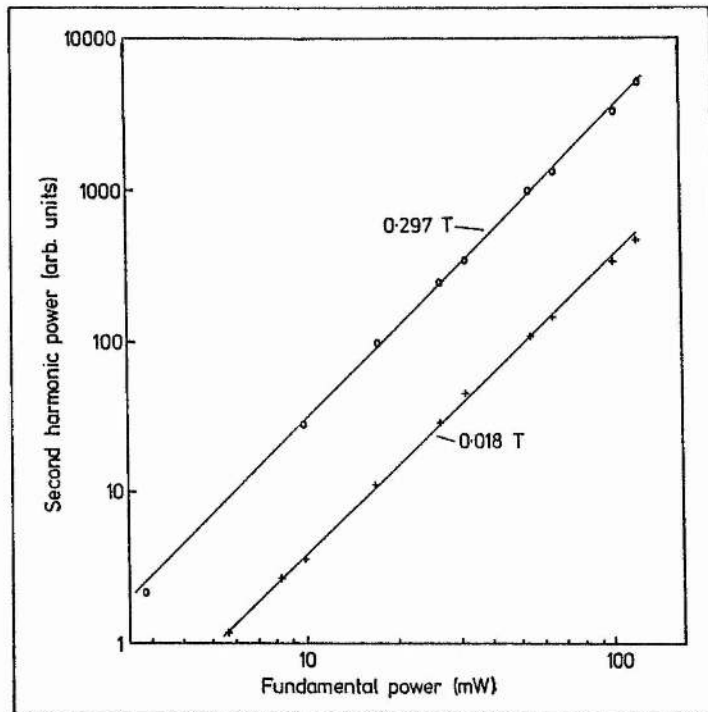


Figure 5.1.1. Dependence of second harmonic power on fundamental power. $f_L = f_0$, $T = 285^\circ\text{C}$, $B = 0.018\text{ T}$ and 0.297 T , $P = 1\text{ mbar}$, heatpipe c.

account, there is no significant deviation from a square law dependence of SH power on fundamental power. The lack of saturation with fundamental power is not surprising, as the optical power densities at the beam focus were modest. The SHG efficiency is expected to be limited at high power densities by competing processes such as multiphoton ionisation and saturation of the two photon absorption [10, 124]. In their non-collinear SFM experiments in sodium vapour Bethune et al [10] measured the fractional ionisation to be 1% when one laser was tuned to be ten wavenumbers from the 3S - 3P transition and the other was tuned such that the sum frequency was in resonance with the 3S - 4D transition; the intensity of each beam was $5 \times 10^9\text{ Wm}^{-2}$. The same authors studied the effects of saturation of the two photon resonance; with a 41.2 cm^{-1} detuning from single photon res-

onance they found a deviation from the sum frequency power being proportional to the product of the intensities of the two laser beams at $3 \times 10^{17} \text{ W}^2 \text{ m}^{-4}$. In the experiments described in this thesis the detuning from single photon resonance was about 300 cm^{-1} , which would lead to a much lower multiphoton ionisation rate and an even higher intensity being required to saturate the two photon absorption than in the case described by Bethune et al. Even if this were not the case, the power densities achieved with the cw laser were less than those that Bethune et al required to observe the limiting effects.

The spatial intensity profiles of the second harmonic and fundamental beams were examined. The former was measured by fixing a 1.1 mm diameter pinhole in front of the SH detector, mounting the combination on a travelling microscope stage, and moving the pinhole across the beam. A similar arrangement was used to measure the fundamental beam profile, but a photodiode was used instead of the photomultiplier tube. In both cases the beams were expanded using a 5 cm focal length quartz lens. The fundamental beam was approximately Gaussian, as it had an intensity distribution close to $I_{\omega}(r) = I_{\omega}(0) \exp[-\alpha r^2]$, where r is the distance from the centre of the beam. As the second harmonic intensity was proportional to the square of the fundamental power, the beam profile of the second harmonic was expected to have an intensity dependence of the form $I_{2\omega}(r) = I_{\omega}^2(0) \exp[-2\alpha r^2]$. Figure 5.1.2 shows the distribution of the intensity of the SH beam and the square of the intensity of the fundamental beam. The two curves are seen to be similar, supporting the above arguments.

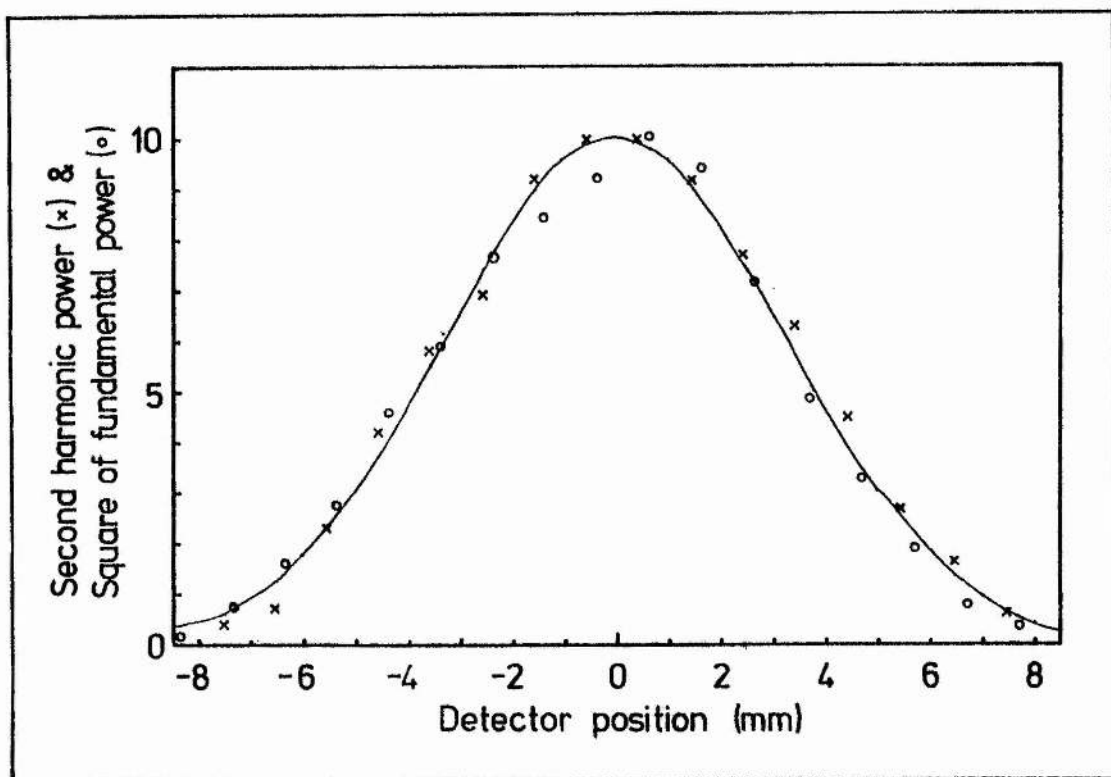


Figure 5.1.2. Spatial distribution of the intensity of the SH beam and the square of the intensity of the fundamental beam. A gaussian curve has been drawn with a similar width as that of the experimental results. $f_L = f_0$, $T = 250^\circ\text{C}$, $B = 0.06 \text{ T}$, $P = 1 \text{ mbar}$, heatpipe e.

5.1.2 Measurement of the homogeneous and inhomogeneous linewidths of the 3S - 4D transition

In modelling the SHG, two important variable parameters are the Doppler width and the pressure-broadened linewidth of the 3S - 4D two-photon transition. The Doppler width may be calculated from the temperature of the vapour; the half width at $1/e$ maximum, Ω , for a transition at frequency ν_0 is

$$\Omega = \nu_0 \sqrt{\frac{2 k_B T}{M c^2}}, \quad (5.1.2)$$

where k_B is Boltzmann's constant, T is the absolute temperature of the vapour, M is the mass of the sodium atom, and c is the speed of light. The Doppler width was measured experimentally by tuning the laser through the transition and observing the ultraviolet radiation emitted in the spontaneous decay of the 4D states. Knowing the fine and hyperfine splittings of the levels, the Doppler width could be estimated if the homogeneous linewidth was assumed to be small.

The homogeneous linewidth (FWHM) is given by $\Delta\nu_H = \Delta\nu_N + \beta P$, where $\Delta\nu_N$ is the natural linewidth of the transition, P is the pressure of the perturbing gas, and β is the pressure broadening constant. This constant is not, in general, the same for all transitions of an atom.

The pressure-broadened linewidth of the sodium 3S - 4D transition has been measured at pressures up to a few tens of mbar by Doppler-free two-photon absorption [131], free induction decay of a coherently excited 4D state [132], and by tri-level echoes [133]. The linewidths of the same transition have been measured at pressures of several atmospheres by Doppler-limited two-photon absorption [134]. The pressure broadening constant β , measured in MHz/mbar, depends on the temperature of the vapour as

$$\beta_1 = \beta_2 \sqrt{\frac{T_2}{T_1}} \frac{\sigma_1}{\sigma_2} \quad (5.1.3)$$

where σ_n is the Ar-Na collisional cross section at an absolute temperature T_n [133]. If the σ_n are approximated to be independent of temperature, it is possible to convert the published values of β_n to one temperature, chosen here to be the temperature at which most of the SHG experiments were carried out. These values are shown in table 5.1.1. In addition to the broadening of the spectral line by the perturbing gas, the energy levels of

the sodium atom are also shifted due to the interaction of the potentials of the sodium and argon atoms.

Reference	β_{558} MHz/mbar, FWHM
131	39 ± 4
132	39 ± 3
133	39 ± 6
134	36 ± 6
This work, 529 K	38.7 ± 1
This work, 558 K	39.8 ± 1

Table 5.1.1. Pressure broadening constant of the 3S - 4D two-photon transition in sodium perturbed by argon buffer gas at 558 K.

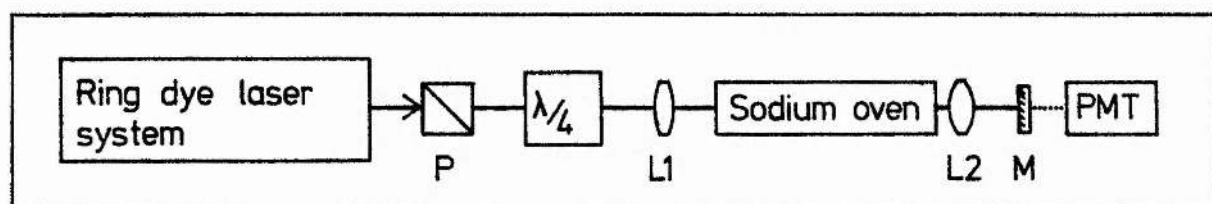


Figure 5.1.3. Experimental setup for two-photon spectroscopy. Key:- P - linear polariser, $\lambda/4$ - quarter wave plate, L1 - 20 cm focal length lens, L2 - 12.7 cm focal length quartz lens, M - dichroic mirror, PMT - filtered photomultiplier tube.

The homogeneous linewidths under the experimental conditions used in this work were measured by Doppler-free two-photon spectroscopy. The experimental arrangement used is shown in figure 5.1.3. A dichroic mirror and a 12.7 cm focal length quartz lens were used to retroreflect the laser light and to focus the spontaneous ultraviolet fluorescence, which monitored the population of the 4D states, on to a filtered photomultiplier tube. This observation of the fluorescence along the direction of the laser beam is different from the conventional two-photon spectroscopy arrangement shown in figure 4.4.3. The experimental geometry had the disadvantage that care

had to be taken to discriminate against the fundamental laser beam. However, it had the advantages that the whole region of two-photon absorption was, to some extent, observable, and the central region of the oven was not subjected to any heat losses due to a side arm. The pressure of the argon gas was measured using a Bourdon gauge which had been calibrated against an oil manometer.

Both pressure-broadening and pressure-shift may be seen in figure 5.1.4, which shows some of the results of two-photon absorption spectroscopy experiments carried out using the heatpipe of figure 4.3.3(c), at a temperature of 256 °C. Eleven traces were recorded at argon pressures from 0.8 to 13 mbar. The measured pressure broadening constant from these traces was $\beta_{529} = 39.8 \pm 1$ MHz/mbar, which gave a value of $\beta_{558} = 38.7 \pm 1$ MHz/mbar.

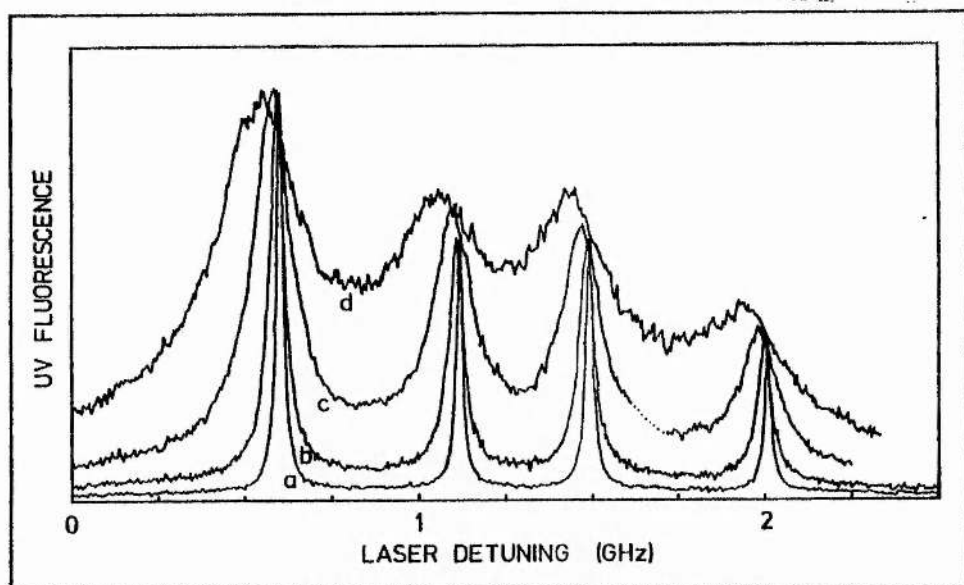


Figure 5.1.4. Two photon excitation spectra of the sodium 3S - 4D transition, at various buffer gas pressures:-
a) $P = 0.8$ mbar, b) $P = 2$ mbar, c) $P = 5.4$ mbar,
d) $P = 12.6$ mbar. The same frequency scale is used for each trace, but the fluorescence maxima have been normalised.
 $T = 256$ °C, $B = 0$, heatpipe (c).

A similar study was carried out at 285 °C, but with six scans. This gave a value β_{558} directly as 39.8 ± 1 MHz/mbar. These measurements were thus consistent with each other, and with the other values in table 5.1.1.

The value of γ_{ds} used in the theoretical calculations is the HWHM of the pressure broadened linewidth at the atomic frequency. This was calculated from the experimentally derived equation γ_{ds} (MHz) = HWHM = $19.4 P(\text{mbar}) + 12$. The agreement of the published values at low and high pressures of argon gas justified using this equation throughout the pressure range investigated in the SHG experiments, 0.8 to 230 mbar. The shift in the resonant frequency with pressure was not included in the SHG model, as it was small compared to the laser frequency, and was equal for all components of the 3S - 4D transition.

The effects on the SHG of changing the buffer gas pressure are studied in section 5.8. For most of the other experiments the buffer gas pressure was set at 1 mbar. The homogeneous linewidth under these conditions at 300 °C was measured to be 35 MHz (HWHM at the atomic frequency), and therefore 35 MHz was the value of γ_{ds} used in the theoretical modelling of these experiments. The effects of changing the homogeneous linewidth are studied theoretically and experimentally in section 5.8. Variations in γ_{ds} are not expected to influence the SHG much around the 35 MHz value measured and used in the calculations. An increase in γ_{ds} is expected to cause a decrease in the SH power, as γ_{ds} is essentially a damping term, though its effect will not be large until it is of the order of the Doppler width.

Two-photon spectroscopy was also used to provide an absolute frequency calibration of the laser with respect to the atomic transition. The centre of the SHG line profile was close to the peak corresponding to 3S (F=2) → 4D (J=3/2) transition, the second peak in figure 5.1.4. This frequency was

defined as f_0 . For certain experiments the laser was tuned to f_0 by measuring the two-photon-induced Doppler-free fluorescence. The laser could then be tuned by a known amount by monitoring the transmission of the 250 MHz free spectral range marker interferometer.

5.2 SECOND HARMONIC POWER DEPENDENCE ON SODIUM ATOM DENSITY

The macroscopic SH polarisation $\underline{P}_{2w}(r,t)$ in the medium [14] is

$$\underline{P}_{2w}(r,t) = N \underline{p}_{2w}(r,t) \quad (5.2.1)$$

where N is the number density of the sodium atoms and \underline{p}_{2w} is the effective dipole for SHG defined by equation 3.2.41. As the amplitude of the generated second harmonic wave is proportional to the macroscopic SH polarisation, the power of the SH generated in any region of the vapour is proportional to N^2 . However, in calculating the total SH power generated in the vapour, the relative phases of the SH generated in different regions of the vapour must be considered. The formalism developed here is similar to that of Yariv [12], and treats the fundamental and SH beams as infinite plane waves.

The electric field of the generated second harmonic is proportional to \underline{p}_{2w} and, from equation 3.2.55, it is seen that \underline{p}_{2w} is proportional to the square of the electric field of the fundamental radiation, though it is shifted in phase by an amount defined here as ϕ . Following Yariv [12], the slowly varying amplitude of the electric field of the second harmonic, \tilde{E}_{2w} , for waves travelling in the positive y direction is

$$d\tilde{E}_{2w} = (fN\tilde{E}_w^2/2) \exp[i(k_{2w} - 2k_w)y] \exp[i\phi] dy, \quad (5.2.2)$$

where \underline{k}_w and \underline{k}_{2w} are the wavevectors of the fundamental and second harmonic radiation respectively, and f is a real number dependent on the magnetic field strength. In the case of a uniform magnetic field strength in the interaction region, ϕ and f are not functions of position. If the intensity of the fundamental beam changes negligibly through the medium, \tilde{E}_w may be regarded as a constant. Defining the wave vector mismatch $\Delta \underline{k} = \underline{k}_{2w} - 2\underline{k}_w$, and integrating over a vapour length L gives

$$\tilde{E}_{2w}(L) = f N \frac{\tilde{E}_w^2(0)}{2} \exp[i\phi] \frac{\exp[i\Delta k L] - 1}{i\Delta k} \quad (5.2.3)$$

The total SH power P_{2w} is proportional to $(\tilde{E}_{2w}^* \tilde{E}_{2w})$, which results in

$$P_{2w} \propto N^2 \tilde{E}_w^4(0) L^2 \frac{\sin^2(\Delta k L/2)}{(\Delta k L/2)^2} \quad (5.2.4)$$

For maximum generation efficiency $\Delta \underline{k}$ should be zero. The wave vector mismatch arises from the change of refractive index between the fundamental and second harmonic frequencies:

$$\Delta \underline{k} = \underline{k}_{2w} - 2 \underline{k}_w = 2w (n_{2w} - n_w)/c \quad (5.2.5)$$

where n_w and n_{2w} are the refractive indices of the medium at the fundamental and second harmonic frequencies respectively.

The refractive index of a vapour at a wavelength λ may be determined from the Sellmeier equation [14]

$$n(\lambda) - 1 = \frac{N r_e}{2\pi} \sum_{ij} \frac{\alpha_i f_{ij}}{1/\lambda_{ij}^2 - 1/\lambda^2} \quad (5.2.6)$$

where N is the number density of the atoms, r_e is the classical electron radius equal to 2.8×10^{-15} m, f_{ij} is the oscillator strength of the transition of wavelength λ_{ij} from level i to level j , and α_i is the fractional population of level i . The wavelength dependence of the refractive index of sodium vapour is shown in figure 5.2.1, which was calculated using the oscillator strengths tabulated in [130]. It was assumed that all the atoms were in the ground state, which is justified in the conditions of the experiments.

The dominant resonances are those of the sodium D lines at 588.9 nm and 589.5 nm. These two transitions account for 98% of the oscillator strength of the ground states. The fundamental wavelength lies in the wings of the D lines; the refractive index of the vapour at the second harmonic wavelength is much less strongly perturbed from 1.0. The wavevector mismatch was calculated to be $\Delta k = 8.97 \times 10^{-20}$ N m⁻¹, where N is the atomic density in atoms m⁻³.

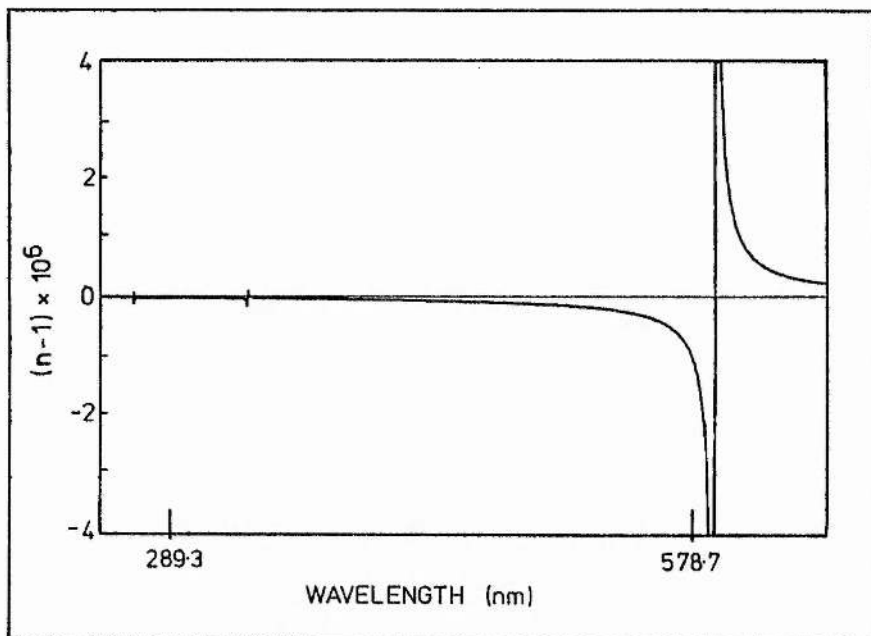


Figure 5.2.1. Refractive index, n , of atomic sodium vapour as a function of wavelength. The ordinate scale was calculated for $N = 2.3 \times 10^{20}$ m⁻³ ($T = 300^\circ\text{C}$).

This calculation of the wavevector mismatch has neglected the effects of the sodium dimer population on the refractive index. These dimers have many allowed transitions across the visible spectrum, but any one transition has a low oscillator strength. The percentage of sodium dimers in the vapour at 400 °C was less than 5%, and less than 1% of these dimers would be in any one vibronic level, resulting in the population of any dimer state being less than 5×10^{-4} that of the atomic density. However, the dimer population increases rapidly with temperature, and will become more significant at higher temperatures.

The dependence of the SH power on particle density may be calculated for the experimental conditions described, using equation 5.2.4. As Δk is proportional to N , $P_{2\omega}$ is proportional to $\sin^2 \Delta k N$; For a vapour zone length of 10 cm, and a fundamental beam power P_w ,

$$P_{2\omega} \propto P_w \sin^2(4.48 \times 10^{-21} N). \quad (5.2.7)$$

A relatively low field of 0.06 T was applied across the oven of figure 4.3.3(b) and the laser was tuned to the peak of the SHG profile; the polarisation of the laser was perpendicular to the magnetic field. The temperature of the oven was slowly increased, and the sodium density was inferred from the oven temperature as described in section 4.3.1. At low particle densities, the wavevector mismatch was negligible, and an N^2 behaviour was obtained as expected. These results are shown in figure 5.2.2, which is plotted on a log-log scale to allow an easy test of the N^2 behaviour at low particle densities. This behaviour is important, as although the power of the parametrically generated wave depends on the square of the particle density, non-parametric processes such as two-photon absorption followed by spontaneous fluorescence would be expected to show a linear dependence on the particle density.

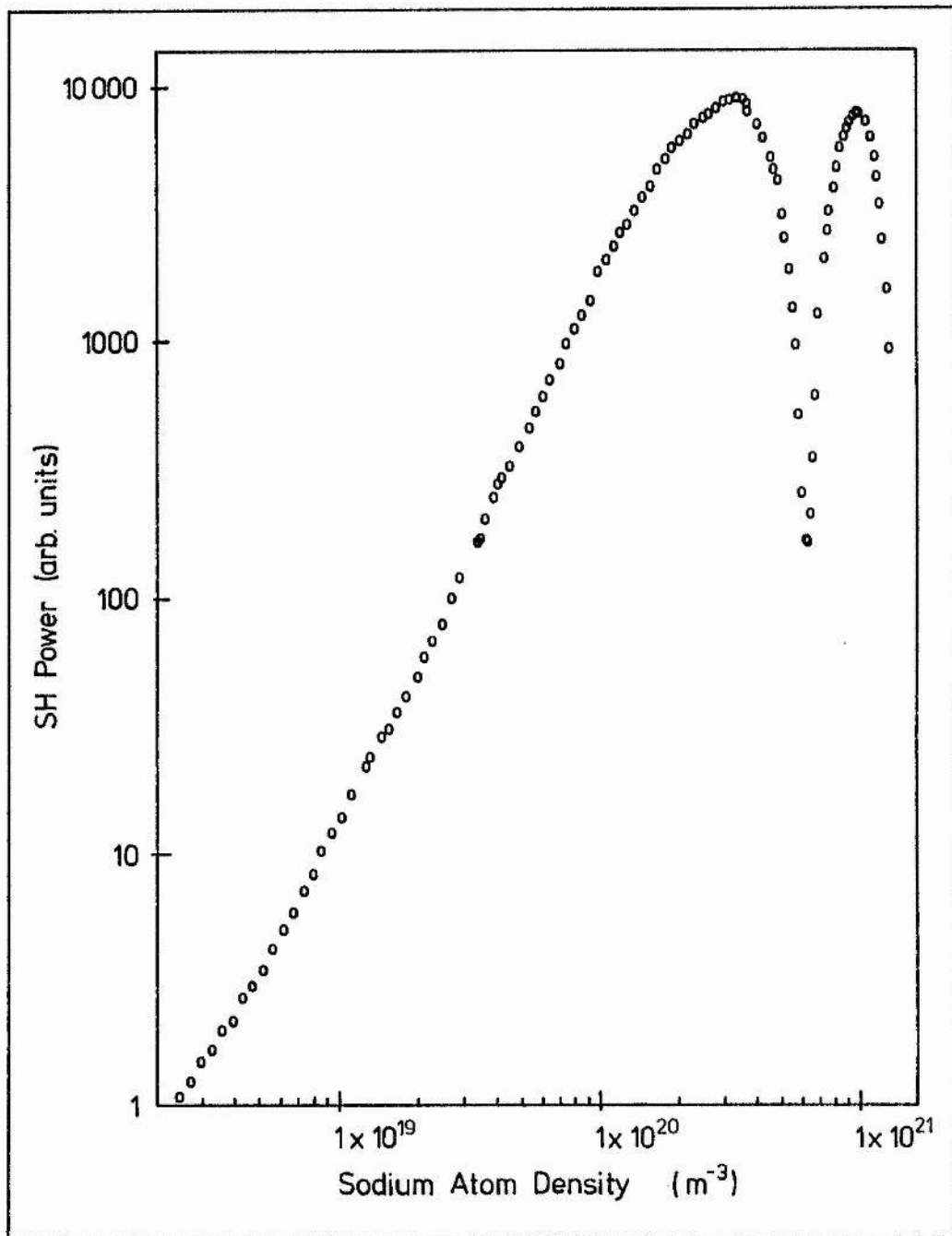


Figure 5.2.2. SH power as a function of atomic density plotted using logarithmic axes. $f_L = f_0$, $B = 0.06$ T, $P = 2$ mbar, heatpipe b.

At higher particle densities, an oscillatory behaviour was observed, as predicted by equation 5.2.7. This equation also predicts that the first peak in second harmonic power should occur at a particle density of $3.4 \times 10^{20} \text{ m}^{-3}$ which is close to the measured value of $3.5 \times 10^{20} \text{ m}^{-3}$. The small discrepancy is well within the error caused from estimating the vapour zone length and approximating the focussed beam to a plane wave.

Figure 5.2.3 shows the results of a similar experiment plotted using linear scales. In this case the heatpipe shown in figure 4.3.3(a) was used. The temperature of the sodium in the pipe was not as accurately known as in the previous experiment. Nevertheless, the $\sin^2(\Delta kN)$ behaviour is obvious, though it is damped due to absorption of the fundamental light by the sodium dimers, the population of which becomes significant at higher temperatures. The increase in Doppler broadening and homogeneous linewidth with increasing particle density will also have contributed to the decrease in the amplitude of these oscillations.

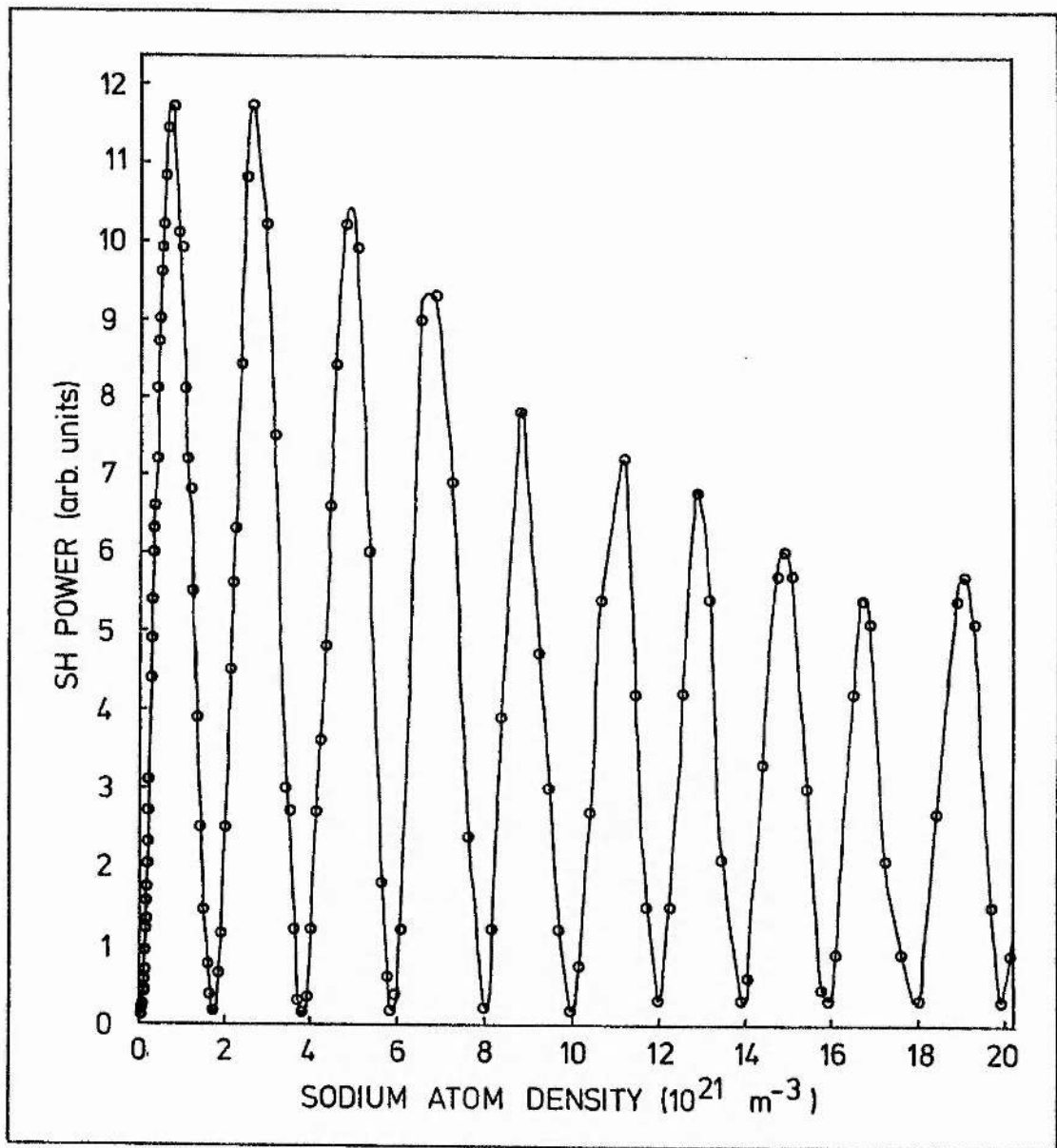


Figure 5.2.3. Second harmonic power as a function of atomic density, linear axes. The line is drawn to guide the eye between the experimental data points. $f_L = f_0$, $B = 0.02 \text{ T}$, $P = 10 \text{ mbar}$, heatpipe a.

5.3 LINE PROFILES

The variation in the second harmonic power as the laser was tuned through the resonantly-enhancing two-photon transition was examined experimentally using the same laser system, and the heatpipe of figure 4.3.3(b). The polarisation of the fundamental was arranged to be at 90° to the magnetic field, and the SH was detected using the filtered solar blind photomultiplier tube. To reduce problems caused by wave vector mismatching, all these experiments were carried out at 300°C , corresponding to a particle density of 2.3×10^{20} atoms m^{-3} ; the buffer gas pressure was 1 mbar.

Sets of SHG line profiles such as those shown in figure 5.3.1(a) were produced; each curve in this figure corresponds to a different magnetic field strength, and the same scale was used for each one. A set of theoretically calculated curves, based on a temperature of 300°C and a γ_{ds} of 35 MHz is shown in part (b) of this figure. The peak SH power varies as the square of the magnetic field strength at low magnetic fields, but when the Zeeman splitting is comparable with the Doppler width there is no further increase in peak SH power with magnetic field. The satisfactory agreement between the theoretically calculated and experimentally observed line profiles is a clear indication of the successful role of selection rules in modelling this nonlinear process. These will be considered further once the line profiles of two-photon absorption have been presented, so that the selection rules for the SHG and the two-photon absorption may be compared and contrasted.

The line profile of the SHG was compared experimentally with that of the two-photon absorption. In these cases the SH and the spontaneous fluorescence at 330 nm were focussed on to the input slit of a 1 m mono-

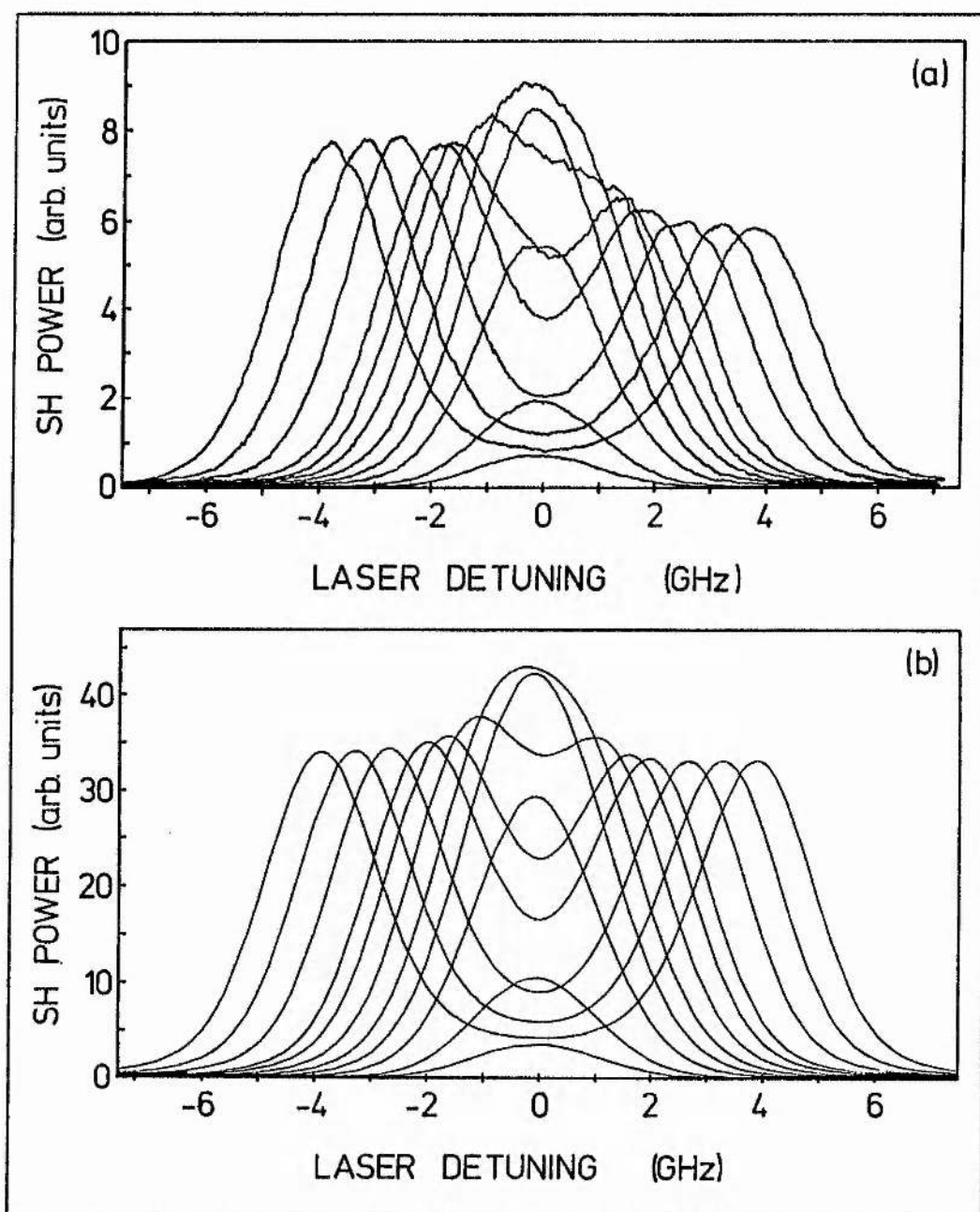


Figure 5.3.1. (a) Experimentally and (b) theoretically obtained variation of second harmonic power with laser frequency, at different magnetic field strengths:- $B = 0.016$ T (the curve with the lowest maximum), 0.028 T, 0.052 T, 0.074 T, 0.096 T, 0.121 T, 0.147 T, 0.167 T, 0.210 T, 0.250 T, and 0.290 T (the widest curve). The magnetic field was perpendicular to the laser polarisation. Zero detuning corresponds approximately to f_0 . $T = 300$ °C, $P = 1$ mbar, heatpipe b.

chromator (Monospek 1000), and detected by a filtered photomultiplier tube. The entry and exit slits of the monochromator were wide open, which allowed the monochromator to act as a spectral filter of 2 nm FWHM. The monochromator was set to 330 nm or 289 nm to separate the SHG and 330 nm radiation. The shapes of the line profiles obtained at 0.02 T and 0.275 T are shown in figure 5.3.2. At the lower field the SH line profile is seen to be similar to, but slightly narrower than, the line profile of the enhancing two-photon transition. The theoretically calculated SHG line profile is shown by a broken line; agreement between theory and experiment is very good.

At the higher magnetic field, when the Zeeman splitting exceeded the Doppler width, the relative contributions of the different magnetic sublevels changed significantly across the line profile, and this resulted in the structure seen on both the fluorescence and SHG profiles in figure 5.3.2(b). The marked difference between the two profiles is due to the different selection rules involved in the two cases.

The effects of the magnetic quantum number selection rules are most readily explained at high magnetic field strengths, as the fine and hyperfine couplings have been broken down, and m_l and m_s approximate well to good quantum numbers, that is S_A^2 , S_B^2 , D_A^2 , and D_B^2 are each close to either zero or one. Figure 5.3.3 shows the energy levels of the 3S and 4D states with the appropriate high field (m_l, m_s) designation for each one. Two-photon absorption of circularly polarised light occurs with $\Delta m_s = 0$ and $\Delta m_l = 0, \pm 1, \pm 2$. This may be expected to give rise to ten groups of two-photon absorption peaks, five for each of $m_s = \pm 1/2$. However, at high magnetic fields the energy difference between the $m_s = 1/2$ and $m_s = -1/2$ ground states is approximately the same as that between the 4D states which differ in m_l by two, so only five sets of absorption peaks should

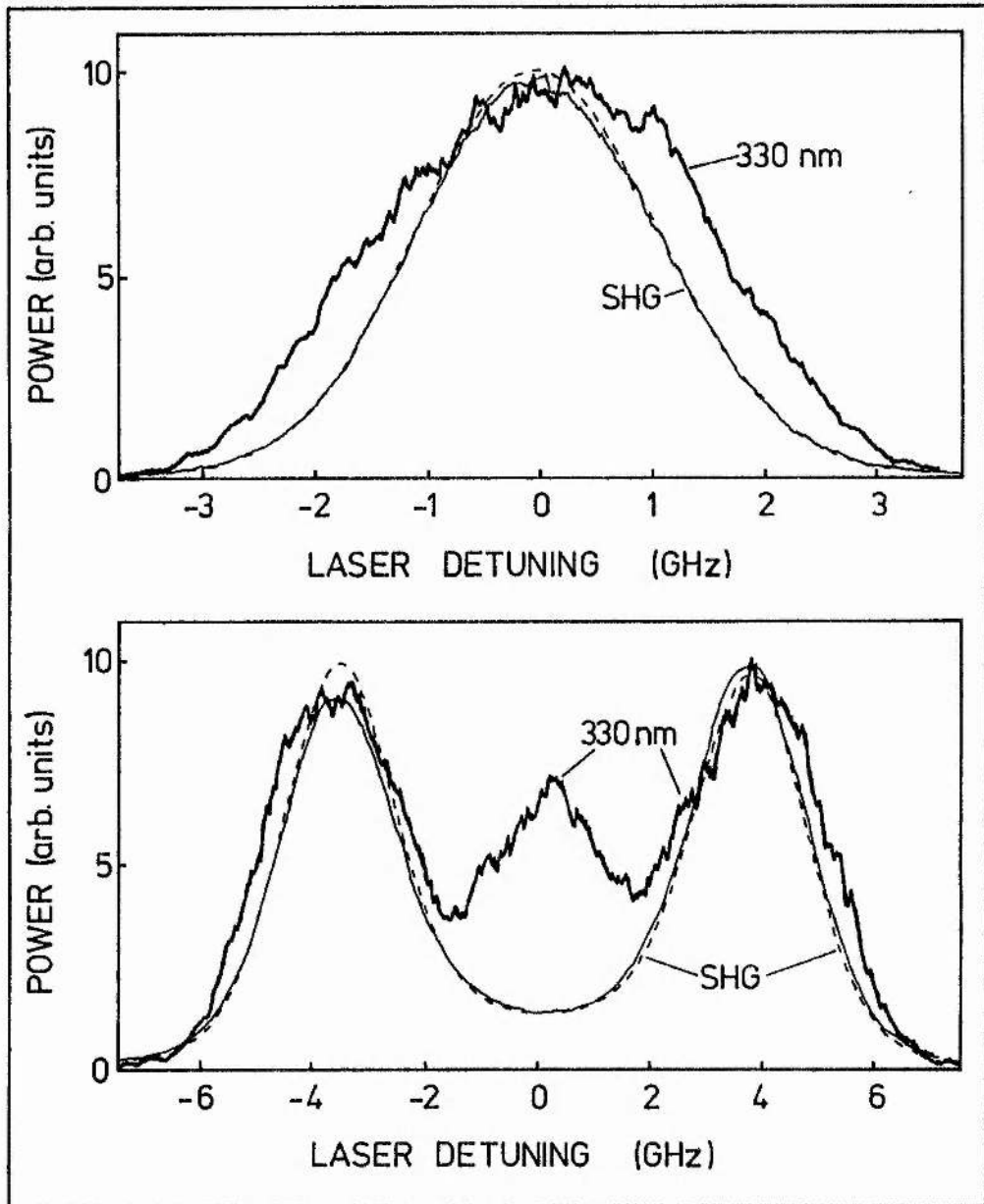


Figure 5.3.2 Line profiles as the laser was tuned across the 3S - 4D resonance (a) at 0.02 T and (b) at 0.275 T, with the laser polarisation at 90° to the magnetic field. The dashed line is the theoretically calculated curve for the SHG, the narrow solid line is the experimentally determined SHG line profile, and the thicker solid line is the line profile of the 330 nm radiation emitted in the cascade decay of the 4D population. $T = 300^\circ\text{C}$, $P = 1$ mbar, heatpipe b.

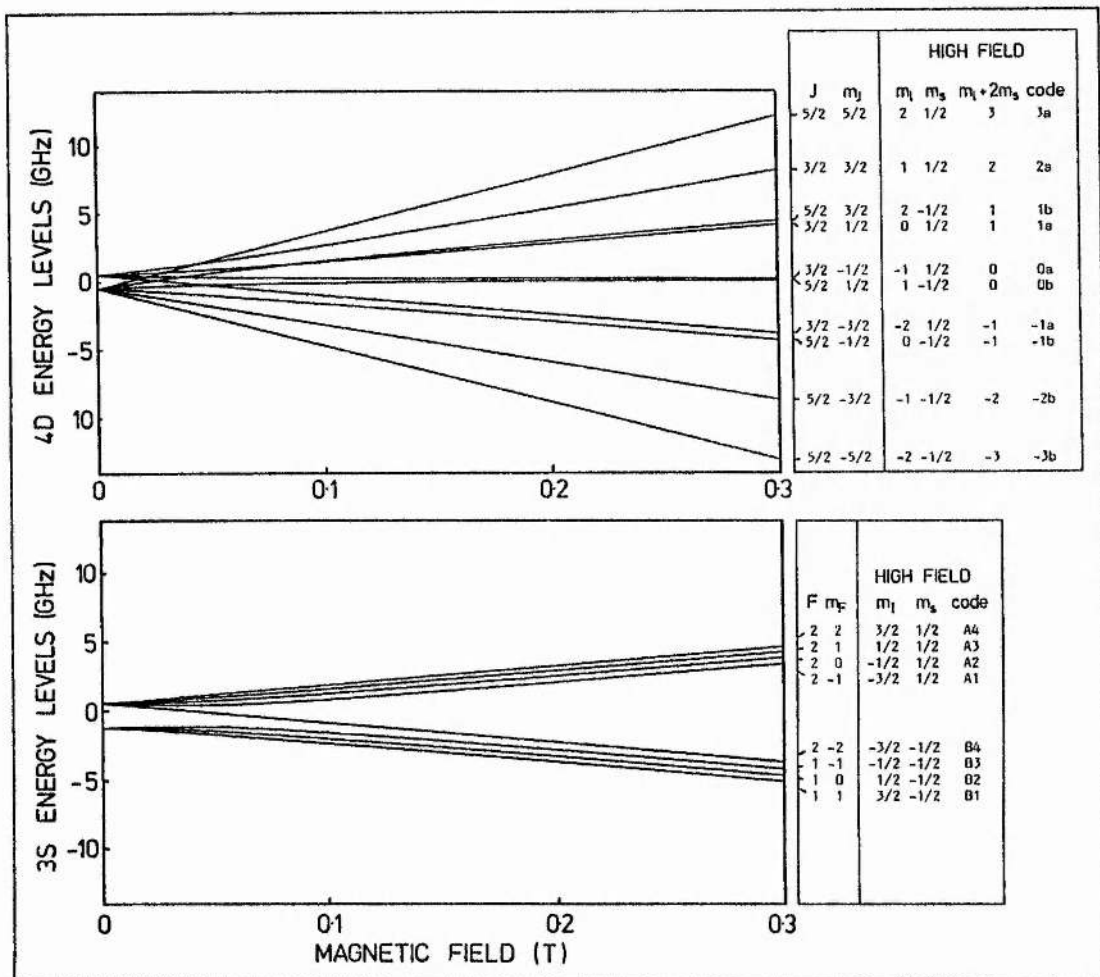


Figure 5.3.3. Energy levels of the sodium 3S and 4D states in the presence of a magnetic field. The boxes at the right hand side of the figure give the magnetic quantum numbers that best describe the states in high magnetic fields. The "code numbers" for the transitions are used in figure 5.3.4.

be expected. These peaks are most readily identified using Doppler-free two-photon spectroscopy, and the result of such a study is shown in figure 5.3.4 for a field strength of 0.2865 T. Five groups of peaks are indeed observed, corresponding (from left to right) to $\Delta m_l = -2, -1, 0, 1, \text{ and } 2$. Plotted under the experimental trace are the theoretically determined frequencies of the transitions which are allowed in a high magnetic field. Each group of peaks is due to two groups of transitions, one with $m_s = -1/2$ and one $m_s = +1/2$. A non-standard notation for the energy levels is defined in figure 5.3.3 and used to describe the origin of each peak in figure 5.3.4. This notation was chosen to emphasise the regular pattern of the transitions. The Zeeman splitting formulae described in section 3.1 obviously work well in describing the energy levels at this magnetic field strength at least.

When the laser radiation was linearly polarised perpendicular to the magnetic field two-photon absorption could occur with only $\Delta m_l = 0, \pm 2$ and $\Delta m_s = 0$, which would correspond to the centre and two outer groups of peaks in figure 5.3.4. These are seen in figure 5.3.2(b) as the three Doppler broadened peaks labelled "330 nm".

The SHG is known to be enhanced by allowed two-photon transitions, so one may at first expect to see three peaks in a SHG line profile recorded under the same conditions as the two-photon absorption spectrum of figure 5.3.2(b). However, as shown in equation 3.2.29, SHG depends on the product of three matrix elements $\langle D | \underline{r} \cdot \underline{\epsilon} | P \rangle \langle P | \underline{r} \cdot \underline{\epsilon} | S \rangle \langle S | Q_{\pm 2}^{(2)} | D \rangle$; only the first two are involved with the two-photon transition. The third matrix element is the quadrupole matrix element, and for this laser polarisation it restricts the transitions to $\Delta m_l = \pm 2$, with $\Delta m_s = 0$, as was determined in the derivation of the $B_{\pm 2}$ terms of equation 3.2.38. Thus the $\Delta m_l = 0$ transitions, which gave rise to the central peak in the two-photon

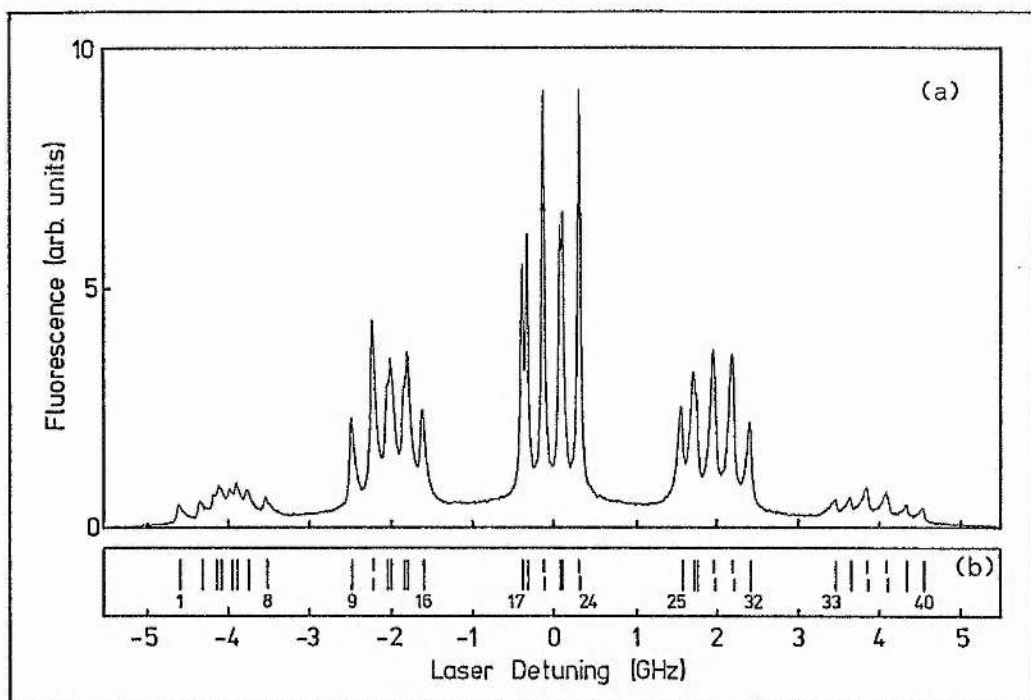


Figure 5.3.4. (a) Experimentally obtained two-photon absorption spectrum of the sodium 3S - 4D transition in a 0.286 T magnetic field. $T = 238^{\circ}\text{C}$, $P = 1$ mbar, heatpipe b. Part (b) shows the theoretically calculated transition frequencies, and numbers them for identification below, using the code numbers in figure 5.3.3.

$\Delta m_L = -2$	$\Delta m_L = -1$	$\Delta m_L = 0$	$\Delta m_L = 1$	$\Delta m_L = 2$
1: B4 \rightarrow -3b	9: B4 \rightarrow -2b	17: B4 \rightarrow -1b	25: A4 \rightarrow 2a	33: A4 \rightarrow 3a
2: B3 \rightarrow -3b	10: A4 \rightarrow 0a	18: A4 \rightarrow 1a	26: B4 \rightarrow 0b	34: A3 \rightarrow 3a
3: A4 \rightarrow -1a	11: B3 \rightarrow -2b	19: A3 \rightarrow 1a	27: A3 \rightarrow 2a	35: B4 \rightarrow 1b
4: B2 \rightarrow -3b	12: A3 \rightarrow 0a	20: B3 \rightarrow -1b	28: A2 \rightarrow 2a	36: A2 \rightarrow 3a
5: A3 \rightarrow -1a	13: B2 \rightarrow -2b	21: A2 \rightarrow 1a	29: B3 \rightarrow 0b	37: A1 \rightarrow 3a
6: B1 \rightarrow -3b	14: A2 \rightarrow 0a	22: B2 \rightarrow -1b	30: A1 \rightarrow 2a	38: B3 \rightarrow 1b
7: A2 \rightarrow -1a	15: B1 \rightarrow -2b	23: A1 \rightarrow 1a	31: B2 \rightarrow 0b	39: B2 \rightarrow 1b
8: A1 \rightarrow -1a	16: A1 \rightarrow 0a	24: B1 \rightarrow -1b	32: B1 \rightarrow 0b	40: B1 \rightarrow 1b

absorption spectra of figure 5.3.2(b), do not contribute to the SHG, and only the two outer peaks are seen in the SHG line profile. It is believed that this is the first report of the direct observation of differences in magnetic quantum number selection rules for two-photon absorption and second harmonic generation.

The theoretically calculated contributions to the SHG of the different two-photon transitions may be seen in figure 5.3.5 where the magnetic field is the same as that for the highest field plotted in figure 5.3.1, that is 0.29 T. The diagrams are plotted in a similar form to figure 3.2.2; the circles contain vectors which represent the magnitude and phase of the effective dipole driving the SH, and the upper and lower axes show the contributions to the real and imaginary parts of the effective dipole respectively.

There are only two groups of transitions which contribute to the SHG, corresponding to the $\Delta m_l = \pm 2$ transitions discussed above. When the laser is tuned far below the 3S - 4D resonance the contributions of the two groups to the real part of the effective dipole are opposite in sign, approximately equal in magnitude, and small. The reversal in sign is a result of the low frequency group being described by the B_{-2} term and the high frequency group by the B_{+2} terms, that is the $q = -2$ and $+2$ elements of the quadrupole matrix respectively. The contributions within each group are of the same sign as all have the same value of q . The imaginary part of Z drops off more rapidly with detuning than does the real part, and so the imaginary contributions to the effective dipole are very small.

As the laser is tuned further into the wings of the Doppler-broadened transition the magnitudes of the contributions to the real part of the effective dipole made by the low frequency group of transitions increase,

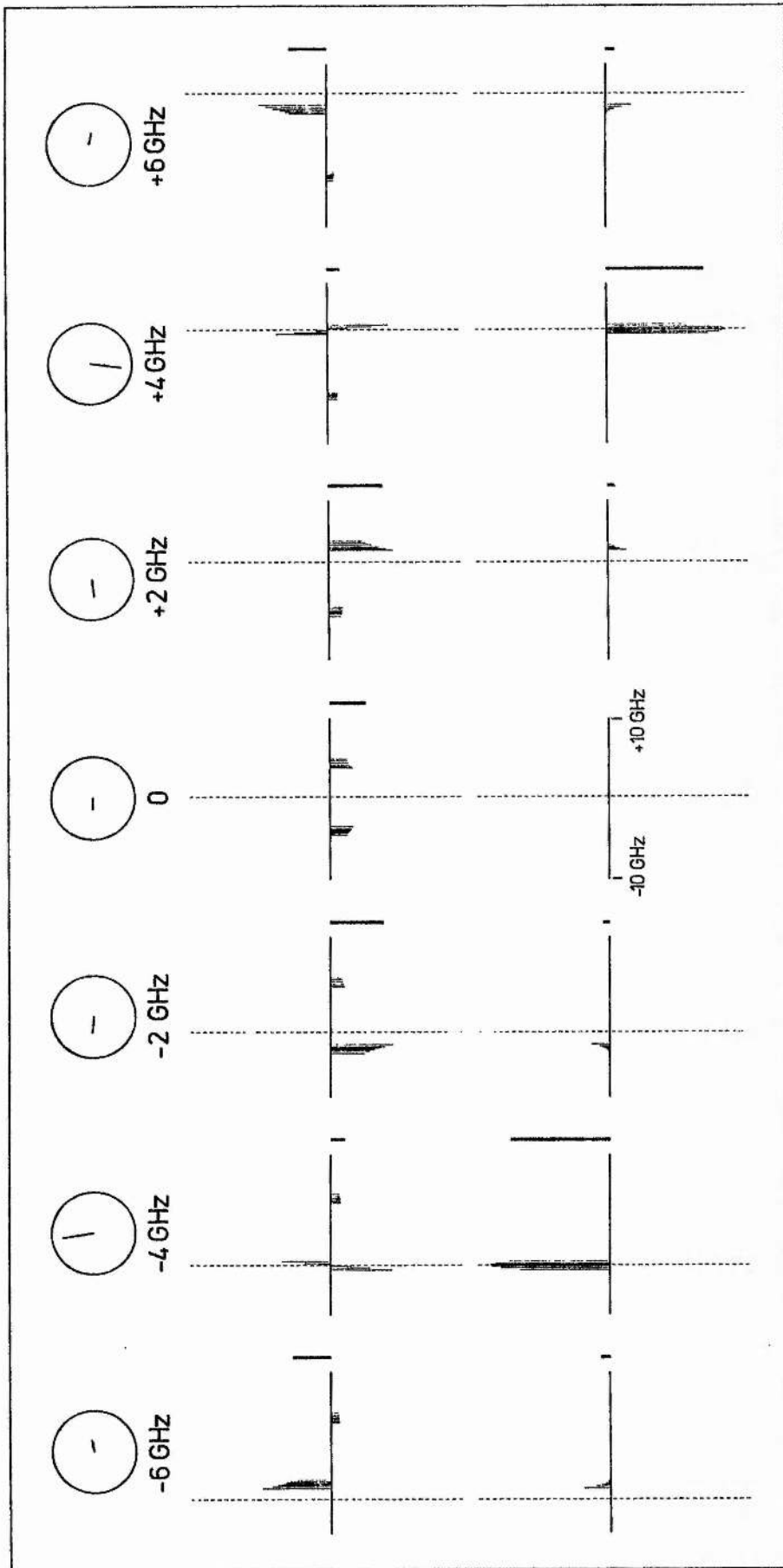


Figure 5.3.5. Contributions to the BSHG made by the 3S - 4D transitions as the Laser was tuned across the line profile, and at a magnetic field strength of 0.29 T; the magnetic field was perpendicular to the Laser polarisation. The vectors in the circles represent the phase and magnitude of the effective dipoles for SHG; the vector for E_{ω} would be drawn in the positive x direction. The top (bottom) row of graphs shows the contributions to the in phase (in quadrature) component of the effective dipole made by each transition, plotted at its centre frequency. The sum of all such contributions is proportional to the length of the thick line at the side of each diagram. The laser frequency is indicated by the dashed line. All the graphs are drawn with the same axes; the frequency detuning is listed at the laser frequency.

as is shown in the -6 GHz diagrams. The contributions of the high frequency transitions are not much changed, as the laser frequency is not yet significantly into the wings of those lines. This results in a net positive value for the real part of the effective dipole, shown at the side of the diagram. There are some small contributions to the imaginary part of the effective dipole, which cause the slight phase difference between the second harmonic and the square of the fundamental; this is shown by the deviation from horizontal of the SH vector at this laser frequency.

The -4 GHz diagrams show the laser frequency approximately in the centre of the low frequency group. In this case, as a result of the shape of $\text{Re}(Z)$, there are both negative and positive contributions from transitions in this group to the real part of the effective dipole. The interference between these transitions results in there being only a small net in-phase component. The sharp peak of $\text{Im}(Z)$ is centred on the same group, and so the imaginary part of the effective dipole is large, resulting in a phase difference of 99 degrees between the effective dipole and E_w^2 .

The other diagrams show the contributions of the various transitions as the laser is tuned further across the line profile, and how the phase and magnitude of the effective dipole are changed as a result of the laser detunings from the various transitions.

At lower magnetic field strengths the roles of the different transitions are not so readily explained, as m_l and m_s are not good quantum numbers, and the Zeeman splitting pattern is much less easily interpreted. However, as shown in figure 5.3.6, the calculated frequencies of the transitions agree well with the experimental trace of Doppler-free two-photon absorption. The $\Delta m_s = 0$ and $\Delta m_l = \pm 2$ selection rules for this geometry of SHG still hold, which is why in section 3.1 the wavefunctions of each atomic energy level were expressed as superpositions of the $m_s = \pm 1/2$

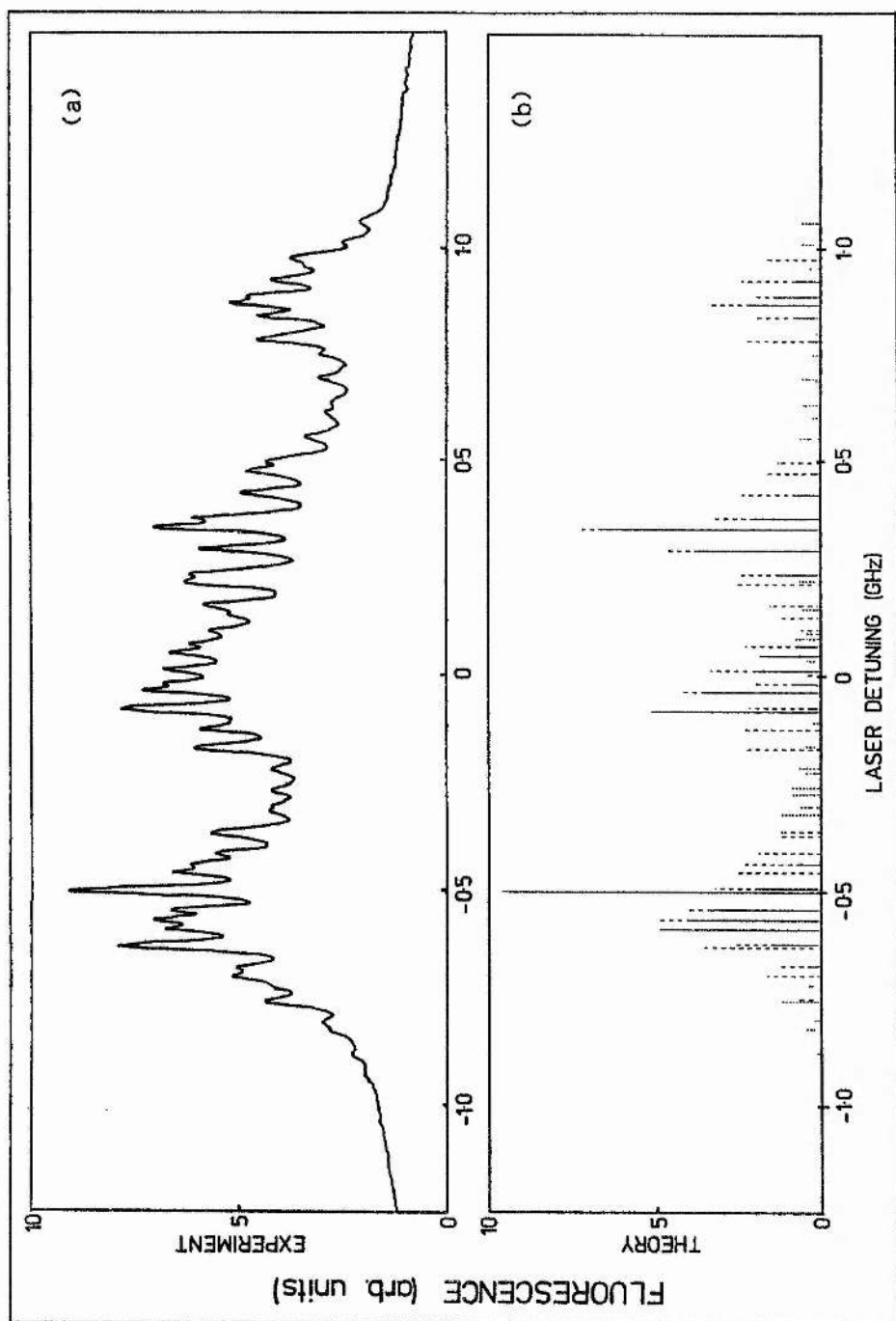


Figure 5.3.6. (a) Experimentally obtained Doppler-free two-photon absorption spectrum of the sodium $3S - 4D$ transition in a 0.016 T magnetic field. $T = 220^\circ\text{C}$, $P = 0.7$ mbar, heatpipe c. Part (b) shows the theoretically calculated transition frequencies at the same magnetic field strength. The complete, long dashed, and short dashed lines represent $\Delta m_l = 0, \pm 1$, and ± 2 transitions respectively.

states. The contribution of any transition to the SHG depends on the amount of the $m_s = 1/2$ (or $m_s = -1/2$) eigenfunction in the two wavefunctions involved. This results in the $B_{\pm 2}$ terms of equation 3.2.55 which were plotted as functions of field in figure 3.2.1. An additional factor to be considered in the low field case is that the (J_d, m_d, F, m_F) and $(J_d, -m_d, F, -m_F)$ transitions lie within a Doppler width of each other, and will interfere in the manner that was described in section 3.2. This causes the peak SH power to be predicted to be proportional to the square of the magnetic field strength at low magnetic fields, as is seen to be the case experimentally. The width of the SH line profile also increases with magnetic field as the Zeeman splitting broadens the range of two-photon absorption frequencies.

A magnetic field strength of 0.016 T (the same field as that which was present for the curve with the lowest maximum in figure 5.3.1) was chosen for figure 5.3.7, which shows the theoretically calculated contributions of the various transitions to the effective dipole for SHG as the laser is tuned across the line profile. In the high magnetic field case depicted in figure 5.3.5 the B_2 and B_{-2} transitions were split into two widely separated groups, but in the low field case this has not yet happened. The transitions are grouped within a much smaller frequency range, and the signs of the contributions of the levels do not seem to follow any regular pattern, though in fact the signs are readily explained. When the laser is tuned to be below all the transition frequencies, as in the -3 GHz diagram, all the positive contributions to the effective dipole come from the transitions with $m_l = -2$, and all those with negative contributions are due to $m_l = +2$ transitions. The sign of the contribution to the real part of the effective dipole made by any transition is expected to change sign as the laser is tuned through the transition's centre frequency, due to the shape of the real part of the

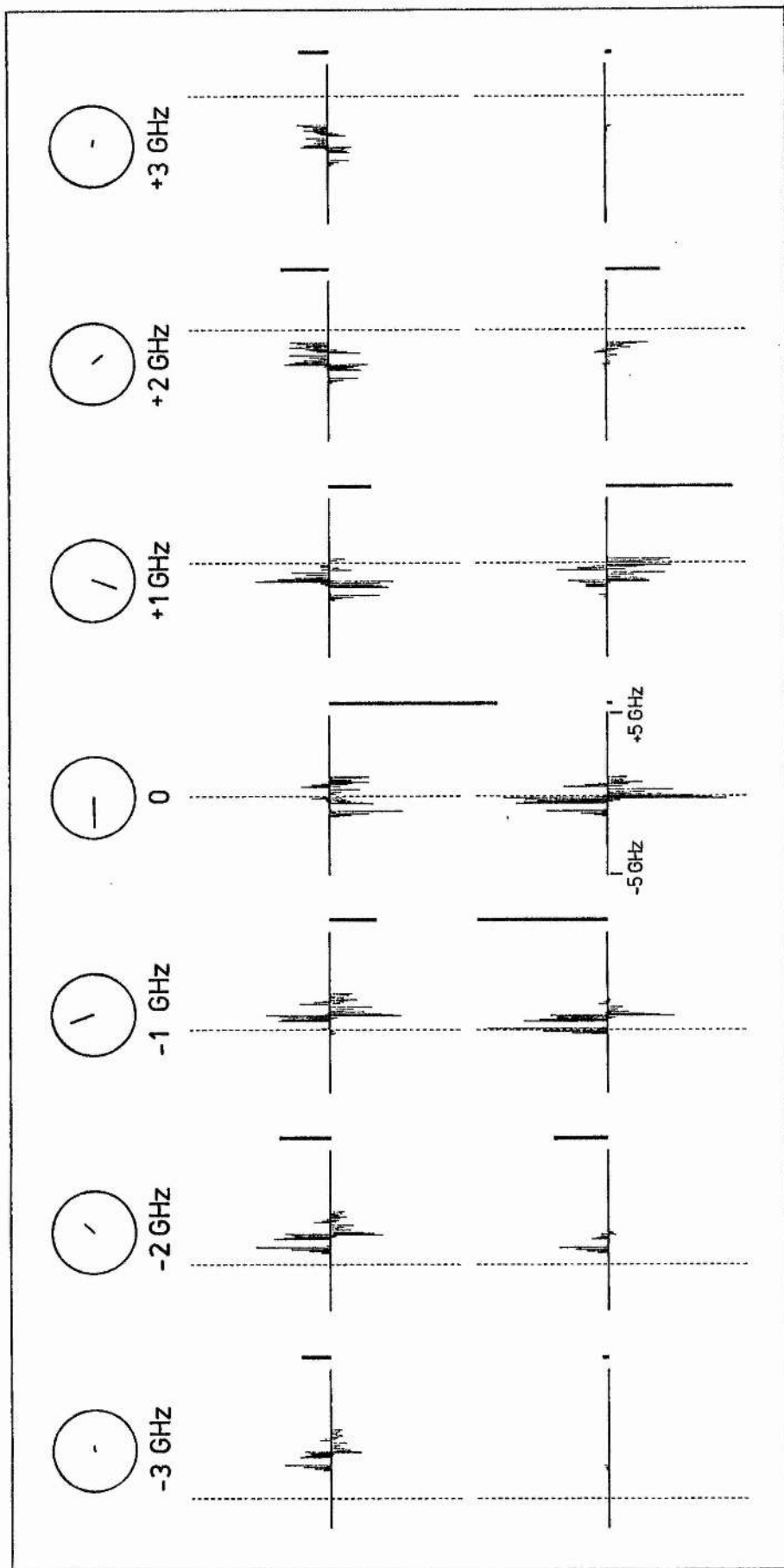


Figure 5.3.7. Contributions to the BSHG made by the 3S - 4D transitions as the laser was tuned across the line profile at a magnetic field strength of 0.016 T; the magnetic field was perpendicular to the laser polarisation. See figure 5.3.5 for further details.

plasma dispersion function. This is indeed seen in figure 5.3.7. The phase and magnitude of the effective dipole change across the line profile due to the changes in the net contributions to the real and imaginary parts of the effective dipole, as shown in the diagrams. Although these diagrams are more difficult to interpret than those of figure 5.3.5, because of the small Zeeman shifting and m_l and m_s not being good quantum numbers, the same general principles still apply. The complexity of the figures gives some idea of the amount of computation required to calculate each line profile. This is, however, well worth it when such good agreement is obtained between theory and experiment.

The asymmetry in the experimental curves of figure 5.3.1 is not expected to such a degree from the theoretical model developed in chapter three. The origin of this asymmetry is discussed further in section 5.6; it was due to the phase mismatching effects in the medium which were frequency dependent due to the non-uniformity of the magnetic field.

Modelling the homogeneous and inhomogeneous linewidths separately involved a substantial increase in computing time. It was therefore gratifying to observe that this model agreed considerably better with the experiment than did the theory which used only a single damping constant related to the Doppler width [97]. This can be seen in figure 5.3.8, in which the experimental line profiles and the predictions of the two theoretical models are compared.

The side-window heat pipe of figure 4.3.3(d) was set up for SHG in a manner similar to that shown in figure 4.1.1, with the addition of a photomultiplier tube to monitor the 330 nm fluorescence through the side-window, and the use of a 23 cm radius of curvature dichroic mirror to reflect the fundamental beam back along its own path. Angular movement of the retro-

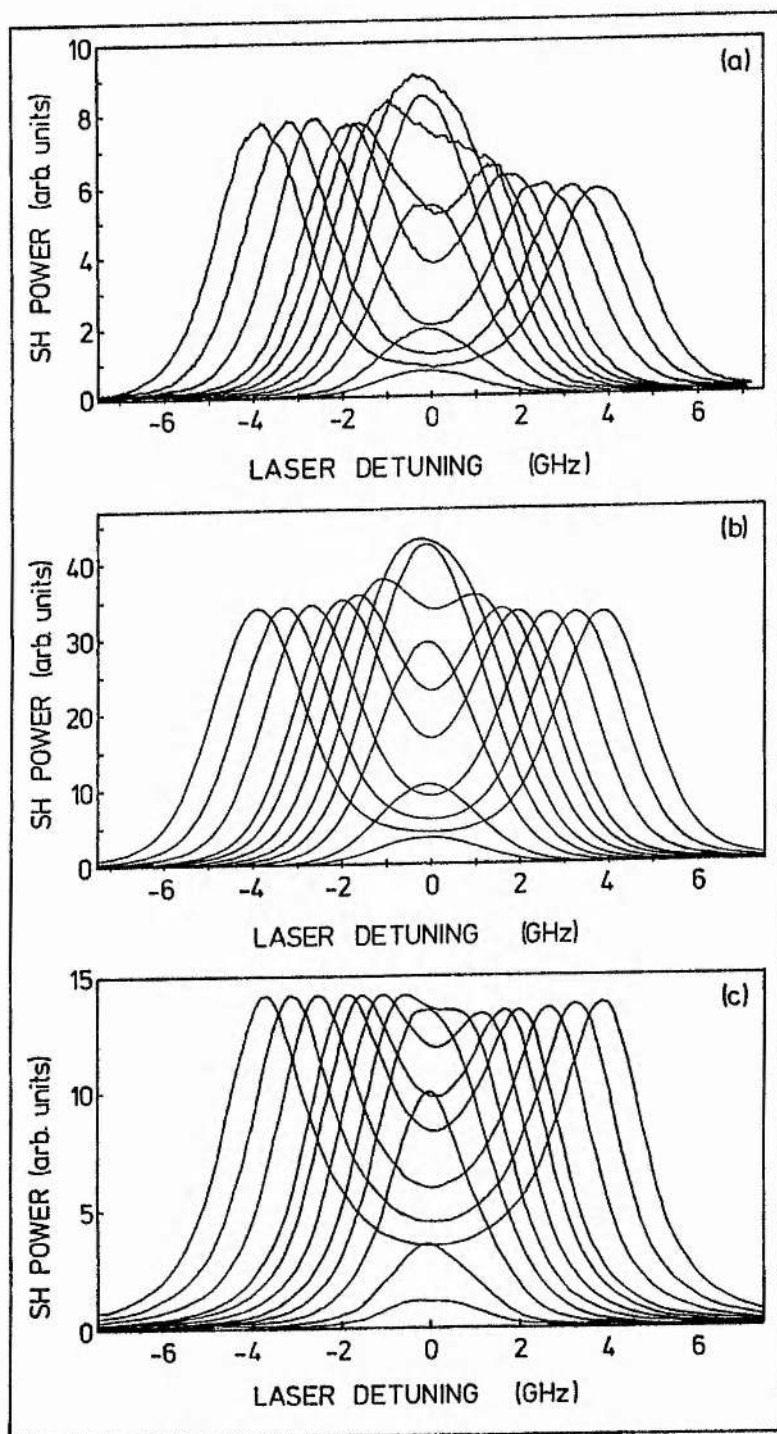


Figure 5.3.8. Second harmonic line profiles at different magnetic field strengths, conditions as in figure 5.3.1. Part (a) shows the experimental line profiles, part (b) shows the line profiles calculated using the model developed in chapter three, and part (c) shows the line profiles calculated using a theoretical model which did not consider homogeneous and inhomogeneous broadening separately, but just used a single damping term in the calculations.

reflecting mirror caused the arrangement to change from a standing wave to a running wave setup. No difference in the shape of the SHG line profile was seen between the two cases, though the conditions for Doppler-free two-photon absorption in the former case were correct, as evidenced by the observation of Doppler-free two-photon absorption peaks through the side window. Unlike two-photon absorption, SHG cannot be a Doppler-free process, as a second harmonic photon can be generated only by the absorption of two photons from one beam. This arises from the conservation of photon momentum discussed earlier; in a parametric process it is not possible for the atom to be made to recoil to conserve total momentum.

Linearly polarised fundamental radiation was once more focussed into the heatpipe, but an out-of-plane three-mirror arrangement was used to align the plane of polarisation of the laser light at 45° to the magnetic field. This allowed both the Q_{xy} and Q_{zy} effective dipoles to be driven, as described by equations 3.2.55, 3.2.56 and 3.2.59. The 45° angle caused the effective dipoles to have the same geometrical weighting factor. The line profiles of the radiation emanating from the two effective dipoles were measured separately by inserting an appropriately orientated linear polariser in the second harmonic beam.

At low field strengths, the line profiles were similar, as shown in figure 5.3.9(a). At a higher field of 0.294 T the line profiles of the two effective dipoles were significantly different, as shown in figure 5.3.9(b). Equation 3.2.38 shows that different two-photon transitions resonantly enhance the two effective dipoles. The Q_{xy} moment is associated with $\Delta m_l = \pm 2$ transitions, while the Q_{zy} moment is associated with $\Delta m_l = \pm 1$ transitions. The differences in frequency dependence of the magnitudes of the Q_{xy} and Q_{zy} moments are therefore most evident at high fields, when the Zeeman splitting is large and m_l approximates to a good quantum number.

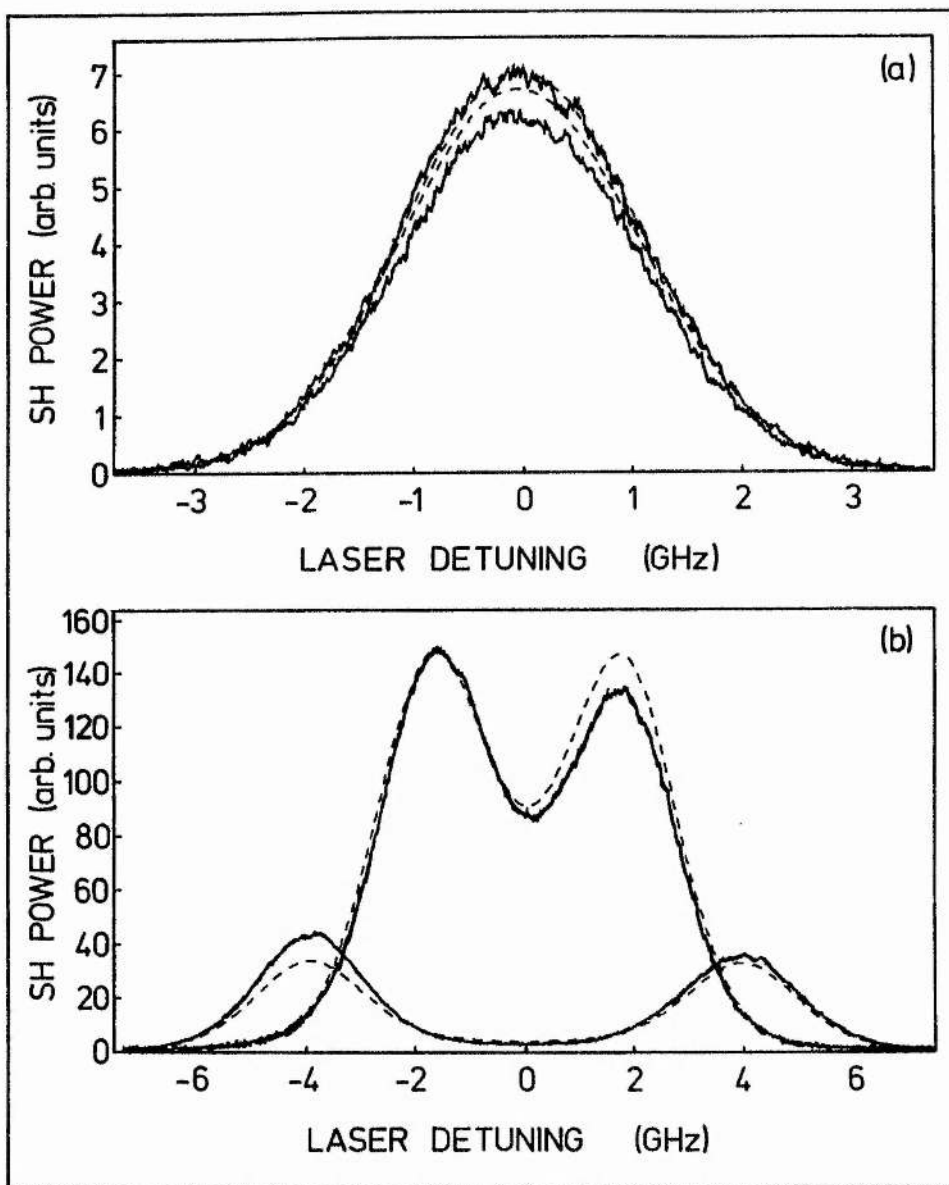


Figure 5.3.9. Line profiles of the second harmonic radiation emanating from the two effective dipoles (a) at 0.022 T and (b) at 0.294 T, with the laser polarisation at 45° to the magnetic field. The solid lines are experimentally determined, the dashed lines are theoretically calculated. The curves with the greater maximum in each case were produced by the z effective dipole, the other by the x effective dipole. $T = 290^\circ\text{C}$, $P = 1$ mbar, heatpipe b.

The four peaks at high magnetic fields may be identified with the resonant enhancement of the outermost four peaks of the two-photon absorption trace of figure 5.3.4. At high fields, the Q_{xy} profile shows about twice the splitting of the Q_{zy} profile due to these differences in selection rules. The maximum intensities of the radiation emitted by the two effective dipoles are different, which is also due to the greater relative Zeeman splitting of levels contributing to Q_{xy} than to Q_{zy} : the greater splitting of the Q_{xy} line profile leads to a lower field being required to split the peaks beyond the Doppler width, at about which value of field the maximum SH intensity no longer increases with magnetic field strength.

At low fields, as in figure 5.3.9(a), the Zeeman splitting is small, and so there is little difference in the resonant enhancement of the two effective dipoles, and thus the two line profiles are similar. In all the cases shown in figure 5.3.9, the agreement between theory (dashed line) and experiment (solid line) is good. Some of the small deviations between the experimental traces and the theoretical ones may have been due to the variation of the sensitivity of the photomultiplier tube with position and polarisation of the beam [128].

When the polariser was removed from the SH beam, both effective dipoles contributed to the second harmonic generation. The SHG line profiles under these conditions are shown in figure 5.3.10; they are considerably different from those of figure 5.3.1 as the Q_{zy} moment was now also contributing to SHG. It is easy to see how the line profiles of the two effective dipoles shown in figure 5.3.9 would add up to give the appropriate curves in figure 5.3.10. As the polarisation of the radiation emitted from the two effective dipoles is (by definition) perpendicular, it is permissible to add intensities, as shown in equation 3.2.60. The two radiation fields cannot

interfere, but the polarisation properties of the SH beam will depend on the relative magnitudes and phases of the two effective dipoles. This is explained further in the following section.

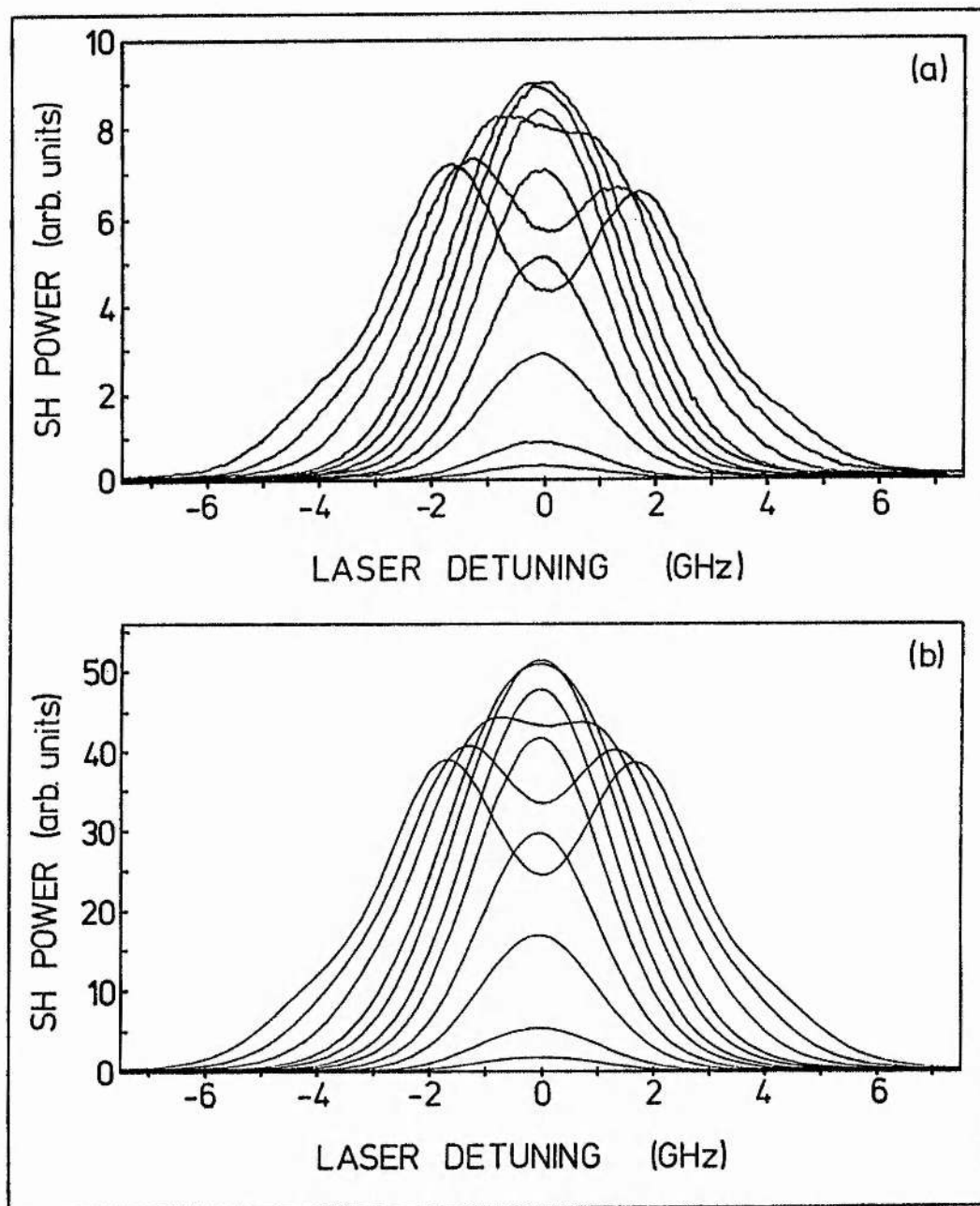


Figure 5.3.10. Line profiles of the second harmonic generation with the fundamental radiation at 45° to the magnetic field. The curves in (a) are experimentally determined, those in (b) are theoretically calculated. The curves are at different magnetic field strengths:- $B = 0.016$ T (the curve with the lowest maximum), 0.028 T, 0.052 T, 0.074 T, 0.100 T, 0.120 T, 0.147 T, 0.168 T, 0.212 T, 0.250 T, and 0.290 T (the widest curve). $T = 284^\circ\text{C}$, $P = 1\text{mbar}$, heatpipe b.

5.4 VARIATION OF THE POWER AND POLARISATION PROPERTIES OF THE SECOND HARMONIC WITH MAGNETIC FIELD

The laser polarisation was set at 45° to the magnetic field so that both effective dipoles were excited. The power and polarisation properties of the SH were examined as the magnetic field strength was varied, at a constant laser frequency. The SH power was measured using the filtered solar blind photomultiplier tube. The polarisation properties of the SH light were measured in two distinct ways. In the first, a linear polariser was inserted between the oven and the detector. The polariser was rotated to the positions of minimum and maximum SH signal; the angle of the polariser gave the polarisation angle of the SH, and the square root of the ratio of the signal strengths at the two positions gave the ratio of the lengths of the ellipse axes. A second, "null", method was devised to measure a/b , in order to avoid problems due to the non-uniform response of the photomultiplier tube [128]. A Soleil Babinet compensator was set up as a quarter-wave plate at 289.3 nm and was inserted in the SH beam with a linear polariser between it and the detector. Zero SH signal was obtained only if the axes of the quarter wave plate were along the axes of the polarisation ellipse, and if the transmission axis of the polariser was at 90° to the linearly polarised light created by the quarter-wave plate. The orientation of the ellipse was then given directly by the angular position of the quarter-wave plate, and the ratio of the lengths of the ellipse axes was given by the tangent of the angle between the quarter wave plate and the linear polariser.

The power and polarisation properties of the SH were investigated at three laser frequencies: f_0 , $f_0 + 1.5$ GHz, and $f_0 + 3$ GHz. The strikingly different results obtained at these three frequencies are shown in figures

5.4.1, 5.4.2, and 5.4.3. In all cases there is good agreement between the theoretically predicted behaviour, which is shown by solid lines, and the experimental readings marked as points on the graphs. The polarisation state of the SH radiation at selected magnetic fields is indicated by the polarisation ellipses at the top of the figures.

At f_0 , which is approximately at the centre of the Doppler-broadened two-photon absorption peak, the SH power is seen (figure 5.4.1(c)) to rise to a peak at 0.16 T, as can also be deduced from figure 5.3.10. The eccentricity of the SH is very close to one (i.e., the polarisation of the SH is almost linear) at all fields as seen in figure 5.4.1(b). This is due to the two effective dipoles being almost exactly in phase with each other at all field strengths; the maximum expected phase difference between them is calculated to be 1.3° . Because of the different growth rates of the two effective dipoles, the polarisation of the SH rotates as the field is increased, as shown in figure 5.4.1(a). At low fields the two effective dipoles have approximately the same magnitude, and so the second harmonic is polarised at the same 45° angle to the magnetic field as the fundamental beam. At this laser frequency at higher magnetic fields the z effective dipole is larger than the x one, as shown in figure 5.3.9, and so the polarisation direction moves towards the z axis.

The power and polarisation properties of the SH at $f_0 + 3$ GHz may be explained with reference to figure 5.4.4, which shows the theoretically calculated size and relative phase of the two effective dipoles when the laser is tuned to this frequency; a damping constant of 35 MHz and a vapour temperature of 300°C were used in the calculation. At this laser frequency the peak in the magnitude of the x effective dipole occurs at 0.23 T, as is seen experimentally in figure 5.3.1. This is due to the transitions which contribute to Q_{xy} being Zeeman-shifted to cause maximum

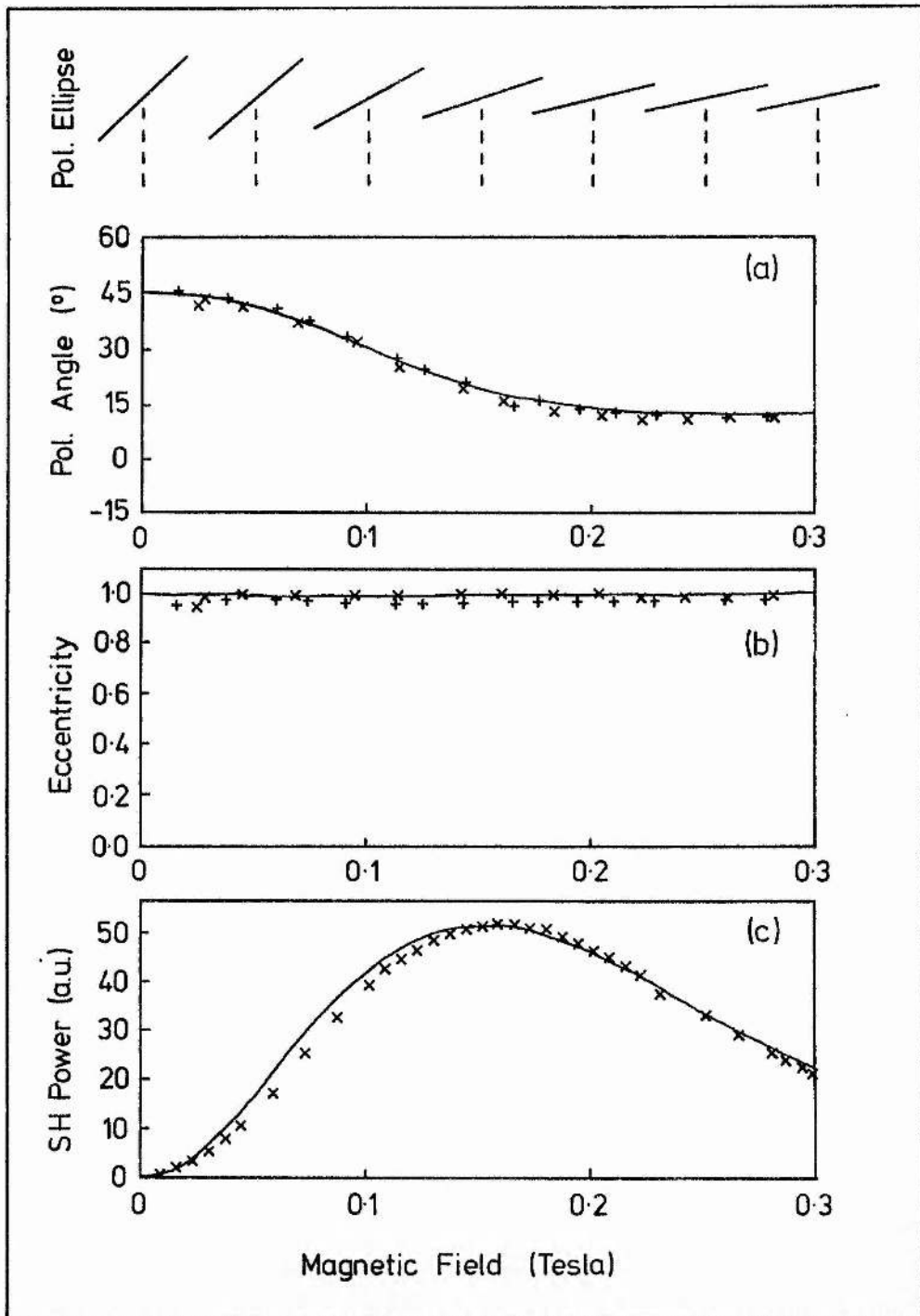


Figure 5.4.1. Power and polarisation properties of the second harmonic radiation as functions of the magnetic field strength. The field was at 45° to the polarisation of the fundamental, and the laser was tuned to f_0 . The experimental points in parts (a) and (b) were taken in the two ways described in the text:- + using the linear polariser alone, x using the null technique. The curves are theoretically calculated; the curve in part (c) was normalised to have the same maximum as the experimental readings. The ellipses at the top of the diagram are drawn to indicate the polarisation state of the light at various magnetic field strengths; in these diagrams the x axis is vertical and the z axis horizontal. $T = 294^\circ\text{C}$, $f_L = f_0$, $P = 1$ mbar, heatpipe b.

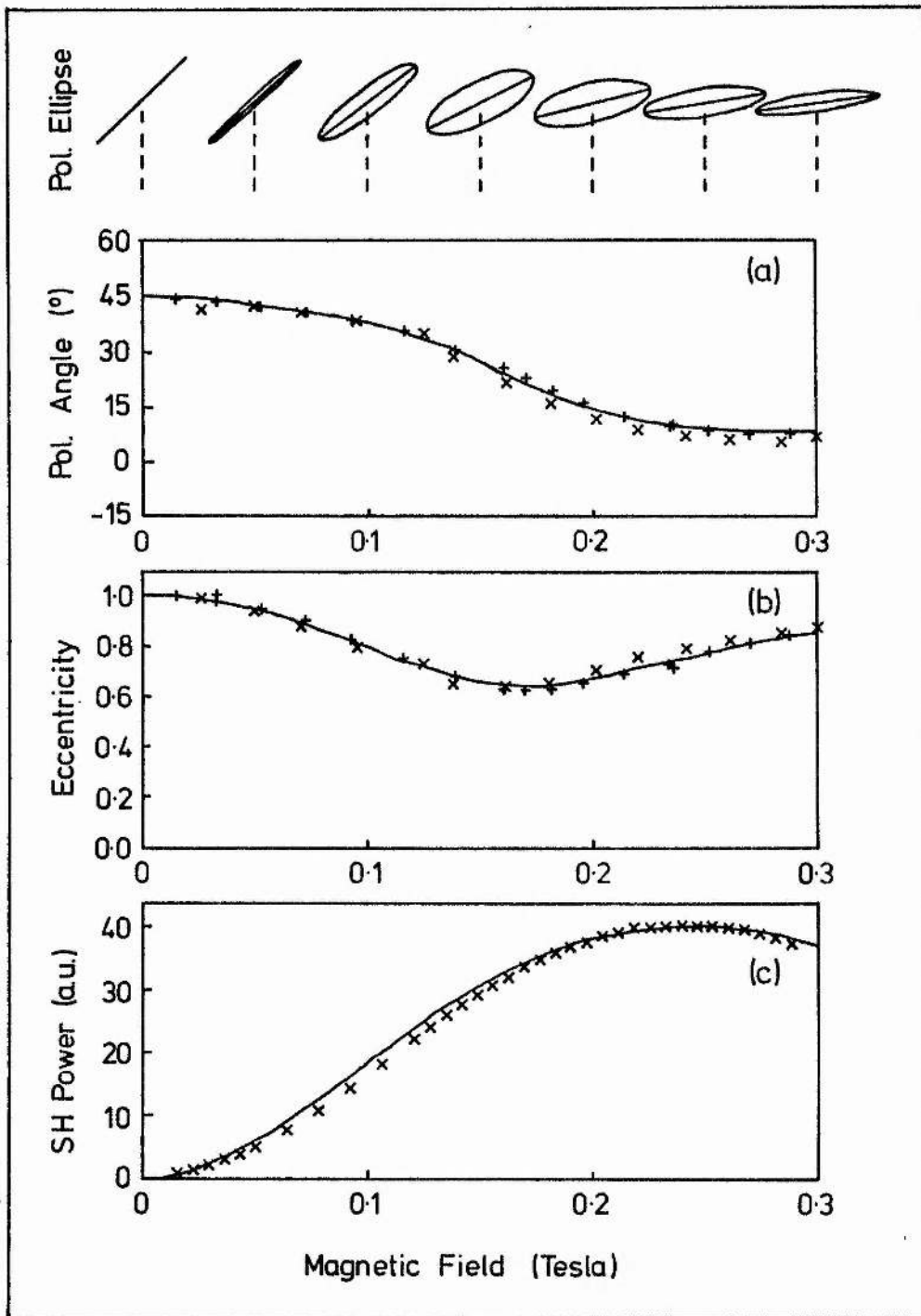


Figure 5.4.2. Power and polarisation properties of the SH as functions of magnetic field strength, at a laser frequency of $f_0 + 1.5$ GHz. Other conditions were the same as those listed with figure 5.4.1.

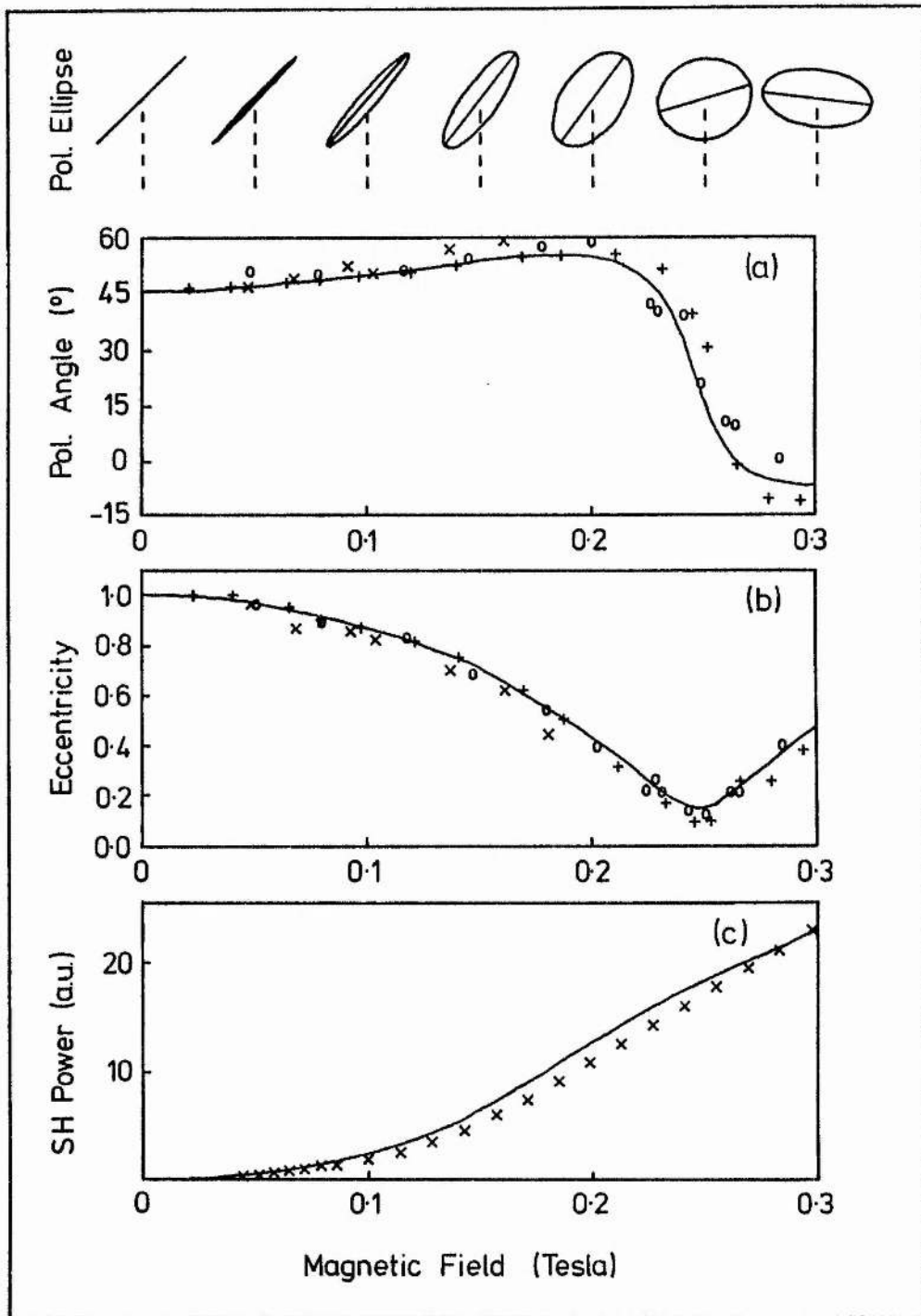


Figure 5.4.3. Power and polarisation properties of the SH as functions of the magnetic field strength, at a laser frequency of $f_0 + 3$ GHz. Other conditions were the same as those listed with figure 5.4.1, but the circles mark another set of experimental results taken using the null method.

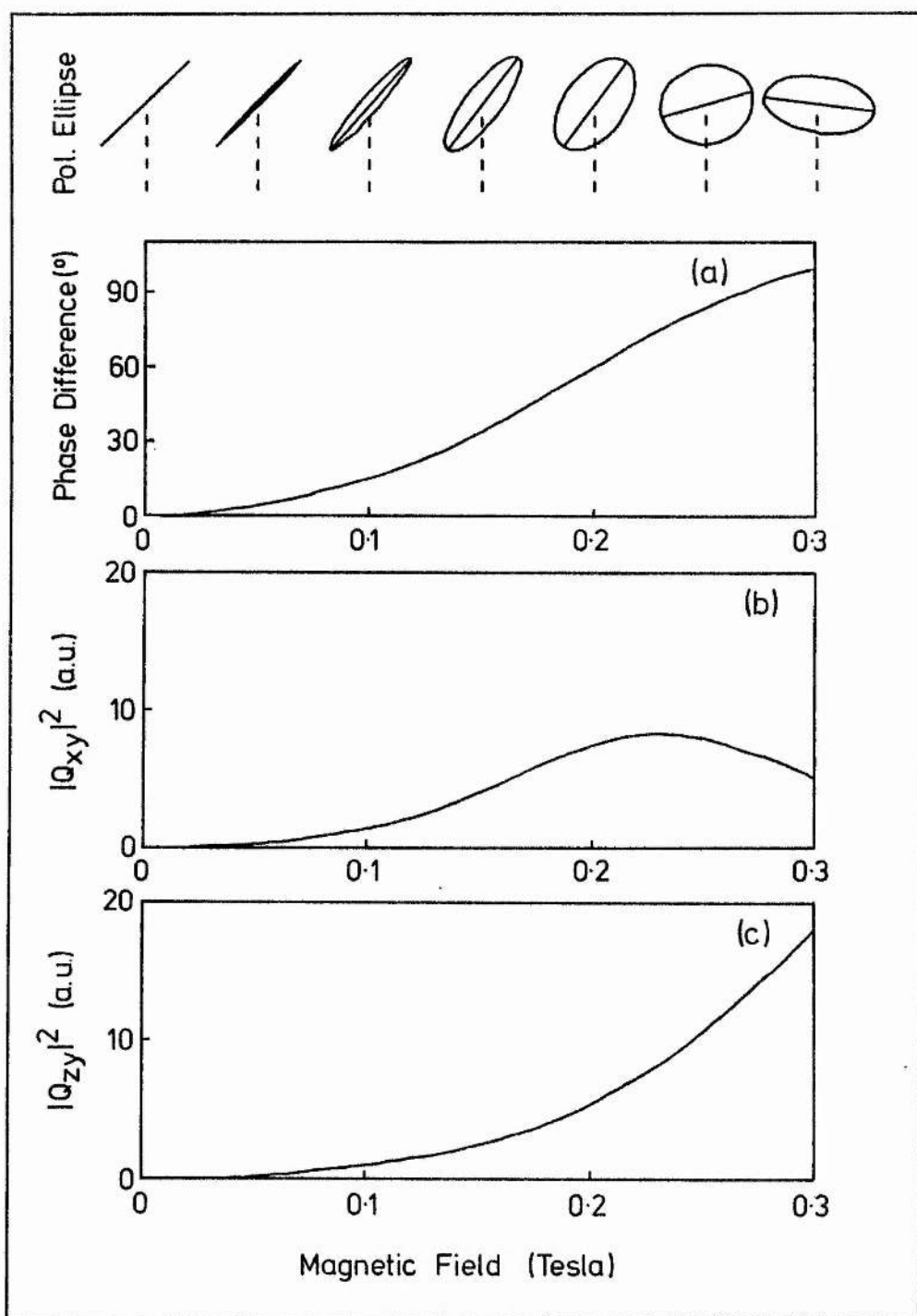


Figure 5.4.4. Calculated magnitudes of, and phase difference between, the two effective dipoles driving the SHG. These are plotted as functions of magnetic field strength, at a laser frequency of $f_0 + 3$ GHz. A vapour temperature of 300 °C and a damping constant γ_{ds} of 35 MHz were assumed.

resonant enhancement, as was shown theoretically in figure 3.2.2. Because the transitions which drive Q_{zy} are subject to less relative Zeeman splitting than those driving Q_{xy} , the size of the former moment is seen still to be increasing at 0.3 T, as the Zeeman effect moves the appropriate level differences closer into resonance with the SH frequency. The sum of the SH powers due to the Q_{xy} and Q_{zy} moments gives the total SH power shown in figure 5.4.3(c). Figures 5.4.1(c) and 5.4.2(c) show peaks in the SH power; as these results were taken closer to line centre than those of figure 5.4.3, a smaller field was required to shift the appropriate levels into positions of maximum resonant enhancement, and the sizes of both the x and z effective dipoles have passed their maxima by 0.3 T.

The calculated phase difference between the two effective dipoles at the laser frequency $f_0 + 3$ GHz is shown in figure 5.4.4(c) as a function of magnetic field. The maximum phase difference at this laser frequency is much greater than at f_0 . The relative phase of the two moments affects the polarisation state of the SH radiation. This is seen in figure 5.4.3(b) as a reduction in the eccentricity of the SH, though circularly polarised light was not produced, as the two moments had different magnitudes. However, a phase difference of greater than 90° would have resulted in the polarisation angle passing into the next quadrant; figures 5.4.3(a) and 5.4.4(a) show this happening at 0.26 T.

The change in the polarisation properties of the SH with magnetic field strength may thus be explained in terms of the changes in the relative phases and magnitudes of the two effective dipoles. These changes are brought about by differences between the resonant denominators applying to the transitions which enhance the two effective dipoles. Near line centre the phase differences between the fundamental and the effective dipoles are always small, and so the eccentricity of the SH is close to 1.0 (the

reasons for the small phase difference in the case of the x effective dipole were shown schematically in figures 5.3.5 and 5.3.7). Further from line centre, as was shown in figure 3.3.2 for the x effective dipole, the imaginary part of the effective dipoles may become significant, and the phase difference between the two effective dipoles causes significant deviations from linear polarisation of the SH. Similarly, the amount of polarisation rotation depends on the relative sizes of the effective dipoles, the rotation being much greater at $f_0 + 3$ GHz than at line centre.

5.5 SECOND HARMONIC POWER DEPENDENCE ON THE FUNDAMENTAL POLARISATION

In order to measure the dependence of the second harmonic power on the fundamental polarisation angle, a half-wave plate was inserted before the oven to vary the angle between the plane of polarisation of the fundamental and the magnetic field. The SH power was measured directly by the filtered solar blind photomultiplier tube.

At low fields, in which the two effective dipoles grow at the same rate when the fundamental polarisation is at 45° to the magnetic field, the SH power is expected to show a $\sin^2 \theta$ dependence on the polarisation angle θ , as $I_{SH} \propto \tilde{q}_{xy}^* \tilde{q}_{xy} + \tilde{q}_{zy}^* \tilde{q}_{zy} = (\epsilon_x^2 \xi_{xy})^2 + (\epsilon_x \epsilon_z \xi_{zy})^2$ where ξ_{xy} represents $\tilde{q}_{xy} / \epsilon_x^2$ and ξ_{zy} represents $\tilde{q}_{zy} / \epsilon_x \epsilon_z$ in equations 3.2.55 and 3.2.56. The ξ_{ij} are approximately equal at low fields, so $I_{SH} \propto (\epsilon_x^2)^2 + (\epsilon_x \epsilon_z)^2 = \sin^2 \theta$. This was observed, and is shown in figure 5.5.1. The difference in the growth rate of the two effective dipoles in higher magnetic fields was described in the previous section. This leads to a more complicated than in the low field case. At a fundamental polarisation angle of 90°

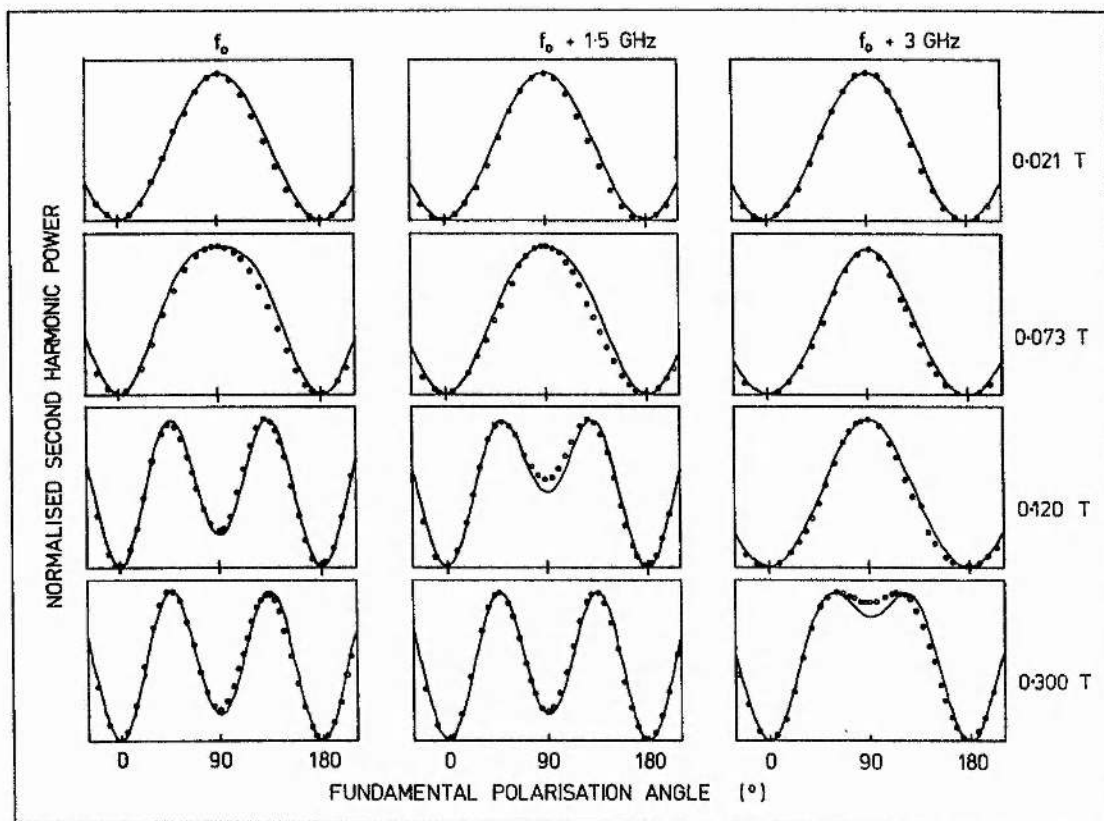


Figure 5.5.1. Variation of the SH power with the fundamental polarisation angle. Each theoretically calculated curve was normalised to have the same peak power as its associated set of experimental results. Columns 1 to 3 show the results for the laser tuned to f_0 , $f_0 + 1.5$ GHz, and $f_0 + 3$ GHz respectively. The different rows show the results for different magnetic field strengths. $T = 285^\circ\text{C}$, $P = 1$ mbar, heatpipe b.

only the x effective dipole is driven, and the SH power appropriate to that dipole alone is obtained. At other angles the z effective dipole is also driven, and it adds to the total SH power. This effective dipole is strongest at angles of 45° and 135° . Figure 5.5.1 shows that the theory and experiment agree that the maximum deviation from the $\sin^2\theta$ behaviour occurs at the highest magnetic fields, in which cases the differences in the magnitudes of the two effective dipoles are generally the greatest. The dependence of the shapes of the curves with respect to laser frequency may be understood with reference to figure 5.3.9; the

frequencies in figure 5.3.9(b) at which there is the greatest difference in magnitudes of the two effective dipoles are the frequencies at which there is greatest deviation from the $\sin^2\theta$ behaviour in the graphs in the lowest row of figure 5.5.1.

5.6 INVESTIGATION OF THE ASYMMETRY OF THE SECOND HARMONIC LINE PROFILES IN HIGH FIELDS

For all the studies reported so far in this thesis, apart from those in section 5.2, the properties of the SH have been calculated from the interaction of a single atom with the field, with allowance made only for the Doppler effect causing differences between atoms. This has given good agreement for most SH properties, but has failed to explain the difference in the heights of the two peaks in the SH line profile in high fields, such as shown in figure 5.3.1. In this section bulk effects in the medium will be included in the model. Three mechanisms for frequency-dependent phase-mismatching effects will be considered as possible reasons for the asymmetry of the high-field line profiles: dispersion due to quadrupole or two-photon resonances on the 3S - 4D transition, and the effects of a non-uniform magnetic field.

As has already been noted, the major contribution to the difference in the phase velocity of the fundamental and the second harmonic is from the 3S - 3P transitions. These are some 300 cm^{-1} off resonance with the laser light, so the variation in refractive index due to these transitions will be negligible across the 3S - 4D line profile. This is not so, however, for the contribution to the dispersion from the 3S - 4D transitions. Although these electric quadrupole and two-photon transitions are very

weak, they would be exactly in resonance, and so may become significant. This is considered in the following paragraphs.

For resonant transitions the Sellmeier equation must be modified to include a damping term; in this case, using the same notation as in equation 5.2.9,

$$n(\lambda) - 1 = \frac{N r_e}{2\pi} \sum_{ij} \frac{\alpha_i f_{ij}}{1/\lambda_{ij}^2 - 1/\lambda^2 + \gamma_i^2/(-1 + \lambda^2/\lambda_{ij}^2)} \quad (5.6.1)$$

where γ_i is the damping constant for level i , which is equal to the FWHM of the absorption line. Tull et al [92] calculated $g_k f_{ik}$ for the 3S - 4D transition to be 9.97×10^{-7} , where g_k is the statistical weight of the 4D level. An estimate of the contribution of this quadrupole resonance to the refractive index was made by calculating $n(\lambda) - 1$ for one of the 3S - 4D transitions, ignoring the Doppler effect, and taking γ_i to be 70 MHz. The maximum values of $|n(\lambda) - 1|$ occur $\pm \gamma_i/2$ from the resonant frequency, and were calculated to be $2.8 \times 10^{-29} \times N$. This figure is two orders of magnitude smaller than the value of the same quantity caused by the sodium D lines. Additionally, the dispersive effects of this quadrupole resonance will be lessened by Doppler broadening and the presence of the other 3S - 4D transitions. Thus it seems unlikely that the asymmetries in the line profiles were due to frequency-dependent phase-mismatching effects due to the dispersion caused by the quadrupole resonance.

As the two-photon absorption strength is dependent on the laser intensity, so is the change in refractive index caused by the two-photon absorption. The relative strengths of the refractive index changes due to the quadrupole and two-photon transitions may be considered by calculation of the relative absorption rates of the two transitions. The 3S - 4D two-photon absorption rate per atom W_{TPA} is given by Hanna et al [14] as

$$W_{\text{TPA}} = \frac{I_L^2}{2\epsilon_0^2 \hbar^4 c^2} \left(\frac{\gamma_d}{(\omega_{ds} - 2\omega)^2 + \gamma_d^2} \right) \left| \sum_P \frac{\mu_{dp} \mu_{ps}}{\omega_{ps} - \omega} \right|^2 \quad (5.6.2)$$

where I_L is the laser intensity, γ_d is the damping constant for the 4D states, and the other symbols are as defined in chapter three. The single-photon quadrupole transition rate W_Q [12, 92, 130] is

$$W_Q = \frac{6.67 \times 10^{-5} g_s f_{sd} I_L}{4\pi \cdot 2 g_d n^2 \hbar \omega_L} \left(\frac{\gamma_d}{(\omega_{ds} - 2\omega_L)^2 + \gamma_d^2} \right) \quad (5.6.3)$$

Miles and Harris [124] tabulate the dipole matrix elements in equation 5.6.2 to be $\langle 3S | er | 3P \rangle = 2.13 \times 10^{-29}$ cm and $\langle 3P | er | 4D \rangle = 7.31 \times 10^{-30}$ cm; the value used for the oscillator strength for the quadrupole transition was the one mentioned above. In this case the ratio of the absorption rates is $W_Q(2\omega_L)/W_{\text{TPA}}(\omega_L) = 1.5 \times 10^8 / I_L$. For a 100 μm diameter laser beam waist and a laser power of 0.5 W, this ratio equals 2. Therefore under the conditions of these experiments the effect of the quadrupole transition on the dispersion is expected to be greater than that of the two-photon absorption. When the beam was not focussed, the effects of two-photon absorption on the dispersion would have been even less.

The phase of the generated second harmonic depends on the strength of the magnetic field and the laser frequency, as was illustrated in figures 3.2.2, 5.3.5 and 5.3.7. Thus, in an inhomogeneous magnetic field, frequency dependent effects may arise from magnetic field gradients causing a variation in the phase of the second harmonic which may tend to counteract or reinforce the phase mismatching processes described in section 5.2. This effect may be significant at particle densities near or above the first phase-match peak of figure 5.2.2 if the change in magnetic

field is not symmetrical about the centre of the vapour zone and beam focus.

Experiments were carried out to determine which of these effects dominated the production of the asymmetry of the line profiles. The laser polarisation was perpendicular to the magnetic field throughout. The asymmetry of the peak heights at 0.3 T was found not to be dependent on the laser power, confirming that the dispersion due to two-photon absorption was not important. The lens that focussed the laser beam into the cell was moved along the beam axis, and SH line profiles were recorded at 0.284 T. The ratios of the heights of the two peaks are plotted against the position of the lens in figure 5.6.1. Here it is seen that the ratio may be greater or

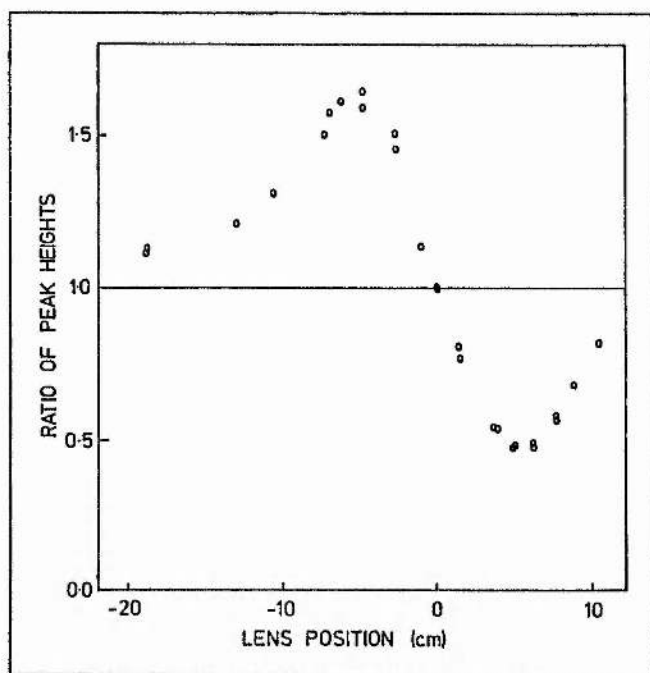


Figure 5.6.1. Ratio of the SH powers at the low and high frequency peaks of SHG in a 0.284 T field, as a function of the position of the 20 cm focal length lens. The lens was 26.4 cm from the centre of the oven at the zero of the lens position axis. $T = 285^{\circ}\text{C}$, $B = 0.284\text{ T}$, $P = 1\text{ mbar}$, heatpipe c.

less than one, depending on the position of the lens. The separation of the maximum and minimum in this curve is approximately the same as the vapour zone length. When no lens was used the peak height ratio was 1.0; in this situation the laser beam was only very slightly divergent during its passage through the vapour. It is unlikely that the dispersion due to the quadrupole resonance would produce this shape of curve, so further work was done to investigate the effect of the non-uniform magnetic field.

The theory of harmonic generation using a focussed beam has been given by Ward and New [135]; the presence of a beam focus introduces phase shifts, and the gaussian beam intensity and phase distribution must be taken into account. To simplify comparison of experiment with theory, further experiments were conducted without using the focussing lens, so that the 2 mm diameter laser beam may be treated approximately as an infinite plane wave. It was shown in section 5.2 that for such a plane wave

$$dE_{2w} = fN(E_w^2/2) \exp[i(k_{2w} - 2k_w)y] \exp[i\phi] dy. \quad (5.6.4)$$

The quantity $f \cdot \exp[i\phi]$ depends on the magnetic field strength, and is proportional to \tilde{Q}_{xy} when the magnetic field and laser polarisation are perpendicular to each other. Putting $\tilde{Q}_{xy} = \tilde{Q}_R + i\tilde{Q}_I$ (where \tilde{Q}_R and \tilde{Q}_I are real), $\Delta k = k_{2w} - 2k_w$, and assuming a non-depleted input wave gives

$$dE_{2w} = Nk' [Q_R \cos(y\Delta k) - Q_I \sin(y\Delta k) + i(Q_I \cos(y\Delta k) + Q_R \sin(y\Delta k))] dy \quad (5.6.5)$$

where k' is a constant. This equation was integrated for the conditions of interest, viz

$$N = \begin{cases} \text{constant} & \text{for } 0 < y < 0.12 \text{ m} \\ 0 & \text{for } 0.12 \text{ m} < y < 0 \end{cases} \quad (5.6.6)$$

$$k = 8.97 \times 10^{-20} \text{ N m}^{-1}.$$

In a uniform magnetic field the result is the same as from equation 5.2.7, and in a situation where the magnetic field is symmetrical about the centre of the vapour zone the heights of the two SH peaks are still approximately equal. However, if the beam experiences more positive magnetic field gradient than negative magnetic field gradient, this is no longer the case. At particle densities below the first phase match peak, and in a positive magnetic field gradient, the change in $\exp[i\phi]$ with position reduces the phase velocity mismatch for the low frequency peak in SHG, but increases the phase velocity mismatch for the high frequency peak.

To test this experimentally the electromagnet was moved 3.5 cm out from the position that was symmetrical about the vapour region. SHG line profiles were recorded with a peak field of 0.288 T over a range of particle densities, and then analysed to give plots of SH power against particle density at a number of frequencies across the line profile. Two such curves are shown in figure 5.6.2 for frequencies that correspond to the two peaks in SHG at low particle densities. The experimental arrangement was such that there was more positive magnetic field gradient than negative; the figure shows the beneficial effect of this arrangement on the low frequency peak and the detrimental effect on the high frequency peak, as expected from the arguments outlined above.

The theoretically calculated curves are shown in part (b) of the same figure. The agreement is fairly good; the main features of theory and experiment correlate well. It was found that the depths of the minima in the theoretically calculated curves were rather sensitive to the magnet position. The small displacement of the peaks between theory and

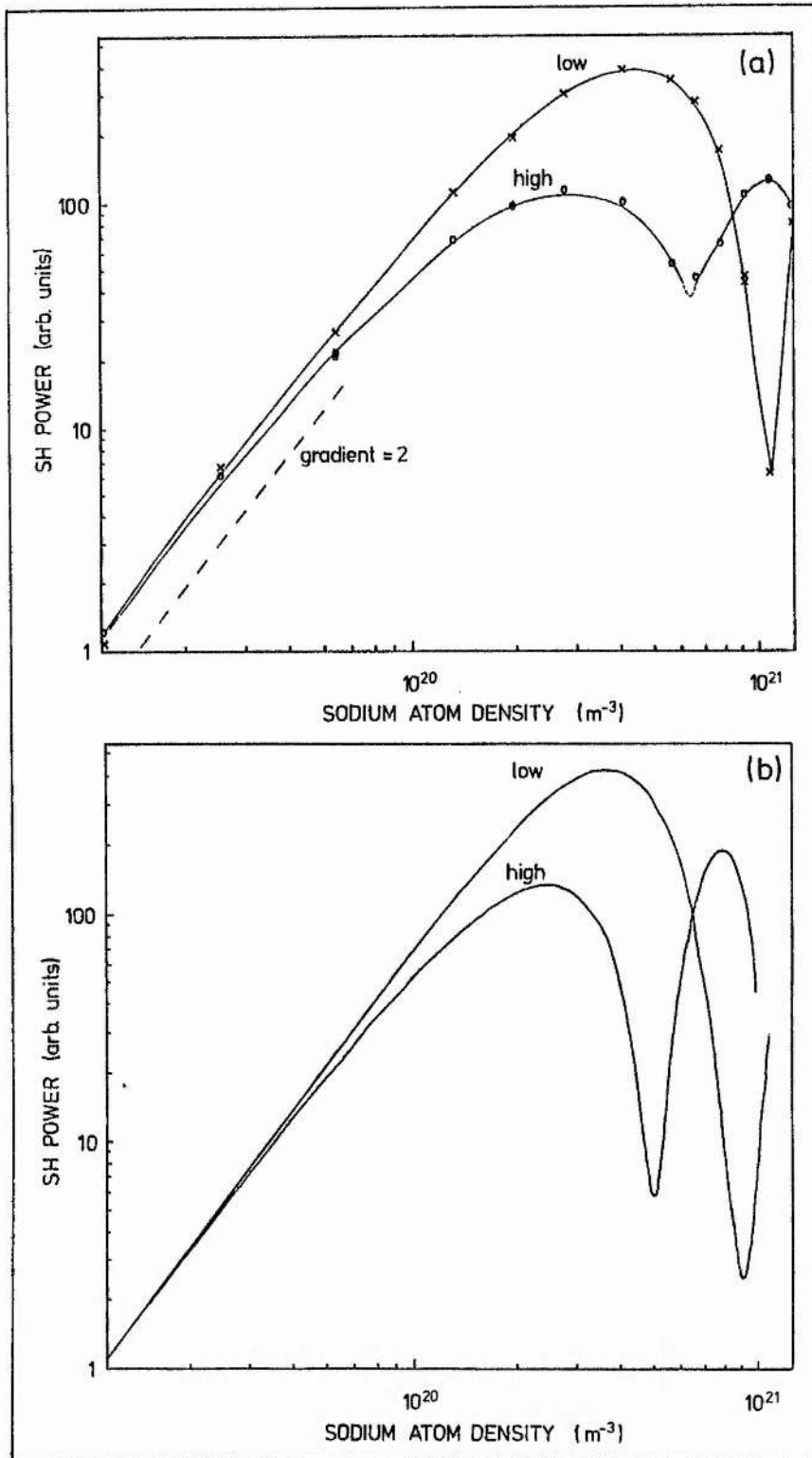


Figure 5.6.2. (a) Experimental and (b) theoretical variation of SH power with sodium atom density in the nonuniform magnetic field described in the text, the peak strength of which was 0.288 T. The laser frequencies were chosen to be close to the two frequencies of peak SHG in this magnetic field strength. The lines drawn in part (a) are to guide the eye. $P = 1$ mbar, $f_L = f_0 + 3.9$ GHz (high), $f_L = f_0 - 4.1$ GHz (low), heatpipe c.

experiment may well have been due to nonuniformities in the vapour density, or an incorrect estimate of the vapour temperature. However, these results verify that the asymmetry in the line profiles was indeed due to the effects of the nonuniform field. Similar considerations will hold for the case of a focussed beam, but the location of the beam focus in the inhomogeneous field must also be considered. Detailed calculations were not carried out for such cases, due to the complications mentioned above. This study has, however, unambiguously determined that changes in the phase of the generated second harmonic due to changes in the magnetic field strength can produce asymmetries in the SHG line profiles such as those that were observed.

At particle densities much less than the first phase match peak the phase changes have little effect in theory; in practice the peaks in the line profiles are seen to have approximately equal peak heights. At particle densities less than, but near, that of the first phase match peak, the low frequency peak in the line profile is greater than the high frequency peak under the conditions described above. At higher particle densities, certain frequencies may correspond to a minimum on the phase match curve, and others to a maximum; this would give rise to a much distorted line profile. Such a trace is shown as the thicker line in figure 5.6.3; the thinner line is a line profile at a particle density below the first phase match peak.

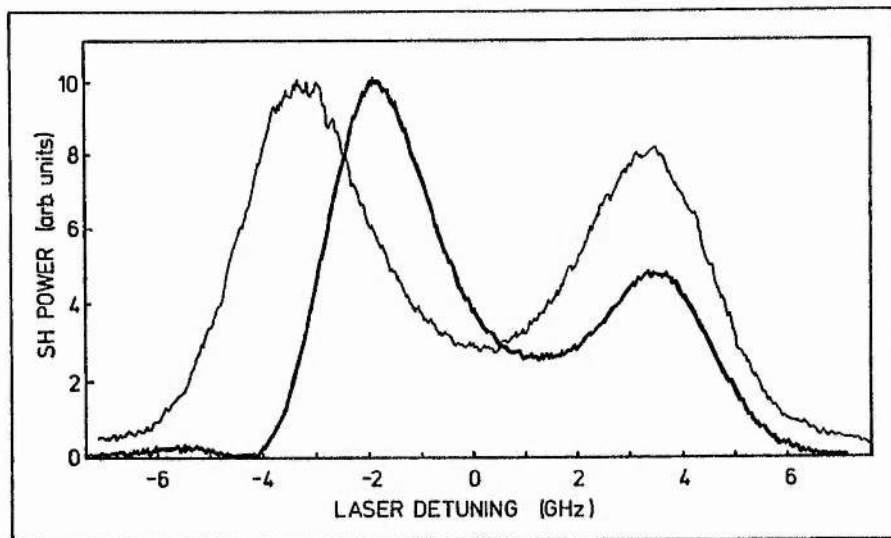


Figure 5.6.3. SHG line profiles well below and far above the first phase match peak. The thin line is the experimentally recorded line profile at an atomic density of 2.79×10^{21} atoms m^{-3} ; the thick line is the same, but at an atomic density of 1.08×10^{21} atoms m^{-3} . $B = 0.289$ T, $P = 1$ mbar, heatpipe c.

5.7 EFFECTS OF TEMPERATURE CHANGE

Changes in the temperature of the sodium vapour cause changes in the particle density, the results of which have been described in sections 5.2 and 5.6. A much less significant effect of a change in vapour temperature is the resulting change of Doppler width. A change in vapour temperature from 238°C to 319°C resulted in a 150-fold increase in SH power, but an increase in Doppler width to a width of only 1.08 times that at the original temperature is expected from equation 5.1.2. The fractional increase in the SHG linewidth is even less, as fine, hyperfine and Zeeman splitting are significant, and independent of the Doppler width. The temperature at which the SHG was a maximum was 319°C , and 238°C was the lowest temperature at which line profiles could be readily recorded with a reasonable signal

to noise ratio. For completeness, sets of line profiles at these temperatures are shown in figure 5.7.1, but there is little to be seen in this figure that has not already been mentioned in the previous sections.

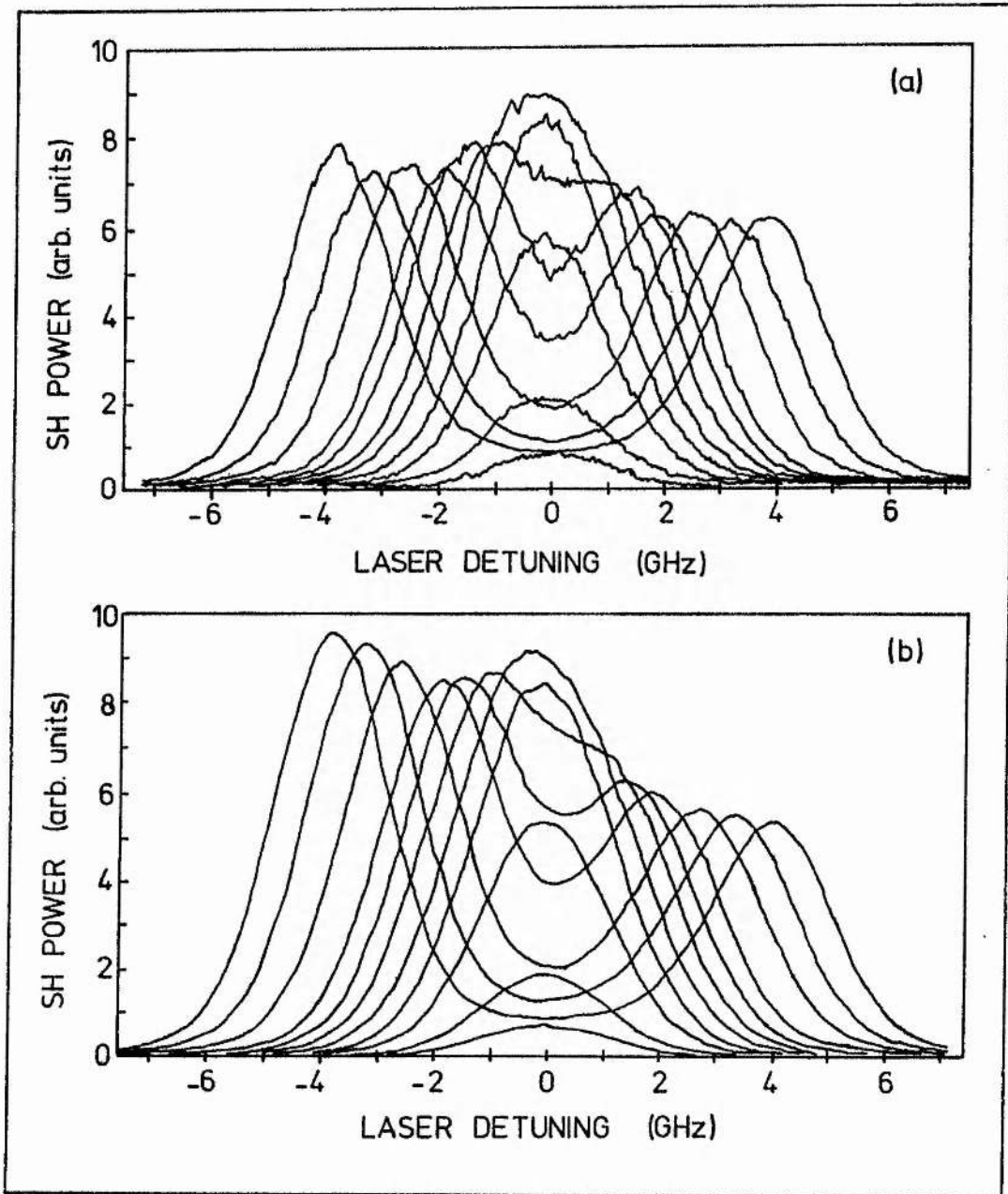


Figure 5.7.1. Experimentally obtained line profiles at (a) 238°C and (b) 319°C . The magnetic field strengths used for both sets of line profiles were: - 0.015 T (the curves with the lowest maximum), 0.028 T, 0.052 T, 0.074 T, 0.096 T, 0.121 T, 0.147 T, 0.167 T, 0.210 T, and 0.290 T (the widest curves). $P = 1$ mbar, heatpipe b.

5.8 EFFECTS OF CHANGES IN THE BUFFER GAS PRESSURE

The pressure of the buffer gas affects the SHG process through changes in γ_{ds} , the damping constant in the equations for the magnitude of the effective dipoles. Collisions of the sodium atoms cause the phase of the atomic wavefunctions to be changed, and thus the coherence between the 3S and 4D wavefunctions is lost. An increase in such collisions decreases the second harmonic generation efficiency, and broadens the linewidth of the resonantly-enhancing two-photon transition. Collision broadening and pressure effects on spectral lines have been reviewed by Hindmarsh and Farr [136], Ch'en and Takeo [137], and Margenau and Watson [138]. The experimental determination of the effects of buffer gas pressure on the two-photon linewidth was described in section 5.1.2.

SHG line profiles were measured in the manner described in section 5.3, but using the oven shown in figure 4.3.3(c). Figure 5.8.1 shows SHG line profiles taken at 1 mbar and 234 mbar, in both cases at 285°C and with a 0.275 T magnetic field which was perpendicular to the laser polarisation.

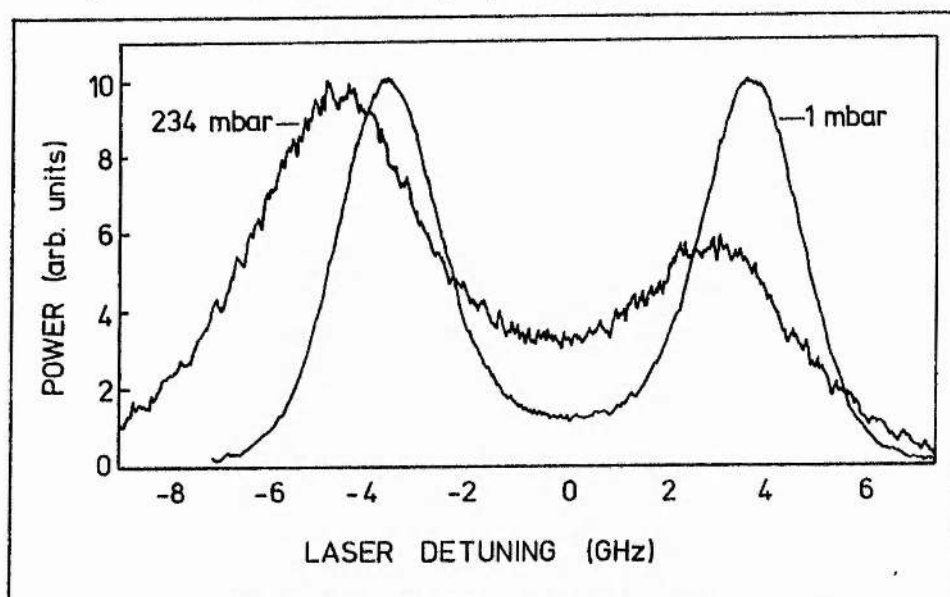


Figure 5.8.1. Experimentally obtained SHG line profiles with a 0.275 T magnetic field perpendicular to the laser polarisation, at buffer gas pressures of 1 mbar and 234 mbar. $T = 285^{\circ}\text{C}$, heatpipe c.

The pressure broadening and shift between the two profiles is readily seen. The peak SH power was also reduced by a factor of 240 by the increase of the buffer gas pressure.

A number of such line profiles were recorded as the buffer gas was increased; the dependences on γ_{ds} of the peak SH power at 0.02 T and 0.275 T are shown in figure 5.8.2.

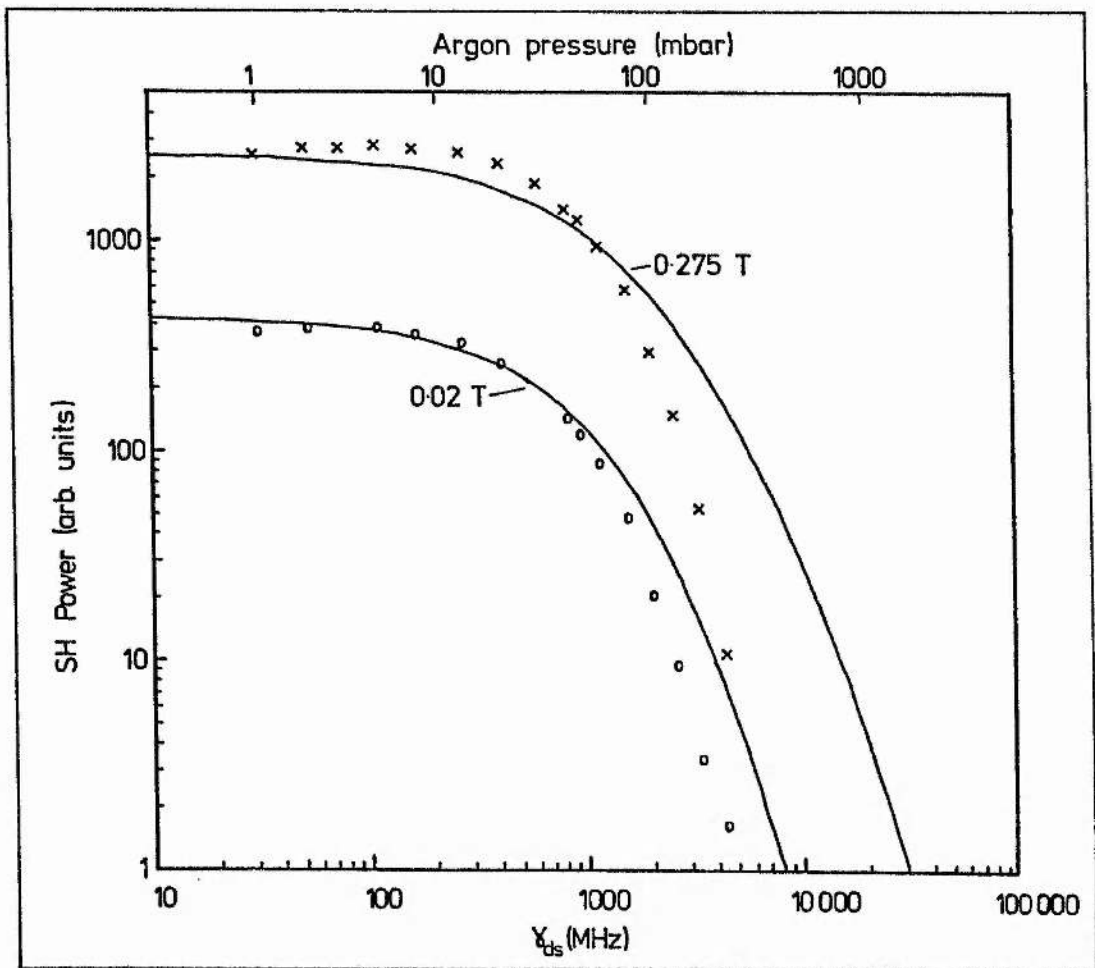


Figure 5.8.2. Dependence of SH power on damping constant γ_{ds} . The circles show the SH power at the peak of the SHG line profile at 0.02 T, the crosses show the SH power at the low frequency peak of the SHG line profile at 0.275 T. The calculated dependence is shown by the solid lines, the maximum intensity of the 0.02 T curve was normalised to fit the experimental data. T = 285 °C, heatpipe c.

Theory and experiment agree that there is little change in peak SH power with γ_{ds} until γ_{ds} becomes a significant fraction of the Doppler width. In contrast, at high pressures, the Doppler broadening is negligible compared with the pressure broadening. In this case, equation 3.2.55 may be simplified to give the expected value of the effective dipole as

$$\tilde{Q}_{xy} \propto \sum_{\substack{F, m_F, \\ J, m_J}} \frac{(B_2 - B_{-2}) [(\omega_{ds} - 2\omega) + i\gamma_{ds}]}{(\omega_{ds} - 2\omega)^2 + \gamma_{ds}^2}, \quad (5.8.1)$$

which leads to the SH power being expected to fall off as the fourth power of γ_{ds} when $\gamma_{ds}^2 \gg (\omega_{ds} - 2\omega)^2$. As the levels are split more in a high magnetic field than in a low one, the above condition is satisfied for all levels at a higher value of γ_{ds} in a higher magnetic field. Thus the -4 power dependence of the peak SH power on γ_{ds} is expected to occur at higher γ_{ds} for higher fields, as is seen in figure 5.8.2.

Although there is a fair qualitative agreement between theory and experiment at these higher pressures, there are substantial deviations between the experimental results and the theoretical predictions, especially at the higher magnetic field strengths. Some of this may be instrumental. At low pressures the SH power sometimes rose slightly with increasing buffer gas pressure, though the amount varied between runs and between ovens. It is suggested that this may have been caused by the buffer gas affecting the evaporation rate of the sodium; similar, but detrimental effects may have been occurring at higher gas pressures. Figure 5.8.3 shows the results of the same experiment, but using the heatpipe of figure 4.3.3(a), and using permanent magnets to produce the 0.02 T magnetic field. In this case the theoretical prediction of the peak SH power at any buffer gas pressure is in reasonable agreement with the experimentally obtained values from the three different runs. The former

heatpipe was operated to keep the temperature measured by the thermocouple constant, the latter heatpipe was operated under conditions of constant heat input. Changing the buffer gas pressure may have changed the temperature distribution and rate of heat flow in the pipes, resulting in a change of particle density or vapour zone length. Further experiments need to be done to investigate whether or not such effects occur.

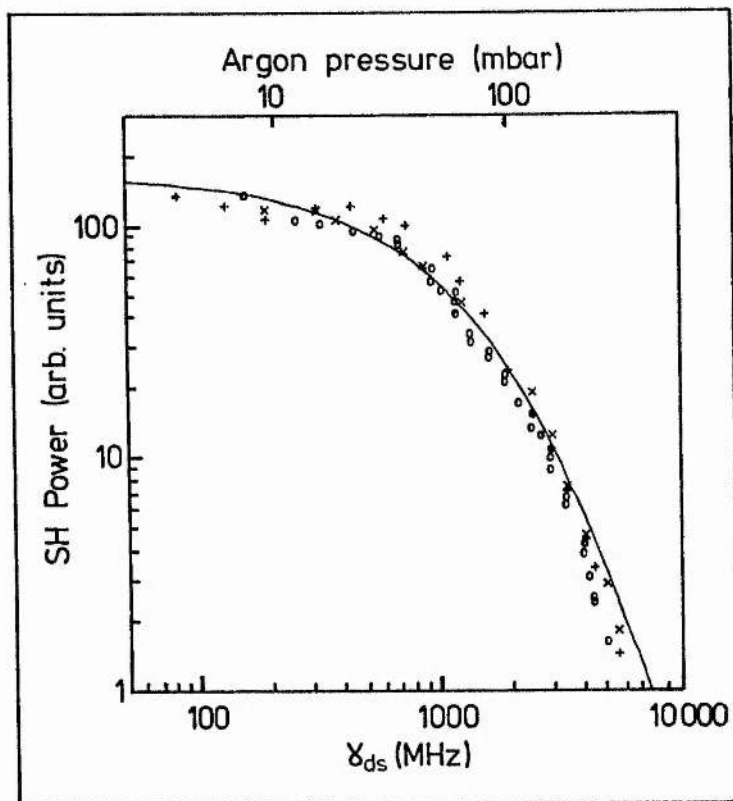


Figure 5.8.3. Dependence of the SH power on damping constant γ_{ds} . The different markers show the experimental results from different runs using heatpipe a, the solid line shows the theoretically calculated dependence, normalised to the experimental results. $T = 330^\circ\text{C}$, heatpipe a.

Another possible explanation for the differences between observed and predicted behaviour is that the modelling of the effects of the buffer gas pressure in terms of γ_{ds} is not realistic; the perturbing atoms may well have more effects than just collisional dephasing. For example, the collisions may induce population redistribution amongst the magnetic sublevels.

Line profiles at various buffer gas pressures at 0.02 T and 0.275 T are shown in figures 5.8.4 and 5.8.5. As described above, the measured drop in SH power with buffer gas pressure is greater than expected, but otherwise fair agreement is obtained between theory and experiment.

Figure 5.8.6(a) shows a family of line profiles taken at a buffer gas pressure of 109 mbar. These agree well with the theoretically modelled curves in figure 5.8.6(b), and contrast with the line profiles in part (c) of the same figure, which were plotted for 1 mbar buffer gas pressure. A higher magnetic field was required to saturate the SH dependence on magnetic field strength in the higher buffer gas pressure, as in the high pressure case a higher field was required to split the line profile beyond the higher pressure and Doppler-broadened linewidth. The same was true of the line profiles taken with the field at 45 degrees to the laser polarisation.

The dependence on magnetic field strength of the power and polarisation properties of the second harmonic were determined at 109 mbar in a similar manner to that described in section 5.4. The results of this study at a laser frequency $f_0 + 3$ GHz are shown in figure 5.8.7. Although there are significant differences between the theoretical and experimental values for the eccentricity, good agreement was obtained for the polarisation angle and the SH power curves. This figure should be contrasted with the low pressure results of figure 5.4.3. The polarisation rotation and deviation of eccentricity from 1.0 are much less in the high pressure case than in the low pressure one.

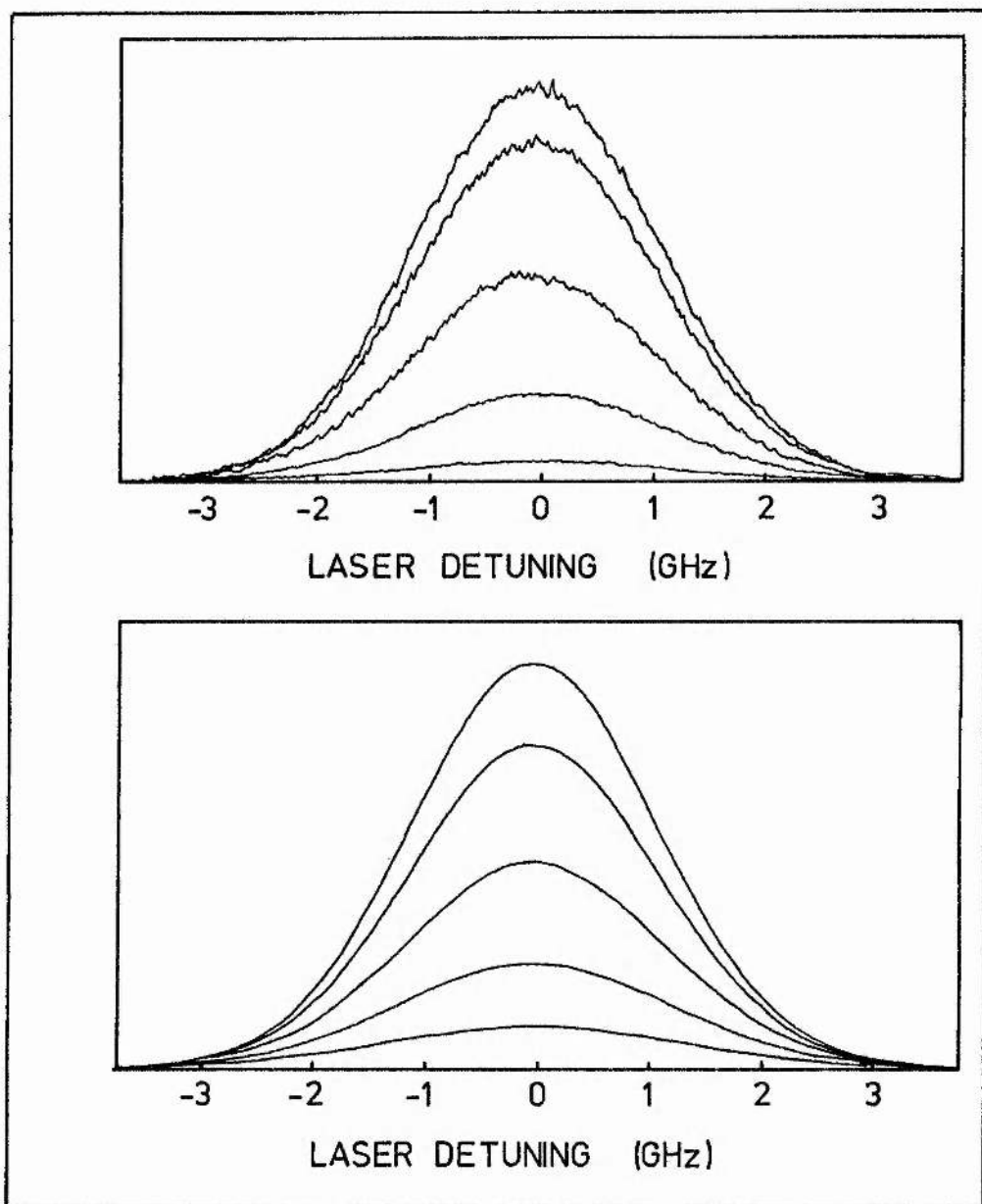


Figure 5.8.4. (a) Experimentally and (b) theoretically calculated variation of second harmonic power with laser frequency at different buffer gas pressures:- 5.3 mbar (the curve with the greatest maximum), 14 mbar, 32 mbar, 61 mbar, 106 mbar (the curve with the lowest maximum). These values correspond to values of γ_{ds} of 120 MHz, 300 MHz, 670 MHz, 1277 MHz, and 2200 MHz. Each experimental curve has been plotted with zero laser detuning at its centre; in reality, the central frequency of each curve was different due to pressure shifting of the energy levels. $T = 285^{\circ}\text{C}$, $B = 0.02 \text{ T}$, heatpipe c.

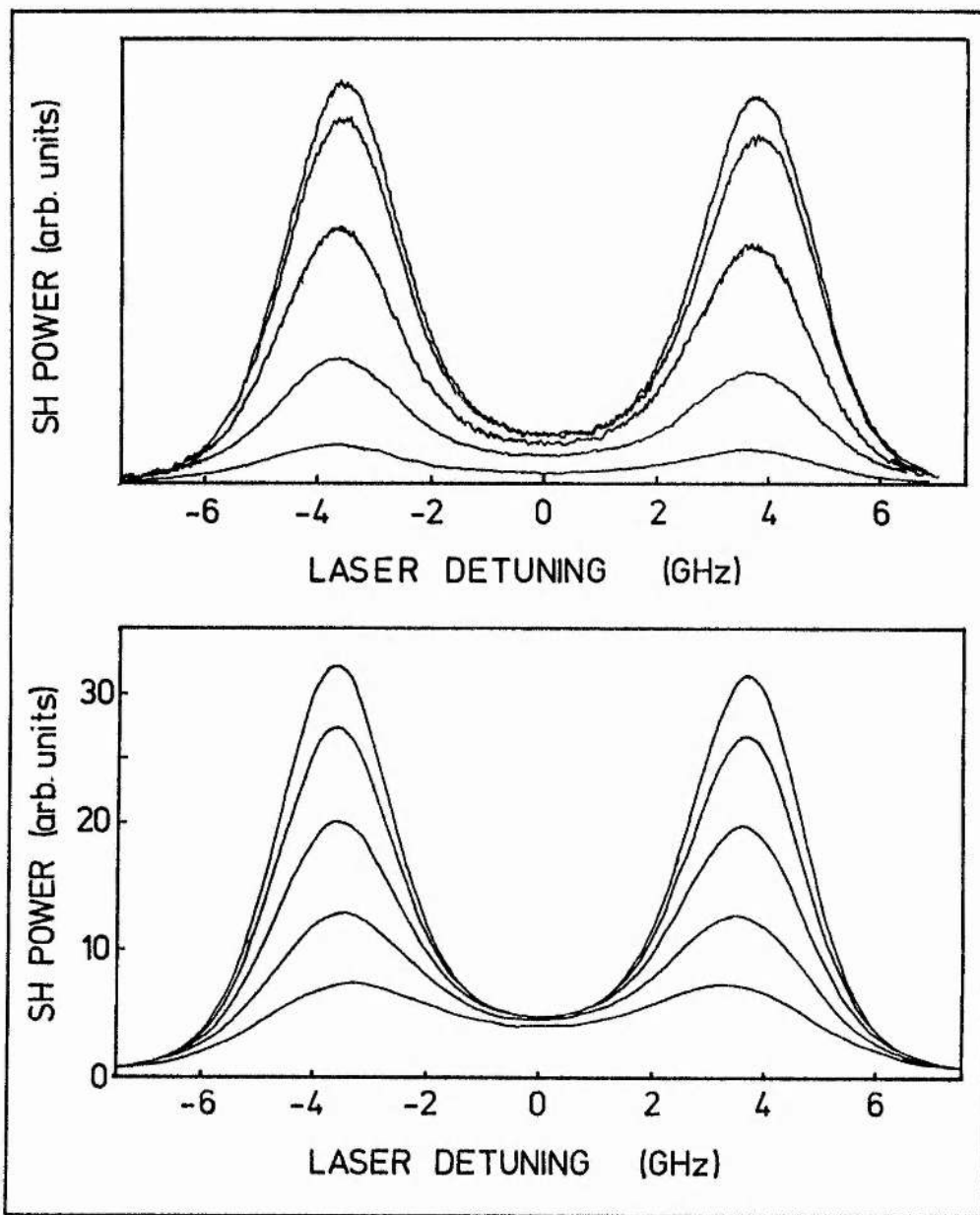


Figure 5.8.5. (a) Experimentally and (b) theoretically calculated variation of second harmonic power with laser frequency at different values of buffer gas pressure as listed in figure 5.8.4, but with a 0.275 T magnetic field. $T = 285^{\circ}\text{C}$, heatpipe c.

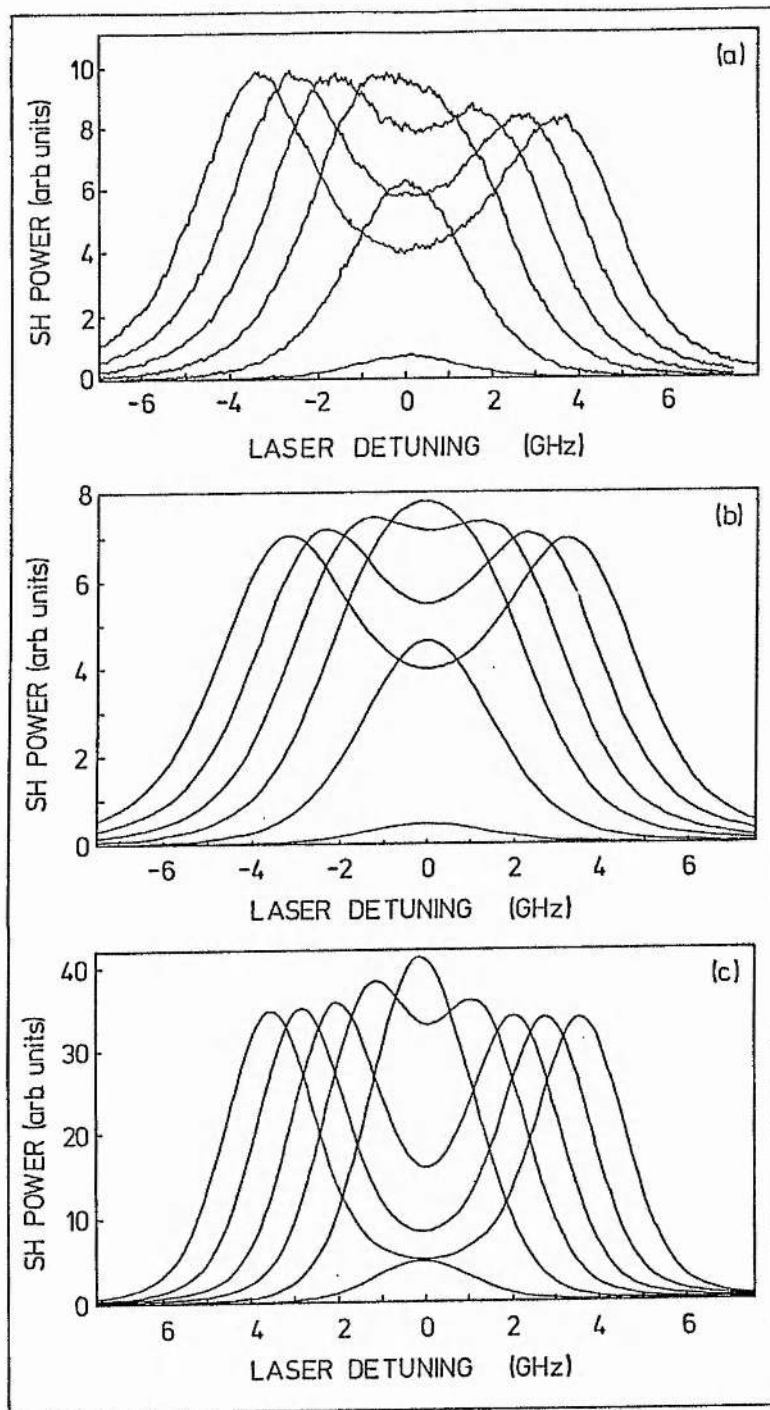


Figure 5.8.6. (a) Experimentally and (b) theoretically obtained variation of the SH power with laser frequency, with 109 mbar argon buffer gas, and at magnetic fields of 0.018 T (the curve with the lowest maximum), 0.068 T, 0.123 T, 0.17 T, 0.218 T, and 0.268 T (the curve with the greatest maximum). $T = 285^{\circ}\text{C}$, heatpipe c. Part (c) show the theoretically calculated line profiles with 1 mbar of buffer gas, but otherwise the same conditions.

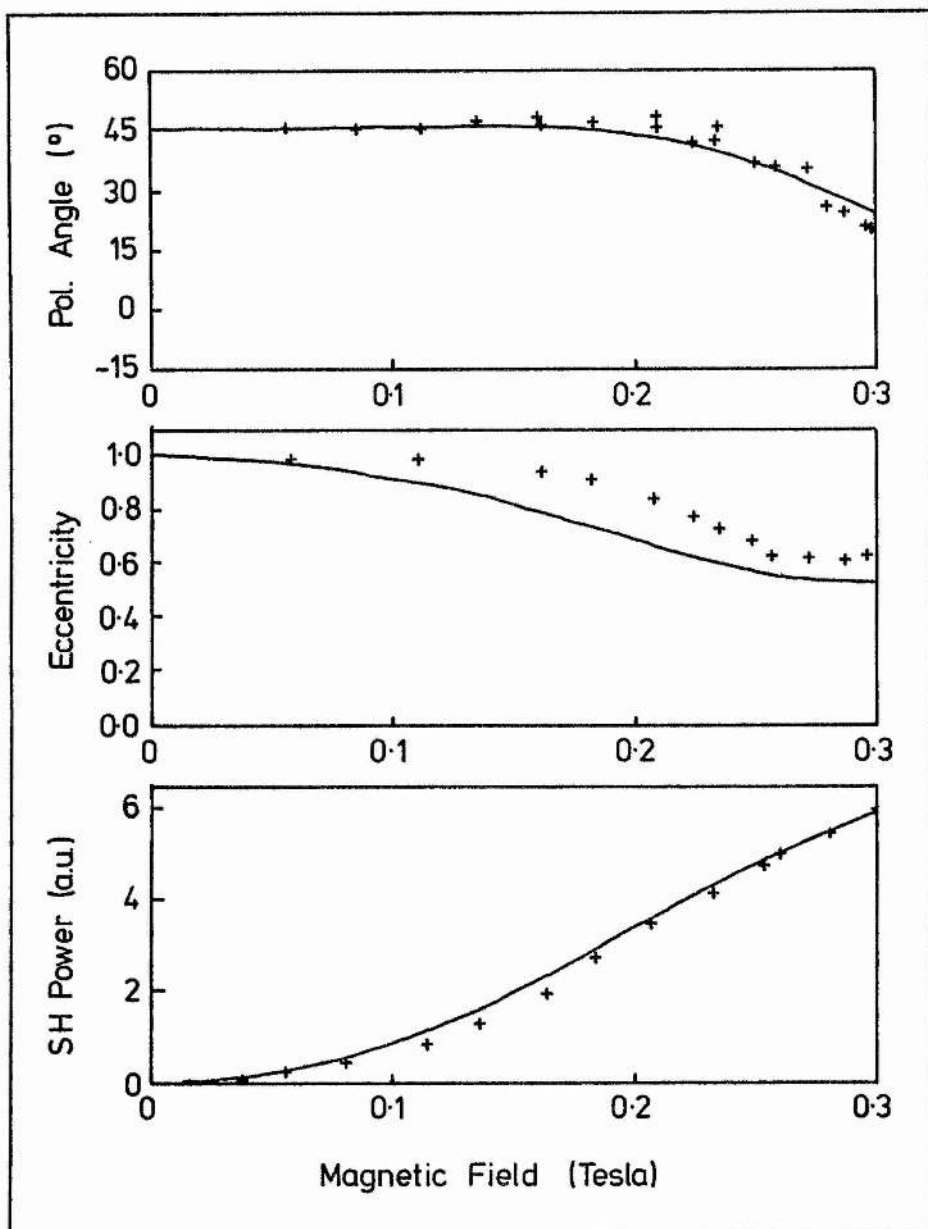


Figure 5.8.7. Power and polarisation properties of the second harmonic radiation as functions of the magnetic field strength, at a buffer gas pressure of 109 mbar ($\nu_{ds} = 2130$ MHz). The magnetic field was at 45° to the laser polarisation, and the laser was tuned to $\nu_0 + 3$ GHz. The curves are theoretically calculated, the curve in part (a) was normalised to have the same maximum as the experimental results. $T = 285^\circ\text{C}$, heatpipe c.

5.9 USE AS A PARTICLE DENSITY PROBE

In the SHG experiments described in the previous sections the second harmonic is generated only in the volume in which the laser beam and magnetic field cross. At relatively low particle densities (that is densities well below the first peak in the relationship between SH power and particle density) the amount of SH generated in such a volume is proportional to the square of the atomic density. Thus measurement of the SH power as the laser beam and a localised magnetic field are moved around would allow a three dimensional mapping of the atomic density to be performed [18].

For such a technique to be useful the magnetic field must be restricted to a relatively small fraction of the length of the region occupied by the vapour. This was achieved using the permanent magnets described in section 4.3.2, but mounting them in stacks tipped by conical polepieces. At the relatively low magnetic field produced at the centre of the polepieces (0.02 T), the SHG efficiency was proportional to the square of the magnetic field strength; the spatial distribution of the SHG efficiency was thus calculated to be as shown in figure 5.9.1.

This magnet assembly was set up across the relatively long heatpipe shown in figure 4.4.3(e). The laser beam was focussed into the pipe with a 0.53 m focal length lens, and the SH was detected as described previously. The peak SHG efficiency occurred when the thermocouple on the outside surface of the heatpipe read 330°C; the experiments were performed at 273°C. The oven was moved relative to the apparatus, thus removing problems such as the spatially non-uniform response of the photomultiplier tube which would have had to have been considered if the laser beam had been moved.

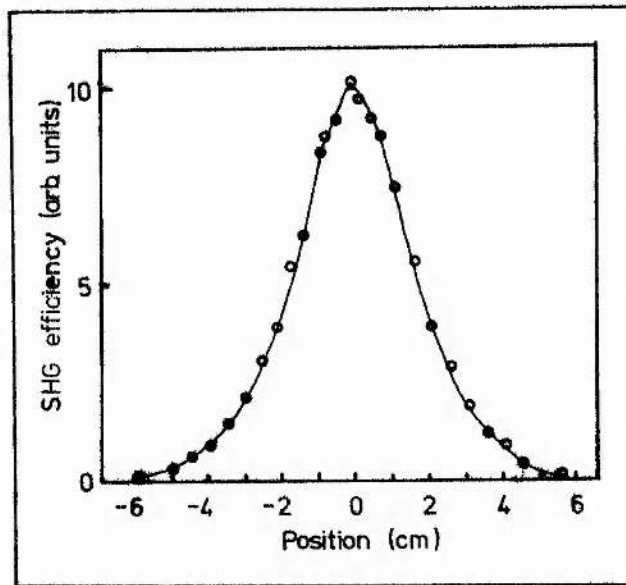


Figure 5.9.1. SHG efficiency as a function of position along the heatpipe. Position 0.0 corresponds to a position in the centre of the magnet's polepieces.

Even with the efforts made to minimise the spatial extent of the magnetic field, the SHG efficiency was greater than half maximum over 34 mm, so the sample length examined by this technique was large. The results for a scan along the axis of the pipe at a buffer gas pressure of 0.02 mbar are shown in figure 5.9.2. The restriction of the sodium vapour to the central region of the pipe is evident, but it is not possible to determine a detailed particle density distribution due to the long sample length. However, it can be seen that the pipe is not operating in a true heatpipe mode, as two peaks are seen in the SH power, corresponding to peaks in the sodium atom density.

The pipe was then moved so that the magnet was in the centre of the vapour zone. Horizontal and vertical movement of the pipe produced the results shown in figure 5.9.3. Although the SH is generated in a relatively large length along the beam, the SHG occurs only across the width of the beam,

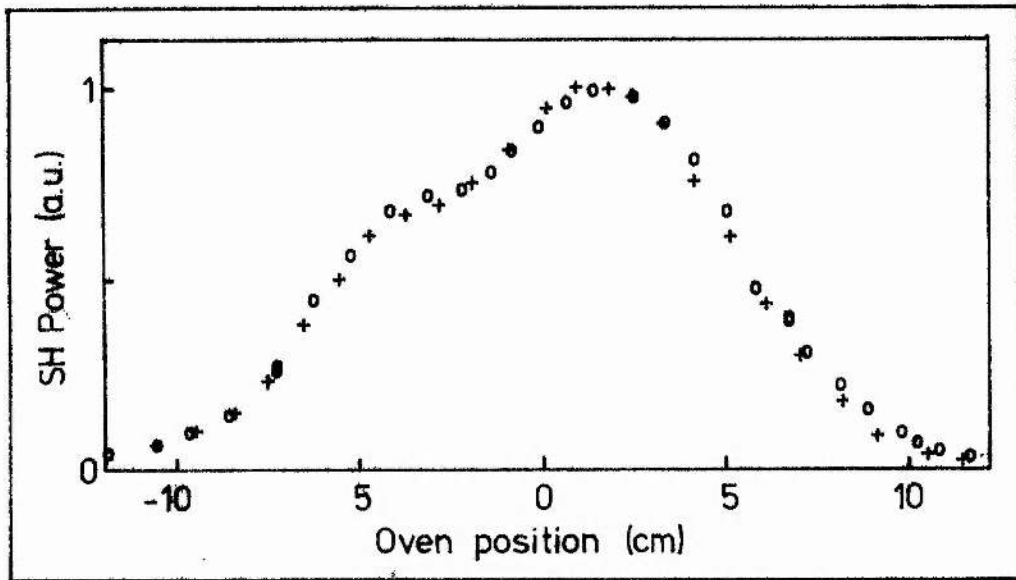


Figure 5.9.2. SH power measured as a function of the position of the intersection region of the laser beam and magnetic field in the oven; the oven was being moved in the direction of the laser beam.

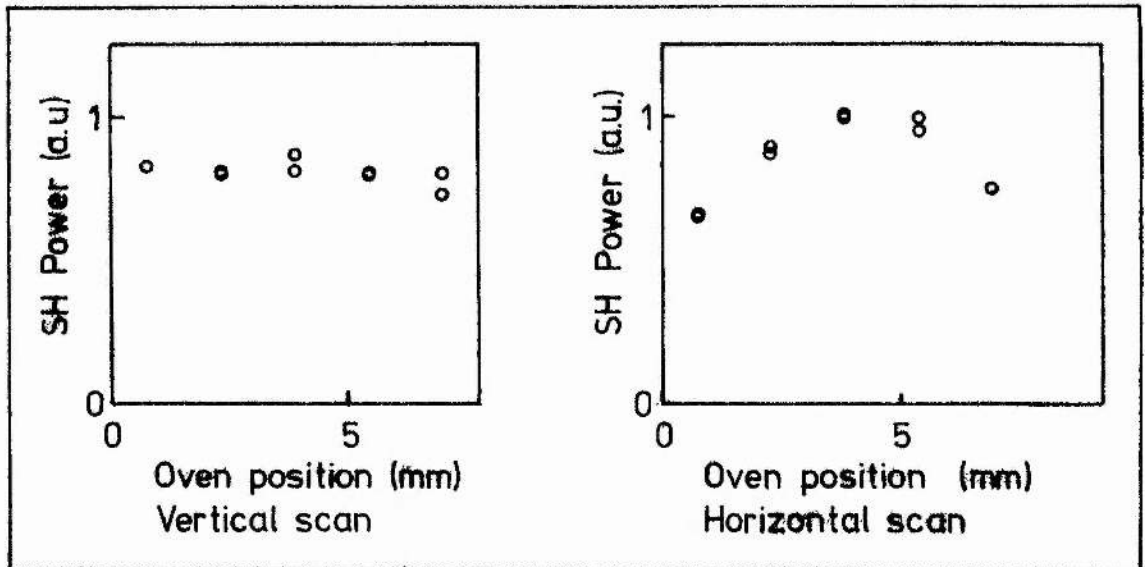


Figure 5.9.3. SH power measured as functions of the position of the intersection region of the laser beam and the magnetic field in the oven; the oven was moved in the directions indicated.

which is less than 1 mm. The scans in figure 5.9.3 therefore show in some detail transverse variations in atomic density. The atomic distribution seems to be constant in the vertical plane through the centre of the pipe, but there are significant variations in the atomic density in the horizontal plane through the centre of the pipe. Obviously a series of such measurements would allow a detailed mapping of the atomic density distribution in the oven.

Similar ideas were used in testing the stability of the FGH temperature control apparatus. The oven of figure 4.3.3(c) was again run at a temperature well below the first phase match peak, but with a magnetic field along the full length of the oven. The oven was brought up by the controller to a temperature of 290 °C (read by the thermocouple embedded in the oven wall), then the temperature set-point of the controller was increased to 300 °C. Figure 5.9.4 shows the slight overshoot in oven temperature as the controller raised the oven temperature to the new set-point. The stability of the oven temperature at this set-point was determined from the variation in the SH power measured for time greater than ten minutes. From equation 4.3.1 and the fact that the second harmonic power is proportional to the square of the sodium atom density, it can be shown that the fractional change in SH power dP_{2w}/P_{2w} is

$$\frac{dP_{2w}}{P_{2w}} = -2 \left(1 - \frac{12423.3}{T}\right) \frac{dT}{T} \quad (5.9.1)$$

where T is the absolute temperature of the vapour. Thus as the variation in P_{2w} was measured to be 3%, the variation in temperature was 0.07%, or 0.4 C.

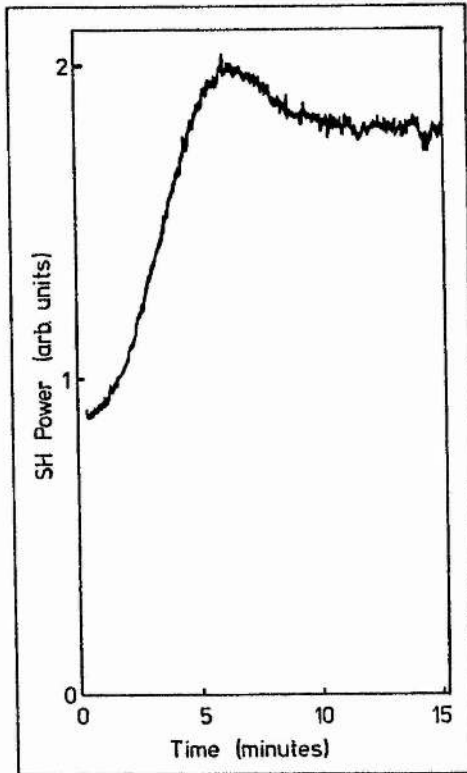


Figure 5.9.4. SH power as a function of time, when the FGH temperature controller was reset at time zero from 290 °C to 300 °C.

6

SUMMARY
AND
FINAL DISCUSSION

CHAPTER SIX

SUMMARY AND FINAL DISCUSSION

6.1 SUMMARY

The role of the 3S - 4D two-photon transition in enhancing magnetic-field-induced second harmonic generation in sodium vapour has been studied in detail, using a single-frequency laser. A theoretical model has been developed which includes the effects of atomic selection rules, Zeeman splitting, the mixing of atomic eigenfunctions in a magnetic field, and homogeneous and inhomogeneous broadening mechanisms.

Experimental measurements of the usual basic properties of second harmonic generation (SHG) were as expected; the second harmonic (SH) power varied as the square of the fundamental power over the range of power densities used ($\sim 10^5$ to 10^7 Wm^{-2}) and the width of the SH gaussian beam was $1/\sqrt{2}$ that of the fundamental.

The SH power was measured to be proportional to the square of the sodium atom density at low particle densities, but this relationship broke down above $10^{20} \text{ atoms m}^{-3}$ as the difference in refractive index of the vapour at the wavelengths of the fundamental and the SH lead to a mismatching of the phase velocities of the two waves. This led to an oscillatory dependence of the SH power on the atomic density.

The theoretical model, which was developed in chapter three, was found to be in excellent agreement with experimental results as long as the homogeneous linewidth was less than the Doppler width. The properties of the

SH were first measured at approximately 300 °C and with 1 mbar of argon buffer gas.

No SHG was expected, or observed, when the magnetic field was zero, or was orientated parallel to the linear polarisation of the fundamental beam. An applied magnetic field induced Zeeman splitting in the atomic energy levels, and caused a change in the relative amounts of the $m_s = \pm 1/2$ components in the atomic wavefunctions. It was shown how this could lead to SHG, and that, as long as the Zeeman splitting was small compared to the Doppler width, the SH power depended on the square of the magnetic field. It was also shown how two perpendicular quadrupole moments could act as "effective dipoles" for the SHG, one enhanced by $\Delta m_l = \pm 2$ two-photon transitions, the other by $\Delta m_l = \pm 1$ two-photon transitions. The experimental line profiles of SHG and two-photon absorption were compared and contrasted; SHG occurred only within the line profile of the resonantly enhancing two-photon absorption, but was not enhanced by the $\Delta m_l = 0$ transitions. The line profiles due to the two effective dipoles were similar at low magnetic fields (~ 0.02 T). However, in higher fields, in which Zeeman splitting was comparable to the Doppler width, these line profiles were significantly different, due to large differences in the amount of resonant enhancement afforded to the two effective dipoles. The different dependences of the magnitudes and phases of the two effective dipoles on magnetic field strength also led to other effects. For example, when both effective dipoles were driven, polarisation rotation and deviation from linear polarisation of the SH resulted; the amount of each was dependent on the magnetic field strength and the laser frequency. Also, at magnetic fields below 0.05 T the SH power was dependent on the square of the sine of the angle between the direction of linear polarisation of the fundamental and the magnetic field, but a more complicated dependence was predicted and observed at higher magnetic field strengths.

The effects of altering the vapour temperature were studied, but few changes were observed apart from those due to the associated change in sodium atomic density. Raising the pressure of the argon buffer gas, however, produced significant changes in the SHG, due to the resulting decrease in the lifetime of the coherence between the 3S and 4D wavefunctions. The peak SH power was expected to decrease as the fourth power of the homogeneous linewidth when the homogeneous linewidth was much greater than the Doppler width. Experimentally, however, the SH power was seen to drop somewhat more rapidly. This disagreement certainly requires further investigation. Raising the buffer gas pressure also caused an increase in the width of the SHG line profiles; good agreement between theory and experiment was obtained for a family of line profiles taken at a buffer gas pressure of 109 mbar. When both effective dipoles were driven, magnetic-field-dependent rotation of the SH polarisation and deviation from linear polarisation of the SH were observed, though, as expected, the magnitudes of these effects were less than in the low pressure case.

The phase difference between the second harmonic and the fundamental radiation was expected to be dependent on the magnetic field strength and the laser frequency. This phase difference was involved in the asymmetry of the SH line profiles in high magnetic fields. The magnetic field that was used was inhomogeneous, which, although it was a defect in the experimental arrangement, gave rise to the asymmetries of the line profiles, the investigation of which led to interesting insights into the SHG process. In a magnetic field gradient the phase of the generated SH changes with position, and this phase change may act to enhance or reduce the effects of the phase velocity mismatch of the fundamental and SH beams. In high magnetic fields the phase of the SH is an odd function of laser detuning from the centre of the two photon transition; thus, in a

magnetic field gradient, the low frequency components of the SHG could be enhanced while the high frequency components were reduced, leading to the observed asymmetries in the line profiles. These ideas led to the suggestion of tailoring the magnetic field to produce specific effects. For example, since a reversal of the magnetic field changes the SH polarisation by 180° , a spatially alternating magnetic field could be used to produce pseudo-phase-matching similar to that used for electric-field-induced SHG by Shelton and Buckingham [39].

The final section of chapter five showed one possible application for magnetic-field-induced second harmonic generation, the production of a three dimensional map of the particle density in a vapour. SHG occurs only in the volume of overlap of the magnetic field and the laser beam, and the magnetic field in any such region is proportional to the square of the sodium density.

Throughout the study, much better agreement was obtained between experiment and theory when the homogeneous and inhomogeneous linewidths were modelled separately instead of just using a damping constant related to the Doppler width [97]. The use of a single frequency laser and an atomic nonlinear medium allowed an experimental investigation of a second harmonic generation process in great detail, providing a stringent test of the model that was developed to predict the properties of the nonlinear effect in terms of fundamental atomic parameters. Apart from some discrepancies at high buffer gas pressures, the model agreed remarkably well with the experimental results.

6.2 RELEVANT FUTURE WORK

The experimental work reported in this thesis has concentrated on the basic physics of magnetic-field-induced second harmonic generation in sodium vapour. The applicability of the model has been confirmed over almost all the experimental conditions used. The conversion efficiency, though small, was quite sufficient to allow such a study to be undertaken. However, in this wavelength region and at the power densities used, the use of a nonlinear crystal such as potassium-dihydrogen-phosphate would allow much more efficient generation of second harmonic. Possible uses for magnetic-field-induced SHG in vapours are more likely to occur at wavelengths at which crystals are not transparent, so any extension of this work should look at the possibility of using other vapours or gases to generate coherent radiation below 200 nm.

Increases in tunability and conversion efficiency are also desirable. The first may come from using a molecular medium, in which there are many closely spaced allowed two-photon transitions which may be able to enhance the SHG, though care must be taken to select levels that are magnetically active, and which do not have high pressure broadening constants. Though such a medium is unlikely to be obtainable for continuously tunable SHG, line tunability should be possible. The most obvious means to increase the efficiency of the SHG is to increase the power density of the fundamental beam (as the efficiency is proportional to the power density of the fundamental laser beam), though to ensure good efficiency the linewidth of the laser should not be much greater than that of the SHG line profile. The maximum useful power density would be limited by processes such as multi-photon ionisation [10]. Higher power densities may be achieved in any of the following ways:- i) by using a higher power, possibly pulsed, laser, ii) by locating the doubling medium inside the laser cavity [8]

where the circulating radiation field is usually substantially larger than the field that is transmitted through the output coupler, and iii) by locating the vapour in an external, resonant, cavity which is locked to the laser frequency [139], which would again produce a high circulating fundamental radiation field.

The SH power is dependent on the square of the sodium atom density, N , as long as the phase velocity mismatch of the SH and fundamental beams is sufficiently small that the SH generated at different points in the vapour contributes to the second harmonic wave in phase. In the experiments reported in this thesis it was found that this relationship broke down at relatively low particle densities (3×10^{20} atoms m^{-3}). If some means of compensating for the dispersion caused by the sodium D lines was available, the N^2 dependence could be extended to higher atom densities, and thus much more efficient SHG could be achieved. Phase matching of third harmonic generation in metal vapours has been reported [14, 124, 140]; by choosing the correct ratio of concentrations of the nonlinear medium and another gas or vapour with the opposite change in refractive index between the two wavelengths of interest, a mixture could be produced which allowed phase matched third harmonic generation. A search was made for possible media to use to phase match SHG in sodium; it was calculated that a 10:1 ratio of calcium:sodium or 70:1 aluminium:sodium should produce phase matched SHG. Although it would be difficult to construct and operate a system in which the vapour pressures of the two atomic species could be varied independently, the heat pipe oven variant described by Bloom et al [140] should have the desired properties. The other possibility would be to use a spatially oscillating magnetic field to achieve pseudo-phase-matching as mentioned earlier in this chapter.

APPENDICES

- A** Plasma Dispersion Function
- B** Computer programs for modelling the second harmonic generation
- C** Computerised system for data collection and analysis
- D** Computer programs for data collection and analysis
- E** Spectroscopic study of the sodium dimer

APPENDIX A

The Plasma Dispersion Function

The plasma dispersion function occurs frequently in modelling damped systems which contain a Maxwellian velocity distribution. The integral

$$Z = \int_{-\infty}^{\infty} \frac{\exp[-mv_y^2/2k_B T] dv_y}{w_{ds} + kv_y - 2w - i\gamma_{ds}} \quad (\text{A.1})$$

must be evaluated to solve equations such as 3.2.55, where w_{ds} is the frequency of the 3S - 4D transition when the sodium atom is at rest, w is the laser frequency, γ_{ds} is the HWHM due to natural and pressure broadening, and v_y is the atomic velocity in the y direction. Equation A.1 may be rearranged to be proportional to the standard form of the plasma dispersion function

$$Z(K) = \pi^{-1/2} \int_{-\infty}^{\infty} \frac{\exp[-t^2] dt}{t - K}, \quad (\text{A.2})$$

where K and Z are complex, and t is real. $K = x + iy$, where $x = (2w - w_{ds})/\Omega$, and $y = \gamma_{ds}/\Omega$; Ω is the Doppler width of the transition, as defined in equation 3.2.57. The methods of Fried and Conte [115] were used to solve this integral.

For $y < 1$, numerical integration of the differential equation defining the plasma dispersion function was appropriate. The function may be characterised by the differential equation and boundary condition

$$Z' = -2(1 + KZ) \quad \text{for all } K, K \text{ complex}, \quad (\text{A.3})$$

$$Z(0) = i\pi^{1/2}. \quad (\text{A.4})$$

The University's VAX 11/785 mainframe computers have various numerical

routines in the "NAG" library suitable for solving real differential equations. Thus equation A.3 was split into its real and imaginary parts. Defining $Z = Z_R + iZ_I$, A.3 becomes

$$Z' = -2([1 + xZ_R - yZ_I] + i[yZ_R + xZ_I]); \quad (\text{A.5})$$

and by definition

$$Z' = \frac{dZ}{dK} = \frac{dZ}{d(x+iy)} = \frac{\partial Z}{\partial x} \frac{\partial x}{\partial K} + \frac{\partial Z}{\partial y} \frac{\partial y}{\partial K}. \quad (\text{A.6})$$

But $\partial K/\partial x = 1$ and $\partial K/\partial y = i$, so

$$Z' = \partial Z/\partial x - i\partial Z/\partial y \quad (\text{A.7})$$

$$= \partial Z_R/\partial x + \partial Z_I/\partial y + i(\partial Z_I/\partial x - \partial Z_R/\partial y). \quad (\text{A.8})$$

The real and imaginary parts are separated to obtain

$$\partial Z_R/\partial x + \partial Z_I/\partial y = -2(1 + xZ_R - yZ_I), \quad (\text{A.9})$$

$$\partial Z_I/\partial x - \partial Z_R/\partial y = -2(yZ_R + xZ_I). \quad (\text{A.10})$$

The NAG routines can cope with these two coupled real equations. To find $Z(x + iy)$ a numerical integration was performed from $(0 + i0)$ to $(0 + iy)$ with $x = 0$, then from $(0 + iy)$ to $(x + iy)$ with y constant to get the final solution for Z in terms of its real and imaginary parts. The NAG routine D02BAF was selected as being the most suitable. Its use is shown in Appendix B. To find the value of Z for negative x , the relationships

$$Z_R(x + iy) = -Z_R(-x + iy), \quad (\text{A.11})$$

$$\text{and } Z_I(x + iy) = Z_I(-x + iy) \quad (\text{A.12})$$

were used.

The above method of evaluation of the plasma dispersion function is not suitable for large values of y due to the accumulation of truncation and round-off errors. Instead a method based on continued fractions was used when $y \geq 1$. The appropriate continued fraction, which may be derived from

the asymptotic form of the plasma dispersion function [115], is

$$Z(K) = K \frac{1}{-K^2 + 1/2 + \frac{(-1)(1/2)}{-K^2 + 5/2 + \frac{(-2)(3/2)}{-K^2 + 9/2 + \frac{a_{n+1}}{b_{n+1} + \frac{a_{n+2}}{\dots}}}}} \quad (\text{A.13})$$

where $a_1 = K,$ (A.14)

$a_{n+1} = -n(2n - 1)/2$ for $n = 1, 2, \dots,$ (A.15)

and $b_{n+1} = -K^2 + 1/2 + 2n$ for $n = 0, 1, \dots,$ (A.16)

The continued fraction may be evaluated [141] by the recursion relations

$$A_{n+1} = b_{n+1}A_n + a_{n+1}A_{n-1} \quad (\text{A.17})$$

and $B_{n+1} = b_{n+1}B_n + a_{n+1}B_{n-1}$ (A.18)

where $A_{-1} = 1, \quad A_0 = 0,$)
 $B_{-1} = 0, \quad B_0 = 1,$) (A.19)

and $Z(K) = \lim_{n \rightarrow \infty} \frac{A_n}{B_n} \quad y > 0$ (A.20)

The Fortran subroutine "CONTFRAC" was incorporated in the computer program shown in appendix B to evaluate Z using these recursion relations.

Negative values of x were dealt with in the same way as in the method for $y < 1.$

The results of the computer code were compared with selected values quoted by Fried and Conte [115], and with each other in the region where both methods were valid, ie at $y = 1.$ The values obtained agreed to at least five decimal places in all the cases tested.

The values of the real and imaginary parts of $Z(a + ib)$ are shown in figure A.1 as functions of a , at two values of b . The values of b have been chosen to correspond to the experimental situations: a vapour temperature of 300°C ($\Omega = 2.2$ GHz) in both cases, with (a) $\gamma_{\text{ds}} = 35$ MHz and (b) $\gamma_{\text{ds}} = 2180$ MHz.

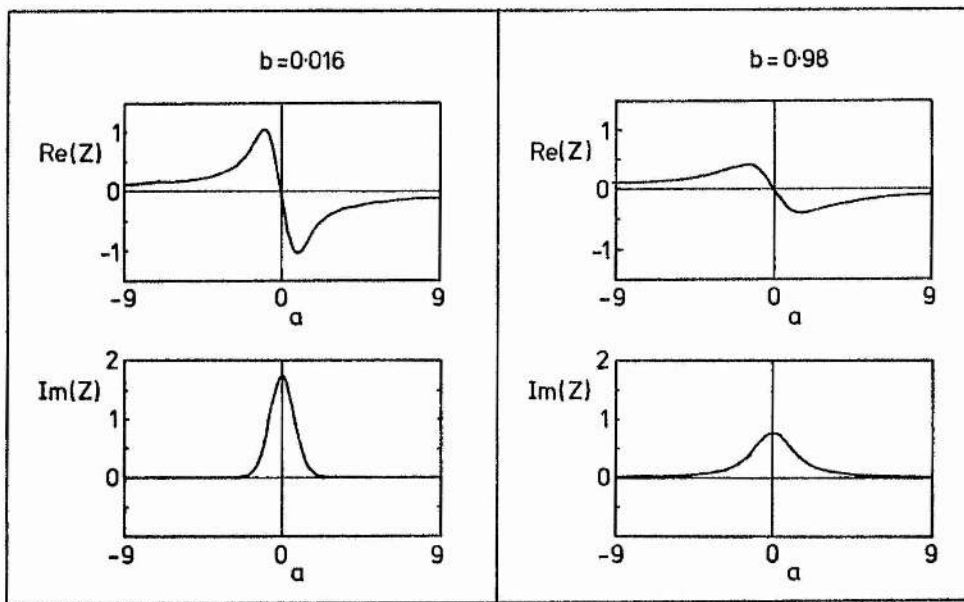


Figure A.1. The real and imaginary parts of the plasma dispersion function plotted as functions of a (the real argument of the function), at two values of b (the imaginary argument of the function).

APPENDIX B

PROGRAMS FOR NUMERICAL MODELLING OF THE SECOND HARMONIC GENERATION

This appendix contains an example of one of the computer programs used to calculate the properties of the SHG using the theoretical modelling described in chapter three. The first program that is listed here was used to generate data files which contained the values of the quadrupole moments at a number of different frequencies across the line profile, at a magnetic field, vapour temperature, and χ_{ds} specified by the user. The second program was used to calculate the line profiles of the SHG from the data in the file produced by the first program.

FORTRAN PROGRAM USED TO CALCULATE LINE PROFILES

This program requires routines from the "NAG" library of numerical routines, so the compiled version of the program must be "linked" with the NAG library.

```
C  BDS 30.7.86  LPGEN.FOR
C  PRODUCES VALUES OF QUADRUPOLE MOMENTS AT SPECIFIED FIELD
C  OVER A RANGE OF LASER FREQUENCIES
C  Contains plasma dispersion function evaluation by
C  numerical integration of differential equation for small
C  homogeneous linewidth, and by method based on continued fractions
C  for larger homogeneous linewidth.
C  To run, first compile and then LINK LPGEN,NAG/LIB

C  F,MF Quantum numbers of lower state
C  JS,MJS Substitute quantum numbers of 4d state:
C
C  JS=J+0.5      MJS=MJ+0.5
C
C  So J          1.5                2.5
C     MJ -1.5 -0.5 0.5 1.5   -2.5 -1.5 -0.5 0.5 1.5 2.5
C
C  become
C
```

```

C          JS          2          3
C          MJS -1      0      1      2      -2      -1      0      1      2      3
C
C          MJS=1-JS to JS
C
C          IMPLICIT NONE
C          declare subroutines involved in plasma dispersion function
C          EXTERNAL PLASMAX,PLASMAY,CONTFRAC
C          declare other variables, including:-
C          H              - magnetic field strength
C          W108           - laser frequency in 100 MHz units
C          ES(F, mF, H)   - energy of S states
C          SAS(F, mF, H)  - spin +1/2 component of S states
C          SBS(F, mF, H)  - spin -1/2 component of S states
C          ED(JS, MJS, H) - energy of D states
C          DAPH(JS, MJS, H) - spin +1/2 component of D states
C          DBPH(JS, MJS, H) - spin -1/2 component of D states
C          QRX(H)         - real part of xy quadrupole moment
C          QIX(H)         - imaginary part of xy quadrupole moment
C          QRZ(H)         - real part of zy quadrupole moment
C          QIZ(H)         - imaginary part of zy quadrupole moment
C
C          REAL ES(1:2,-2:2,0:3100)
C          REAL SAS(1:2,-2:2,0:3100)
C          REAL SBS(1:2,-2:2,0:3100)
C          REAL DAPH(2:3,-2:3,0:3100)
C          REAL DBPH(2:3,-2:3,0:3100)
C          REAL ED(2:3,-2:2,0:3100)
C          REAL ISH(2000),GRAPHX(200),GRAPHY(200)
C          REAL SH(0:500)
C          REAL QRX(0:3100),QRZ(0:3100),QIX(0:3100),QIZ(0:3100)
C          REAL QRXMAX,QRZMAX,QIXMAX,QIZMAX
C          REAL B1,B2
C          REAL Y,DA,DB,J,MJ,ROO,N,K
C          REAL SUM,SA,SB
C          REAL ISHMAX
C          REAL A,B,C,CAPA,E,SIG
C          REAL HP,HR
C          REAL GAMDS,GAMDS2,W,W2
C          REAL DENOM,DELTA,SUMRX,SUMRZ
C          REAL SUMIX,SUMIZ
C          REAL SINTH,COSTH,THETA
C          REAL TC,T,OMEGA,XEND4,YEND4,IMAG,ZR,ZI
C          REAL DELTAO
C          REAL*8 YEND
C          COMMON YEND
C          REAL*8 ZMID(2)
C          INTEGER GAMDSI,VI
C          INTEGER W108,BDH
C          INTEGER I,H,F,MF,MJS,JS
C          INTEGER FILESTART,FILEEND,FILEINT
C          INTEGER COUNT,NOPOINTS
C          CHARACTER*15 NME
C
C          Constants
C
C          Hyperfine Splitting Constant
C          CAPA=885.813E6
C          Fine Splitting Constant

```


K=-4.112E8

C Ground state energy levels ES and components of wave-
C functions SA and SB.

```
DO 52 F=1,2
DO 50 MF=-F,F
DO 40 H=0,3100,5
A=(CAPA*MF+2.0028*1.399E6*H)/2
B=-CAPA/4-MF*0.0008*1.399E6*H
C=CAPA*((2-MF)*(2+MF))*0.5/2
IF (F.EQ.1) SIG = -1
IF (F.EQ.2) SIG = 1
IF (MF.EQ.-2 .AND. A.GT.0.0) SIG = -1
E=B+SIG*(A**2+C**2)**0.5
ES(F,MF,H) = E
SUM=SIG*(A**2+C**2)**0.5
DENOM=((A+SUM)**2+C**2)**0.5
IF (DENOM.NE.0) GOTO 30
SA=0
SB=1
GOTO 35
30 SA=(A+SUM)/DENOM
SB=C/DENOM
35 SAS(F,MF,H) =SA
SBS(F,MF,H) =SB
40 CONTINUE
50 CONTINUE
52 CONTINUE
```

C 4D wavefunction components DAPH and DBPH

```
DO 59 H=0,3100, 5
DAPH(3,3,H)=1
DAPH(3,-2,H)=0
DBPH(3,3,H)=0
DBPH(3,-2,H)=1
59 CONTINUE
DO 70 JS=2,3
IF (JS.EQ.2) N= -1
IF (JS.EQ.3) N= 1
DO 65 MJS = -1,2
MJ=MJS-0.5
DO 60 H=0,3100, 5
Y=-3.41E-3*H
ROO=MJ+Y+N*(Y**2+2*MJ*Y+6.25)**0.5
DENOM=((2.5+MJ)*(2.5-MJ)+(ROO**2))
IF (DENOM.EQ.0) DENOM = 1.0E-20
DAPH(JS,MJS,H)=ROO/(DENOM**0.5)
DBPH(JS,MJS,H)=((2.5+MJ)*(2.5-MJ)/DENOM)**0.5
60 CONTINUE
65 CONTINUE
70 CONTINUE
```

C 4D state energy levels ED

```
DO 98 H=0, 3100, 5
Y=-3.41E-3*H
ED(3,3,H)=(1+3*Y)*K
```

```

ED(3,-2,H)=(1-3*Y)*K
DO 90 MJS=-1,2
MJ=MJS-0.5
R00=(4*Y**2+8*MJ*Y+25)**0.5
ED(3,MJS,H)=(-0.25+MJ*Y+0.25*R00)*K
ED(2,MJS,H)=(-0.25+MJ*Y-0.25*R00)*K
90 CONTINUE
98 CONTINUE

PRINT*,'Energy level calculations finished'
C START OF B BIT
C W108 integer frequency in 100 MHz units
C W real frequency in MHz
C W2 2 * W
C SUMRX real part of effective dipole summation in x
C SUMIX imaginary "
C GAMDS DS damping term
C QXR(W108) Real part of effective dipole in x at W108
C PLASMAX/Y Numerical Routines to evaluate Plasma Dispersion
C Function when imaginary part of argument < 1
C CONTFRAC used to evaluate plasma dispersion function when
C imaginary part of argument greater than or equal to 1
C
C COLLECTED CONSTANTS
C Natural linewidth HWHM
GAMDS=35.0E6
PRINT*,'NATURAL DAMPING, 35MHZ?'
READ*, GAMDS
C Temperature of vapour in Celsius
TC=360.0
PRINT*,'TEMPERATURE OF VAPOUR IN CELSIUS, 360?'
READ*,TC
C Temperature of vapour in Kelvin
T=TC+273.0
C Hence Doppler half width at 1/e point
OMEGA=9.27E7*SQRT(T)
C Imaginary part of plasma dispersion function argument
C =doppler width/homogeneous width
IMAG=GAMDS/OMEGA
C YEND is "common" throughout subroutines etc carrying double
C precision value of imaginary part of plasma dispersion function
C argument
YEND=DBLE(IMAG)
OMEGA=OMEGA*1.0
PRINT*,'FIELD?'
READ*, H
PRINT*,'FILENAME IN QUOTES?'
READ*, NME

NOPOINTS=0
IF (IMAG.LT.1.0) CALL PLASMAY(ZMID)

C values of quadrupole moments are filed as result of program
C in file specified by program user. Range of laser frequencies
C for which moments are calculated is defined by filestart,end,
C int, where units are in 0.1 GHz.

```

```

FILESTART=20
FILEEND=180
FILEINT=3
DO 495 W108=FILESTART,FILEEND,FILEINT
W=W108*1.0E8
W2=2*W
SUMRX =0.0
SUMRZ =0.0
SUMIX =0.0
SUMIZ =0.0

```

```

DO 490 F=1,2
DO 480 MF=-F,F
DO 470 JS=2,3
DO 460 MJS=1-JS,JS
MJ=MJS-0.5

```

```

IF (MJS.EQ.-2) THEN
  B2=(DBPH(JS,-2,H)*SBS(F,MF,H))**2
  B1= 0
ELSE IF (MJS.EQ.-1) THEN
  B2=(DAPH(JS,-1,H)*SAS(F,MF,H))**2
  B1=(DBPH(JS,-1,H)*SBS(F,MF,H))**2
ELSE IF (MJS.EQ.0) THEN
  B2=0
  B1=(DAPH(JS,0,H)*SAS(F,MF,H))**2
ELSE IF (MJS.EQ.1) THEN
  B2=0
  B1=-(DBPH(JS,1,H)*SBS(F,MF,H))**2
ELSE IF (MJS.EQ.2) THEN
  B2=-(DBPH(JS,2,H)*SBS(F,MF,H))**2
  B1=-(DAPH(JS,2,H)*SAS(F,MF,H))**2
ELSE IF (MJS.EQ.3) THEN
  B2=-(DAPH(JS,3,H)*SAS(F,MF,H))**2
  B1=0
ENDIF

```

C Real part of plasma dispersion function argument is
C calculated as XEND4

```

XEND4=(W2-ED(JS,MJS,H)+ES(F,MF,H)-2.0E10)/OMEGA
IF (IMAG.LT.1.0) THEN
  CALL PLASMAX(ZMID,XEND4,ZR,ZI)
ELSE
  CALL CONTFRAC(IMAG,XEND4,ZR,ZI)
ENDIF

```

```

SUMRX=SUMRX+ZR*B2
SUMIX=SUMIX+ZI*B2
SUMRZ=SUMRZ+ZR*B1
SUMIZ=SUMIZ+ZI*B1

```

```

400 CONTINUE
460 CONTINUE
470 CONTINUE
480 CONTINUE
490 CONTINUE

```

```

QRX(W108)=1.0E10*SUMRX/OMEGA
QRZ(W108)=2.0E10*SUMRZ/OMEGA
QIX(W108)=1.0E10*SUMIX/OMEGA
QIZ(W108)=2.0E10*SUMIZ/OMEGA

IF (QRX(W108).GT.QRXMAX) QRXMAX=QRX(W108)
IF (QRZ(W108).GT.QRZMAX) QRZMAX=QRZ(W108)
IF (QIX(W108).GT.QIXMAX) QIXMAX=QIX(W108)
IF (QIZ(W108).GT.QIZMAX) QIZMAX=QIZ(W108)
NOPOINTS=NOPOINTS+1
GRAPHX(W108)=W
495 CONTINUE

C      Filing values of curve produced
OPEN(UNIT=1,FILE=NME,STATUS='NEW')
WRITE (UNIT=1,FMT=601) GAMDS
WRITE (UNIT=1,FMT=601) OMEGA
WRITE (UNIT=1,FMT=600) H
WRITE (UNIT=1,FMT=600) NOPOINTS
WRITE (UNIT=1,FMT=601) QRXMAX,QRZMAX,QIXMAX,QIZMAX
WRITE (UNIT=1,FMT=604) FILESTART,FILEEND,FILEINT
DO 499 I=FILESTART,FILEEND,FILEINT
WRITE (UNIT=1,FMT=602) GRAPHX(I),QRX(I),QRZ(I),QIX(I),QIZ(I)
499 CONTINUE
600 FORMAT(I5)
601 FORMAT(4E12.5)
602 FORMAT(5E12.5)
604 FORMAT(3I6)
CLOSE (UNIT=1)
STOP
END

C      Numerical Integration Routines for Plasma Dispersion
C      Function

SUBROUTINE PLASMAX(ZMID,XEND4,ZR,ZI)
C      To integrate differential equation definition of Z
C      from (0,YEND) to (XEND,YEND) when YEND=IMAG < 1.0
C      ZMID holds real(1) and imaginary(2) values of Z(0,YEND)
C      Z holds real(1) and imaginary(2) values of Z(XEND,YEND)
C      ZReal(-X,Y)=-ZReal(X,Y), hence ZEROCH
C      Equations are of form QXY=iZ, so x+iy -> ix-y
C
IMPLICIT NONE
REAL ZR,ZI,XEND4
REAL*8 X,XEND,TOL,Y,ZEROCH
INTEGER IFAIL,N
REAL*8 W(2,7),Z(2),zmid(2)
EXTERNAL FCN1
ZEROCH=1.0
IF (XEND4.LT.0.0) THEN
XEND4=-1.0*XEND4
ZEROCH=-1.0
ENDIF
N=2
TOL=0.000005

```

```

X=0.0
XEND=DBLE(XEND4)
Z(1)=ZMID(1)
Z(2)=ZMID(2)
IFAIL=0
CALL D02BAF(X,XEND,N,Z,TOL,FCN1,W,IFAIL)
Z(1)=Z(1)*ZEROCH
ZR=-SNGL(Z(2))
ZI=SNGL(Z(1))
RETURN
END

```

```

SUBROUTINE PLASMAY(ZMID)
C      Numerical Integration of Differential Equation for Z
C      from (0,0) to (0,YEND)
C      Paired with plasmax
C

```

```

IMPLICIT NONE
REAL*8 Y,YEND,TOL
INTEGER IFAIL,N
REAL*8 W(2,7),Z(2),ZMID(2)
EXTERNAL FCN
COMMON YEND
N=2
TOL=0.000000001
Y=0.0
Z(1)=0.0
Z(2)=SQRT(3.1415927)
IFAIL=0
CALL D02BAF(Y,YEND,N,Z,TOL,FCN,W,IFAIL)
ZMID(1)=Z(1)
ZMID(2)=Z(2)
RETURN
END

```

```

SUBROUTINE FCN(T,Z,F)
C      Equations for integration along imaginary axis
C

```

```

REAL*8 T
REAL*8 F(2),Z(2)
F(1)=+2*(T*Z(1))
F(2)=-2*(1-T*Z(2))
RETURN
END

```

```

SUBROUTINE FCN1(T,Z,F)
C      Equations for integration along y=yend to (xend,yend)
C

```

```

REAL*8 T,YEND
REAL*8 F(2),Z(2)
COMMON YEND
F(1)=-2*(1+T*Z(1)-YEND*Z(2))
F(2)=-2*(YEND*Z(1)+T*Z(2))
RETURN
END

```

```

SUBROUTINE CONTFRAC(IMAG,XEND4,ZR,ZI)
C      To calculate Z by the continued fractions method
C      when YEND(=IMAG) > 1.0.

```

```

C      ZRC and ZIC hold real and imaginary parts of
C      Z(XEND4,IMAG). Final eqns are of form
C      QXY=iZ so x+iy -> ix-y
      IMPLICIT NONE
      REAL ZR,ZI,ZRC,ZIC,IMAG,XEND4,ZEROCH
      INTEGER n,I
      COMPLEX w
      COMPLEX AC(-1:40),BC(-1:40),a(-1:40),b(-1:40),ZC(-1:40)
      AC(-1)=(1.0,0.0)
      AC(0)=(0.0,0.0)
      BC(-1)=(0.0,0.0)
      BC(0)=(1.0,0.0)
      ZC(0)=0.0
      n=0
      ZEROCH=1.0
      IF (XEND4.LT.0.0) THEN
        XEND4=-1.0*XEND4
        ZEROCH=-1.0
      ENDIF
      w=CMPLX(XEND4,IMAG)
9930  IF (n.GT.4.AND.ABS((ZC(n)-ZC(n-1))/(ZC(n)+ZC(n-1))).LT.
z     0.000001) GOTO 9939
      IF ((n+1).EQ.1) THEN
        a(n+1)=w
      ELSE
        a(n+1)=-1.0*n*(2*n-1)/2
      ENDIF
      b(n+1)=-w**2+0.5+2*n
      AC(n+1)=b(n+1)*AC(n)+a(n+1)*AC(n-1)
      BC(n+1)=b(n+1)*BC(n)+a(n+1)*BC(n-1)
      ZC(n+1)=AC(n+1)/BC(n+1)
      n=n+1
      GOTO 9930
9939  CONTINUE
      ZRC=REAL(ZC(n))
      ZIC=AIMAG(ZC(n))
      ZRC=ZRC*ZEROCH
      ZR=-ZIC
      ZI=ZRC
      RETURN
      END

```

FORTRAN PROGRAM TO PLOT OUT LINE PROFILES

This program requires routines from the "GHOST" graphics package, and so the compiled version of this program must be linked with the appropriate GHOST libraries.

```
C      BDS 6.86 PTGEN.FOR
C      Reads data from files generated by LPGEN to produce
C      line profiles of SHG process. In this case the line profiles
C      of the Z and X effective dipoles are plotted for the case of
C      the fundamental polarisation at 45 degrees to the magnetic field.
C      The other curve is the line profile expected if a linear
C      polariser were placed in the SH beam at 45 degrees to the
C      magnetic field.
C      To run, compile then LINK PTGEN,GHOST/LIB,GRID/LIB
C      graphical output will appear in DEFAULT.GRD. To examine
C      graphical output type T4010 at VAX command level and follow
C      question and answer sequence.
```

```
IMPLICIT NONE
REAL QRXMAX,QIXMAX,QRZMAX,QIZMAX
INTEGER FILESTART,FILEEND,FILEINT
REAL GRAPHAMAX,GRAPHBMAX,GRAPHCMAX
REAL GAMDS,OMEGA,ISHMAX
REAL GRAPHX(200),GRAPHA(200),GRAPHB(200),GRAPHC(200)
REAL QRX(200),QIX(200),QRZ(200),QIZ(200)
INTEGER H,J,I,NOPOINTS
INTEGER REP
CHARACTER*15 NME
```

```
C      Obtain filename
```

```
100  PRINT*, 'FILE?'
      READ 2, NME
2     FORMAT(A15)
```

```
C      Set up Ghost graphics package
```

```
CALL PAPER(1)
CALL AXNOTA (1)
CALL PSPACE(0.08,0.948,0.2,0.672)
CALL BORDER
```

```
C      Read file contents into appropriate arrays
```

```
OPEN (UNIT=1,FILE=NME,STATUS='OLD')
READ (UNIT=1,FMT=601) GAMDS
READ (UNIT=1,FMT=601) OMEGA
READ (UNIT=1,FMT=600) H
READ (UNIT=1,FMT=600) NOPOINTS
READ (UNIT=1,FMT=601) QRXMAX,QRZMAX,QIXMAX,QIZMAX
READ (UNIT=1,FMT=604) FILESTART,FILEEND,FILEINT
I=0
DO 499 J=FILESTART,FILEEND,FILEINT
I=I+1
READ (UNIT=1,FMT=602) GRAPHX(I),QRX(I),QRZ(I),QIX(I),QIZ(I)
499  CONTINUE
CLOSE(UNIT=1)
600  FORMAT(I5)
```

```
601  FORMAT(4E12.5)
602  FORMAT(5E12.5)
604  FORMAT(3I6)
9898  CONTINUE
```

```
C      Plot out the three line profiles on the same scale,
C      with the scale chosen to place the greatest maximum
C      at 0.9 of the way up the vertical axis.
```

```
      GRAPHAMAX=0.0
      DO 328 I=1,NOPOINTS
      GRAPH(I)=QRX(I)**2+QIX(I)**2
      IF (GRAPH(I).GT.GRAPHAMAX) GRAPHAMAX=GRAPH(I)
328   CONTINUE
      GRAPHBMAX=0.0
      DO 329 I=1,NOPOINTS
      GRAPHB(I)=QRZ(I)**2+QIZ(I)**2
      IF (GRAPHB(I).GT.GRAPHBMAX) GRAPHBMAX=GRAPHB(I)
329   CONTINUE
      GRAPHCMAX=0.0
      IF (GRAPHAMAX.LT.GRAPHBMAX) GRAPHAMAX=GRAPHBMAX
      IF (GRAPHAMAX.LT.GRAPHCMAX) GRAPHAMAX=GRAPHCMAX
      CALL MAP(0.25E10,1.75E10,0.0,GRAPHAMAX*1.1)
      CALL SCALES
```

```
      CALL BROKEN (10,10,10,10)
      CALL CURVE0(GRAPHX,GRAPHA,1,NOPOINTS)
      CALL CURVE0(GRAPHX,GRAPHB,1,NOPOINTS)
      CALL CURVE0(GRAPHX,GRAPHC,1,NOPOINTS)
      CALL FRAME
      CALL GREND
```

```
STOP
END
```


APPENDIX C
COMPUTERISED SYSTEM FOR DATA COLLECTION AND ANALYSIS

All the line profiles shown in this thesis were recorded using the computerised data collection system described in section 4.2.3. This system was developed in co-operation with Mr Alistair Poustie; he describes an early version of the setup in reference 142. A block diagram of the data collection apparatus is shown here as figure C.1.

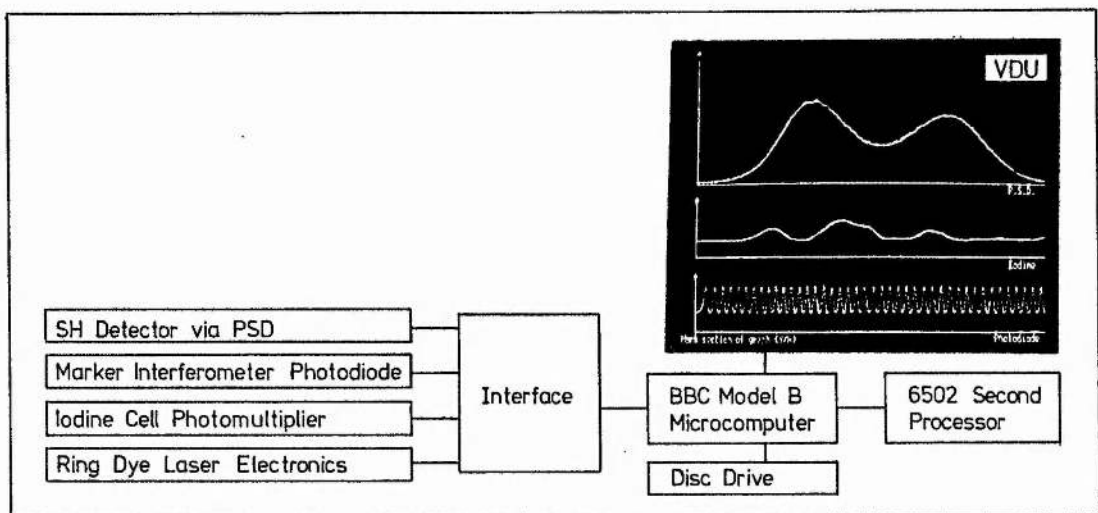


Figure C.1. Block diagram of the computerised data collection system.

The data collection program, which was written in BBC Basic and is listed in appendix D, first ran through a question and answer sequence to set up parameters such as the laser scan time. The computer then checked that the laser was locked to the reference interferometers and waited for the operator to start the laser scanning. The 'scan on' signal started the data collection part of the program, which read the values of the experimental parameters via the computer's analogue to digital converter. These values were displayed graphically on the screen and stored in three

arrays in RAM, 3600 points for the SH signal, and 1200 points for each of the other two parameters. At the end of the scan another question and answer sequence allowed the operator to store some or all of these values on the floppy disc.

At the end of an experimental session the files of line profiles stored on the discs were transferred to the University's VAX 11/785 mainframe computer. The Fortran program which was used to analyse this data is also listed in appendix D. Its main function was to linearise the laser scan. This was done by expanding and contracting parts of the scan data to ensure that the interferometer transmission period remained the same throughout the scan. Graphs could then be drawn to specified scalings on the computer screen or graphics plotter. As the absolute frequency of the laser was recorded in the form of parts of the iodine spectrum, line profiles taken under different conditions could be plotted out and combined on one graph for comparison. This would have been nearly impossible without the computerised system.

The linearisation was tested by Doppler-free two-photon spectroscopy of the sodium $3S - 4D$ transition. The SH detector was replaced by a photomultiplier tube which monitored the 330 nm radiation as described in section 4.4.2. Figure C.2 shows the output from the plotter; the top trace is the two photon absorption spectrum, the middle trace is the signal from the photodiode of the marker interferometer, and the bottom trace is the iodine absorption spectrum. The graph is annotated in units of the free spectral range of the marker interferometer. This is 250 MHz at the laser frequency, corresponding to 500 MHz at the atomic frequency. The separations of the peaks were measured, and are shown in table C.1. Agreement was good to 0.5%, so the linearisation obviously worked well.

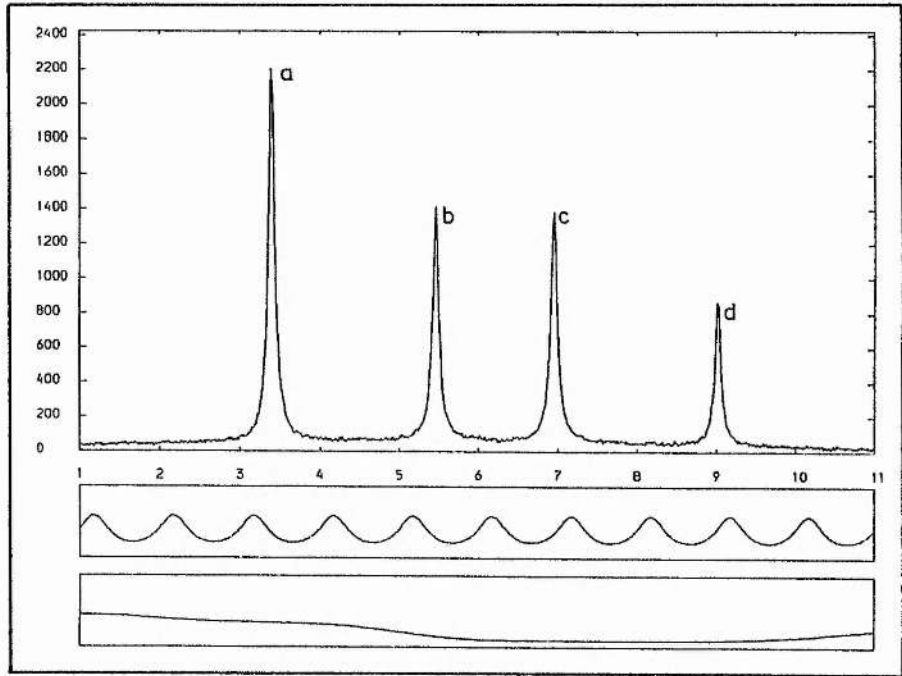


Figure C.2. Doppler free trace of the sodium 3S - 4D transition as recorded and displayed by the system described in this appendix, see text for full explanation. The transitions are:-
 a) 3S (F=2) \rightarrow 4D (J=5/2), b) 3S (F=2) \rightarrow 4D (J=3/2),
 c) 3S (F=1) \rightarrow 4D (J=5/2), d) 3S (F=1) \rightarrow 4D (J=3/2).

Peaks	Peak Separation (GHz)	
	Experimental	Accepted
a-c	1.775	1.772
b-d	1.777	
a-b	1.032	1.028
c-d	1.034	

Table C.1. Measured and accepted values for the hyperfine splitting of the sodium 3S state and the fine splitting of the 4D state.

APPENDIX D

DATA COLLECTION AND ANALYSIS PROGRAMS

Data Collection Program

To be run on a BBC model B microcomputer with a 6502 second processor and a single density floppy disc drive. The hi-basic chip must be in use; in our case the command *FX142,1 enabled this chip. The data recorded in RAM is subsequently stored on the disc in ASCII format by use of the *SPOOL command. This is the data format in which the mainframe computer would most readily accept the data.

```

10 REM DATA RECORD PROGRAM FOR SODIUM SPECTROSCOPY EXPERIMENT
20 REM *****
30*FX 16,3
40 MODE 1:COLOUR 2:CLS
50 V=0:CBM$="BLANK":LX=0:BDX=1
60 DIM PSDX(3693),IODX(1233),PHX(1233),LKOFFX(50),PBX(15),POITX(20)
70 PRINT"*****":PRINT"*":TAB(39);"*":PRINT"*":TAB(39);"*":
PRINT"*":TAB(5);"Sodium Spectroscopy Experiment":TAB(39);"*"
80 PRINT"*":TAB(5);"*****":TAB(39);"*"
90 PRINT"*":TAB(39);"*":PRINT"*":TAB(39);"*":PRINT"*":TAB(17);"By":TAB(39);"*":PRINT"*":T
AB(39);"*":PRINT"*":TAB(39);"*":PRINT"*":TAB(10);"AP and BS":TAB(39);"*"
100 PRINT"*":TAB(39);"*":PRINT"*":TAB(16);"1985":TAB(39);"*":PRINT"*":TAB(39);"*":PRINT"****
*****"
110 T=TIME+2:REPEAT:UNTIL TIME>T
120 R=0
130 MODE 1:VDU 26:V=0:REPEAT:PRINT:V=V+1:UNTIL V=10:PRINT TAB(3);"MAIN MENU :-":PRINT TAB(3);"
-----":PRINT:PRINT
140 PRINT TAB(6);"1. Data Recording":PRINT:PRINT TAB(6);"2. Reset PSD Range":PRINT:PRINT TAB
(6);"3. Spare"
150 PRINT:PRINT TAB(6);"4. Record results on disc":PRINT:PRINT TAB(6);"5. Graphics Notepad":
PRINT:PRINT TAB(6);"6. Exit program"
160 PRINT:PRINT:PRINT:PRINT
170 PRINT " SELECTION? "; SEL#=GET#: SELX=VAL(SEL#):IF SELX>6 OR SELX<1 THEN GOTO 170
180 ON SELX GOTO 200,185,130,630,970,1130
185 PROCRange:BDX=0: GOTO 130
190
200 REM ***** DATA RECORDING *****
210 IF BDX=1 THEN PROCRange:BDX=0
220 MODE 0:CLG:CLS
230 PROCaxes
240 VDU 24,0,50,1280,1024;
250 VDU 28,0,31,65,30
260 PRINT:INPUT"Enter the laser scan time (secs):- ",LST
270 IF LST<=72 THEN NOX=1:DPLUS=0:GOTO 380
280 D=((LST*100)-7200)/(1228*3)
290 IF D<2 THEN NOX=1:DPLUS=D:GOTO 310
300 NOX=INT(D):DPLUS=D-NOX
310 ON NOX GOTO 380,380,380,320,320,330,330,340,340,350,350,360,360,370
320 NOX=NOX+1:GOTO 380
330 NOX=NOX+2:GOTO 380
340 NOX=NOX+3:GOTO 380
350 NOX=NOX+4:GOTO 380
360 NOX=NOX+5:GOTO 380
370 NOX=NOX+6
380 LOCKX=ADVAL(0) AND 3:IF LOCKX=2 OR LOCKX=0 THEN 410
390 PRINT:PRINT"Lock the laser....."
400 LOCKX=ADVAL(0) AND 3:IF LOCKX=2 OR LOCKX=0 THEN 410 ELSE 400
410 PRINT"Confirmation:- Stabilock On"
420 T=TIME+60:REPEAT:UNTIL TIME>T
430 PRINT:PRINT"Start laser scan to begin...."

```

```

440 SCANX=ADVAL(0) AND 3:IF SCANX=0 THEN 450 ELSE 440
450 PRINT
460 SDX=1
470 PLTX=0
480 PLTX=PLTX+1
490 HX=1:PROCpsd
500 PLOT 69,PLTX+50,TXDIV 10+575
510 IOX=ADVAL(2) DIV 16:IODX(PLTX)=IOX:PLOT 69,PLTX+50,IOXDIV21+325
520 HX=2:PROCpsd
530 PX=ADVAL(3) DIV 16:PHX(PLTX)=PX:PLOT 69,PLTX+50,PXDIV21+75
540 HX=3:PROCpsd
550 IF PLTX=1230 THEN GOTO 580 ELSE 480
570 GOTO 130
580 PRINT"Mark section of graph (Y/N) ":ANS#=BET$:IF ANS#="N" THEN LX=1:GOTO 600
590 LX=0:PROCexp
600 PRINT:PRINT TAB(10);"1. Main Menu 2. Notepad :- Selection ":A#=BET$:AX=VAL(A#):ON AX
GOTO 130,1220
610 GOTO 1130
620
630 REM ***** WRITE RESULTS TO DISC *****
640 CLOSEEO
650 MODE 1:PRINT:PRINT:PRINT:PRINT"Writing results to disc :-":PRINT"-----"

660 PRINT:PRINT:PRINT TAB(3);"1. P.S.D. and Photodiode data points":PRINT:PRINT TAB(3);"2. P.S
.D. , Photodiode and Iodine":PRINT:PRINT TAB(6);"data points":PRINT:PRINT TAB(3);"3. Return to M
ain Menu"
670 PRINT:PRINT:INPUT"Selection ":AX:IF AX<1 OR AX>3 THEN 670
680 ON AX GOTO 690,820,130
690 R=R+1:IF R=4 THEN PRINT"Disc Full- Insert new Disc" ELSE 720
700 PRINT:PRINT:INPUT"Continue (Y/N) ",C#:IF C#="N" THEN 130
710 GOTO 120
720 ON R GOTO 730,750,770
730*SPOOL PSRUN1
740 GOTO 780
750*SPOOL PSRUN2
760 GOTO 780
770*SPOOL PSRUN3
780 PRINT COM#
790 UX=1:PROCdisc
800*SPOOL
810 GOTO 650
820 R=R+1:IF R=3 THEN PRINT"Disc Full- Insert new Disc" ELSE 850
830 PRINT:PRINT:INPUT"Continue (Y/N) ",C#:IF C#="N" THEN 130
840 GOTO 120
850 ON R GOTO 860,880,900
860*SPOOL ALRUN1
870 GOTO 910
880*SPOOL ALRUN2
890 GOTO 910
910 PRINT COM#
920 UX=0:PROCdisc
930*SPOOL
940 GOTO 650
960
970 REM ***** GRAPHICS NOTEPAD *****
980 PROCrange
990 PROCaxes
1000 PRINT "A TO ABORT"
1010 PLTX=0
1020 REPEAT
1030 KEY#=INKEY$(0):IF KEY#="A" THEN 1100 ELSE 1040
1040 TX=ADVAL(1) DIV 16:PLOT 69,PLTX+50,TXDIV 10+575
1050 IOX=ADVAL(2) DIV 16:PLOT 69,PLTX+50,IOXDIV21+325
1060 PX=ADVAL(3) DIV 16:PLOT 69,PLTX+50,PXDIV21+75
1070 PLTX=PLTX+1
1080 IF PLTX=1230 THEN PLTX=0:PROCaxes
1090 UNTIL KEY#="A"
1100 PRINT"Run Again (Y/N) ":V#=BET$
1110 IF V#="N" THEN 130
1120 GOTO 970
1130 VDU 4
1140 VDU 26
1150 MODE 0:END
1160 DEF PROCmark
1170 MOVE PLTX+50,75:PLOT 21,PLTX+50,1100
1180 IF SDX=50 THEN 1200
1190 LKOFF$(SDX)=PLTX:SDX=SDX+1
1200 ENDPROC
1210

```

```

1220 REM ***** NOTEPAD *****
1230 VDU 26:CLG:CLS:PRINT:PRINT:PRINT TAB(30);"NOTEPAD":PRINT TAB(30);"*****"
1240 VDU 24,0;0;1280;1000;
1250 MOVE 0,0:DRAW 1279,0:DRAW 1279,1000:DRAW 0,1000:DRAW 0,0:MOVE 15,15:DRAW 1264,15:DRAW 1264
,987:DRAW 15,987:DRAW 15,15
1260 VDU 5
1270 MOVE 100,800:PRINT"Enter comments here and then press <return>"
1280 VDU 4:VDU 28,10,25,70,10
1290 INPUT COM#:VDU 5
1300 MOVE 400,75:PRINT "Press Space-Bar to continue"
1310 AX=GET:IF AX<>32 THEN 1310
1320 VDU4:VDU26
1330 GOTO 130
1340
1350 DEF PROCpsd
1360 IX=0
1370 REPEAT
1380 IX=IX+1
1390 PSX(IX)=ADVAL(1) DIV 16
1400 CHECKX=ADVAL(4) AND 3:DN (CHECKX+1) GOTO 1440,1410,1420,1430
1410 VDU 7:PROCmark:GOTO 1440
1420 VDU 7:PRINT"Scan off":GOTO 580
1430 VDU 7:PRINT"Scan and Stabilock off":GOTO 580
1440 UNTIL IX=NOX
1450 SUMX=0:XX=0:REPEAT:XX=XX+1:SUMX=SUMX+PSX(XX):UNTILXX=NOX:TX=SUMXDIVXX
1460 PSDX(3*PLTX+HX)=TX
1470 DEEXX=INT(DPLUS*85):FOR FX=1 TO DEEXX:NEXT
1480 ENDPROC
1490
1500 DEF PROCexp
1510 LOCAL
1520*FX4,1
1530 DX=0:BX=1
1540 PRINT:XX=60:INCX=1:SPX=1:NX=0:FX=22
1550 PROCIn
1560 REPEAT
1570 SX=GET
1580 IF SX=136 THEN 1590 ELSE 1600
1590 PROCIn:XX=XX-(INCX*SPX):PROCIn
1600 IF SX=137 THEN 1610 ELSE 1620
1610 PROCIn:XX=XX+(INCX*SPX):PROCIn
1620 NX=NX+1:IF NX<=20 THEN SPX=1 ELSE SPX=10
1630 IF INKEY(-122)<>-1 AND INKEY(-26)<>-1 THEN NX=0
1640 UNTIL SX=88:DX=DX+1:POITX(DX)=XX-50:FX=21:PROCIn
1650 IF DX=2 THEN 1670
1660 GOTO 1540
1670*FX4,0
1680 ENDPROC
1690
1700 DEF PROCIn
1710 IF XX>=1279 THEN XX=1279:GOTO 1730
1720 IF XX<=51 THEN XX=51
1730 MOVE XX,75:PLOT FX,XX,1024
1740 ENDPROC
1750
1760 DEF PROCaxes
1770 MODE 0
1780 MOVE 50,75:DRAW 50,275:MOVE 50,325:DRAW 50,525:MOVE 50,75:DRAW 1280,75:MOVE 50,325:DRAW 12
80,325
1790 VDU 5
1800 MOVE 44,525:PRINT"^":MOVE 44,273:PRINT"^":MOVE 1150,315:PRINT"iodine":MOVE 1100,65:PRINT"P
hotodiode"
1810 IF MARK=1 THEN 1820 ELSE 1850
1820 MOVE 50,575:DRAW 50,1024:MOVE 50,580:PRINT STRING$(77,"-"):MOVE 44,1020:PRINT"^":MOVE 1150
,560:PRINT"P.S.D."
1830 VDU 4
1840 GOTO 1870
1850 MOVE 50,575:DRAW 50,1024:MOVE 50,785:PRINT STRING$(77,"-"):MOVE 44,1020:PRINT"^":MOVE 1150
,775:PRINT"P.S.D."
1860 VDU 4
1870 ENDPROC
1880
1890 DEF PROCrange
1900 MODE 1:CLG
1910 V=0:REPEAT:PRINT:V=V+1:UNTIL V=10
1920 PRINT "Phase Sensitive Detector ranges 1-"
1930 PRINT "-----"
1940 PRINT:PRINT:PRINT:PRINT TAB(10);"PSD:- 1. 0 TO +1 ":PRINT:PRINT TAB(10);" 2. -1 TO
+1"
1950 PRINT:PRINT:PRINT
1960 PRINT "Selection? ":S#=GET#:SX=VAL(S#):IF SX<1 OR SX>2 THEN GOTO 1960
1970 IF SX=1 THEN MARK=1 ELSE MARK=0
1980 ENDPROC
1990

```

```

2000 DEF PROCdisc
2010 IF LX=1 THEN ENX=1230:STX=1:GOTO 2050
2020 TX=-1
2030 TX=TX+2
2040 STX=POITX(TX):ENX=POITX(TX+1):IF ENX<STX THEN ENX=POITX(TX):STX=POITX(TX+1)
2050 QX=&05:PRINT
2060 PRINT STX,ENX,SDX-1
2070 PRINT
2080 FOR IX=1 TO SDX-1:PRINT LKOFFX(IX):NEXT IX
2090 PRINT
2100 FX=(3*STX)-2
2110 FOR IX=STX TO ENX
2120 IF UX=0 THEN 2130 ELSE 2140
2130 PRINT PSDX(FX),PHX(IX),I0DX(IX):GOTO 2150
2140 PRINT PSDX(FX),PHX(IX)
2150 FX=FX+1
2160 NEXT IX
2170 FOR IX=FX TO (3*ENX)-2 STEP 5
2180 PRINT PSDX(IX),PSDX(IX+1),PSDX(IX+2),PSDX(IX+3),PSDX(IX+4)
2190 NEXT IX
2200 FOR GX=IX+1 TO (3*ENX)-2
2210 PRINT PSDX(GX)
2220 NEXT GX
2230 IF LX=1 THEN 2240
2240 QX=&10
2250 ENDPROC

```

Data Analysis Program

To run on the VAX computer system. The program must first be compiled, then linked with ghost/lib,gridt4010/lib. It is designed to work on a terminal compatible with the Tektronix T4010 standard.

```
C    BD2.FOR    REVISED 9.5.86
C    Prog to analyse and plot BBC data
C
C    Developed by Alistair Poustie and Bruce Sinclair
C    August 1985. To run, compile the program and
C    LINK BD2,GHOST/LIB,GRIDT4010/LIB
C    The data from the BBC collection must be in
C    a suitably formatted file with a .DAT
C    file specification. Various operations can be
C    performed on the data; if specified, the final
C    graphs and annotations are filed in a gridfile
C    called BD.GRD.

C *** DECLARATIONS

    IMPLICIT NONE
    INTEGER BDI
    INTEGER I,R,M,C,IPEAK(100),PSDPK1,PSDPK2,CODE
    INTEGER ST,PHMAX,S,DUM,EN,ICHR,IPK,F,PSDST,PSDEN
    INTEGER REPEAT,PDIO
    INTEGER PHMX,PMAX,PHMIN,PMX(1000),PHMN,PMN(1000),PMIN
    INTEGER ITR,ITRO(1000),STT,ENN,MID(100),MD(100)
    INTEGER START,PSDFIN,AP,PSDF,STAR,MIDD,STA,FIN
    REAL PHPOX,PHPOY,IPOX,IPOY,PSDPOX,PSDPOY
    REAL BDPSDMAX, BDPSDMIN
    REAL TOP,BOTTOM,HALF,LEFT,RIGHT
    REAL CONT,MK(2),OFF(20)
    INTEGER EX,TR,A,D,SD,LKOFF(20),Q,K
    REAL PSDNO(3900),PSD(3900),PHNO(1300),PH(1300),
Z   IOD(1300),V,DIFF,COUNT
    REAL OFFSET
    REAL PS,P,IO,PSDDIFF,MAG,X,PSDSCL,PHSCL,PHSC,IOSCL
    REAL XMIN,XMAX,Y
    REAL XMARK,YMARK
    INTEGER FM
    INTEGER BDREPEAT
    CHARACTER*30 NME,NME1
    CHARACTER*100 COM
    CHARACTER*1 ANS

C
C *** MAIN MENU, DATA INPUT
C
    PRINT*,' '
    PRINT*,' '
    PRINT*,' '
```



```

PRINT*, 'Ghost Plotting of BBC Data'
PRINT*, '===== '
PRINT*, ' '
PRINT*, '          1. P.S.D. & Photodiode Data'
PRINT*, ' '
PRINT*, '          2. P.S.D., Photodiode & Iodine Data'
PRINT*, ' '
PRINT*, '          3. Exit Program'
PRINT*, ' '
PRINT*, 'Selection ?'
1 READ*, S
  IF (S.EQ.1) GOTO 10
  IF (S.EQ.2) GOTO 19
  IF (S.EQ.3) GOTO 210
  IF (S.LT.1.OR.S.GT.3) GOTO 1

C
C   PSD & Photodiode points
C
10 PRINT*, ' '
   PRINT*, ' '
   PRINT*, 'P.S.D. & Photodiode'
   PRINT*, '-----'
   GOTO 29

C

C   PSD, Photodiode and Iodine points
C
19 PRINT*, ' '
   PRINT*, ' '
   PRINT*, 'PSD, Photodiode & Iodine'
   PRINT*, '-----'
29 PRINT*, ' '
   PRINT*, 'Enter the Data File name:'
   READ 2, NME
2   FORMAT(A30)
C

C *** READ IN FROM DATA FILE

C
   OPEN (UNIT=1, FILE=NME, STATUS='OLD')
   READ(UNIT=1, FMT=3) COM
3   FORMAT(A100)
   READ(UNIT=1, FMT=4) DUM, DUM
   READ(UNIT=1, FMT=4) ST, EN, SD
4   FORMAT(I5, I5, I5)
   READ(UNIT=1, FMT=4) DUM, DUM
   IF (SD.EQ.0) SD=1
   DO 9 I=1, SD
   READ(UNIT=1, FMT=11) LKOFF(I)
9   CONTINUE
   PRINT*, 'NUMBER OF LOCKOFF POINTS IS', SD-1
11  FORMAT(I5)
   PSDST=(3*ST)-2
   PSDEN=(3*EN)-2
   F=PSDST
   READ(UNIT=1, FMT=4) DUM, DUM
   DO 7 I=ST, EN
   READ(UNIT=1, FMT=5) PS, P, IO

```

```

5   FORMAT(F5.0,F5.0,F5.0)
   PSDNO(F)=F
   PSD(F)=PS
   PHNO(I)=I
   PH(I)=P
   IOD(I)=IO
   F=F+1
7   CONTINUE
   DO 20 I=F,PSDEN,5
   READ(UNIT=1,FMT=8) PSD(I),PSD(I+1),PSD(I+2),PSD(I+3),
Z  PSD(I+4)
8   FORMAT(F5.0,F5.0,F5.0,F5.0,F5.0)
   PSDNO(I)=I
   PSDNO(I+1)=I+1
   PSDNO(I+2)=I+2
   PSDNO(I+3)=I+3
   PSDNO(I+4)=I+4
20  CONTINUE
   DO 22 R=I+1,PSDEN
   READ(UNIT=1,FMT=21) PSD(R)
   PSDNO(R)=R
22  CONTINUE
21  FORMAT(F5.0)
   CLOSE(UNIT=1)
   PRINT*,'FILE READ'
   BDPSDMIN=4095.0
   BDPSDMAX=0.0
   DO 23 BDI=PSDST,PSDEN
   IF (PSD(BDI).GT.BDPSDMAX) BDPSDMAX=PSD(BDI)
   IF (PSD(BDI).LT.BDPSDMIN) BDPSDMIN=PSD(BDI)
23  CONTINUE
   PDIO=0
C
C *** DETERMINATION OF MAX AND MIN VALUES OF PHOTODIODE TRACE
C
   PHMAX=PH(ST)
   PHMIN=PH(ST)
   DO 30 I=ST,EN
   DO 25 Q=1,SD
   IF (LKOFF(Q).EQ.I) PH(I)=PH(I-1)
25  CONTINUE
   IF (PH(I).GT.PHMAX) PHMAX=PH(I)
   IF (PH(I).LT.PHMIN.AND.PH(I).GT.0.0) PHMIN=PH(I)
30  CONTINUE
   MIDD=((PHMAX-PHMIN)/2)+PHMIN
   PRINT*,'MEAN POINT FOUND, STARTING ON PEAKS'
C
C *** FINDING POSITIONS OF MAXIMA OF PHOTODIODE TRACE
C
   C=1
   PHMX=PHMAX-((PHMAX-PHMIN)/3)
   PMAX=PHMX
   DO 35 I=ST,EN
   IF (PH(I).GE.PMAX) THEN
   PMAX=PH(I)
   IPK=I
   ENDIF
   IF (PH(I).LT.MIDD.AND.PMAX.GT.PHMX) GOTO 33
   GOTO 35

```

```

33  PMX(C)=PMAX
    IPEAK(C)=IPK
    C=C+1
    PMAX=PHMX
35  CONTINUE
C
C    Troughs and positions of troughs
    PRINT*,'STARTING ON TROUGHS'
C
    C=1
    PHMN=PHMIN+((PHMAX-PHMIN)/3)
    PMIN=PHMN
    DO 34 I=ST,EN
    IF (PH(I).LT.PMIN) THEN
    PMIN=PH(I)
    ITR=I
    ENDIF
    IF (PH(I).GT.MIDD.AND.PMIN.LT.PHMN) GOTO 60
    GOTO 34
60  PMN(C)=PMIN
    ITRO(C)=ITR
    PMIN=PHMN
    C=C+1
34  CONTINUE
C
C    Set TR=1 if trough before peak
    TR=0
C
    IF (IPEAK(1).GT.ITRO(1)) TR=1
    IF (TR.EQ.1) C=C-1
C
    PRINT*,'STARTING TO FIND',C-1,' MIDPOINTS'
C    Mid points
C
    M=1
    DO 70 I=1,C-1
    MID(M)=((PMX(I)-PMN(I))/2)+PMN(I)
    IF (TR.EQ.1) THEN
    STT=ITRO(I)
    ENN=IPEAK(I)
    ELSE
    STT=IPEAK(I)
    ENN=ITRO(I)
    ENDIF
    EX=0
    MD(M)=0
41  DO 40 R=STT,ENN
    IF (PH(R).EQ.(MID(M)+EX).OR.PH(R).EQ.(MID(M)-EX)) MD(M)=R
40  CONTINUE
    IF (MD(M).EQ.0) THEN
    EX=EX+1
    GOTO 41
    ENDIF
    M=M+1
70  CONTINUE
C
C    Distance between mid-points
    PRINT*,'STARTING TO FIND DISTANCES BETWEEN MID POINTS'
C
    COUNT=0

```

```

K=1
DO 80 I=2,M-1
PSDDIFF=((3*MD(I))-2)-((3*MD(I-1))-2)
DIFF=MD(I)-MD(I-1)
D=(3*MD(I-1))-2
V=0
DO 81 R=MD(I-1),MD(I)
PHNO(R)=COUNT+(V*(1/DIFF))
PSDNO(D)=COUNT+(V*(1/PSDDIFF))
V=V+1
D=D+1
81 CONTINUE
DO 82 A=D,(3*MD(I))-2
PSDNO(A)=COUNT+(V*(1/PSDDIFF))
V=V+1
82 CONTINUE
COUNT=COUNT+1
80 CONTINUE
C
C Plot these points on Ghost
C
XMIN=0
XMAX=COUNT
PSDPOSX=PSDNO(MD(1))
PSDPOSY=PSD(MD(1))
START=(3*MD(1))-2
PSDFIN=(3*MD(M-1))-2
PHPOSX=PHNO(MD(1))
PHPOSY=PH(MD(1))
STA=MD(1)
FIN=MD(M-1)
IOPOSX=PHNO(MD(1))
IOPOSY=IOD(MD(1))
CALL PAPER(1)
PRINT*, ' M to mark the boundaries of expansion'
PRINT*, ' E to expand but not file anything'
PRINT*, ' F to file all that is on screen'
PRINT*, ' Q to quit'
PRINT*, ' L to mark left hand point'
PRINT*, ' R to mark right hand point'
PRINT*, ' W to plot at cursor L-R separation'
PRINT*, ' T to mark top of peak'
PRINT*, ' B to mark bottom of peak and plot'
PRINT*, ' a half height marker'
PRINT*, ' H to plot at cursor T-B separation'
PRINT*, ' X to mark x coord in MHz'

C MAIN EXECUTION LOOP
BDREPEAT=0

85 PRINT*, ' '
CALL ERASE
C SET EXPANSION PARAMETERS FOR NEXT SCREENLOAD

145 CALL ERASE
PRINT*, 'EXPANSION PARAMETERS'
PRINT*, ' '
PRINT*, ' 0 To exit from the program'
PRINT*, ' '
PRINT*, ' 1 For the frequency axis limits'

```

```

PRINT*, '          as marked on graph, or unchanged'
PRINT*, '          '
PRINT*, '          2      To insert numerical values for'
PRINT*, '          axis limits'
PRINT*, ' '
PRINT*, 'Input choice'
READ*, FM
IF (FM.EQ.1) GOTO 150
IF (FM.EQ.0) GOTO 200
PRINT*, ' '
PRINT*, 'Input minimum frequency'
READ*, MK(1)
PRINT*, 'and now the maximum frequency'
READ*, MK(2)
150  IF (BDREPEAT.EQ.0.AND.FM.EQ.1) THEN
      MK(1)=XMIN
      MK(2)=XMAX
      ENDIF
      IF (MK(2).GT.MK(1)) THEN
XMAX=MK(2)
XMIN=MK(1)
ELSE
XMIN=MK(2)
XMAX=MK(1)
ENDIF

PRINT*, 'Type 1 for PSD only'
READ*, PDIO
86  PRINT*, 'File header comment is ', COM

PRINT*, ' '
PRINT*, 'Input integer code number for graph'
READ*, CODE
CALL ERASE
PRINT*, 'Input the zero offset'
READ*, OFFSET
PRINT*, 'Input 0 to the next question to'
PRINT*, 'get bdsstandard scaling'
PRINT*, 'For standard psd mag use', 4095/
Z (1.1*(BDPSDMAX)-OFFSET)
PRINT*, 'Input the PSD magnification '
READ*, MAG
IF (MAG.EQ.0) THEN
MAG=4095/(1.1*(BDPSDMAX-BDPSDMIN))
DO 4010 BDI=1,PSDEN
PSD(BDI)=PSD(BDI)-BDPSDMIN
4010 CONTINUE
ENDIF
CALL ERASE
IF (S.EQ.1) THEN
PSDSCL=0.2
PHSCL=0.16
PHSC=0.08
ELSE
PSDSCL=0.3
PHSCL=0.26
PHSC=0.18
IOSCL=0.16
ENDIF

```

```

CALL PSPACE(0.08,1.0,0.72,0.75)
CALL MAP(0.0,1.0,0.0,1.0)

CALL CTRMAG (20)

CALLPLOTNI(0.45,0.1, CODE)
C Plot PSD points
IF (PDIO.NE.1) THEN
CALL PSPACE(0.08,0.948,PSDSCL,0.772)
ELSE
CALL PSPACE(0.08,1.0,0.08,0.7)
ENDIF
CALL MAP(XMIN,XMAX,0.0,4095.0/MAG)
CALL SCALES
CALL BORDER
CALL POSITN(PSDNO(START),PSD(START))
DO 90 I=START,PSDFIN
CALL JOIN(PSDNO(I),PSD(I)-OFFSET)
90 CONTINUE

C Plot Photodiode Points
IF (PDIO.EQ.1) GOTO 101
AP=1
CALL PSPACE(0.08,0.948,PHSC,PHSCL)
CALL MAP(XMIN,XMAX,0.0,4095.0)
CALL BORDER
CALL POSITN(PHPOX,PHPOY)
DO 94 I=STA,FIN
DO 99 Q=1,SD
IF (LKOFF(Q).EQ.I) THEN
CALL CTRMAG(15)
CALL PLOTNC(PHNO(I),0.0,192)
CALL POSITN(PHNO(I-1),PH(I-1))
CALL CTRMAG(10)
OFF(AP)=PHNO(I)
AP=AP+1
ENDIF
99 CONTINUE
CALL JOIN(PHNO(I),PH(I))
94 CONTINUE

C Plot Iodine Points
IF (S.EQ.1) GOTO 101
CALL PSPACE(0.08,0.948,0.08,IOSCL)
CALL MAP(XMIN,XMAX,0.0,4095.0)
CALL BORDER
CALL POSITN(IOPOX,IOPOY)
DO 93 I=STA,FIN
CALL JOIN(PHNO(I),IOD(I))
93 CONTINUE

C SETTING UP AND USING CURSOR TO ANNOTATE ETC

BDREPEAT=1
101 IF (PDIO.NE.1) THEN
CALL PSPACE(0.08,1.0,PSDSCL,0.7)
ELSE
CALL PSPACE(0.08,1.0,0.08,0.7)
ENDIF

```

```

CALL MAP(XMIN,XMAX,0.0,4095.0/MAG)
CALL CTRMAG (25)
MK(1)=XMIN
MK(2)=XMAX
I=0
98 I=I+1
96 CALL CURSOR(X,Y,ICHAR)
IF (ICHAR.EQ.88) CALL PLOTNF(X,Y,X*250,1)
IF (ICHAR.EQ.84) GOTO 104
IF (ICHAR.EQ.72) CALL PLOTNF(X,Y,(TOP-BOTTOM),1)
IF (ICHAR.EQ.76) GOTO 105
IF (ICHAR.EQ.82) GOTO 106
IF (ICHAR.EQ.87) CALL PLOTNF(X,Y,(RIGHT-LEFT)*250,1)
IF (ICHAR.EQ.77) GOTO 97
IF (ICHAR.EQ.66) GOTO 103
IF (ICHAR.EQ.81) GOTO 200
IF (ICHAR.EQ.70) GOTO 140
IF (ICHAR.EQ.69) GOTO 145
GOTO 96

C BOTTOM AND HALF HEIGHT

103 BOTTOM=Y
CALL PLOTNC (X,Y,176)
HALF=(TOP+BOTTOM)/2
CALL POSITN(XMIN,HALF)
CALL JOIN(XMIN+(XMAX-XMIN)/50,HALF)
GOTO 96

104 TOP = Y
CALL PLOTNC (X,Y,176)
GOTO 96

105 LEFT=X
CALL PLOTNC (X,Y,124)
GOTO 96

106 RIGHT=X
CALL PLOTNC(X,Y,124)
GOTO 96

C MARKERS FOR EXPANSION

97 CALL BROKEN(10,10,10,10)
CALL POSITN(X,0.0)
CALL JOIN(X,4095.0/MAG)
CALL FULL
IF (I.GT.2) I=2
MK(I)=X
GOTO 98

C SAVE INTO GRIDFILE

140 CALL FRAME
CALL PICTSAV('USER2:[PHRBS]BD.GRD',A,19,0)

GOTO 85

200 CALL GREND
210 STOP
END

```

APPENDIX E
STUDIES INVOLVING THE SODIUM DIMER

Rather than treat the sodium dimer population as an undesirable but unavoidable loss mechanism for second harmonic generation in sodium atoms, it was decided to investigate the possibility of using transitions in the dimer for resonant enhancement of magnetic-field-induced second harmonic generation. The many degrees of freedom of the molecule result in a large number of possible transitions; it was hoped that some of these would be suitable for enhancing the SHG process, thus giving many more frequencies at which the second harmonic could be generated. A disadvantage of a molecular medium is that many molecular states are not significantly perturbed by a magnetic field, which restricts their use in a magnetic-field-induced process. Another problem is that the spectroscopy of the highly excited states of the sodium dimer is not well understood, though strong two-photon absorption has been reported [143].

The theory of the structure and spectra of diatomic molecules is given by Herzberg [144], and his notation will be used throughout this appendix. The angular momenta involved in describing the states of the sodium dimer are shown in figure E.1. The angular momentum of the electrons, L , precesses around the inter-nuclear axis; the component of this momentum about this axis is $\Lambda = |m_L|$. Any angular momentum due to electron spin will also precess about the inter-nuclear axis, with a component Σ along this axis. The total angular momentum along this axis is then $\Omega = \Lambda + \Sigma$. The electronic angular momentum and the total angular momentum, J , are quantised, the nuclear angular momentum, N , is not. The angular momenta are coupled according to Hund's rule (a). States with $\Lambda = 0, 1, 2$ are classified as Σ, Π, Δ respectively. All states with $\Lambda \neq 0$ are doubly

degenerate, as m_L can have the two values $\pm\Lambda$. In diatomic molecules any plane passing through the internuclear axis is a plane of symmetry. The electronic eigenfunctions either remain the same (positive states), or change sign (negative states) when reflected in such a plane. If, as in the sodium dimer, the nuclei have the same charge, the electric field experienced by the electrons remains the same on reflection of the nuclei in the centre of symmetry. As a consequence, the electronic eigenfunction remains the same (even, gerade state) or changes sign (odd, ungerade state), when it undergoes such a transformation. The symmetry of the rotational levels with respect to an exchange of nuclei leads to positive rotation levels being symmetric and the negative levels antisymmetric for even electronic states (for example, Σ_g), and vice versa for odd electronic states (for example Σ_u).

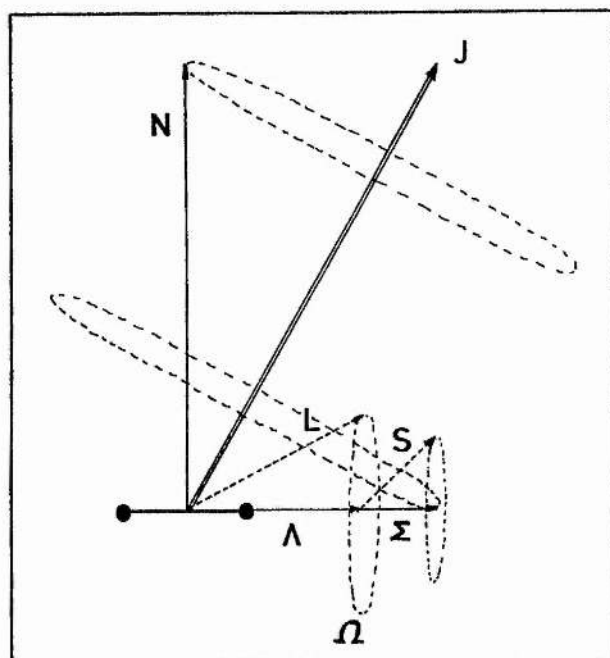


Figure E.1. Coupling of angular momenta in a diatomic molecule in Hund's case (a), see text for details.

Consideration of the symmetry properties of the molecular wavefunctions and their interaction with radiation [86, 144] gives the selection rules for electric dipole radiation shown in table E.1. Two photon selection rules are found by a repeated application of the selection rules for single photon transitions. The quadrupole selection rules are given in table E.2.

$g \longleftrightarrow u$	$s \longleftrightarrow s$	$a \longleftrightarrow a$	$g \longleftrightarrow g$	$u \longleftrightarrow u$
$+$	$-$	$+$	$-$	$-$
Σ^+	Σ^+	Σ^-	Σ^-	Σ^-

$\Delta J = 0, \pm 1,$ but $J=0 \not\leftrightarrow J=0$
 $\Delta S = 0$
 $\Delta \Sigma = 0$
 $\Delta \Lambda = 0, \pm 1$

Table E.1. Selection rules for electric dipole transitions in homonuclear dimers. g and u denote gerade and ungerade states, s and a are symmetric and antisymmetric wavefunctions, and $+$ and $-$ denote even and odd parity wavefunctions.

$g \longleftrightarrow g$	$u \longleftrightarrow u$	$g \longleftrightarrow u$
$s \longleftrightarrow s$	$a \longleftrightarrow a$	$a \longleftrightarrow s$
$+$	$-$	$+$
Σ^+	Σ^+	Σ^-

$\Delta J = 0, \pm 1, \pm 2$
 but $J=0 \not\leftrightarrow J=0, J=1/2 \not\leftrightarrow J=1/2, J=1 \not\leftrightarrow J=0$
 $\Delta S = 0$
 $\Delta \Sigma = 0$
 $\Delta \Lambda = 0, \pm 1, \pm 2$

Table E.2. Quadrupole transition selection rules for Na_2 .

The Σ states, of which the ground state of the sodium dimer is one, have very small Zeeman splittings ΔW

$$\Delta W = g \mu_N B M \tag{E.1}$$

where g is the g factor, μ_N is the nuclear magneton, and M is the

magnetic quantum number. For other electronic states belonging to Hund's case (a) the Zeeman shifts are

$$\Delta W = \frac{(\Lambda + 2\Sigma)(\Lambda + \Sigma) \mu_B B M}{J(J + 1)} \quad (\text{E.2})$$

where μ_B is the Bohr magneton. Thus the splitting is very much greater than for the Σ states. However, the rotational averaging results in the $J(J + 1)$ term in the denominator, and thus the Zeeman splitting decreases rapidly with increasing J . This is illustrated in figure E.2 for a ${}^1\Pi_g$ state.

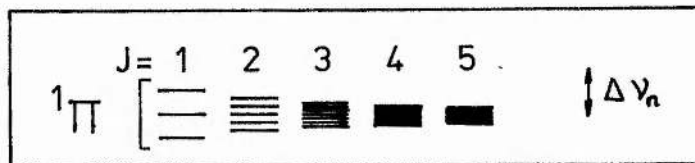


Figure E.2. Energy level splitting in a magnetic field for a ${}^1\Pi$ or a ${}^3\Pi$ state. The magnitude of the normal Zeeman splitting is given by the broken line arrow. From [144].

A possible scheme for magnetic-field-induced SHG must include magnetically active states; one such scheme is shown in figure E.3. ${}^1\Pi_g$ states were found by Morgan [143, 145] in his study of high lying gerade Rydberg states of the sodium dimer. He used Doppler free two-photon absorption to populate such states, and classified four of them as ${}^1\Pi_g(3s + 4d)$ states, as shown in table E.3.

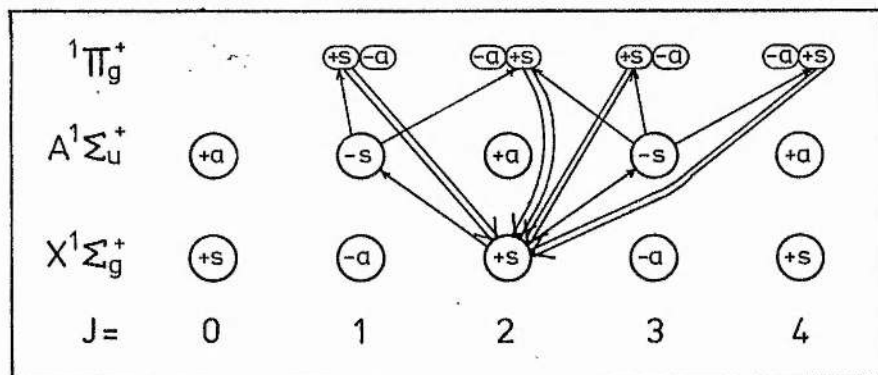


Figure E.3. Possible scheme for BSHG in sodium. Single lines represent enhancing single photon transitions, the double lines represent the quadrupole return route. Similar schemes are possible for other J values.

Laser frequency (cm^{-1})	Ground State $X^1\Sigma_g^+$ (v', J')	Enhancing State $A^1\Sigma_u^+$ (v'', J'')	Upper State $1\Pi_g^+$ (3s + 4d) (v''', J''')
16948.120	(3, 30)	(26, 31)	(6, 30)
16960.285	(4, 35)	(28, 34)	(8, 34)
17049.480	(2, 1)	(25, 2)	(6, 2)
17086.985	(1, 60)	(26, 59)	(7, 60)

Table E.3. Two photon transitions from $X^1\Sigma_g^+$ to $1\Pi_g^+$ (3s + 4d) assigned by Morgan et al [143].

Doppler free two-photon spectroscopy of the type described in section 4.4.2 was carried out with the aim of finding magnetically active upper levels, such as would be expected from the above classifications. The heatpipe of figure 4.3.3(d) was used at a temperature of approximately 400°C . The dye laser was tuned to the transitions listed by Morgan; these transitions, and others that were found nearby, were examined. Portions of the spectrum from 584 nm to 602 nm were examined. The linewidths of the two photon absorption peaks were measured in zero and 0.13 T fields. The detuning of some of the intermediate states were determined using saturation spectroscopy. These results are summarised in table E.4.

This study left us in some confusion; some transitions that had been classified by Morgan as $\Sigma \rightarrow \Sigma \rightarrow \Sigma$, which were not expected to be

magnetically active, were found to be so, and one of the $\Sigma \rightarrow \Sigma \rightarrow \Pi$ transitions showed no broadening whatsoever. Other recent work by an Anglo-French [146] group using Fourier-Transform spectroscopy disputes some of Morgan's classifications, but some of the transitions that they classed as $\Sigma \rightarrow \Sigma \rightarrow \Sigma$ still showed some broadening in a magnetic field in our experiments. Schawlow [147] comments that very few of the lines listed in reference 143 had been given the careful tests described in that reference. His group is continuing to investigate the energy level structure of this molecule [148]. Part of the problem may well have been due to levels of different terms being close to each other in energy, and their wavefunctions mixing slightly [149], thus giving each level some character of the other.

In the light of the uncertainty regarding the assignments of the Na_2 Rydberg levels, the study of the sodium dimer as a nonlinear medium was discontinued. Obviously much work has yet to be done to determine the level structures unambiguously. It was, however, considered worthwhile to tabulate the results that had been obtained, in the hope that they may be useful at some later date. Certain transitions looked very interesting; a transition near 16799.40 cm^{-1} , for example, grew greatly in intensity when the magnetic field was applied. This may have been due to the resonantly enhancing intermediate state being Zeeman shifted closer into resonance, or an increase in the wavefunction mixing mentioned above.

Table E.4 shows the wavenumbers of the transitions that were found, and lists the magnitudes of the peak two-photon absorption signals from the photomultiplier tube at 0.0 and 0.13 T magnetic fields. The widths of the resonances (FWHM at the laser frequency, HWHM at the atomic frequency) are also listed at the same fields. The cells were heated to 400°C , and were filled with 1 mbar of argon buffer gas. These experiments were carried out

over several weeks; although there were significant differences between peak heights between different runs (up to a factor of two), the values listed should give some idea of the relative strengths of the transitions. The assignments of Morgan et al [145] and Cooper et al [146] have been given alongside the experimental data when the measured transition frequency was less than 0.1 wavenumber from that listed by these authors.

Wavenumber	Strength	Width	Comments
17103.22	SO 38 SB 29	WO 75 WB 72	Ratio of strengths with linear and circular polarisation 0.82. Morgan X' $\Sigma_3^+(0,30) - \Sigma_3^+(3s+5s)(26,28)$ Cooper X' $\Sigma_3^+(1,61) - \Sigma_3^+(?,63)$
17088.369	SO 0.72 SB 0.63	WO 80 WB 100	
17088.209	SO 0.76 SB 0.67	WO 67 WB 83	On side of next peak.
17088.174	SO 0.77 SB 0.77	WO 134 WB 128	Cooper classification includes collisional energy transfer in intermediate state: Cooper X' $\Sigma_3^+(2,34) - A \Sigma_u^+(26,35)$ then A' $\Sigma_u^+(26,35) - A \Sigma_u^+(26,37)$ jump and A' $\Sigma_u^+(26,37) - \Sigma_3^+(?,38)$
17087.271	SO 0.17 SB 0.17	WO 27 WB 27	
17087.269	SO 0.31 SB 0.31	WO 34 WB 34	
17087.259	SO 0.3 SB	WO 266 WB flat	Peak flattens at 0.01 T.
17086.985			Morgan X' $\Sigma_3^+ - \Pi_3^+$
17049.735	SO 3 SB 3	WO 52 WB 45	
17049.480	SO 32 SB 20	WO 114 WB 160	Ratio of peak strengths in linear and circular polarisation 2.8. Linewidth increases at 0.6 GHz/T. Morgan X' $\Sigma_3^+(2, 1) - \Pi_3^+(3s + 4d)(6,2)$ Cooper X' $\Sigma_3^+(0,63) - \Sigma_3^+(?,63)$
17006.292	SO 86 SB 27&60	WO 95 WO -->	Splits into two peaks, at a rate of 1.08 GHz/T. Peak height $\propto P^{1.5}$, but saturates at 100 mW. Saturation behaviour of the two peaks different: peak height ratio at low pressure and laser power density was 12, "usually" was 2.7. Pressure broadening 40 MHz/mbar (FWHM at atomic frequency). Peak signal rises by factor of three from 1 to 5 mbar argon, then decreases by 6% by 15 mbar. Saturated absorption and intermodulated fluorescence spectroscopy show no change in intermediate "enhancing" levels with magnetic field. Nearest one photon resonance at 17006.294 cm^{-1} . Morgan X' $\Sigma_3^+(0,54) - \Sigma_3^+(3s + 5s)(25,54)$ Cooper X' $\Sigma_3^+(1,61) - \Sigma_3^+(?,61)$

Table E.4, continued overleaf

Wavenumber	Strength	Width	Comments
17005.490	SO 9.3 SB 9.0	WO 34 WB 26	
17005.122	SO 9.0 SB 8.7	WO 59 WB 63	
17004.49	SO 0.63 SB 0.45	WO 30 WB 53	
17004.4	SO 0.51 SB 0.46	WO 36 WB 39	
17002.49	SO 22.0 SB 18.0	WO 41 WB 28	
16960.369	SO 23.7 SB 26.1	WO 43 WB 92	Broadening 0.36 GHz/T.
16960.285			Morgan X $^1\xi_3^+ - ^1\pi_3$
16960.143	SO 26.1 SB 27.2	WO 49 WB 49	
16959.721	SO 0.4 SB 0.4	WO 29 WB 30	Morgan X $^1\xi_3^+ - ^1\xi_2^+(3s + 4d)$
16959.689	SO 0.8 SB 0.9	WO 192 WB 191	Large pedestal
16948.804	SO 0.3 SB 0.3	WO 33 WB 33	
16948.692	SO 0.4 SB 0.4	WO 25 WB 25	
16948.120			Morgan X $^1\xi_3^+ - ^1\pi_3$
16933.949	SO 0.94 SB 0.75	WO 42 WB 33	
16933.632	SO 24 SB 21	WO 83 WB 88	
16933.148	SO 1.1 SB 0.9	WO 42 WB 39	
16933.027	SO 0.17 SB 0.11	WO 65 WB 90	
16932.994	SO 0.4 SB 0.4	WO 62 WB 63	

Table E.4, continued overleaf

Wavenumber	Strength	Width	Comments
16927.014	SO 0.48 SB 0.46	WO 32 WB 29	
16926.285	SO 0.33 SB 0.32	WO 60 WB 72	
16925.507	SO 0.69 SB 0.6	WO 39 WB 37	
16925.267	SO 0.51 SB 0.42	WO 27 WB 23	
16923.970	SO 0.27 SB 0.18	WO 70 WB 70	
16923.653	SO 33 SB 30	WO 61 WB 60	
16922.688	SO 0.1 SB	WO 24 WB 24	
16922.710	SO 1.0 SB 0.8	WO 35 WB 36	
16922.453	SO 3.7 SB 2.8	WO 35 WB 41	Morgan X $^1\Sigma_3^+ - ^1\Sigma_3^+(3s + 5s)$
16914.988	SO 27 SB 27	WO 58 WB 58	
16914.952	SO 0.7 SB 0.7	WO 68 WB 68	Morgan X $^1\Sigma_3^+ - ^1\Sigma_3^+(3s + 5s)$
16898.435	SO 1.0 SB 1.0	WO 53 WB 56	
16890.408	SO 0.18	WO 150	Peak flattens out in field. Morgan X $^1\Sigma_3^+ - ^1\Sigma_3^+(3s + 5s)$
16883.27	SO 4.3		Active group of transitions; shows structure at zero magnetic field, and in an increasing magnetic field splits into a lone peak, which remains at the same frequency, and two group of peaks, one of which moves to higher frequencies at 1 GHz/T, while the other moves to lower frequencies. Single photon transition at 16883.286 cm^{-1} .
16883.00	SO 4.3		Two main peaks split from 200 MHz separation in zero field to 800 MHz separation at 0.13 T. Single photon transition at 16883.0 cm^{-1} .

Table E.4, continued overleaf

Wavenumber	Strength	Width	Comments
16850.574	SO 100 SB 94	WO 93 WB 79	Morgan $X^1Z_3^+ - Z_3^+(3s + 5s)$
16846.367	SO 0.9 SB 0.9	WO 30 WB 30	
16845.749	SO 6.3 SB 6.3	WO 27 WB 29	
16845.570	SO 35 SB 33	WO 36 WB 34	Morgan $X^1Z_3^+ - Z_3^+(3s + 5s)$
16844.677	SO 12 SB 7	WO 50 WB 113	Active doublet. Low frequency peak remains approx. constant, high frequency peak broadens. Morgan $X^1Z_3^+ - Z_3^+(3s + 4d)$
16817.349	SO 2.9 SB 1.4	WO 164 WB 250	Active doublet. Main peak broadens and moves up in frequency 1.4 GHz/T; subsidiary peak moves down in frequency at 7.4 GHz/T.
16816.321	SO 3.8 SB 3.6	WO 26 WB 28	
16815.89	SO 4.3 SB 4.2	WO 30 WB 32	Measurements taken at 1/10 usual fundamental power, Doppler free peak in dip at top of Doppler broadened peak.
16812.430	SO 1.1 SB 0.3	WO 250 WB 512	Structured peak at zero field, values listed here for 0.03 T field. Broadening 10 GHz/T.
16806.212	SO 14 SB 14	WO 55 WB 51	
16806.066	SO 5.6 SB 5.4	WO 42 WB 38	
16805.981	SO 0.6 SB 0.2	WO 52 WB 144	
16799.399	SO 1.9	WO 360	Structured Doppler free peak broadens and moves to higher frequency with increasing field, and another peak grows from zero at 5 GHz lower frequency. Doppler broadened UV peak grows by factor of 11. Small changes in fluorescence at visible frequencies.
16794.648	SO 13.5 SB 13.5	WO 25 WB 26	
16794.18	SO 22 SB 22	WO 33 WB 34	

Table E.4, continued overleaf

Wavenumber	Strength	Width	Comments
16793.971	S0 8.6 SB 8.7	WO 29 WB 26	
16789.676	S0 68 SB 65	WO 47 WB 44	Morgan X $^1\xi_3^+ - ^1\xi_3^+(3s + 5s)$
16785.423	S0 1.1 SB 1.0	WO 221 WB 235	Morgan X $^1\xi_3^+ - ^1\xi_3^+(3s + 5s)$
16785.087	S0 0.9 SB 1.0	WO 28 WB 28	
16781.785	S0 1.9 SB 1.8	WO 81 WB 98	Morgan X $^1\xi_3^+ - ^1\xi_3^+(3s + 5s)$
16779.668	S0 1.0 SB 2.0		Active group of transitions. Structured peak splits into two main components. No noticeable change in visible fluorescence.
16738.501	S0 8.4 SB 8.4	WO 32 WB 34	
16738.304	S0 1.5 SB 1.5	WO 35 WB 30	
16738.173	S0 1.9 SB 1.8	WO 32 WB 32	
16736.626	S0 1.0 SB 1.0	WO 27 WB 27	
16724.974	S0 0.5 SB 0.5	WO 240 WB 240	Morgan X $^1\xi_3^+ - ^1\xi_3^+(3s + 5s)$
16720.373	S0 74 SB 73	WO 61 WB 54	
16705.34	S0 2.1 SB 2.1	WO 52 WB 48	
16704.2	S0 0.5 SB 0.6	WO 30 WB 37	Morgan X $^1\xi_3^+ - ^1\xi_3^+(3s + 5s)$
16704.028	S0 50 SB 50	WO 45 WB 50	
16698.451	S0 3.4 SB 3.4	WO 29 WB 29	
16694.223	S0 4.5 SB 1.8	WO 261 WB 490	This and next line in list are magnetically active, decreasing their separation by 5.8 GHz/T. Morgan X $^1\xi_3^+ - ^1\xi_3^+(3s + 5s)$

Table E.4, continued overleaf.

Wavenumber	Strength	Width	Comments
16694.172	S0 4.5 SB 2.9	WO 178 WB 220	
16691.831	S0 0.8 SB 0.8	WO 28 WB 26	
16691.636	S0 1.2 SB 1.3	WO 29 WB 28	Morgan $X \xi_3^+ - \xi_9^+(3s + 5s)$
16691.376	S0 2.8 SB 2.7	WO 32 WB 32	
16690.646	S0 1.8 SB 1.8	WO 26 WB 27	
16689.952	S0 4.6 SB 4.5	WO 32 WB 38	
16672.623	S0 8.8 SB 8.1	WO 56 WB 47	Morgan $X \xi_3^+ - \xi_9^+(3s + 5s)$
16668.783	S0 12 SB 11	WO 65 WB 58	
16635.5	S0 20 SB 19	WO 57 WB 57	Morgan $X \xi_3^+ - \xi_9^+(3s + 5s)$
16614.4	S0 36 SB 35	WO 55 WB 50	Morgan $X \xi_3^+ - \xi_9^+(3s + 5s)$
16612.2	S0 1.3 SB 1.2	WO 21 WB 23	
16611.9	S0 0.6 SB 0.6	WO 144 WB 156	Morgan $X \xi_3^+ - \xi_9^+(3s + 4d)$
16610.7	S0 0.4 SB 0.4	WO 180 WB 190	
16609.41	S0 1.0 SB 0.4	WO 380 WB2900	Structured peak. Total pattern width increases at 20 GHz/T.
16601.8	S0 30 SB 29	WO 61 WB 63	Line studied in detail by Woerdman [150]. Morgan $X \xi_3^+ - \xi_9^+(3s + 5s)$
16583.6	S0 28 SB 28	WO 41 WB 42	Morgan $X \xi_3^+ - \xi_9^+(3s + 5s)$

Table E.4 (continued). Observed Doppler-free two-photon transitions in the sodium vapour. S0 and SB are the peak heights of the two-photon absorption trace at 0 and 0.13 T magnetic fields respectively. WO and WB are the linewidths (FWHM at the laser frequency) of the transitions under the same conditions, measured in MHz. See text for further comments.

REFERENCES

REFERENCES

- 1] P A Franken, A E Hill, C W Peters, and E Weinreich, Phys. Rev. Lett. **7**, 118 (1961).
- 2] L G Cohen and C Lin, J. Quantum Electron. **QE-14**, 855 (1978).
- 3] R G Smith, Appl. Opt. **11**, 2489 (1972).
- 4] R W Minck, R W Terhune, and C W Wang, Proc. IEEE **54**, 1357 (1966).
- 5] N Bloembergen, Rev. Mod. Phys. **54**, 685 (1982).
- 6] Y R Shen, "The Principles of Nonlinear Optics" (Wiley, New York, 1984).
- 7] F Zernike and J Midwinter, "Applied Nonlinear Optics" (Wiley, New York, 1973).
- 8] C E Dunn, "The Development of a Single-Frequency, Frequency-Doubled, Ring Dye Laser, and its Application to High Resolution Spectroscopy in the Ultraviolet" (PhD thesis, University of St Andrews, 1982).
- 9] D M Kane, "Atomic Laser Spectroscopy in the UV and Visible" (PhD thesis, University of St Andrews, 1983).
- 10] D S Bethune, R W Smith, and Y R Shen, Phys. Rev. A **17**, 277 (1978).
- 11] P A Franken and J F Ward, Rev. Mod. Phys. **35**, 23 (1963).
- 12] A Yariv, "Quantum Electronics" (2nd edition, Wiley, New York, 1975).
- 13] Quantel Nd:YAG laser model YG480, instruction manual.
- 14] D C Hanna, M A Yuratich, and D Cotter, "Nonlinear Optics of Free Atoms and Molecules" (Springer Verlag, Berlin, 1979).
- 15] M Göppert-Mayer, Ann. der Physik **9**, 273 (1931).
- 16] N Bloembergen and M D Levenson, in "High Resolution Laser Spectroscopy", edited by K Shimoda (Springer Verlag, Berlin, 1976).

- 17] G Grynberg and B Cagnac, *Rep. Prog. Phys.* **40**, 791 (1977).
- 18] M H Dunn, *Opt. Commun.* **45**, 346 (1983).
- 19] N Bloembergen and Y R Shen, *Phys. Rev.* **133**, A37 (1964).
- 20] B W Shore and D H Menzel, "Principles of Atomic Spectra" (Wiley, New York, 1968).
- 21] G K Woodgate, "Elementary Atomic Structure" (Clarendon Press, Oxford, 1980).
- 22] D S Bethune, R W Smith, and Y R Shen, *Phys. Rev. Lett.* **38**, 647 (1977).
- 23] R W Terhune, P D Maker, and C M Savage, *Phys. Rev. Lett.* **8**, 404 (1962).
- 24] P S Pershan, *Phys. Rev.* **130**, 919 (1963).
- 25] J A Litwin, J E Snipe, and H M van Driel, *Phys. Rev. B.* **31**, 5543 (1985).
- 26] G Mayer, *C. R. Acad. Sci. Paris Serie B* **54**, 267 (1968).
- 27] G Hauchecorne, F Kerherve, and G Mayer, *Jour. de Physique* **32**, 47 (1971).
- 28] R S Finn and J F Ward, *Phys. Rev. Lett.* **26**, 285 (1971).
- 29] S Kielich, *Chem. Phys. Lett.* **2**, 569 (1968).
- 30] S Kielich, *IEEE J. Quantum Electron.* **QE-5**, 562 (1969).
- 31] A D Buckingham and B J Orr, *Quarterly Rev. Chem. Soc.* **21**, 195 (1967).
- 32] J F Ward and I J Bigio, *Phys. Rev. A* **11**, 60 (1975).
- 33] V Mizrahi and D P Shelton, *Phys. Rev. A* **31**, 3145 (1985).
- 34] I J Bigio and J F Ward, *Phys. Rev. A* **9**, 35 (1974).
- 35] R S Finn and J F Ward, *J. Chem. Phys.* **60**, 454 (1974).
- 36] C K Miller and J F Ward, *Phys. Rev. A* **16**, 1179 (1977).
- 37] J F Ward and D S Elliott, *J. Chem. Phys.* **69**, 5438 (1978).
- 38] J F Ward and C K Miller, *Phys. Rev. A* **19**, 826 (1979).
- 39] D P Shelton and A D Buckingham, *Phys. Rev. A* **26**, 2787 (1982).

- 40] H F Hameka and E N Svendsen, *Int. J. Quantum Chem: Quantum Chem. Symp.* **18**, 525 (1984).
- 41] D S Elliott and J F Ward, *Molec. Phys.* **51**, 45 (1984).
- 42] J W Dudley and J F Ward, *J. Chem. Phys.* **82**, 4673 (1985).
- 43] V Mizrahi and D P Shelton, *Phys. Rev. Lett.* **55**, 696 (1985).
- 44] V Mizrahi and D P Shelton, *Phys. Rev. A* **32**, 3454 (1985).
- 45] B F Levine and C G Bethea, *Appl. Phys. Lett.* **24**, 445 (1974).
- 46] B F Levine and C G Bethea, *J. Chem. Phys.* **60**, 3856 (1974).
- 47] B F Levine and C G Bethea, *J. Chem. Phys.* **65**, 2429 (1976).
- 48] B F Levine and C G Bethea, *J. Chem. Phys.* **65**, 2439 (1976).
- 49] T S Song, C H Cho, J H Lee, and J S Chang, *New Phys. (Korean Phys. Soc.)* **24**, 300 (1984).
- 50] G M Krochik and Y G Khronopolo, *Sov. J. Quantum Electron.* **4**, 1076 (1975).
- 51] R L Abrams, A Yariv, and P A Yeh, *IEEE J. Quantum Electron.* **QE-13**, 79 (1977).
- 52] R L Abrams, C K Asawa, T K Plant, and A E Popa, *IEEE J. Quantum Electron.* **QE-13**, 82 (1977).
- 53] D S Bethune, R W Smith, and Y R Shen, in "Coherence and Quantum Optics IV", edited L Mandel and E Wolf (Plenum, New York, 1978).
- 54] R W Boyd and L Q Xiang, *IEEE J. Quantum Electron.* **QE-18**, 1242 (1982).
- 55] D J Gauthier, J Krasinski, and R W Boyd, *Opt. Lett.* **8**, 211 (1983).
- 56] R W Boyd, D J Gauthier, J Krasinski, and M S Malcuit, *J. Opt. Soc. America B* **1**, 507 (1984).
- 57] R W Boyd, D J Gauthier, J Krasinski, and M S Malcuit, *IEEE J. Quantum Electron.* **QE-20**, 1074 (1984).
- 58] I J Bigio, R S Finn, and J F Ward, *Appl. Opt.* **14**, 336 (1975).
- 59] J K Guha, *Appl. Opt.* **15**, 2381 (1976).

- 60] C G Bethea, *Appl. Opt.* **14**, 2435 (1975).
- 61] J W Dudley and J F Ward, *Appl. Opt.* **20**, 1777 (1981).
- 62] Y T Lam and T Thirunamachandran, *J. Chem. Phys.* **77**, 3810 (1982).
- 63] D P Shelton and V Mizrahi, *Phys. Rev. A* **33**, 72 (1986).
- 64] V Mizrahi and D P Shelton, *Phys. Rev. A* **33**, 1396 (1986).
- 65] T Mossberg, A Flusberg, and S R Hartmann, *Opt. Commun.* **25**, 121 (1978).
- 66] K Miyazaki, T Sato, and H Kashiwagi, *Phys. Rev. Lett.* **43**, 1154 (1979).
- 67] J Heinrich and W Behmenburg, *Appl. Phys.* **23**, 333 (1980).
- 68] K Miyazaki, T Sato, and H Kashiwagi, *Phys. Rev. A* **23**, 1358 (1981).
- 69] J Okada, Y Fukuda, and M Matsuoka, *J. Phys. Soc. Japan* **50**, 1301 (1981).
- 70] J Bokor, R R Freeman, R L Panock, and J C White, *Opt. Lett.* **6**, 182 (1981).
- 71] D S Bethune, *Phys. Rev. A* **23**, 3139 (1981).
- 72] D S Bethune, *Phys. Rev. A* **25**, 2845(E) (1982).
- 73] V G Arkhipkin, N P Makarov, A K Popov, V P Timofeev, and V S Epstein, *Opt. and Quantum Electron.* **13**, 436 (1981).
- 74] V G Arkhipkin, N P Makarov, A K Popov, V P Timofeev, and V S Epstein, *Sov. J. Quantum Electron.* **11**, 656 (1981).
- 75] R R Freeman, J E Bjorkholm, R Panock, and W E Cooke, in "Laser Spectroscopy V" edited A R W McKellar, T Oka, and B P Stoicheff (Springer Verlag, Berlin, 1981).
- 76] R R Freeman, R Panock, and J E Bjorkholm, *IEEE J. Quantum Electron.* **QE-17**, 10 (1981).
- 77] W Jamroz, P E Laroque, and B P Stoicheff, *Opt. Lett.* **7**, 148 (1982).
- 78] S Dinev, A de Garia, P Meystre, R Salomaa, and H Walther, in "Laser Spectroscopy VI" edited H P Weber and W Luthy (Springer Verlag, Berlin, 1983).

- 79] V A Kiyashko, A K Popov, V P Timofeev, N P Makarov, and V S Epstein, Sov. J. Quantum Electron. **14**, 1645 (1984).
- 80] V A Kiyashko, A K Popov, V P Timofeev, N P Makarov, and V S Epstein, Appl. Phys. **B 36**, 53 (1985).
- 81] D S Bethune, Opt. Lett. **6**, 287 (1981).
- 82] W J Duffin, "Advanced Electricity and Magnetism" (McGraw Hill, London, 1968).
- 83] H A Bethe and E E Saltpeter, "Quantum Mechanics of One and Two Electron Atoms" (Plenum, New York, 1977).
- 84] E U Condon and G H Shortley, "The Theory of Atomic Spectra" (Cambridge Univ. Press, 1953).
- 85] J D Jackson, "Classical Electrodynamics" (Wiley, New York, 1962).
- 86] R H Garstang, in "Atomic and Molecular Processes" edited D R Bates (Academic Press, New York, 1962).
- 87] D S Bethune, R W Smith, and Y R Shen, Phys. Rev. Lett. **37**, 431 (1976).
- 88] A Flusberg, T Mossberg, and S R Hartmann, Phys. Rev. Lett. **38**, 694 (1977).
- 89] A Flusberg, T Mossberg, and S R Hartmann, in "Coherence and Quantum Optics IV", edited L Mandel and E Wolf (Plenum, New York, 1978).
- 90] B Couillard and A Ducasse, Phys. Rev. Lett. **35**, 1276 (1976).
- 91] P F Liao and G C Bjorklund, Phys. Rev. Lett. **36**, 584 (1976).
- 92] C E Tull, M Jackson, R P McEachran, and M Cohen, Can. J. Phys. **50**, 1169 (1972).
- 93] T Hansch and P Toschek, Z. Physik **236**, 373 (1970).
- 94] A Flusberg, T Mossberg, and S R Hartmann, Phys. Rev. Lett **38**, 59 (1977).
- 95] M Matsuoka, H Nakatsuka, H Uchiki, and M Mitsunaga, Phys. Rev. Lett. **38**, 894 (1977).

- 96] H Uchiki, H Nakatsuka, and M Matsuoka, *Opt. Commun.* **30**, 345 (1979).
- 97] H Uchiki, H Nakatsuka, and M Matsuoka, *J. Phys. Soc. Japan* **52**, 3010 (1983).
- 98] L Yiqun, *Chinese J. Lasers* **12**, 568 (1985).
- 99] B D Sinclair and M H Dunn, *Phys. Rev. A* **34**, 3989 (1986).
- 100] B D Sinclair and M H Dunn, *J. Opt. Soc. America B* **3**, P120 (1986).
- 101] E Arimondo, M Ingusio, and P Violino, *Rev. Mod. Phys.* **49**, 31 (1977).
- 102] A Beckmann, K D Boklen, and D Elke, *Z. Physik.* **270**, 173 (1974).
- 103] Y W Chan, V W Cohen, and H B Silsbee, *Bull. Am. Phys. Soc.* **15**, 1521 (1970).
- 104] G Breit and I I Rabi, *Phys. Rev.* **38**, 2082L (1931).
- 105] N F Ramsey, "Molecular Beams", (Oxford University Press, 1956).
- 106] C Fabre, M Gross, and S Haroche, *Opt. Commun.* **13**, 393 (1975).
- 107] H Walther, in "Laser Spectroscopy of Atoms and Molecules", edited H Walther (Springer Verlag, Berlin, 1976).
- 108] R W Meissner and R F Luft, *Ann. Phys.* **29**, 698 (1937).
- 109] D R Beck and H Odabasi, *Ann. Phys.* **67**, 274 (1971).
- 110] D Pritchard, J Apt, and T W Ducas, *Phys. Rev. Lett.* **32**, 641 (1974).
- 111] T W Hansch, K C Harvey, G Meisel, and A L Schawlow, *Opt. Commun.* **11**, 50 (1974).
- 112] K Fredriksson and S Svanberg, *Phys. Lett.* **53A**, 61 (1975).
- 113] P S Shenck and H S Piloff, *Bull. Am. Phys. Soc.* **20**, 678 (1975).
- 114] A R Edmonds, "Angular Momentum in Quantum Mechanics" (Princeton University Press, 1957).
- 115] B D Fried and S D Conte, "The Plasma Dispersion Function, The Hilbert Transform of the Gaussian" (Academic Press, New York, 1961).
- 116] S G Lipson and H Lipson, "Optical Physics" (Cambridge University Press, 1969).
- 117] F P Schafer (editor), "Dye Lasers", (Springer Verlag, Berlin, 1977).

- 118] Spectra Physics Model 380D Frequency Stabilized Dye Laser
Instruction Manual.
- 119] F V Kowalski, R T Hawkins, and A L Schawlow, *J. Opt. Soc. America*
66, 695 (1976).
- 120] F V Kowalski, R E Teets, W Demtroder, and A L Schawlow, *J. Opt. Soc.
America* **68**, 1611 (1978).
- 121] S Gerstenkorn and P Luc, "Atlas du spectre d'absorption de la
molecule d'iode, 14800 - 20000 cm^{-1} ", (CNRS, Paris, 1978).
- 122] "CRC Handbook of Chemistry and Physics, 63rd Edition", edited R C
Weast and M J Astle (CRC Press, Florida, 1982).
- 123] A N Nesmayanov, "Vapour Pressure of the Elements" (Infosearch,
London, 1963).
- 124] R B Miles and S E Harris, *IEEE J. Quantum Electron.* **QE-9**, 470
(1973).
- 125] M Lapp and L P Harris, *J. Quant. Spectrosc. Radiat. Transfer* **6**, 169
(1966).
- 126] J P Woerdman, *Chem. Phys. Lett.* **43**, 279 (1976).
- 127] C R Vidal and J Cooper, *J. Appl. Phys.* **40**, 3370 (1969).
- 128] Hamamatsu Photomultiplier Tube Catalogue (1986).
- 129] V S Letokhov and V P Chebotayev (editors), "Nonlinear Laser
Spectroscopy" (Springer Verlag, Berlin, 1977).
- 130] W L Wiese, M W Smith, and B M Miles, "Atomic Transition
Probabilities, Volume Two, Sodium through Calcium" (US Dept. of
Commerce, Nat. Bur. Standards, Washington, 1969).
- 131] F Biraben, B Cagnac, E Giacobino, and G Grynberg, *J. Phys. B: Atom.
and Molec. Phys.* **10**, 2369 (1977).
- 132] P F Liao, N P Economou, and R R Freeman, *Phys. Rev. Lett.* **39**, 1473
(1977).
- 133] T Mossberg, A Flusberg, R Kachru, and S R Hartmann, *Phys. Rev. Lett.*
39, 1523 (1977).

- 134] D M Bruce, M Y Mirza, and W W Duley, *Opt. Commun.* **27**, 76 (1978).
- 135] J F Ward and G H C New, *Phys. Rev.* **185**, 57 (1969).
- 136] H R Hindmarsh and J M Farr, *Prog. Quantum Electron.* **2**, 141 (1972).
- 137] S Ch'en and M Takeo, *Rev. Mod. Phys.* **29**, 20 (1957).
- 138] H Margenau and W Watson, *Rev. Mod. Phys.* **8**, 22 (1936).
- 139] R G Beausoleil, "Continuous-wave Measurement of the 1S - 2S Transition Frequency in Atomic Hydrogen: The 1S Lamb Shift" (Thesis, Stanford University, 1986).
- 140] D M Bloom, J F Young, and S E Harris, *Appl. Phys. Lett.* **27**, 390 (1975).
- 141] H S Wall, "Analytic Theory of Continued Fractions" (Van Nostrand, Toronto, 1948).
- 142] A Poustie, "Computerised Data Recording and Analysis of a High Resolution Spectroscopy Experiment" (Report to Carnegie and Physics Trusts, 1985).
- 143] G P Morgan, H R Xia, and A L Schawlow, *J. Opt. Soc. America* **72**, 315 (1982).
- 144] G Herzberg, "Molecular Spectra and Molecular Structure, Spectra of Diatomic Molecules" (Van Nostrand, New York, 1950).
- 145] G P Morgan, "Identification of cw Two-Photon Transitions in Na₂ and NaK" (Thesis, Stanford University, 1983).
- 146] D L Cooper, R F Barrow, J Verges, C Effantin, and J D'Incan, *Can. J. Phys.* **62**, 1543 (1984); *Chem. Phys. Lett.* **114**, 483 (1985); and references therein.
- 147] A L Schawlow, private communication.
- 148] G Y Yan, private communication.
- 149] C Effantin, O Babaky, K Hussein, J D'Incan, and R F Barrow, *J. Phys. B:Atom and Molec. Phys.* **18**, 4077 (1985).
- 150] J P Woerdman, *Phys. Lett.* **69A**, 18 (1978), and references therein.